Molecular Dynamics of Kapitza Resistance at the Solid-Liquid Interface of Nanofluidic Channels

By

Michael Tamuno Elekima Kio

A THESIS SUBMITTED TO CRANFIELD UNIVERSITY

IN PARTIAL FULFILMENT OF THE REQUIREMENTS

FOR THE DEGREE OF

DOCTOR OF PHILOSOPHY

Cranfield University

Centre for Fluid Mechanics and Computational Science

Institute of Aerospace Sciences

School of Aerospace Transport and Manufacturing

2014

1

[1]This page is intentionally left blank

CRANFIELD UNIVERSITY

INSTITUTE OF AEROSPACE SCIENCES

SCHOOL OF AEROSPACE TRANSPORT AND MANUFACTURING

PHD THESIS

2014

MICHAEL TAMUNO ELEKIMA KIO

Molecular Dynamics of Kapitza Resistance at the Solid-Liquid Interface of Nanofluidic Channels

Supervisors: Dr L*ászló* K*önözsy* and Professor Dimitris Drikakis

Cranfield University, 2014.

[2]This page is intentionally left blank

Except where acknowledged in the customary manner, the material presented in this thesis is, to the best of my knowledge, original and has not been submitted in whole or part for a degree in any university.

_____

Name of the Student

[3]This page is intentionally left blank

Abstract

This project sought to study the heat transfer and Kapitza resistance of fluids across interfaces, nanopores and nanochannels with varying stiffness constants, mass and energy intermolecular interaction strength of wall and fluid particles. An Einstein-Maxwell molecular dynamics thermal wall model is developed. The developed modeling approach is shown to provide dual energy and momentum transport exchange across solid-liquid interfaces and nanofluidic channels. A computational domain is implemented, using spring potential, ranging from 100-8000$\varepsilon\sigma^{-2}$ in two parallel walls. In the first detailed study a wall-fluid interaction molecular dynamic thermal wall model is developed to investigate the effect of mass of the wall particles on the Kapitza resistance, temperature profile and density distribution across the solid-liquid interface and nanofluidic channel. The results revealed that for low values of surface stiffness, the thermal resistance is dictated by the value of the mass. The results also reveal that the temperature jump at the solid interface is not accurately described by the theoretical vibrational frequency $\sqrt{\kappa/m_w}$ of the walls but increases as a fifth-order polynomial with respect to $log(m_w k)$, where the rate of increase gradually decays until the curve reaches a plateau. The second study develops a wall-wall interaction molecular dynamics thermal wall model. The model is implemented to investigate the effect of energy intermolecular interaction strength of wall particles, on the Kapitza resistance at the solid-liquid interface, temperature profile and density distribution across a nanofluidic channel with simple harmonics of a lattice system. The finding aided in the understanding of heat transport and Kapitza resistance due to the intermolecular interaction energy strength of the walls on the solid-liquid interface and across the nanofluidic channel. The results revealed, an increase in Kapitza resistance for higher values of wall bonding stiffness κ, and lower values for wall particle energy intermolecular interaction strength. The third study implements and combines the wall-wall and wall-fluid thermal wall models that have been developed to investigate the wall size effect on the Kapitza resistance, temperature profile, and density distribution of fluid molecules across the solid-liquid interfaces and nanofluidic channels. The investigation reveal an increase in thermal transport and Kapitza resistance across the nanopore as the wall size and fluid molecular layer becomes smaller due to fewer bulk-like liquid layers formed. The MD wall models were compared with analytical models, which include Acoustic mismatch model (AMM), Diffuse mismatch model (DMM) and Lattice dynamic model (LDM) with good agreement obtained. This study has increased our physical understanding regarding nano-scale phenomena of fluid flow, thermal transport and Kapitza resistance across interfaces, thin films and nanofluidc channels by implementing molecular dynamic atomistic modelling.

4

[4]This page is intentionally left blank

Acknowledgements

Sincere thanks goes to our Lord Jesus Christ for his love, inspiration and guidance towards the successful completion of this programme. Special gratitude to my supervisors, Dr. Nikolaos Asproulis, Professor Dimitris Drikakis and Dr László Könözsy of the Centre for Fluid Mechanics and Computational Science for their constant help, support, encouragement and supervision which contributed to the timely completion of this thesis. Gratitude also to Andy Gittings of the Cranfield High Performance Computing Unit for helping me with the High Power Computing end. Sincere thanks to my parents Rev and Mrs. Sunday Bethuel Kio for their moral/financial support and leading me down the right path till this stage of my life. Gratitude is expressed to the chairman and members of the Dissertation committee Prof Peter Malkin, Prof Patrick Luk and Dr Antoniadis Antonios for their valuable contributions during the development of this thesis and review process. Thanks to Professor David Mba and Dr Stephen Ogaji for their mentorship and guidance through the entire duration of the Ph.D. programme. Sincere thanks also goes to the pastor of Holding Forth Bible Church, senior pastor Biyi Ajala for his counsel, moral and spiritual support and encouragement. Thanks to Dr Uyioghosa Igie, Dr. Daniel Kamunge, Dr. Patrick Oduguwa, Dr. Sola Adesola, Dr. Crispin Allison, and Dr.Gareth David for the mock viva and initially proofreading this dissertation. Thanks to National Space Research and Development Agency (NASRDA) for the sponsorship of this programme. Thanks also to my friends Deacon leye, Dr Christos Barmparousis and Martins Brown for their friendship and support during the whole process of this journey. Thanks to my friends Corentin, Sophie, Veranga, Yuji, Lam, and all others of Cranfield lawn tennis club for the good times and winter tennis sessions. Finally, special thanks goes to my wonderful wife Mrs. Tema Kio-Michael and excellent children Nimi and Nengi for their love, prayers, understanding and confidence in me, which motivated me to maintain focus till the end of this Ph.D. programme. This thesis is dedicated to my wonderful wife Tema Alawari Kio-Michael without whose continous commitment, encouragement and support, it would have been a challenge in the completion of this programme.

5

[5]This page is intentionally left blank

Contents

List of Figures

List of Tables

Nomenclature

Symbol	Definition
a	Unit cell
c	Speed of sound
m	Mass
k	Thermal conductivity
vr	Potential energy
v	Velocity vector
p	Periodicity
q	Heat flux
rc	Cut-off radius
ro	Distance of nearest neigbour
A	Area
C	Chirality
D	Dissociation energy
E	Total energy
F	Force vector
K	Kapitza resistance
L	Length
N	Number of atoms
P	Pressure
T,ΔT	Temperature, change in temperature
H	Hamiltonian
r,rij	Position vector distance of seperation
k_B	Boltzman constant
t, δt	Time, time step
Greek symbols	
ζ	Thermostat multiplier
θ	Bond angle
ρ	Density
σ	Lennard jones lenght parameter
χ	Velocity scaling factor
μ	Transmission coefficient
ϕ	Angle

ω	Frequency
τ	Relaxation time
ϵ	Lennard jones energy parameter
η	Viscosity
ϕ	Dihedral
Subscripts	
e_{wf}	Wall-Fluid molecular interaction strength
e_{ww}	Wall-Wall molecular interaction strength
w-w	Wall-wall
f-f	Fluid-fluid
ne	Nonequilibrium
eq	Equilibrium
Prefixes	
n	nano ($\times 10^{-9}$)
f	Femto ($\times 10^{-15}$)
m	meter
nm	nanometer
Abbreviation	
ZT	Figure of merit
MD	Molecular dynaimics
NS	Navier-stokes equation
EDL	Electrostatic diffuse layer
NVE	Number of atoms,volume and energy of system
FCC	Face centered cubic
CNT	Carbon-nanotube
BTE	Boltzman transpot equation
CSS	Carbon storage system
AMM	Acoustic Mismatch Model
DMM	Diffuse Mismatch Model
LDM	Lattice Dynamics Model

Chapter 1

Introduction

The end of the 19th and 20th century saw important advances in Nanotechnology. This has offered the improvement of performance in devices and across applications such as food, information technology, aerospace, cosmetics, medicine and entertainment. Currently, more than 32% of scientific publications from the European Union are related to the field of Nano-technology [1]. Experimental, computational, and theoretical investigations have over the years aided in an increased and detailed understanding of molecular scale phenomena. Experiments have been reported to predict global properties such as the frictional force, shear response, relaxation time in ultra-thin liquid films; however, the direct extraction of significant local variables in the nano-scale such as pressure, temperature and density is still beyond the scope of experiments. Currently, these local variables can only be obtained by computer simulations due to the increased speed and processing power of modern computers. Computer simulations applied to fluids can either be achieved, using the continuum hypothesis or from first principle. The first principle approach uses Molecular Dynamics (MD), which is the approach used in this study.

Molecular Dynamics is a method that simulates physical movements of atoms and molecules by means of computer codes. The study of Molecular Dynamics (MD) in Meso and Nano-scale is an expanding and interesting area in Computational Nanotechnology and interfacial studies, which are concerned with measurements ranging between 0.1nm-100nm ($1nm = 10^9m$). Molecular Dynamics simulate atoms and molecules as point masses whose motions are obeyed by Newton's equations [2].

Interfaces and thin films are prevalent in aeronautical, medical and electronic devices. Transistors with Sio_2 dielectric compartments can have diameters of up to $1nm$, with some other types of transistors having a gate length of $10nm$. As transistors become smaller processors become more efficient and heat removal becomes a challenge [3-4]. Thermal transport is prevalent in

semi-conductor transistors, and is made possible by phonons and impedements that cause thermal resistance [5-7]. Therefore, reducing the thermal resistance or Kapitza resistance in silicon interfaces located inside processors will aid better themal interfacial transport out of the transistors, which enhances the reliability and performance of the system [8-10].

Detailed knowledge of the Kapitza resistance in interfaces leads to improvement of energy conversion efficiency in thermoelectric devices and an increase in thermal conductivity enhancement in nanofluids. Various commercially available thermoelectric materials such as Si-Ge alloys and Bi_2Te_3 have a figure of merit, $ZT \simeq 1$ at maximum operating temperature [11-12]. For deep space missions involving the stabilization of temperatures, materials with figure of merit $ZT > 4$ are required, to match their efficiency with traditional thermoelectric devices. Such high figures of merit can only be achieved by increasing the Kapitza resistance of the thermoelectric material. This phenomenon has aided the engineering and increase of $ZT > 2.4$ by the aid of molecular dynamics [13-14].

To solve the challenge of thermal management and large interfacial density, engineers are required to design devices and materials with large figure of merit (ZT). Therefore, accurate and good physical models that describe thermal transport, and Kapitza resistance in interfaces, thin films, superlattices and nanofluidic channels are required. The existing models are mostly based on traditional Fourier and Snell's law and do not accurately predict the bahavior of thermal transport and Kapitza resistance in nanoscale interfaces. Molecular dynamics take into consideration the molecular interaction of surface particles and describes interface distances on the same regime as the mean free path of the energy carrier (phonons) in bulk materials. This makes it very suitable for studying nano-scale thermal interfacial phenomena.

1.0.1 Continuum and Molecular Regime

The nanometer by definition is 1-billionth of a meter, to put this in perspective, a strand of black hair has a diameter between 50,000-180,000 nanometers, and the diameter of a strand of blond hair is likely to be 15,000-50,000 nanometers. Nanofluidics have recently been playing a role in the area of microfluidics and tends to also benefit continuum scale applications. Nanofluidics provide solutions for nano-length scales where matter behaves differently from known phenomena. Leading to the understanding of specific and special phenomena or things that occur in the transport of fluid when contained in channels of nano-metric scale. From the point of length scale and time scale, the possible use of Navier-Stokes equation (NS) up to 10nm length scale and time scale of $\tau_0 \sim 10^{-12}$ has been implemented to model fluid flow, viscosity η bulk transport coefficients and thermal transport of water in nanometric confinement. However, below 10nm the viscosity η can

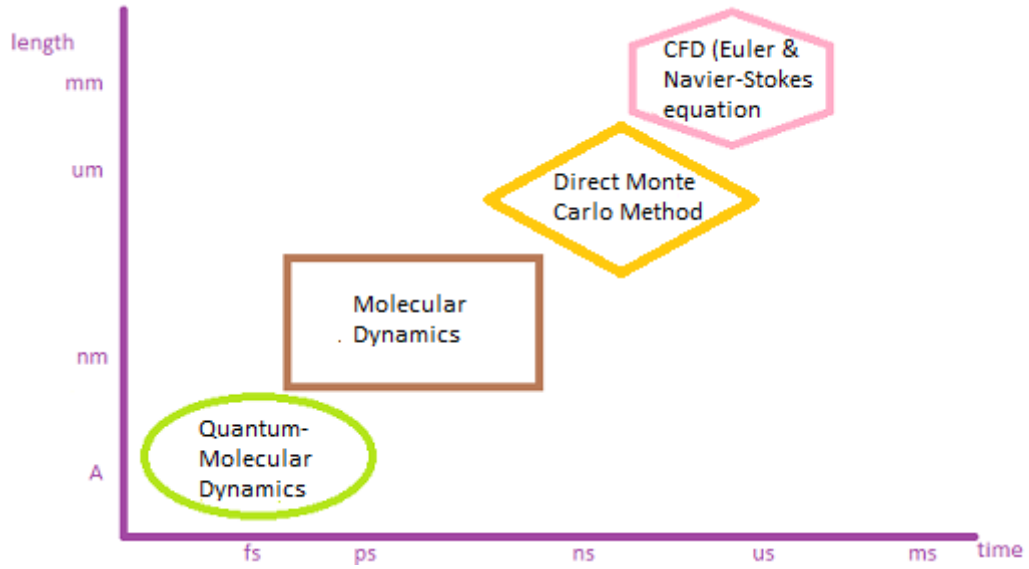

Figure 1.1: Continuum and free molecular transition.

no longer be predicted using the Navier-Stokes Equation (NS).

The continuum approach breaks down during surface to volume interaction, where the Knudsen number is ≥ 10 describing the free molecular range. This means that, the equations and formulations used to obtain the solutions of interested quantities in the continuum regime can not be applied at this regime. Fig. 1.1 shows the time and lenght scales with models applied from the molecular to the continuum regime.

Most molecular scales encompass the electrostatic diffuse layer (EDL), which is a diffused layer of ions that appear on the surface of a material on exposure to fluid. The diffuse-layer has an important role in most known substances, e.g. milk, which exists because fat droplets are encapsulated with a diffused layer that prevents them from been cooagulated into butter. The diffuse-layer is also present in virtually all heterogeneous fluid systems like paint, ceramic, cement slurry, ink and blood. The EDL is not affected by the charge on the surface of the material but is influenced by the density or (bulk ion concentration).

The debye length that measures the charge carriers net electrostatic effect and its surrounding in solution is imperative in the field of nanofluidics, this region characterises the fluids that are close to the charged surfaces, where charge electroneutrality vanishes, meaning volume electric forces becomes negligible and even non-existent, as the charge density ($\rho_e \rightarrow 0$) tends to go away from the surface. Manipulating the properties of the fluid particles in the EDL, will affect the response of the whole system, even up to the macroscopic scale that is much bigger than the debye length. The practical aspect of the debye length is the presence of debye layer which overlaps, and can be attained in fabrication at the nanoscale that produces nanopores in 1-dimension at 10nm range.

Another important parameter is the phenomenon that holds some molecules down the surface of an object, known as the slip length (b), when compared with a pore size, can enhance fluid and thermal transport and pressure drop, along a nanofluidic channel. For ideal gases the slip length is approximated as $\beta \approx 1.15l$, where l is the mean free path. The debye length can also affect and be compared to the slip length. The relation can also be compared to the Kapitza length, which is an allegory of slip length that characterises thermal transport boundary condition across interfaces. The last parameter that is worth mentioning is the flow rate in nanofluidic channels.

Recently nanofluidic channels have been reported to have upper bounds that don't impose flow rates, with friction on the surface of the bound relatively subtle. Flow rate in nanofluidic channels are mostly determined by end effect friction [15]. Nanochannels present in carbon-nanotube (CNT) and aquaporins have been reported to have high flow rates when compared to micro and macro-channels. Membranes made of carbon-nanotubes have been shown to have flow rates of 100-100,00 times higher than most conventional membranes measured [16-19].

Despite five decades of research, realistic and accurate physics and models for describing and studying Kapitza resistance across interfaces in semi-conductors, nanopores and nanochannels are scarce and unavailable due to uncertainty in comparing experimental measurements and theoretical predictions. Molecular dynamics simulation and modelling has been predicted to address the challenge of accurately describing the physical reality at the nano-scale, thereby connecting experimental and theoretical models [2]. The MD model developed in this research will reduce the uncertainties associated with accurately describing the physics involved in heat transfer and Kapitza resistance across solid-liquid interfaces and nanofluidic channels.

1.0.2 Project Motivation

The field of microelectronics demands miniscule and better energy efficient devices. These devices with silicon have been manufactured from the process of 65nm dimension in the 2000s to 15nm in the most recent intel processors. The trend will continue beyond the 2030's with devices having required dimensions of 1-2nm likely, applying materials alternative to silicon. Therefore, there is a need to develop computational modelling paradigms to aid the implementation and interpretation of experiments guiding the development of alternative and smaller silicon materials.

Space technology applications require manned and unmanned spacecraft thermal control devices that uses interface materials that are fusible, a detailed knowledge of solid-liquid interface is needed to undertake excellent thermal design of spacecraft systems. The phenomena of heat transfer, Kapitza resistance, diffusion rate and rate of heat dissipation in spacecraft thermal control sub-system mostly occur in the nanoscale, with lack of detailed understanding and modelling causing

Figure 1.2: Sabatier Assembly; Co_2 Removal System in the International Space Station [Node 3]. See in [213] CDRA.

component degradation and malfunction, which can leading to the loss of spacecrafts.

Frequently flying modules, and nodes on board the international space station (ISS) to meet carbon-dioxide/oxygen eradication requirement will be too expensive, making their application impractical. Currently, the International Space Station (ISS) have the carbon-dioxide removal system (CDRA) using zeolite membranes, multifilters for advanced water recovery and the new Sabatier assembly Fig.1.2. More efficient and cheaper operations can be achieved in the ISS with reusable and optimized nanoporous membranes.

The installation of nanomembrane filters in aero-engines gasification units and the introduction of nano-thermal barrier coatings in jet-engines can reduce fuel consumption and greenhouse gases emited from their exhaust. These applications are beginning to generate interest, making relevant research significant.

Applying MD studies in the understanding of heat transfer and adsorption in nanofluidic channels and across interfaces have been proposed to aid in the designing, optimization and development of novel and more efficient commercial filters and thermal resistance barrier coatings [19].

1.0.3 Aim and Objectives and Research

The aim of this project is stated thus:
To increase the physical understanding regarding thermal transport and Kapitza resistance phenomena across interfaces and nanonofluidic channels, guiding experimental interpretation and enhancing theoretical models, implementing molecular dynamics atomistic modelling.

To achieve this aim the objectives are as follows:

- To develop Maxwel-Einstien solid molecular dynamics thermal wall and geometrical models using Large Atomic-Molecular Massively Parrallel Simulator (LAMMPS).

- To investigate the effect of mass of the wall particles on the Kapitza resistance, temperature profile and density distribution across solid-liquid interfaces and nanofluidic channels.
- To investigate the effect of energy intermolecular interaction strength of wall particles on the Kapitza resistance, temperature profile and density distribution across solid-liquid interfaces and nanofluidic channels.
- To investigate and compare the effect of wall size on the Kapitza resistance, temperature profile and density distribution across solid-liquid interfaces and nanofluidic channels with simple harmonics of a lattice system.
- To compare the molecular dynamics model with commercially used theoretical models, such as acoustic mismatch model (AMM), diffuse mismatch model (DMM) and lattice dynamic model (LDM).

1.0.4 Advantages of Molecular Dynamics Simulation

- Molecular dynamic simulation is used to validate, predict and compare with experiments that are difficult to perform in the nanoscale. It is a numerical experiment and has proven to be more reliable than other molecular-based techniques used.
- Molecular dynamic simulation is suitable for real-time visualization of atomic trajectories.
- MD is used to analyze various range of fluids and materials in the nano and micro-scale to obtain reliable engineering parameters and constants.

1.0.5 Limitation of Molecular Dynamics Simulation

- The classical treatment of forces in molecular dynamics makes it an approximation.
- There is the problem of different length scales, where the diameter and the length of the domain can be orders of magnitude apart.
- Molecular dynamics simulation is computationally very expensive.

1.0.6 Contribution to Knowledge

- Determined the effects of stiffness and mass, energy intermolecular interaction strength and channel size on the Kapitza resistance, temperature profile and density distribution across solid-liquid interfaces and nanofluidic channels with simple harmonics of a lattice system applying molecular dynamics atomistic modelling.
- Reduction of atomic layers from 4σ (atomic layers) that is popularly applied in MD studies, to 2σ (atomic layers) by the use of Einstein springs and thermostats..
- Determined that the Kapitza resistance or temperature jump across a solid-liquid interface correlated with the product of the bonding stiffness and wall mass ($logm_wk$) rather than the frequency of harmonic springs $\sqrt{k}/m$ and increases as a fifth-order polynomial with respect to ($logm_wk$).
- Development of Einsten-Maxwell molecular dynamics thermal wall model as a fix known as tether_wall, that can be included in LAMMPS register and command. This is written in C++ and LAMMPS codes. LAMMPS is an open source code developed by Sindia Laboratory in the United States.

1.0.7 Overview of Thesis

Chapter 2 introduces the literature review that includes the critical idea behind the latest knowledge on atomistic modelling, the gap in knowledge, and findings of interest concerning this area of research. Past works are best presented by mentioning works that are important and related to the research area which includes studies in molecular dynamics and monte-carlo simulations applied to interfaces, nanochannels, nanopores and nanomembranes. Researchers have studied extensively the fluid transport mechanism of diffusion and adsorption in nanomembranes. There has been less effort in understanding the phenomena of thermal transport in nanomembranes, nano-interfaces and nanofluidic channels for engineering applications.

Chapter 3 gives details of the method, technique and implementation of molecular dynamic simulation. The Hamiltonian and Boltzmann probability theory will be introduced in the micro-canonical NVE ensemble. The theory behind fluctuation and time correlation function are also explained. The pair potential for this study and other pair potential functions applied in modelling the inter-atomic attraction and repulsion is defined. The theory behind Maxwell model, Acoustic mismatch model, Diffusse mismatch model, Lattice dynamic model, Einstein solid model and Maxwell-Einstein thermal wall model that is developed in the process of this work and further

written as a fix and script in LAMMPS will be highlighted.

Chapter 4 reports the effect of mass of the wall particles on the Kapitza resistance, temperature profile and density distribution across solid-liquid interfaces and nanofluidic channels with various values of stiffness constant and wall temperatures.

Chapter 5 reports the effect of energy intermolecular interaction strength of wall particles on the Kapitza resistance, temperature profile, and density distribution across solid-liquid interfaces and nanofluidic channels with simple harmonics of a lattice system. The molecular interaction between the surfaces of the wall and fluid and their effects on the nanofluidic channels are also reported.

Chapter 6 reports the effect of different wall sizes on the Kapitza resistance, density distribution and temperature profile across solid-liquid interface and nanofluidic channels with various values of stiffness constant.

Chapter 7 provides the conclusion of this work and recommendation for future work.

As a summary, these chapters show that the Kapitza resistance, density distribution and temperature profiles across interfaces and nanofluidic channels, are influenced by a) mass of the wall atoms, b) wall-wall and wall-fluid (wetting) intermolecular interaction energy strength and c) wall size of the nanofluidic channels. These findings are achieved implementing molecular dynamics atomistic modelling.

1.0.8 Publications

Journal and Conference Publications

- Kio, M.T.E., Drikakis, D., K*önö*zsy L. (2014) " Equilibrium Molecular Dynamics Modeling of Diffussion and Adsorption of Fluids in Armchair Single Walled Carbon-nanotube". Paper presented in the International Astronautical Congress, Toronto Canada.

- Kio, M.T.E., Frank, M., Asproulis, N., Drikakis, D., K*önö*zsy, L. (2014) "Wall mass effect on the thermal resistance of solid-liquid interface". International Journal of Heat and Mass transfer . In Review.

- Kio, M., Abgoola, O. (2012). Molecular dynamic simulation of heat transfer of gases in a spacecraft-heat pipe. Paper presented at the Proceedings of the International Astronautical Congress, IAC, 9, pp. 6885-6889

Poster Presentations

- Kio, M.T.E., Asproulis, N., Drikakis, D., Könözsy L. (2014) " Equilibrium Molecular Dynamics Modeling of Diffussion and Adsorption of Fluids in Armchair Single Walled Carbon-nanotube". Poster presented at the International Astronautical Congress, Toronto Canada.

- Kio, M.T.E and Asproulis, N. "Computational Molecular Dynamics of Phonon-Heat transfer and Adsorption of Gases in Nanochannel for Aerospace and other Applications". Poster conference of Aerospace and Engineering Doctoral Training Centre. Cranfield University, United Kingdom. March 2014.

- Kio, M.T.E and Asproulis, N. "Computational Molecular Dynamics of Heat transfer in a Nanochannel". Poster conference of A&E Doctoral Training Centre. Cranfield University, UK February 2013.

[1]

[1]This page is intentionally left blank

Chapter 2

Literature Review

This chapter explores the direction of the research and forms the basis for the framework of this study. Researchers have extensively studied the fluid transport mechanism of fluid-solid interface interaction phenomena in nanochannels and nanomembranes, with less insight into the phenomena of nanoscale interfacial thermal transport. This chapter will highlight previously undertaken investigations by other researchers that is foundational to this work. The gap in knowledge will be obtained from the review of authentic literatures, providing a pathway for further in-depth study and understanding of nanoscale interfacial thermal transport.

2.1 Wall-Fluid Interfacial Thermal Resistance

Molecular Dynamics Simulation was implemented to obtain the thermal resistance in fluid-solid interface [21]. Their study used regions, having fluids and a wall with saturated vapor sandwiched in between fluid regions. The Lennard-Jones pair potential was applied with walls modelled with triple layers of face-centered cubic FCC crystal [22]. They chose platinum (pt) as the wall mass, having different values of spring constant. The temperature given to the solid system was maintained at $100k$ and $200k$ and was controlled by phantom molecules. Different values of energy interaction intermolecular stregth of the fluid-solid interface were given to enable studies of surface wettability. They reported a lower jump in temperature at the fluid-solid interface as the surface wettability increases.

An inter-atomic transfer model developed with simulation domain removing the region of the vapor was reported [23-24]. There results revealed that the temperature jump is influenced by the energy exchange at the fluid-wall interface and was in opposition to the heat flux direction.

Further studies using MD simulation and experiments have been reported [25]; they stud-

ied individual carbon-nanotubes with interfacial thermal resistance inside liquid carbon. Their experimental report showed that with high thermal conductivity of the CNTs, the interfacial thermal resistance between the CNTs and liquid increased. They further explained that due to less vibrational modes of the CNT fluid having low frequency, attributed to the conversion from high-frequency modes to low-frequency modes due to phonon-phonon coupling was observed in the fluid region. Longer CNTs with thermal boundary resistance were also studied. They reported that interfacial thermal resistance remained fixed for lengths of CNTs above 25-500 $\overset{o}{A}$. There investigation also showed that the liquid matrix have more layered thermal resistance than solids, which is due to resonant coupling of low-frequency phonon modes of CNT and matrix. These frequency modes that are lower carry a small portion of the total energy, causing CNT heat dissipation to decrease due to the lower intermodal energy transfer between the CNT. This observation was later supported by using MD, they used CNTs that have shorter lengths and contact areas, their study further reported larger interfacial resistance due to their low-frequency modes and weaker endurance and coupling to the liquid.

Current studies by [26] reported that the Kapitza resistance can be reduced across oil and graphene sheet interfaces by the functionalization of graphene using alkanes having vibrational modes that couples perfectly with the oil matrix. For non-wetting and wetting of wall surfaces, [27] reported the increase of wall-fluid interfacial Kapitza resistance where they used the Lennard-Jones potential to model the wall-fluid interaction with no molecular interaction at the wall-wall. Their study used mass values that are ten times bigger than the fluid-fluid interaction, with various values of wall-fluid energy intermolecular interaction strength. For strong interaction energy strength that translated to wetting in the interface, thermal resistance was observed to be inversely proportional to energy interaction (ε). However, for the non-wetting case, weak interaction strength at the interface with an exponential decrease in the thermal resistance was observed. The study further reported that there was no influence on liquid layering by thermal transport across the interface, while for gas wall interface they reported that gas layering increases the thermal transport [28].

The effect of the structure of the wall, on fluid-wall thermal and momentum transfer at the interface, was studied by [29], they observed thermal transport at the interface with normal component, this was reported to be due to the mass density of wall surface plane in interaction with the fluid at the interface. The studies by [30] showed the possibility of reducing fluid-wall interface thermal resistance applying the principles obtained from the acoustic mismatch model. They reported that increasing the temperature in a constant volume system and facilitating the increment of liquid layering can decrease the fluid-wall interface thermal resistance.

Fluid wall thermal transport in water-silica system was studied by [31]. They observed water

molecules layering that is adsorbed in the wall surface and penetrates the silica membrane at a depth of 28σ using the Lennard-Jones pair potential. They reported a significant decrease in the liquid-wall interface thermal resistance. This adsorption/absorption of water molecules through layering in the interface and silica cells is proposed to have enhanced phonon ballistic transport across the fluid-wall interface. Temperature jump, due to controlling a solid temperature was also observed. They further carried out their work by cooling and heating water molecules between parallel silicon walls. There investigation reported that Kapitza resistance affects and hinders fluid-wall interface thermal transport in the nanoscale. They further reported that an increase in the temperature of the fluid brings about bigger interfacial thermal resistance.

MD simulations were carried out for fluid-wall interface thermal conductance across the self-assembled monolayer (SAMS) and water interfaces, having various ranges of chemistries [32]. The results reported were in agreement with experiments performed [33]. This success suggests that MD can be applied to measure fluid-wall interface thermal transport and forecasting bonding strengths in interfaces.

Fluid-wall interface thermal conductivity of argon-liquid, and the influence of the argon liquid layer thickness on the conductivity, were studied [34]. They reported higher thermal conductivity for the liquid argon for higher film thickness and larger fluid-wall interaction strength. They further observed that with a further increase in fluid-wall interaction, the thermal conductivity of the film is reduced, because of larger depletion in second fluid layering, with the migration frequency of larger temperature fluid atoms affected. The bulk thermal conductivity and Kapitza resistance of liquid argon layers adsorbed were correlated [35]. They reported a factor of 2, which is an improvement from the bulk fluid atoms having higher density of the layered fluid close to the wall. They further investigated the effect of thickness of the slab on the thermal conductivity of the fluid, and they observed an increase in thermal conductivity with a reduced slab thickness. Their study reported the reason to be due to the excellent vibrational similarity between wall atoms and fluid atoms at the interface.

The effect and influence of functionalizing interface surfaces were studied by [36]. They reported improvements in fluid-solid thermal conductivity while increasing the hydrophilicity with (-OH) functionalized group. They further used nano-pillars made of silica and observed an improvement of thermal conductance in the interface. They concluded that these improvements were due to vibrational matching and coupling between the solid-liquid interface.

2.1.1 Analytical and Numerical Wall models

There are several analytical wall models employed for wall-fluid interaction, the most common being the thermal wall and reflective model proposed by Maxwell [37]. These models describe the particles as being reflected totally when they collide with a wall, making the velocity of the particle perpendicular to impinge on the wall and reverses, while the components that are parallel to the wall remain unchanged. The thermal wall model predicts that a particle when in collision, is given a new velocity by the wall temperature, causing a diffusive reflection. The new velocity attained by the particle obeys Gaussian distribution, while Rayleigh distribution is assigned to the velocity component that is perpendicular to the wall. Particles will lose their memory of where they started after collision on the thermal wall.

Maxwell also formulated a linear combination of his model, taking a reflecting wall and surface as half reflecting and half absorbing [38]. Recently there is a study that used Maxwell model in combination with Gaussian and Rayleigh distribution having thermal wall with each particle colliding with the wall, reflecting diffusely or specularly [39]. They reported that the particle motion depended on the direction of perpendicular or parallel collision with the wall, when different accommodation coefficient is applied. The model by Cercingnani and Lampis [40] and extended by a later study, which is observed to be close to molecular dynamic simulation model was reported [41]. This study takes the velocity components independently and uses two accommodation coefficients.

Simulation models have been mostly studied by the confinement of a fluid between two parallel plates with periodic boundary condition at the outlet and inlet using Monte-Carlo methods with non-equilibrium molecular dynamics technique [42]. They used wall models to describe fluid molecules interacting freely with thermal walls that are oscillating, and observed a temperature distribution that is parabolic and exhibits a jump. Lattice models that are fixed and interacts with the fluid using intermolecular forces were implemented in molecular dynamics [43]. They observed that the wall model conserves energy of the fluid in the channel, but viscous heating, due to shearing motion was recorded, which will need to be removed by thermostats. Another approach against fixing the molecules of the wall in lattice position was implemented by [44], they applied heavy mass of fluid (10^{10}) to the molecules of the wall so that the fluid will be unable to be swept away during the simulation process.

2.1.2 Thermal Transport in Nanofluidic Channels

Thermal characteristics of gases in parallel plates using combined MD and Monte-Carlo methods were studied [42], they considered the hydrophilic and hydrophobic nature of the walls and its effects on the gases, heat flux, density and temperature distribution in a nanofluidic channel. They derived the energy accommodation coefficient (EAC) which predicted the heat flux in the channel effectively. Their work revealed that the wall-fluid strength of interaction was more relevant when compared to the fluid-fluid interaction strength. The effects of wettability were also studied experimentally by [45], gaseous layers, surface roughness on interfacial slip, and they observed partial slip and slip lengths which are bigger than most simulation studies. They also used the wettability and roughness to determine the interface thermal boundary conditions. Engineered fluid flow close to interfaces in several regimes, to bring down flow friction was also investigated by [46], they also discussed current theoretical concepts of the flow of fluid on solid interfaces with length and time scales that differ, heat transfer and the effect on slip surface interface.

The isosteric heat and adsorption energy of single-wall carbon nanotube (SWCNT) bundles containing mixture of N_2 O_2, CO, CO_2 H_2O and HF, using kinetic Monte-Carlo methods was studied [47]. Their study revealed that, the gases adsorbed into the interstitial channels of the CNT bundles, where the isosteric heat is calculated, is in agreement with experimental studies. This study proposes the need to use improved size homogeneity of the SWCNTs to account for molecular selection at the interstitial channels, so that accurate behavior of adsorption in CNT bundles, and results very close to experimental studies can be obtained.

Kapitza or thermal resistance is a phenomenon attributed to the different vibrational nature between atoms of different materials (or different electrostatic properties for materials where electrons, rather than phonons, are the main energy carriers). As the system size increases from nano to micro scales, phenomena at the solid-liquid interface become increasingly important [48]. Macroscopic models fail to accurately describe such processes [49]. Molecular Dynamics (MD), which treats systems from first principles at an atomic level, is one of the most accurate methodologies for obtaining a better understanding of complex systems on micro/nano-scale [50]. MD simulations have been used extensively for micro and nano-fluidics to understand the physical processes at liquid solid-interfaces. Many of these studies focused on the slippage of the liquid on the channel walls [51] complementing experimental observations and providing insight into interfacial phenomena. Another important area of applications in connection with interfacial phenomena is the area of molecular membranes [52]. Finally, the thermodynamic behaviour of both liquids and solids has also been studied using MD, interpreting atomic trajectories into transport properties

such as the thermal conduction of materials [53].

Previous studies so far have revealed the sensitivity of the various channel properties, such as the strength of interaction between the wall and liquid particles [54], as well as liquid density and bonding stiffness [21]. The thermal interface resistance has also been linked with the vibrational frequency of the walls [55].

2.2 Statistical Mechanics in Nanofluidic Channels

Physics and statistical mechanics connect the atomistic or microscopic regime to macroscopic quantities. Statistical treatment of non-equilibrium systems is often difficult. There are two non-equilibrium treatments that have been identified in the past. The first method uses correlation functions to explain non-equilibrium systems. The second explains the probability for the occurrence of each microstate. Due to the very small time scale dealing with obtaining any hydrodynamic quantity, such as pressure, density, and velocity these quantities are averaged to neutralise the fluctuations in the system. These fluctuations originate, due to the thermal motion of atoms, and are also known as thermal noise. The probability of a given microstate to evolve at time (t) is described by phase space distribution function (PSDF) $(f\Gamma, t)\delta\Gamma$. This is expressed as

$$d\Omega = f(\Gamma, t)\delta\Gamma, \tag{2.2.1}$$

this is integrated over the phase space and expressed as

$$\int f(\Gamma, t)d\Gamma = 1, \tag{2.2.2}$$

where the distribution function gives the fraction of the system $\delta\Omega$ in a small space volume of element $\delta\Gamma$ at time t.

Having knowledge of the distribution function, the instantaneous ensemble averages property of the system can be obtained. With the advancement of the simulation with time(t) the system evolves in phase space, averaging regions with higher probability and spending more time over that region, and lesser time with regions having zero or lower probability. This technique is achieved by the probability density and is obtained by sampling points in phase space. Information is obtained by averaging over ensembles with an ergodic system, ensemble averaging and time averaging as applied in MD and Monte Carlo simulations are the same. If a system is termed to be ergodic, every microstate that has non-zero probability is attained. In systems that are ergodic, every microstate that has non zero probability is attained. For systems that are ergodic, the average

over phase-space can be replaced by the time averaging of any phase variable ($B\Gamma$), referred to as the ergodic hypothesis and is expressed as

$$\int_0^t B(\Gamma(t')dt' = \int f(\Gamma)B(\Gamma)d\Gamma, \tag{2.2.3}$$

where $\Gamma(t) = [r(t), p(t)]^{T'}$is a phase space point at time (t) with phase space distribution function $(f\Gamma)$ [56-57].

Computer simulations are currently applied for these multi-dimensional and multi-body systems with phase space of 6N-dimensional. Their probability distribution can describe the properties of a system of particles. The case where the energy E, the number of particles N and the volume V are conserved, is known as the microcanonical ensemble. The probability distribution of microstates is expressed as

$$f_\epsilon(\Gamma) = \frac{\delta(H_o - E)}{\int \delta(H_o - E)d\Gamma}, \tag{2.2.4}$$

the equation $\int f_\epsilon(\Gamma)d\Gamma = 1$ satisfies the distribution function and H_o is known as the Hamiltonian and is given as

$$H_o = \sum_{i=1}^{N} \frac{p_i.p_i}{m} + U(r_1.....r_N), \tag{2.2.5}$$

where p_i the momenta, $m - mass$ and U the potential energy.

The microscopic model for enthalpy in a microcanonical ensemble is derived by Boltzman and is expressed as

$$S = k_B \int f_\epsilon In f_\epsilon d\Gamma = k_B In\Omega(N, V.E), \tag{2.2.6}$$

where Ω describes the entropy of a given state, the canonical ensemble with temperature T, number of particles, N and volume V. These ensemble properties are conserved, close to reality and mostly applied in MD simulations. The probability distribution of a microstate Γ of canonical ensemble is expressed as

$$f_\epsilon(\Gamma) = \frac{e^{-BH_O}}{\int e^{-BH_O} d\Gamma}. \tag{2.2.7}$$

where $B = (k_B T)^{-1}$, T is thetemperature and k_B the Boltzmann constant.

Recent studies have investigated connections and relationships between dynamics at atomic or microscopic levels and macroscopic properties, in essence the reason that transport occurs in chaotic and non-chaotic systems [58-59]. Previous studies investigated dynamic properties of a particle, located in a nanopore, which interacts with confined atomistic walls [60]. The results of their study predict that the ergodic hypothesis is correct for particles with several ranges of energy, and systems with different channel width.

2.2.1 Pair Distribution Functions

The pair correlation function is expressed as $g(r_{ij}, \nabla u)$, while $S(k, \nabla u)$ is the structure factor and k is the wave vector [61- 62]. Models for pair distribution function are given as registers in LAMMPS to be applied in equilibrium and non-equilibrium MD. This function is utilized as a fix to obtain the density distribution in the results of this work. The simplified distribution function is applied because distribution interactions between particles in homogeneous atomic fluid that is in equilibrium does not have a preferred direction. This type of distribution is called radial distribution function (RDF) and is expressed as

$$g(r) = \frac{V}{8\pi r^2 N^2} \Big\langle \sum_{I=1}^{N} \sum_{J \neq 1} \delta(r - r_{ij}) \Big\rangle, \tag{2.2.8}$$

where V is the volume of the system and N, Number of atomic particles, $g(r)$ describes the density of the particles, normalized by average fluid density which converges to unity in long-range limits. Densities shows peaks at distances of $r \approx 2^{1/6}$. The peak distance is due to minimum potential energy between two Lennard-Jones atoms. An increase in density over the solid-liquid transitional phase ($0.92 \leq \rho \leq 0.96$) forms a solid. The radial distribution function of solids shows large and pronounced peaks with distances relating to their lattice type and spacing.

To understand the behaviour of fluids in confined systems and the reason for fluid layer formation, attention is focused on the physics of structural layering. Fluids in confined systems maximize entropy by the formation of layers. From the principles of molecular packing spheres, the density of the peaks becomes high when the particles are packed efficiently, and the slit width is narrowly less than the integer multiple of sphere diameter σ. The particles frequently collide with the walls and tend to push apart, compared with wall packing that is less efficient with lower density, which generates oscillations [63]. Particles interact and impact the walls, thereby transferring momentum to the walls. Contact number density at walls, n_{wall}, have maxima and minima slit widths. The packing density of the particles between the walls is expressed as

$$\Gamma = \int_{-b/2}^{b/2} [n(z) - n_{bulk}] dz, \tag{2.2.9}$$

where $b = l - \sigma$, is the thickness of the fluid film in slit, n is the number density.

Understanding the behaviour of $\Gamma-$parking density, gives the reason for layering.

At equilibrium conditions of chemical potential μ and for hard spheres with no external field, μ can be expressed as

$$\mu/k_B T = log[n(R)\Lambda^3] - log\omega(R), \tag{2.2.10}$$

where $\omega(R)$ describes the probability of inserting a particle at location R, $\Lambda - thermal$ wavelength. The density at particular point is proportional to the probability of particle insertion.

2.2.2 Models of Kapitza resistance in interfaces

The theory of thermal phonon transport in an interface and the traditional expression for the Kapitza resistance k is given as

$$k = \frac{T_W - T_F}{q}, \tag{2.2.11}$$

where T_W and T_F are temperatures of the wall and fluid boundaries, and q is the heat flux of the wall. To obtain the heat flux in the nanoscale, an expression can evaluate the properties of phonon obtained from harmonic lattice dynamics calculated with assumption of no inelastic scattering within the boundary of solid and fluid. This assumption also defines the Kapitza resistance as the temperature drop across the solid-fluid interface which is the same as the boundary thermal resistance, irrespective of change in the boundary width of solid or fluid. The solid wall emits and absorbs phonons from the boundary. The net heat flux across the fluid-wall interface is expressed as

$$q = \frac{1}{(2\pi)^3}\int_L \sum_v^+ \hbar\omega(k,v)v_{g,z}(k,v)\alpha_{W\to F}(k,v)F_W(k,v)dk +$$

$$+\frac{1}{(2\pi)^3}\int_R \sum_v^- \hbar\omega(k,v)v_{g,z}(k,v)\alpha_{W\to F}(k,v)F_F(k,v)dk, \tag{2.2.12}$$

where W and F is the wall and fluid, $\hbar$ is the Planck constant, ω is the phonon frequency, v is the phonon group velocity, k is the wave number and α is the transmissivity. The summations are over phonons moving in the z-direction. The two variables F_w and F_f represents mode-dependent phonons and are distribution functions in the wall and fluid. These distributions are represented as

$$F_W(k,v) = f_{BE}[\omega(k,v), T_W] + f_W^{'}(k,v), \tag{2.2.13}$$

and

$$F_W(k,v) = f_{BE}[\omega(k,v), T_F] + f_F^{'}(k,v), \tag{2.2.14}$$

where f_{BE} is known as the equilibrium Bose-Einstein distribution function and $F_W^{'}$ and $F_F^{'}$ are deviations from equilibrium distribution.

The Bose-Einsten distribution function is written as

$$f_{BE}(\omega, T) = \Big[exp\Big(\frac{\hbar\omega}{k_B T}\Big) - 1\Big]^{-1}, \tag{2.2.15}$$

where k_B is the Boltzmann constant and T is the temperature.

The Kapitza resistance when the phonon properties are assumed to become temperature independent from the temperature of the solid wall (T_w) and fluid (T_f) is expressed as

$$k = \left[\frac{1}{(2\pi)^3}\int_W \sum_v \hbar\omega v_{g,z}\alpha_{W\to F}\frac{\partial f_{BE}}{\partial T}\partial k\right]^{-1}, \tag{2.2.16}$$

where the *subscripts* are the phonons in the fluid-wall interface and follows the Bose-Einstein equilibrium distribution function and ω is the frequency. Equation 2.2.16 is the most popular expression applied for obtaining the Kapitza resistance in the nanoscale [64-68]. However, this equation is not correct if average phonon transmission coefficient is approaching unity and also assumes a system having perfect crystal with no interface. The inaccurate assumption of no presence of interface and $f_W^{'}$ and $f_F^{'}$ being zero, makes the equation inconsistent and erroneous. The study of the Kapitza resistance was taken further by [69], who obtained and derived the junction Kapitza resistance for non-equilibrium phonon distribution and is expressed as

$$k = 1 - \frac{1}{(2\pi)^3}\int_W \sum_v^+ B_W\alpha_{F\to W}dk - \frac{1}{(2\pi)^3}\int_F \sum_v B_F\alpha_{W\to F}dk, \tag{2.2.17}$$

where B_W and B_F is fraction of total heat flux moved by specific phonon mode in the solid wall. Equation 2.2.17 was further developed [70] and expressed as

$$k = \frac{1}{(2\pi)^3}\int_W \sum_v \hbar\omega v_{g,z}^2\tau\frac{\partial f_{BE}}{\partial T}\partial k, \tag{2.2.18}$$

where τ is the equilibrium lifetime.

To determine the accuracy of these equations for the Kapitza resistance molecular dynamics studies for Si/Ge interface was reported [8]. There study did not require any assumption for the phonon scattering and obtained error bars for MD prediction, which represented a 95% confidence interval when five simulations where implemented and compared to various models. Temperature independence of the Kapitza resistance in low temperature was also observed indicating an elastic phonon interface scattering in the Si-Ge interface [8].

2.2.3 Chapter Summary

From reviewed literature, there is a need to further study and understand how nanoscale thermal transport and Kapitza resistance in interfaces, thin films, nanofluidic channels, nanopores and nanomembranes occur. Wall models that tend to mimic physical reality were also found from some studies undertaken, to describe thermal transport and Kapitza resistance in interfaces and nanofluidic channels. Analytical wall models were highlighted in the review; they include Maxwell model, Ceignani-Lampis and Lord model, with simulation models including the fixed lattice model and harmonic bonding thermal model. The simulation models include molecular interaction due to Lennard-Jones pair potentials, while the analytical model is limited due to non-inclusion of the intermolecular interaction potential term in their models. The simulation models are reported to be superior to the analytical models due to the closeness of their values to thermo-dynamical measurements and their wide application in large temperature ranges [47]. MD simulation described the physics of solid-fluid thermal interfacial interaction in these reviews and is adopted in this study. Most molecular studies reviewed did not include and capture the effect of mass, energy intermolecular interaction strength and vibrational frequency of the wall atoms; thereby lacking in addressing the critical challenges in nanoscale heat transfer and interfacial phenomena. This study will attempt to address these issues by developing an appropriate combination of the Einstein and Maxwell thermal wall models, by implementing molecular dynamics. The MD model of this study is predicted to accurately mimic the properties of the wall, fluid, and interfacial particles, thereby correctly describing the physics of the system.

This review has enabled this thesis to develop and focus on the objectives of this research, and also highlight areas that needs improvement and further studies of nanoscale thermal interfacial phenomena. The areas of research and interest identified, forms the basis of this research and are as follows:

- From previous studies, it is clear that weak vibrational coupling and matching of wall-fluid phonons are responsible for improvements in Kapitza resistance in interfaces and nanofluidic channels. The Kapitza resistance of these studies were mostly obtained from rigorous mathematical manipulations (Analytical methods) with many approximations leading to inconsistent and inaccurate results. In such circumstances, nanoscale thermal interfacial phenomena applying direct molecular dynamics to determine the thermal transfer and Kapitza resistance in interfaces and nanofluidic channels that are more accurate, has less extrapolation, few approximations and mathematical manipulation, becomes very desirable and significant.

- There is also need for the development of improved thermal wall models, using molecular

dynamics to describe the physics of thermal transfer and Kapitza resistance across solid-liquid interfaces and nanofluidic channels.

- To study in details and understand the influence and effects of mass, vibrational frequency, energy intermolecular interaction strength of the wall atoms and the wall size on the Kapitza resistance, temperature profile and density distribution across interfaces and nanofluidic channels.

Chapter 3

Molecular Dynamic Simulation

3.1 Introduction

Molecular dynamics holds a powerful potential to study and provide solutions to phenomena and challenges at the nanoscale. In order to properly analyze and understand the process in the nanoscale region, computer simulations provide a good method to visualise and understand what is going on. The increase of processing power of a computer has made molecular dynamics crucial and relevant in these applications, especially studies involving thermal transfer, Kapitza resistance and adsorption in the nanoscale.

Molecular Dynamic (MD) is a computer simulation method of physical movements of atoms and molecules. It is also a classical and deterministic process of simulation that uses potential energy functions to model the basic interaction of atoms and molecules [2]. The small time scales that micro and nano-systems undergo makes experiments very complex and complicated in this region. There are scenarios where experiments cannot be carried out especially in very small time and length scales with extreme conditions making it very expensive, in such cases molecular dynamic simulation becomes important and comes handy. MD is a numerical experimental method with atomistic time scale of femtoseconds (10^{-15}), this time region covers dynamics in the nano-region and makes the time to process the dynamics in this region very short. Considering the growth of computational resources available for modern computing, simulation time is still not sufficient to observe the dynamics of molecules in a suitable and desired time frame. This chapter will highlight some techniques in statistical mechanics applied to molecular dynamics simulation implementing Large atomic-molecular massively parallel simulator (LAMMPS).

There are two types of mechanics that describes motion in the nano-scales. They are quantum mechanics, which is based on density functional theory and gives better prediction of position

and momenta of particles and the classical mechanics which is an approximation of quantum mechanics. There are two methods of simulation that also uses the classical mechanics principle, and they include Monte Carlo simulation and the Molecular dynamics simulation (MD). The classical mechanics approximation can be related to the velocity using the Boltzmann theory which is simulated in the microcanonical NVE ensembles [2]

$$E_o = \sum_i {}^1\!/_2 m_i v_i^2 = {}^3\!/_2 N k_B T, \tag{3.1.1}$$

where E_o is the kinetic energy, m_i the mass of particles, v_i the velocity, k_B the Boltzmann constant and T the temperature.

Statistical mechanics has been able to bring to the understanding the connection between microscopic molecular motion and macroscopic dynamics. Statistical mechanics also makes it possible to interpret micro-scales (ensembles) to macro-scales so that useful parameters and quantities can be obtained. Ensembles are a conglomeration of points describing a particular thermodynamic state. An atom is identified by position and momenta in $1, 2, 3$ dimensions. Interacting atoms are contained in the phase space of a maximum of $6N$ phase space for 3-dimensional systems. There are different microscopic states (ensembles) which are described by thermodynamic values of energy temperature, pressure, volume, chemical potential and number of particles. The reality of a micro-state passing through all other microstates and visiting itself, predicts the transformation of a micro-state to macroscopic properties of the system.This process is described as egordicity where all micro-states are attained in a system [60]. For ease of analysis and overcrowding of variables, three thermodynamic variables are grouped to make an ensemble.

The NVE ensemble which is known as micro-canonical ensemble describes molecular dynamics simulation process but since all the ensembles attain the same state and are identical in a system they are worthy of note and they are expressed as

Ensembles	Constraint
Micro-canonical	N, E, V (Constant)
Canonical	N, T, V
Grand Canonical	μ, T, V
Isothermal-Isobaric	N, T, P

Modelling free phase space in a configuration of a system of N particles in 3−dimensions is $3N$. If there are $N-$particles, positions and velocities need to be specified for the particles ($6N$ variables) uniquely identifying the dynamical system as

$$X = A\left(\{r\}\{p\}\right), i = 1, 2, 3, 4, 5, 6N, \tag{3.1.2}$$

where r is the position and p is the momenta.

Boltzmann proves that the probability when a system visits a microstate is proportional to the energy of that microstate when you include the Boltzmann factor [2].

The probability for an absolute value is given by

$$P\left(\{r_i\}, \{p_i\}\right) = \frac{e^{-BH(\{r_i\}\{p_i\})}}{\sum e^{-BH(\{r_i\}\{p_i\})}}, \tag{3.1.3}$$

where the divisor in the equation is known as partition function Z and expressed as

$$Z(N, V, T) = \sum_{microstate} e^{-BH(\{r_i\}\{p_i\})}, \tag{3.1.4}$$

which can also be given as

$$Z\left(N, V, T\right) = \Omega\left(N, V, \overline{E}\right)^{-\frac{E}{K_B T}}, \tag{3.1.5}$$

where k_B is known as the Boltzmann constant, N is number of particles, V the volume, E the energy and T the temperature.

At the atomistic level, properties of a microstate in thermodynamic equilibrium is fluctuating or changing continuously. When determining any property in the microstate, difference between its instantaneous value and ensemble average of its trajectory are distinguished, this is what the Boltzmann equation is describing; a macroscopic state that is related to the microstate, and that is what is observed during experiments. The instantaneous values were correctly defined for properties concerning energy [2], which includes kinetic and potential energy. These entities are not correctly defined for properties such as pressure and temperature which are obtained by statistical mechanics from ensemble averages.

In equilibrium the ensemble average (A) is defined as

$$< A >= \sum_{microstate} AP = \frac{\sum A\left(\{r_i\}, \{p_i\}\right) e^{-BH(\{r_i\}, \{p_i\})}}{\sum e^{-BH(\{r_i\}, \{p_i\})}}, \tag{3.1.6}$$

where r is the particle postion, p is the momenta and $Z = \sum_{microstate} e^{-BH(\{r_i\}\{p_i\})}$ is the partition function.

Molecular dynamic simulation does a time average and the quantity A is given as

$$A = \frac{1}{T}\int_0^T A(t)dt. \tag{3.1.7}$$

At equilibrium conditions the ensemble average and time averages are equal (egordicity) and is expressed as

$$< A >= \frac{\int Aexp(-\beta E)drdp}{\int exp(-\beta E)drdp}, \tag{3.1.8}$$

where $< A >$ signifies that all the microstates are achieved, β is the Boltzmann factor and E is the energy.

3.2 Hamiltonian mechanics

This mechanics state that a system that has a dynamic property can be determined by its total energy which is a sum of the kinetic and potential energies. This is given in the form [2]

$$H = K + V, \tag{3.2.1}$$

and is written as

$$H\left(\{r_i\};\{p_i\}\right) = V\left(\{r_i(t)\}\right) + \sum_{i=1}^{3N}\frac{(P_i(t))^2}{2m_i}, \tag{3.2.2}$$

where i denotes atom and Cartesian component x, y and z. The equation of motion can be derived from the Hamiltonian [71]

$$r = \frac{\partial H}{\partial p_i}; \dot{p} = \frac{\partial H}{\partial r_i}, \tag{3.2.3}$$

taking the Hamiltonian with respect to time gives

$$\frac{\partial p_i}{\partial t} = -\frac{\partial H}{\partial t}; \frac{\partial r}{\partial t} = \frac{\partial H}{\partial P_i}, \tag{3.2.4}$$

from the following expression the time derivation of the Hamiltonian can be obtained using chain rule

$$\frac{\partial H}{\partial t} = \sum_{i=1}^{3N}\left(\frac{\partial H}{\partial r}\dot{r_i} + \frac{\partial H}{\partial p}\dot{p_i}\right), \tag{3.2.5}$$

which gives by substitution

$$\frac{\partial H}{\partial t} = \sum_{i=1}^{3N} \left(\frac{\partial H}{\partial r_i} \frac{\partial H}{\partial p_i} + \frac{\partial H}{\partial p_i} \left(-\frac{\partial H}{\partial r_i} \right) \right) = 0, \tag{3.2.6}$$

where r is the particle position and p is the momenta.

The Hamiltonian as in Equation 3.2.6 is conserved, i.e. the system having constant energy. This describes the micro-canonical ensemble used for molecular dynamic simulation [2]. An important approximation in the Hamiltonian is the equipartition of energy that states that any degree of freedom that is squared inside the Hamiltonian, is approximated as $1/2k_BT$ of energy. This theorem leads to the relationship between the macroscopic state of absolute temperature and microscopic state of average kinetic energy. The temperature is obtained from the kinetic energy of a system.and is expressed as

$$< k >= \frac{3N}{2} k_B T, \tag{3.2.7}$$

the center of mass motion is mostly set to zero at $t = 0$, therefore the equation becomes

$$< k >= \frac{3N - 3}{2} k_B T. \tag{3.2.8}$$

The temperature is related to average kinetic energy, thereby obtaining the instantaneous temperature as

$$k(t) = \frac{N_{eff}}{2} k_B T(t), \tag{3.2.9}$$

the microscopic temperature i.e. kinetic temperature is written as

$$T = \frac{1}{3Nk_B} \sum_{i=1}^{N} |\dot{r_i}|^2 m_i, \tag{3.2.10}$$

where N is the degree of freedom, m_i the mass, $\bar{r_i}$ is the velocity and k_B is known as the Boltzmann constant.

The system temperature will surely fluctuate in time. This is one of the reasons for equilibration. For pressure the Clausuis Virial theorem is commonly used and this gives for N-system of particles

$$\left\langle \sum_{i=1}^{N} r_i . f_i^{TOT} \right\rangle = {}^1\!/_3 N k_B T = -pv, \tag{3.2.11}$$

where f_i^{TOT} is the total force on the ith particles. The internal viral $< w >$ can be defined if internal forces are considered. For NPT ensemble this needs thermostating and barostating

inputs that controls the pressure to make it constant. The internal viral is expressed as

$$< w >= \sum_{i=1}^{N} r_i.f_i^{INT} = \sum_{i=1}^{N} r_i.\nabla r_i.v(r_i), \tag{3.2.12}$$

this can be obtained from the trajectory and gives the relation

$$PV = Nk_BT + \langle w \rangle, \tag{3.2.13}$$

where P is the pressure, V the volume, k_B is the Boltzmann constant, T is the temperature and $< w >$ the internal viral.

The instantaneous pressure of the system is obtained. Just as in the case with the temperature, macroscopic pressure is not the same as the microscopic pressure because this pressure can still fluctuate. However, the thermodynamic pressure (macrostate pressure) is obtained as an ensemble average.

3.3 Potential functions

In an ideal case the potential function determines the efficiency, accuracy and simplicity of molecular dynamic simulation. The potential functions are derived from the potential energy of the system. The potential of any microstate $V(r_1,\ r_2, r_3 \ldots\ldots\ldots\ldots r_N)$ is assumed as the sum of a pair between atoms or molecules in a system $\Phi(r_{ij})$. This can be expressed [2] as

$$V = \sum_i V_1(r_i) + \sum_i \sum_{j>1} V_2(r_i, r_j) + \sum_i \sum_{j>i} \sum_{k>j>i} V_3(r_i, r_j, r_k) + \ldots\ldots\ldots\ldots\ldots \tag{3.3.1}$$

where $V_1(r_i)$ describes the effect of an external force impacting the system. The other terms $V_2(r_i, r_j)$ and $V_3(r_i, r_j, r_k)$ describe particle-particle interactions. The summation is limited to interaction potentials of not more than three atoms at once.The use of more than two body interaction is computationally expensive, making the use of pair particle interaction desirable given as

$$V_i = \sum_i \sum_{j>1} V(r_{ij}), \tag{3.3.2}$$

and

$$V(r_{ij}) = \sum_i^n \sum_{j>1} V_{ij}\left(|r_i - r_j|\right), \tag{3.3.3}$$

where $V(r_{ij})$ is the Potential between i and j, r_{ij} is the distance between molecules i and j in a simple system, for complex systems there are different types of potential functions used to describe

the system.

3.3.1 Lennard-jones potential

The Lennard-Jones potential (LJ) popularly known as (12-6) potential, is the most used potential function in molecular dynamic simulation [2], and it is defined as

$$V(r_{ij}) = 4\varepsilon \left[\left(\frac{\sigma}{r}\right)^{12} - \left(\frac{\sigma}{r}\right)^{6} \right], \tag{3.3.4}$$

where $V(r_{ij})$ is the Potential between i and j, ε is the Lennard- Jones energy coefficient, σ is the Lennard- Jones distance, r is the distance between two parts.

The force obtained from the potential is given as

$$F = -\nabla r_{ij}(V), \tag{3.3.5}$$

and this becomes

$$F = \left(\frac{48\varepsilon}{\sigma^2}\right) \left[\left(\frac{\sigma}{r_{ij}}\right)^{14} - 1/2 \left(\frac{\sigma}{r_{ij}}\right)^{8} \right] r_{ij}, \tag{3.3.6}$$

for LJ potential function, the force becomes

$$F = \sum_{j=1}^{N} \frac{24\varepsilon}{r_{ij}^2} \left[2\left(\frac{\sigma}{r}\right)^{12} - \left(\frac{\sigma}{r}\right)^{6} \right] r_{ij}, \tag{3.3.7}$$

where force F is obtained for all molecules with potential V. Atomic pair i, j is only evaluated once, since r_{ij}=$-r_{ji}$.

It is important to choose dimensionless (MD units) for Lennard – Jones potential using m_i, σ and ε as units of mass, length and energy. Lengths are known in terms of Armstrong, the energy units ε can be erg/ atom or converted to kcal/ mole or J/mole. The MD unit of the mass is taken as unity and for specific atoms can be grams and the time is expressed as $\sqrt{m\sigma^2/t}$ or in seconds.

3.3.2 Buckingham potential

The Buckingham potential is very expensive because of the high usage of computing resources. The potential is represented as

$$V\left(r_{ij}\right) = A_{ij} exp\left(-B_{ij} r_{ij}\right) - \frac{c_{ij}}{r_{ij}^{b}}, \tag{3.3.8}$$

and this potential does not contain the attractive part and is very rigid, as the potential between the atoms increases, it is expressed [72] as

$$V_{ij}(r) = \varepsilon \left(\sigma/\mathrm{r_{ij}}\right)^{v} = 9r^{-v}ij, \tag{3.3.9}$$

where v is the hardness of the sphere and ε the energy coefficient of the pair.

For a whole system or ensemble, the total potential function can be expressed as

$$V(r)_{ij} = v^{non-bonded}\tau_{ij} + v^{bonded}\tau_{ij} + v^{reserved}, \tag{3.3.10}$$

where $v^{non-bonded}/v^{bonded}$ means the potential function due to bonded and non-bonded interaction [2] while v^{reserved} connects contributions that are to the potential by other interactions.

Expressing the non–bonded potential becomes

$$v^{non-bonded} = \sum_{i}\sum_{j>i} v_{ij}^{col} + \sum_{i}\sum_{j>i} v_{ij}^{vwdl}, \tag{3.3.11}$$

where v^{vwdl} is the vanderwaals potential (LJ) and v^{col} is the coulomb potential, which is given in the form

$$v_{ij}^{col}(r) = \frac{q_i q_j}{4\pi\varepsilon_o r_{ij}}, \tag{3.3.12}$$

where ε_o means permittivity of the free space, r_{ij} is the distance and $q_i q_j$ are partial charges.

The bonded potentials are described from the Leonard Jones potential, Soft sphere potential and Buckingham potential we discussed earlier. The potential function for bonded interaction is given as

$$v_{ij}^{bonded} = \sum_{bond} v_{ij}^{stretch} + \sum_{angles} v_{i.j.k}^{bond} + \sum_{properdihedals} v_{i,j,k,l}^{tors} + \sum_{improperdihedrals} v_{i,j,k,l}^{impdi}, \tag{3.3.13}$$

where v^{bonded} means the potential function due to bonded interaction and other parameters describing the different dynamics of the bonds.

The reserved potentials are modelled by other special potentials primarily due to boundary conditions. For example, spring potential can be represented as

$$v_{\tau ij}^{spring}(r) = {}^{1}/_{2}k(r_i - r_{j\tau})^2, \tag{3.3.14}$$

where r_i is the atom i (current position), spring constant k and r_{ij} position obtained during atomic vibration or bond stretching.

3.3.3 Pair potential for water

Water is a non-linear molecule made up of three atoms, and its pair potential has been studied extensively [73]. Forty-six various water models have been studied, focusing on their geometry, but few will be considered, which includes the simple point charge SPC, TIP4P, TIP5P and SPC/E (SPC extended) models. The popular usage of a potential function for different water models which includes all states involves Lennard Jones interaction between oxygen – oxygen interaction and electrostatic interaction between hydrogen – oxygen and is expressed [74] as

$$v_{ij}^{water} = 4\varepsilon_{00}\left[\left(\frac{\sigma}{r_{ij}}\right)^{12} - \left(\frac{\sigma}{r_{ij}}\right)^{6}\right] + \sum_{i}\sum_{j}\frac{q_i q_j e^2}{4\pi\varepsilon_o r_{ij}}. \tag{3.3.15}$$

where v_{ij}^{water} is the Potential between i and j, ε is the Lennard- Jones energy coefficient, σ is the Lennard- Jones distance, r is the distance between two parts, ε_o means permittivity of the free space and $q_i q_j e$ are the partial charges.

3.3.4 Simple water models

Water models are applied to the simulation of liquid clusters and aqueous solutions of water. These models are classical models because they are approximated from experiments and molecular dynamic simulation. They are classified according to points created to describe the model. They can be in the form of real atoms or dummy sites.

Water models are classified according to their sites, these include 2,3,4,5,6 sites with other modified and special types [73]. Due to its relevance to wider applications, only 3,4 and 5 site models will be mentioned.

3.3.5 3 Site-water model

The most commonly used water models are the 3-site water models that focuses on the non-bonded interactions in the water molecule, where there are interactions due to electrostatics and vander-waals forces. This can be described by the Lennard-Jones potential and coulombs law [74] and is expressed as

$$E_{non-bonded} = E_{vwdl} + E_{col}, \tag{3.3.16}$$

where $E_{non-bonded}$ means the non-bonded energy function, E_{vwdl} is the vanderwaals energy function and E_{col} is the electrostatic energy function.

which can be written as

$$V(r) = \sum_{i}^{a}\sum_{j}^{b} 4\varepsilon_{ij}\left[\left(\frac{\sigma_{ij}}{r_{ij}}\right)^{12} + \left(\frac{\sigma_{ij}}{r_{ij}}\right)^{6}\right] + \sum_{i}^{a}\sum_{j}^{b}\frac{q_i q_j}{4\pi\varepsilon_0 r_{ij}}, \tag{3.3.17}$$

where ε_o is the electrostatic or dielectric constant and has a value of $332\overset{o}{A}.kcal/mol$. $q_i q_j$ are partial charges of the atoms or molecules; $\sigma_{ij}^6, \sigma_{ij}^{12}$ are the attraction and repulsion coefficients of Lennard-Jones. Water models are distinguished according to their structure; rigid, in this case the geometry of the model is fixed. Flexible; this includes polarization effects and vibration with a degree of freedom. The most commonly used 3-site water models include SPC (Simple point charge), SPE/E (extended SPC), TIP3P (Transferable intermolecular potential with three interaction sites). The charge distribution of these models include $-2q_e$ in the oxygen site and $+q_e$ in the two hydrogen sites. The 3-site model is computationally attractive when compared to other water models [75].

The detailed form of the energy function used for a 3-site water model is expressed [76] as

$$E_{bonded} = E_{bond.lenght} + E_{bond.angles}, \tag{3.3.18}$$

E_{bonded} means the bonded energy function, which is expressed as

$$V_{(w)} = \sum K_{a_{bond.lenght}}(b_i - b_j)^2 + \sum K_{\theta_{bond.angle}}(\theta_i - \theta_j)^2, \tag{3.3.19}$$

where $V_{(w)}$ is the potential function bonded interaction with bond angles and can be written with energy parameters $K_a, b_{ij}, K_\theta, \sigma_{ij}, r_{ij}, q_{ij}$ and shift function $sf(r)$. For SPC/E model an average polarization is added to the energy function which is given as

$$V_{pol} = {}^1\!/_2 \sum_{i} \frac{(\mu - \mu^o)^2}{\alpha_i}, \tag{3.3.20}$$

where μ is the dipole of polarized water molecules and the value is $2.35D$, μ^o is the dipole moment of isolated water molecule given as $1.85D$ from experiment, α_i is the isotropic polarizability constant that has a value of 1.608 x $10^{-40} Fm^2$. The above polarization correction adds $1.25kcal/mol$ ($5.22kj/mol$) to the overall energy; therefore, this model gives a more reliable diffusion constant and density than the 3-site SPC model [77].

3.3.6 4 site-water model

For the TIP4P (Transferable intermolecular potential with four interaction site), the Lennard-Jones coefficients (C_{ij}) of the oxygen atom is not located in the same interaction site. The charge that is negative is located $0.015nm$ from its previous position from the oxygen site, close to the hydrogen

along the HOH angle axis. The negative charge is placed on a dummy site close to the bisector of H-O-H angle, with this placement, the electrostatics in the water molecules are improved. An Earlier model used was the Bernal-Fowler model obtained in 1933 [78]. The accepted TIP4P model was obtained in 1983 and is widely used for bio-molecular simulations. Modifications and improvements of the TIP4P water models, which includes TIP4P-ewald, TIP4P/ice and TIP4P/2005 are also commonly used [76].

The potential of TIP4P water model is descibed and expressed [73] as

$$V = \sum_{i=1}^{k-1} \sum_{j=i+1}^{k} \left[\left(\frac{C_{12}}{r_{ij}} \right)^{12} - \left(\frac{C_6}{r_{ij}} \right)^{6} + \sum_{k=1}^{3} \sum_{l=1}^{3} \frac{q_k q_l e^2}{r_{ij}^{kl}} \right], \tag{3.3.21}$$

where q is the electronic charges and k and l represent sites of electronic charges in two molecules i and j, respectively. C_{12} and C_6 are potential coefficients obtained.

TIP4P water model when compared to experimental data gave close values [73]. There study reported that the TIP4P model gave properties of water close to the experiment in % deviation such as density (+0.2%), heat capacity (+7.3%), entalpy of vaporiztion (1.4%) and internal energy (1.5%).

3.3.7 5-site water model

This model places negative charge on a dummy atom in lone pairs of oxygen. Their geometry is tetrahedral in nature. The earliest model found is known as BNS model of Stillinger and Ben-Naim, that was obtained in 1971, its predecessor the 512 model was obtained in 1974. The TIP5P model is computationally less attractive than the current five site models which bring about improvements in geometry (tetrahedral) and density. These models are rigid non-polarizable models. The TIP5P model uses Lennard-Jones parameters to determine the vanderwaals interaction of oxygen-oxygen atoms [76].

The Hamiltonian model for TIP5P model is given below [79] as

$$V = \sum_{i} U_i + \sum_{i \neq j} U_{i,j} + U_{pol}, \tag{3.3.22}$$

and further expresses as

$$V = \sum_{bonds} K_o (r - r_{eq})^2 + \sum_{angle} K_\theta (\theta - \theta_{eq})^2. \tag{3.3.23}$$

The pair potential is given as

$$V = \sum_{ij} \frac{q_i q_j e^2}{r_{ij}} + 4\varepsilon \left[\left(\frac{A_{12}}{r_{ij}} \right)^{12} - \left(\frac{C_6}{r_{ij}} \right)^{6} \right], \tag{3.3.24}$$

where i and j represent the molecules, A_{12} and C_6 are potential coefficients obtained.

The parameters obtained from the TIP5P model includes temperature-dependent density, energy and dielectric constant. TIP5P parameters are produced from the spherical cut-off method from long-range electrostatic interactions and its coefficients are given [63] as

$$\sigma = \left({}^{A_{12}}/_{4\epsilon}\right)^{\frac{1}{12}} ; \epsilon_o = \left({}^{C_6}/_{4\sigma}\right)^{\frac{1}{6}}, \tag{3.3.25}$$

where the $coefficients$ are independent and were obtained from the model that are done at 1atm and 298K with ewald sums. The values for A and C are 5.45 x $10^5 \overset{o}{A} kcal/mol$ and $590 \overset{o}{A} kcal/mol$ [59].

Contemplating on the most accurate water models for molecular dynamic simulation, [65] came up with the view that in future it will be realizable, however the current water models being used is close to the real values for water. They further stated that non-polarizable water models that are closest to the experimental values for water are SPC/E models, which gives an improvement to many parameters. The limitations of the SPC/E model is that they obtain doubtful results when simulating solute inside water. In conclusion, they observed that using reaction fields improved the outcome of their simulation; potential energy and density parameters are better obtained by TIP4P and SPC models.

3.3.8 Pair potential for carbon-nanotubes

Tersoff introduced a many-body potential function for carbon, silicon, germanium and mixtures of these atoms. This potential function was modified by Bremer [72], which in simplified form is popularly used to model fullerene and carbon-nanotubes.

The potential form by Tersoff and the one simplified by Brenner is expressed as

$$V = \sum_{i} \sum_{j(i<j)} f_c(r_{ij}) \{ V_R(r_{ij}) - B *_{ij} V_A(r_{ij}) \}, F_R(r_{ij})$$

$$= exp(-\lambda r_{ij}), f_A(r_{ij}) - Bexp(\mu r_{ij}), \tag{3.3.26}$$

where λ is the thermal conductivity and the term $V_R(r_{ij})$ and $V_A(r_{ij})$ are the attractive and

repulsive parts of Morse potential of bond stretching, and the summation represents chemical bond. The Morse bond stretching potential is given as

$$v_R^{morse}(r) = f_c(r)\frac{D_e}{S-1}exp\{-\sqrt{2s(r-R_e)}, \tag{3.3.27}$$

and

$$v_A^{morse}(r) = f_c(r)\frac{D_e s}{S-1}exp\{-B^*\sqrt{2/s(r-R_e)}, \tag{3.3.28}$$

where f_c(cut of function) is a decaying function centered at $r = R$ with $D/2$ width, and

$$f_c(r_{ij}) = \left\{1/2 - 1/2sin\frac{\pi}{2}\left[\frac{1}{0}\frac{\pi}{2}(r-R)/D\right]\right\}\begin{cases} r > & R+ & 0) \\ R < & r < & R+ \quad D) \\ & r > & R+ \quad D) \end{cases}, \tag{3.3.29}$$

where $B*$ modifies the force of attraction $V_A(r)$ relying on $\theta_{ijk}$with bond angle between, bonds $i-k$ and $i-j$ [72] and expressed as

$$B* = \frac{b_{ij}+b_{ji}}{2}, b_{ij}, \tag{3.3.30}$$

where

$$b_{ij} = \left[1 + a^n\left(\sum_{k(\neq i,j)} f_c(r_i k)g(\theta_{ijk})\right)^n\right]^{-\delta}, \tag{3.3.31}$$

and

$$g(\theta) = 1 + \frac{c^2}{d^2} - \frac{c^2}{d^2} - \frac{c^2}{d^2 + (h - cos\theta)^2}, \tag{3.3.32}$$

where $g(\theta)$ is the geoometrical model, obtaining the parameters c, d, h and θ for each term of atoms provides unique models.

3.4 Equation of motion

Molecular dynamic simulation uses the Newton's equation of motion to determine the position, velocity and trajectories of atoms and molecules in an ensemble. The Newton's second law is given by

$$\frac{\partial^2 r}{\partial t^2} = \frac{F}{M}, \tag{3.4.1}$$

where r is the position, t is the time, M the mass of atom and F the total force acting on the atom. This can further be expanded as

$$F_{ij} = -\sum F_{ij} = -\sum_{i \neq j} \frac{\partial u(r_{ij}) \partial r_{ij}}{\partial r_{ij} \partial r_{ij}} \tag{3.4.2}$$

therefore

$$F_{ij} = -\sum_{i \neq j} \frac{\partial u(r_{ij}) \ddot{r}_{ij}}{\partial r_{ij}}, \tag{3.4.3}$$

where F_{ij} the total force acting on the atom i and j.

Equation 3.4.3 determines how the microstate moves in time. For a simple system, the Newton second equation is desirable, but for complex and large systems such as rigid molecules, the Euler equations that are explained by Hamiltonian quaternion are required. In the case of molecules that are flexible and subject to constraints and are internal, the use of Lagrange is adopted [20].

The Lagrange equation is given as

$$m\ddot{q}_i = ma, \tag{3.4.4}$$

where m is the mass of atom, a is the acceleration. The Euler-Lagrange equations is written in the form as

$$m\ddot{q} + \nabla v_r = 0, \tag{3.4.5}$$

where

$$ma = -\nabla v_r, \tag{3.4.6}$$

and when written in the potential form it becomes

$$\overrightarrow{F} = -\nabla v_r, \tag{3.4.7}$$

where $-\nabla v_r$, is the negative gradient of the potential energy.

For MD method, the Newtonian equation for fluid molecules is expressed as

$$m_i \frac{d\vec{r}^2}{dt^2} = \sum_{j \neq i, j=1}^{N} \vec{F_{ij}} + \sum_{j_w \neq i, j=1}^{N_w} \vec{F}_{ijw} + \vec{F}_{sou}\vec{i}, \tag{3.4.8}$$

where subscript i represents particle i, and $\vec{i}$ is unit vector in the x-cordinate. The 1st term in the RHS is molecular force as a course of the LJ potential , and second term is molecular force between solid wall atom j and fluid particle i. The last term in the RHS is the external force, like

gravity, pressure or electric force.

3.5 Integration Methods

Molecular Dynamics simulation is a time integration method where positions and momentum (velocity) are determined with the trajectory of the molecules and atoms obtained with time. There are different types of time integration methods used in molecular dynamics which differ according to their different efficiency, accuracy and stability [2]. They include verlet algorithm, Leap-frog algorithm, velocity verlet algorithm, shake algorithm, Beeman algorithm, explanation of these algorithms will be based on the ones that are of interest.

3.5.1 The verlet algorithm

Amongst the most commonly used methods to solve and determine trajectories of atoms and molecules is the verlet Algorithm. This is a position scheme based on determining the future position $r_i(t)$. It is obtained from Taylors series centred difference as

$$r_i = (t + \triangle t) = r(t) + \dot{r}(t)\triangle t + {}^1\!/_2\ddot{r}(t)\triangle t^2 + {}^1\!/_6\dddot{r}(t)\triangle t^3 + 0(\triangle t)^4, \tag{3.5.1}$$

and

$$r_i = (t - \triangle t) = r(t) - \dot{r}(t)\triangle t + {}^1\!/_2\ddot{r}(t)\triangle t^2 - {}^1\!/_6\dddot{r}(t)\triangle t^3 + 0(\triangle t)^4, \tag{3.5.2}$$

summing the two equations gives

$$r_i(t + \triangle t) = 2r(t) - r_i(r - \triangle t) + a(t)\triangle t^2 + 0(\triangle t^4), \tag{3.5.3}$$

where the current position is $r(t)$, acceleration a_i(t), past position $r_i(t - \triangle t)$ and $r_i(t + \triangle t)$ as the future position. This scheme does not need the velocity to compute the future position. But velocities are necessary to compute the total energy, temperature, kinetic energy; therefore velocities can be obtained using the central difference method.

$$v(t) = \frac{r(t + \triangle t) - r(t - \triangle t)}{2\triangle t}. \tag{3.5.4}$$

3.5.2 Leap frog algorithm

This is a half-step scheme that is based on the triplet $\{r(t)\}$, current position, v$(t - 1/2)$ half step past velocity, $\{a(t)\}$ acceleration calculated from forces

$$v(t + 1/2) = v(t + 1/2) + a(t), \tag{3.5.5}$$

and

$$r(t + \triangle t) = r(t) + v(t + 1/2), \tag{3.5.6}$$

gives

$$v(t) = \frac{v(t + 1/2\triangle t) + v(t - 1/2\triangle t)}{2}, \tag{3.5.7}$$

where $\{r(t)\}$is the current velocity and is obtained from the mid values of half of the time step.

3.5.3 Velocity verlet scheme

This is a variant of the verlet method that is based on $\{r(t)\}$,$\{v(t)\}$ and $\{a(t)\}$ to obtain the future position (trajectory) and velocities. It minimizes the round off error and is considered the most suitable for molecular dynamic simulation.

$$v(t + 1/2\triangle t) = v(t) + 1/2a(t)\triangle t^2, \tag{3.5.8}$$

the future position is expressed as

$$r_i(t + \triangle t) = v(t + 1/2\triangle t) + 1/2\triangle t[a(t) + a(t + \triangle t)], \tag{3.5.9}$$

where $a(t+\Delta t)$ is the current acceleration. The kinetic energy is obtained, based on the calculation of $v(t + \Delta t)$. The acceleration is obtained from $a = \frac{f}{m}$. A good time step chosen from Leonard – Jones potential is about 0.005τ or $10fs$ time scale. This time step was chosen to cover the frequency of atomic bond stretching vibration which is about $10fs$ in range.

3.6 Correlation and Time Correlation Functions

Time correlation function uses statistical mechanics to transform from one microstate to another via a correlation coefficient that is time averaged. With A and B obtained at separate time, the

correlation coefficient (t) is defined as

$$c_{AB} = \frac{< \delta A \delta B >}{\sigma(A)\sigma(B)}, \tag{3.6.1}$$

where A and B are correlated quantities, when A and B describe same terms it is called auto-correlation function and expressed as

$$c_{AA}(t) = \frac{C_{AA}(t)}{C_{AA}(0)}. \tag{3.6.2}$$

Ensemble averages are also known as correlation function $C_{AB}(t)$ and is a function of separation in time (t) of correlated quantities A and B. The correlation delay describes the dynamical properties of a system. The phase space distribution function is used to derive the time correlation function, expressed as

$$C_{AB} =< A(t)B(0) >= \int f(\Gamma)B(\Gamma)e^{iLt}A(\Gamma)d\Gamma, \tag{3.6.3}$$

where e^{iLt} is a propagator of observed quantity A, with the bracket <.....> describing the ensemble average [71]. The mathematical operator e^{iLt} which is the propagator, applies Newton's equation of motion to obtain phase variable evolutions from an initial value. Equation 3.6.3 has theoretical relevance but cannot be applied in MD, as it entails a knowledge of sampling of microstate and phase space distribution function. Correlations in non-equilibrium and equilibrium steady state becomes invariant when the time origin is shifted. Therefore, the correlation is obtained by the averaging of trajectories in time. For MD, the time is discretised with the correlation function obtained from a steady state simulation

$$C_{AB}(t) = \frac{1}{N_t}\sum_{i=1}^{N_i} A(t_i + t)B(t_i); t_i = 0, \tau, 2\tau.....(N_{t-1}), \tag{3.6.4}$$

where t_i is starting time of a trajectory and τ is the time between starting points of two trajectories to be averaged.

In the event of phase space mixing, the correlation function will decay from $< A(0)B(0) >$ at $t = 0$, to $< A >< B >$with limit t$\to \infty$ [80-81], satisfying the following expression

$$C_{AB}(t) =< A(t)B(0) >=< A(0)B(-t) >= C_{AB}(-t), \tag{3.6.5}$$

given the Taylor series expansion of the correlation function at $t = 0$ as

$$C_{AB}(t) = \sum_{n=0}^{\infty} \frac{t^{2n}}{(2n)!} < A^{(2n)}(0)B(0) >, \tag{3.6.6}$$

where C_{AB} is the correlation function of quantity A and B, t is the time lag.

Correlating a quantity with itself is known as autocorrelation functions and is useful in obtaining transport coefficient. The stress autocorrelation function (SACF) and velocity autocorrelation function (VACF) are the most applied autocorrelation function in MD.

From the infinite time integral of correlation function the transport coefficient is expressed as

$$\gamma = \int_0^{\alpha} < A(t)A(0) > dt, \tag{3.6.7}$$

where A is a correlated quantity at initial and current time.

Transport coefficients can also be calculated using velocity correlation e.g. the diffusion coefficient (D) and the phonon density in $3D$ is obtained through velocity autocorrelation and is given by

$$D = \frac{1}{3} \int_0^{\alpha} < V_i(t)V_i(0) > dt, \tag{3.6.8}$$

where $V_i(t)$, the mass centre for velocity of a single atom.

Links between correlation function and transport coefficient is made possible through linear response theory which is described by the Einstein relation [2] as

$$\gamma = \frac{< (A(t) - A(0))^2 >}{2t}. \tag{3.6.9}$$

where A is an ensemble average. The position of the molecule and other heat transport coefficients including λ_T (Thermal conductivity), viscosity(bulk) η_v and viscosity(shear) η, can also be obtained from correlation function.

3.7 Periodic boundary conditions

Simple systems using Leonard-Jones potential are not very effective for complex systems but are computationally efficient and have obtained reliable and acceptable results; therefore, it will be adopted in this study. MD uses periodic boundary conditions which are an endless array of replaced images in a simulation box, meaning the box of interest is seamless. To avoid confusing the potential of a molecule and its replica, the potential is cut-off at a length shorter than half the width of the box (cell) of interest. There are different methods proposed to reduce the computational time

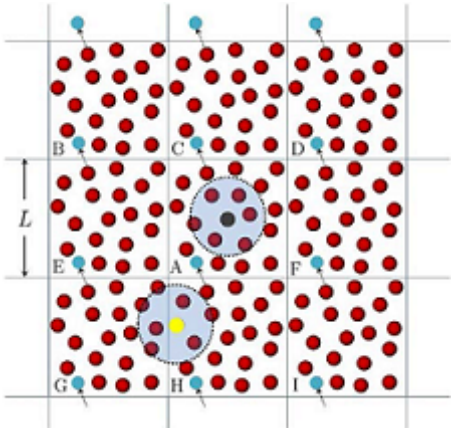

Figure 3.1: Periodic boundary condition in 2-D. Cells B-I are mirrow images of cell A. see in [2] pp.16

during the simulation when considering the periodic boundary conditions, they include cut-off distance and shifted potential, neighbour list method, cell subdivision method [2]. The simulation size of a typical MD simulation is restricted to hundreds of nanometers due to computational efficiency and time. This restriction is being overcome by the application of periodic boundary condition.

The cell of interest is infinitely replicated to obtain a two-dimensional space without boundaries. As atoms crosses the boundary of cell A, atoms that are the mirror image on cell H enters cell A. The atom at the left boundary of cell H interacts with atoms in the adjacent and neighboring cell. This process is called minimum image convention, this is shown in Fig. 3.1.

3.8 Initialization of molecular dynamic simulation

Appropriate initialization in MD simulation is very crucial, this is to avoid instabilities. One of the ways of ensuring proper initialisation is to make sure atoms are started at equilibrium states, where the effect of their interaction is null. The simulation will have to commence by setting certain parameters, which means the atoms and molecules have to be generated randomly by placing them inside a simulation box. The Lennard-Jones model is implemented and a distribution function which in this case is the Boltzmann relation. For an MD simulation, the initial velocities of the molecules and atoms have to be specified, this is obtained by choosing random velocities with values corresponding to the start temperature so that there is no momentum in the system. The positions are initialized by choosing a natural structure of any element of choice; this structure will preferably be in a lattice form. After Initialization, simulation in the form of equilibration using a time integration method of choice can commence, this will determine future positions (trajectory)

and future velocities of the atoms and molecules [2]. To start any simulation, random velocities are assigned to atoms using the Maxwell-Boltzmann distribution given by

$$p(v_{\alpha,i}) = \left(\frac{m_i}{2\pi k_B T}\right)^{1/2} exp\left[\frac{-1/2 m_i V_{\alpha,i}^2}{k_B T}\right], \tag{3.8.1}$$

where m_i the mass of particles, v_i the velocity, k_B the Boltzmann constant, T is the temperature and $\alpha = x, y, z$.

Obtaining the forces is the most computationally demanding task which is obtained from the negative gradient of the potential energy. For a shorter distance between two atoms as in Lennard-Jones (LJ) potential, the forces are obtained with the inclusion of a cut-off radius r_c making the computation reduced by a factor $4/3\pi r_c^3/V$ which makes $r_c = 2.5\sigma$. Where σ is the Lennard Jones length parameter. The potential becomes 1.63% of the energy well depth, thereby obtaining computational savings.

3.9 Thermostating

Molecular dynamics simulation is done in the microcanonical ensemble (NVE) which involves a constant number of atoms (N), the volume of the system (V) and the total number of energy (E). The other alternative to the microcanonical ensemble is the control of the system temperature also known as the canonical ensemble. Temperature control can also be performed in the (NVE) ensemble by controlling the kinetic energy of the system; this process is known as velocity rescaling.

The fluid flow in these ensembles leads to irreversible dissipation of kinetic energy to thermal energy and can be mathematically expressed as

$$E_v = -\int p(r) : \nabla u(r) d^3 r, \tag{3.9.1}$$

where p is the density and u the velocity, $E_v = -vp : \nabla u$, is applied for fluids that are homogeneous. For homogenous fluid with periodic boundary condition temperature will be distributed evenly with no heat sink to remove the excess heat, thereby causing an increase of temperature in the system. To maintain the temperature at a given value, the use of a thermostat is applied [82]. A thermostat can be used for all fluids or groups in a system.

Taken the instataneous temperature (which is contrary to the average temperature of the ensemble) for system T_1 and the adjusted temperature of the ensemble T_2. The ratio of the temperature

is given as

$$\frac{T_2}{T_1} = \frac{\sum_i^N (\chi^{vxi})^2 + (\chi^{vyi})^2 + (\chi^{vzi})}{\sum_i^N v_{xi}^2 + v_{yi}^2 + v_{zi}^2}, \tag{3.9.2}$$

where T_1 is the initial temperature and T_2 is the required or adjusted temperature, taking the velocity scaling factor as $\chi = \sqrt{T_2/T_1}$. This system of velocity rescaling does obtain the required temperature of T_2, it also prevents fluctuation of the system temperature.

3.9.1 Berendsen Thermostat

The thermostat by Berendsen [83] allows temperature fluctuation in the system which is the ideal case. This thermostat is achieved by relaxing or allowing the temperature of the system towards the set or target temperature T_2 over a time period τ. This can be expressed as

$$T_2 = T_1 + \left((\partial t/\tau) \left(T_0 - T_1 \right) \right), \tag{3.9.3}$$

from eqn 3.9.2 the expression can be given as

$$\chi T_2 = T_1 + \frac{\partial t}{\tau}(T_0 - T_1), \tag{3.9.4}$$

or

$$\chi = \sqrt{1 + \frac{\delta t}{\tau}\left[\frac{T_0}{T_1} - 1\right]}. \tag{3.9.5}$$

where τ is a parameter that has been coupled to the heat bath and is the controlling parameter. τ is chosen to obtain the right temperature that will not overly suppress the fluctuations. The berendsen thermostat is mostly used for initializing the system temperature.

3.9.2 Gaussian Thermostat

A velocity rescaling technique was developed by [84] and [85] which keeps the fluctuation of the kinetic energy constant but allows the fluctuation of the total energy. This study was further treated by [86] and [87], where they added a term in the motion equation expressed as

$$\dot{P}_i = F_i - \zeta P_i, \tag{3.9.6}$$

The instanteneous parameter of thermostat multiplier while the kinetic energy fluctuation is constant in a system is given as

$$\frac{dk}{dt} = \frac{d}{dt}\sum_{i=1}^{N}\frac{p_i.p_i}{2m_i} = \sum_{i=1}^{N}\frac{p_i - \dot{p_i}}{m_i} = \sum_{i=1}^{N}\frac{p_i}{m_i}.(F_i - \zeta P_i) = 0, \tag{3.9.7}$$

thus the multiplier is expressed as

$$\zeta = \frac{\sum_{i=1}^{N}\frac{P_i.F_i}{M_i}}{\sum_{i=1}^{N}\frac{P_i.F_i}{M_i}}, \tag{3.9.8}$$

where ζ is the thermostat multiplier which can be controlled to add or remove heat from the system and M is the mass of particles, P_i is the momenta and F_i the force.

The Gaussian thermostat mostly applies to non-equilibrium equations of motion. This thermostat fixes fluctuations of kinetic energy of the system. Sometimes single particles can have different thermal velocities. The Gaussian thermostat in some cases also follows targeted distribution functions. Generally wall particles can be coupled with groups of fluid.

3.9.3 Braga-Travis Thermostat

In cases where the driving force is big, velocity profile of the fluid is unknown, a priori; making it hard to contrast between the streaming velocity and fluctuation velocity. The streaming velocity for boundary driven flows are unknown, a priori, but have to be calculated, for the kinetic temperature to be controlled. In another approach, the atomic positions can be controlled through a thermostat. Different thermostats have been developed by [83-87]. These thermostats where modified by [86] with better implementation, their algorithm is expressed as

$$\dot{r} = \frac{P_i}{m_i} - \zeta\frac{\partial u}{\partial r_i}, \tag{3.9.9}$$

with

$$\zeta = \frac{1}{Q_n}\left[\sum_{i=1}^{N}\left(\frac{\partial u}{\partial r_i}\right)^2 - k_B T\sum_{i=1}^{N}\frac{\partial}{\partial r_i}.\frac{\partial u}{\partial r_i}\right]. \tag{3.9.10}$$

The potential interaction laplacian for a lennard jones pair is expressed as

$$\frac{\partial}{\partial r_i}.\frac{\partial u}{\partial r_i} = \frac{\varepsilon}{r^2}\left[528\left(\frac{\sigma}{r}\right)^{12} - 120\left(\frac{\sigma}{r}\right)^{6}\right], \tag{3.9.11}$$

where ζ is the thermostat multiplier, P is the momenta, T is the temperature and k_B is known as the Boltzmann constant.

3.9.4 Nose-Hoover Thermostat

The initial thermostating technique is expressed using Nose Hamiltonian

$$\mathcal{H}_{\mathcal{N}}(r,p,s,\rho_s) = \sum_{i=1}^{N} \frac{P_i.\dot{P}}{2m_i s} + U + \frac{P_s^2}{2Q} + (N_f+1)k_B T_{Ins}, \tag{3.9.12}$$

and modified to

$$\mathcal{H}_{\mathcal{N}}(r,p/s) = \frac{P_s^2}{2Q} + (N_f+1)k_B T_{Ins}, \tag{3.9.13}$$

where s is the included degree of freedom to the system, Q is Nose mass, N_f the number of degrees of freedom for N-body fluid, U is the potential energy, T_{Ins} the instantaneous temperature and P_s the momentum.

Due to the challenges involved in rescaling the momenta, Nose, Hamiltonian formulation cannot calculate the velocity autocorrelation functions. This idea was further expanded by [87], who captured the equations of motion in a convenient and easier form to obtain the velocity autocorrelation. This now became the Nose-Hoover thermostat and is expressed as

$$\zeta = {}^{1}/_{Q}\left[\sum_{i=1}^{N} \frac{P_i.\dot{P}_i}{M} - N_f k_B T\right], \tag{3.9.14}$$

where ζ is Gaussian having a zero mean and variance of $(\zeta^2) = k_B T/m$. m is the mass of fluid, N_f is the degree of freedom and $M = \sum_{i=1}^{N} m_i$. The mass must be chosen to allow critical damping of the system.

Heat is extracted from the system if the thermostat multiplier ζ becomes positive; while the thermostatic multiplier becomes negative, when heat is added into the system. On average, the multiplier is zero since there is no external force acting on the system.

3.10 Fluctuation technique in Molecular Dynamics

Fluctuations are obtained from changes and distribution of possible energies and volume, temperature or pressure in an ensemble, which is given [2] as

$$\delta < \delta A >^2 = \frac{1}{\tau}\int_0^{\tau} [A(t) - < A >]^2 dt >, \tag{3.10.1}$$

where τ is the time averaged.

Fluctuation can be used to obtain other thermodynamic properties like the specific heat, C_v and C_p at constant pressure and volume, thermal expansion coefficient α_p, isothermal compressibility

$B\tau$, thermal pressure coefficients γ_v, and is expressed as

$$C_v = |\frac{\partial E}{\partial T}|_{NVT}, \tag{3.10.2}$$

$$C_p = |\frac{\partial E}{\partial T}|_{NPT}, \tag{3.10.3}$$

where E is the energy and T is the temperature C_v and C_p are specific heats at constant volume and pressure.

The equilibrium molecular dynamic simulation method for calculating the Kapitza resistance applying the temperature difference fluctuation was implemented by [88]. The Kapitza resistance R between heat bath A and heat bath B, exchanging a net heat flux Q at equilibrium temperatures T_1 and T_2 is expressed by the relation

$$Q = R\Delta T, \tag{3.10.4}$$

where Q is the heat flux, R is the Kapitza resistance and ΔT is the temperature difference.

The time dependent energy conservation formulation is used for obtaining and measuring the Kapitza conductance and is expressed as

$$\frac{\partial T_1}{\partial t} = \frac{1}{k_B N_{1-2}} G\Delta T, \tag{3.10.5}$$

with the equation of the temperature difference $\triangle T$ expressed as

$$\frac{\partial \Delta T}{\partial t} = \frac{1}{k_B}\Big(\frac{1}{N_1} + \frac{1}{N_2}\Big) G\Delta T, \tag{3.10.6}$$

where N is the degree of freedom of the heat bath kinetic energy. The ΔT solution is an exponential function that decays with relaxation time τ and gives the Kapitza resistance as

$$Rk_B = \tau\left(\frac{1}{N_1} + \frac{1}{N_2}\right), \tag{3.10.7}$$

and

$$\tau = \int_0^\infty \Big\langle \Delta T(0)\Delta T(t)\Big\rangle / \Big\langle \Delta T^2(0)\Big\rangle dt, \tag{3.10.8}$$

where τ is the time integral of normalized temperature difference autocorrelation and is very suitable for MD simulation that directly processes the temperature and velocities. This is the technique that is applied in this research to obtain the temperature and Kapitza resistance across the interfaces and nanofluidic channels.

Equation 3.10.8 is normally used in non-equilibrium MD, where the exponential decay of temperature difference on relaxing the thermal constraints is used to estimate the time τ.

When Equation 3.10.8 is corrected with langevin flux it is expressed as

$$\frac{d\Delta T}{dt} = -\frac{1}{k_B}\left(\frac{1}{N_1}+\frac{1}{N_2}\right)\int_0^t G(t-t')\Big\langle \Delta T(t')dt' + F(t)\Big\rangle. \tag{3.10.9}$$

Focker Planck equation proposes the Langenvin term having a white noise with time evolution and copies fluctuations that has to do with equilibrium quantities. Phase averaging and removing the $F(t)$ term in equation 3.10.5 and multiplying by ΔT gives the expression

$$\frac{d\Big\langle \Delta T(0)\Delta T(t)\Big\rangle}{dt} = -\frac{1}{k_B}\left(\frac{1}{N_1}+\frac{1}{N_2}\right)\int_0^t G(t-t')\Big\langle \Delta T(0)\Delta T(t')dt'\Big\rangle, \tag{3.10.10}$$

where N_1 and N_2 are the first and second degree of freedom of the heat bath kinetic energy the brackets $\langle.....\rangle$ describe the phase average or autocorrelation function (ACF), k_B is the Boltzmann constant, G is the heat flux and t is the time. This function applies to equilibrium fluctuations in temperature difference ΔT.

3.11 Thermal Wall Model

In fluids that flow inside a nanopore or nanochannel, having a molecular fluid close to the wall will cause a repulsive force to push away the fluid particle from the surface. In reality, due to the Pauli exclusion principle, the fluid particles will never penetrate the wall surface. However, in computations, it is not a guarantee that fluid particles will not penetrate the walls, due to the impossibility of using time steps that are infinitely small. Therefore, thermal wall models are required as a boundary condition to prevent this from occuring. The thermal wall model ensure that the fluid particles are positioned in the parallel walls without penetrating the walls, by the reallocation of the velocity vector of fluid particles trying to penetrate the wall. When a particle strikes a wall with T_w, the three velocity components are reset to a biased Maxwellian or Gaussian distribution. The three velocity component in the Cartesian cordinate system, after fluid molecules strike wall surfaces are expressed as

$$v_x = \sqrt{\frac{k_B T_w}{m}}\psi_G, \tag{3.11.1}$$

$$v_y = \sqrt{\frac{k_B T_w}{m}}\psi'_G, \tag{3.11.2}$$

$$v_z = \pm\sqrt{-\frac{2k_B T_w}{m} In\psi}, \tag{3.11.3}$$

where v_z with a positive sign, are the fluid molecules striking the lower wall surface, while the negative sign is for the fluid molecules striking the top wall surface, ψ this is the random number $(0, 1)$ and $\psi_G^{'}$, ψ_G, represents gaussian-distributed random numbers having zero mean and unit variance.

To avoid expensive computational time, the Maxwell thermal walls with the diffussive and specular model is widely used and desirable, the reflected molecule velocity is obtained from Gaussian distribution and expressed as

$$f(V) = \sqrt{\frac{m}{2\pi k_B T} exp(-\frac{mv^2}{2k_B T})}, \tag{3.11.4}$$

where m is the mass, v is the velocity, k_B is the Boltzmann constant and T is the temperature.

The Einstein theory was also used to develop the atomic structure of a wall model [89-90], stating that the atoms of the wall vibrates around lattice sites with fcc (face centered cubic) having Einstein frequency. The model uses a spring stiffness with harmonic vibrations of an atom in a solid and is expressed as

$$K_{stiff} = \frac{mk_B^2 T_E^2}{\hbar}, \tag{3.11.5}$$

where m mass of solid wall atoms, k_B Boltzmann constant, T_E is the Einstein temperature for solid wall and $\hbar$ reduced Planck's constant.

The model used for this study combines the Einstein solid and Maxwell thermal wall model to obtain an appropriate wall model with spring potential. A particle that has mass is attached to a massless spring from an equilibrium position and has a stiffness or force constant k, even with no external force applied to it, the particle will continue to vibrate with regards to its equilibrium position. Assuming the particle vibrates only in the x-direction equipartition of energy in equilibrium conditions will be present and is expressed as

$$\frac{1}{2}k(\Delta x^2) = \frac{1}{2}m(v^2) = \frac{1}{2}k_B T, \tag{3.11.6}$$

where k is the force constant, m is the mass of spring, Δx is the displacement of particles, k_B Boltzmann constant, T is the temperature and v is the velocity. The relation can also be expressed as

$$k_s = \frac{k_B T}{< \triangle x >}, \tag{3.11.7}$$

where Δx is the displacement of particles and the bracket $< >$ used, describes the ensemble average. k_B is the Boltzmann constant, T is the temperature and k_s is the force constant [91].

Equations 3.11.7 is applied for real crystals undergoing harmonic vibrations.

The harmonic potential have been found to work well in most MD and multiscale systems [92]. Substituting the harmonic potential of eqn (3.11.7) into the probability density distribution gives the expression

$$P(x) = C.exp(\frac{-k(r_i - r_o)}{k_B T}) = C.exp(\frac{1(r_i - r_o)}{2k_B T/2k}), \tag{3.11.8}$$

Giving a Gaussian distribution mean x_o with variance $k_B/2k$. The expression can be estimated as

$$k_s = \frac{k_B T}{2 < r - r_o) >}. \tag{3.11.9}$$

where $r_o =< r >$and $<..>$ describes averaging over available samples.

Molecular dynamics (MD) allows for the inclusion of atomic level studies and an-harmonic effects that are not possible with experiments and analytical models. Since molecular dynamics uses the classical assumption, its simulations are mostly performed above the Debye temperature. In the MD method for studying interfaces and nanofluidic channels, the solid-wall modelling is very important and still a problem because lots of computational time is needed to simulate boundary walls [93].

3.11.1 Acoustic Mismatch Model

The acoustic mismatch model (AMM) can only determine thermal transport in very low temperature ($<$ 1K) and fails at elevated temperatures ($>$10K) [94]. The AMM bases its assumption that interfacial walls are treated in continuum. In the AMM, phonons are said to be incident in form of plain waves undergoing transmission that are specular at the interface. The model assumes that the interface is perfect with only elastic phonon-phonon scattering. Reflection and transmission probabilities are obtained with phonons taken as plane waves without scattering at interface. These assumptions holds for very low temperatures; however; for temperatures that are higher ($>$10K) and interfaces that are rough, diffusive scattering is very probable. This model predicts thermal conductance and Kapitza resistance for surfaces with small differences in densities and speeds of sound of different media.

The thermal boundary conductance using AMM theory in the phonon density form is repre-

sented mathematically as

$$h_{wf} = \frac{1}{2}\sum_{j}\frac{\partial}{\partial T}\int_{0}^{\frac{\pi}{2}} n(\omega,T)\hbar\omega c_i, jx\alpha_i, j(\phi,j,\omega)cos(\phi)sin(\phi)dwd\phi, \tag{3.11.10}$$

where, h_{wf} is the thermal boundary conductance (TBC) from wall to fluid, $n(\omega,T)$ the distribution function for occupancy, $\hbar$ Plancks constant, ω phonon frequency, ω_{max} maximum frequency of phonon on the wall c_{ij} propagation velocity of phonon mode j, α_{ij} transmission coefficient incident on wall, ϕ, phonon angle of incidence.

The AMM conductance model is generally expressed as

$$G_L^{AMM} = \frac{3}{2}n_i k_B c_i \left(\frac{c_2}{c_1}\right)^3 \int_0^1 t_{12}(\mu_1)\mu_1 d\mu_1, \tag{3.11.11}$$

where n_1 is the number density, c_1 and c_2 are speed of sound in the respective medium, μ_1 is the phonon incident angle and t_{12} is the transmission coefficient.

The phonon lifetime is generally expressed as the Collaway model [95] and expressed as

$$\tau_i(\omega) = A_i\omega^{-2}, \tag{3.11.12}$$

where A is a constant and ω is the phonon frequency.

The transmission coefficient for AMM is expressed as

$$t_{12} = \frac{4Z_1Z_2\mu_1\mu_2}{(Z_1\mu_1 + Z_2\mu_2)^2}, \tag{3.11.13}$$

where $\mu_i = cos\theta_i$ the cosine of incident angle and μ_2 the cosine of refracted angle. Z_i is expressed as

$$Z_i = \rho_i c_i. \tag{3.11.14}$$

where Z_i is the acoustic impedances.

The AMM model cannot appropriately predict the interfacial conductance in the simulation if the acoustic impedance ratio $\frac{Z_1}{Z_2} \rightarrow 1$, which makes the conductance diverge [96]. Though the AMM gives an appropriate conductance prediction within a large range of acoustic impedance, if the acoustic impedance is far less than 1. The AMM does not account for out-of-equilibrium distribution of phonons across the interfaces in a smaller ratio of acoustic impedance, hence, predicting the conductance to be finite for materials that are identical. If the acoustic ratio is approximately 0.7 the AMM model will be wrong with a factor greater than three [97], for an acoustic ratio $\simeq$0.8

the model under-predicts the conductance with a factor of 5-9 [98].

3.11.2 Diffuse Mismatch Model

The diffuse mismatch model was proposed by [99]. The model infers that incident phonons undergo diffuse scattering that is elastic at the interface and is emitted at both sides of the media. It also states that the probability of scattering at both sides of the media is proportional to the phonon density of state (PDOS) of the media. The memory of the incident wave is assumed to be lost after transmission from one side to the other, and the transmissivity from side 1 to 2 is independent of the incident angle, phonon mode and wave vector. As the memory of the phonons are lost, the transmissivity from one side is assumed to be equal to the reflectivity of the other. With incident angle θ the phonon transmissivity from medium 1 to 2 is expressed as

$$\Gamma_{1\to2} = \int_0^{\omega} \alpha_{1\to2}(\theta, p).cos(\theta).sin(\theta)d\omega, \tag{3.11.15}$$

where p is the phonon mode, θ is the incident angle. When the debye approximation and different transverse and longitudinal phonon velocities is included, the diffuse phonon transmissivity is expressed as

$$\Gamma_{1\to2} = \frac{1}{2}\frac{\sum_p(\upsilon_{2\to1,p})^{-2}}{\sum_p(\upsilon_{1\to2,p})^{-2} + \sum_p(\upsilon_{2\to1,p})^{-2}}, \tag{3.11.16}$$

where $\Gamma_{1\to2}$ is the phonon transmissivity, υ are the phonon velocities and p is the density.

Though this assumption is untrue because elastic scattering does not allow the frequency of the phonon to change, or mode to mode conversion of phonon. For example if two media 1 and 2 possess a big mismatch in their frequency or phonon dispersion relation, phonons having specific range of frequency or dispersion relation will not be able to transmit across the interface, due to the possiblity of no mode to mode conversion of some phonons. Therefore, for transmission to occur across the interface inelastic scattering has to take place to modify the phonon frequency or instigate mode to mode conversion. Therefore, to obtain accurate results and description of the physics in these media, MD is inevitable for studies involving solid-liquid interfaces that have a big mismatch [100].

3.11.3 Lattice Dynamic Model

The lattice dynamic model (LDM) is suitable in predicting the thermal boundary resistance (TBR) at very high temperatures and frequency ($> 100GHZ$) and is predicted on pure specular phonon scattering.

The expression obtained for thermal boundary conductance for LDM is given [101] as

$$G_L^{LDM} = \frac{\partial q_{A\to B}}{\partial T} = \frac{1}{V}\int_0^\infty \frac{\partial_n(\omega,T)}{\partial T}\hbar\omega \sum_{k,p} v_z(k,p)t(k,p)\delta(\omega-\omega(k,p)), \tag{3.11.17}$$

where, $\omega(k,p)$ is the phonon frequency having wave vector k with polarization p. $\sum$ is the sum of all incident phonons on the surface from atom lattice A. $v_z(k,p)$ is the normal group velocity for incident phonons on the interface, $t(k,p)$ is transmission coefficient showing probability of phonon transfer in the interface and the kronecker delta function is given as $\delta(\omega-\omega(k,p))$.$q_{A\to B}$ is the heat flux of interface/unit area and V is the volume. The transmitted phonon for LDM is expressed as

$$t(k,p) = M_2 \sum_{q=4}^{6} v_{qz}A_q^2/M_1 v_{oz}A_0^2, \tag{3.11.18}$$

where M is the mass of particles, v_{qz} with $q = 4,5,6$ is the normal group velocity of phonons that are transmitted, v_{oz} normal group velocity for phonons that are incident. The interface boundary conditions are used to solve the equation and are expressed as

$$\sum_{q=1}^{6} M_{p'q}A_q = M_{p'0}A_0, \tag{3.11.19}$$

where A is amplitude of incident phonon, 3 reflected, 3 transmitted in both media, $M_{p'q}$ is the mass of media 1 and $M_{p'0}$ is the mass of media 2.

For MD simulations, phonon scattering is not diffuse but specular in the interface due to transmission of incidence phonons [102-103] with larger wavelengths compared to interfacial roughness.

3.12 LAMMPS

The open source codes used for this work is the Large Atomic-Molecular Massively Parallel Simulator (LAMMPS) developed by Sandia National Laboratory in the United States. The documentation, source codes and examples can be obtained as a GNU license [104]. LAMMPS uses different algorithms to integrate the atomic trajectories in time, and for this work the velocity verlet algorithm is applied, the reasons having been explained in earlier chapters. It uses optimisation techniques for computing the different segments of its implementations and includes the computation of pair potentials, interatomic interactions, cell linked list algorithm, neighbour list and cut-off distance. Simulations are implemented with the aid of script files, containing necessary LAMMPS commands and fixes. The LAMMPS source code is written in c++ class with object-oriented structure. This feature allows modifications, creations, plug-ins, subroutines and code

extensions into existing LAMMPS codes.

Several extensions and modules have been developed and included into LAMMPS source codes to implement the MD models and simulations vital for this study. Though LAMMPS is widely used in the research community, the version used for this work is validated and verified for different test cases. For the verification, a 3-D atomic model with LJ potential is used, having time step of $\delta t = 0.005$ and cut-off distance $r_c = 2.2$ in real units.

[1]

[1]This page is intentionally left blank

Chapter 4

Effect of Wall Mass on the Kapitza resistance

4.1 Introduction

This chapter investigates the effects of wall mass and stiffness on the Kapitza resistance at the solid-liquid interface in nanofluidic channels. The study aims to shed light on the heat transition between two states of matter in the nanoscale. The vibrational motion and surface stiffness of the walls are simulated using spring potentials. The results show that for low values of surface stiffness, the thermal or Kapitza resistance is dictated by the value of the mass of wall particles (m_w). The results also reveal that the temperature jump at the solid interface is not accurately described by the theoretical vibrational frequency $\sqrt{\kappa/m_w}$ of the walls [55], but increases as a fifth-order polynomial with respect to $log(m_w k)$, where the rate of increase gradually decays until the curve reaches a plateau.

The increasing heat generated by modern electronics, results in temperature jumps that can cause devices to fail. The use of micro and nanochannel heat sinks as cooling devices [105], have motivated research into optimizing the heat transfer capacity by adjusting the nanochannel's geometry, increasing the surface to volume ratio, and/or by using fluids with higher thermal conductivities. Although significant improvements have been made through the use of highly conductive liquids, such as nanofluids [106], the thermal resistance at the solid-liquid interface will always pose a bottleneck, restricting heat from entering the stream and being disposed via convection. The present study investigates the importance of wall stiffness and atomic mass of wall particles to the temperature jump and indicates that it is, in fact, the synergy between the mass and bonding stiffness that governs thermal or Kapitza resistance in interfaces. This finding can potentially guide the optimization of materials for achieving better thermal properties at the solid-liquid interface of nanofluidic channels.

4. Effect of Wall Mass on the Kapitza resistance

The objectives of this chapter are to Develop 3D molecular dynamic algorithm and codes of the simulation domain and thermal wall model with wall-fluid intermolecular interaction energy strength (ε_{wf}). Also to investigate the effect of wall mass and stiffness constant ranging from $\kappa = 100\varepsilon\sigma^{-2} - 1600\varepsilon\sigma^{-2}$ on the Kapitza resistance, temperature and density distribution across the solid-liquid interfaces and nanofluidic channels. To study the effect of various ranges of temperature difference of the walls on the Kapitza resistance, temperature and density distribution across the solid-liquid interface and nanofluidic channels. To develop a master curve and model describing the actual relationship between the temperature jump, the bonding stiffness and wall mass.

4.1.1 Simulation Method and Justification

There have been several wall models developed to describe the heat transfer between solid and liquid interfaces [107-111]. To date, there is no single wall model that is accepted. From these studies, it can be deduced that constant temperature at the walls should be attained to depict experimental scenarios, and there should be thermal equilibrium between the liquid and solid interface layers. Wall models using fixed and frozen wall atoms were validated with liquid argon between parallel platinum walls, fixed at different temperatures [93]. The steady state properties obtained in their study is in agreement with experimental thermodynamic tables of argon. The structure of the wall model of this study adopts a combination of wall atoms that are connected by springs and velocity rescaling of the walls [107-108], which are similar to most solid-liquid heat transfer wall models. This study also took into account and included observations made by a previous study [111]. Their study reported that thermal wall model using vibrating walls, gives temperature control similar to an actual experiment and is better than freezing and fixed wall atoms [108]. The wall model of this study simulates the heat transfer and thermal energy interaction through the Lennard Jones potential and harmonic springs. There is a tendency for the wall temperature to vary due to the energy exchange with the liquid particles, as 99% of the heat flux is because of the energy transfer between neighboring liquid and solid layers.The solid-liquid thermal energy exchange takes place with walls thermostated to obtain a specified constant temperature of the solid walls in this study [108].

Most MD studies implement more than 2-wall layers in studying fluid and thermal transport phenomena in interfaces and nanofluidic channels [107-108]. Two layered wall models are developed in this study to obtain reduction in thickness of the walls, lesser computational time and expenses. The 2-wall model of this study clearly shows the density distribution in the wall lattices and how they are affected by varying the mass and bonding stiffness of the wall. The wall model also shows inelastic thermal and density oscillations at the walls. Simulation for 2 and 7 thermostated wall

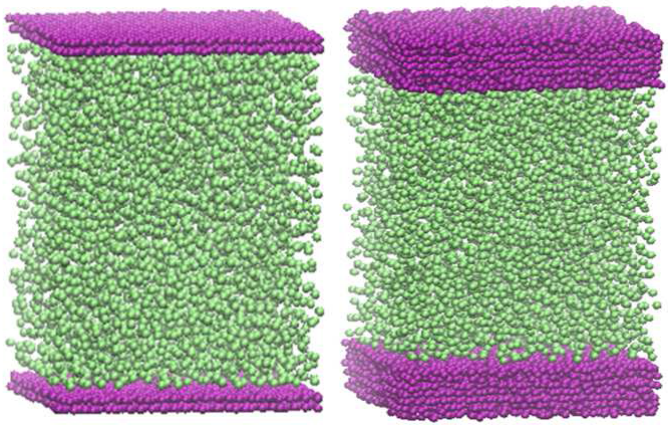

Figure 4.1: Equilibration of 2 and 7 wall layers

No of walls	2walls with r_c	2walls without r_c	7walls with r_c	2walls without r_c
$\kappa = 100$	0.01299	0.01299	0.00573	0.00573
$\kappa = 1600$	0.02729	0.02729	0.01247	0.01247

Table 4.1.1: Kapitza Resistance Values of Temperature Jump for Lower wall

layers were undertaken and compared, to ascertain the effects of increased thermostated wall layers on the properties of the system. There is no significant change in temperature jump and other properties when the 2-wall layer model is compared to the 7-wall layer model. Fig. 4.1, shows the reduction and equilibration behaviour of 2 and 7 wall models. The simulation study also observed that the absence and presence of cut-off (rc) within the 2 and 7 thermostated wall layers makes no difference on the temperature jump. The 2-wall and 7-wall layers with the same cut-off where compared. There is also no significant change to their temperature jumps for the same input parameters. Hence the justification for the use of 2-atomic layers, saving computational time and resources, the comparison are shown in tables 4.1.1-4.1.3.

Since this study is not interested in studying one particular system, the parameters applied in the model are expressed in dimensionless units, this is for numerical stability and error estimation, which can be converted to SI or other units of interest. The computational model consists of liquid argon particles, confined by two parallel solid walls. The walls of the channel are fixed perpendicularly to the y-direction (parallel to the xz plane) with the dimensions in the x and z directions being $L_x = 16.8\sigma$ and $L_z = 17.0\sigma$, respectively, where σ denotes the molecular length scale [51]. L_y is the distance separating the walls (in the y direction) and is set to $L_y = 20.5\sigma$.

No of walls	2walls with r_c	2walls without r_c	7walls with r_c	2walls without r_c
$\kappa = 100$	0.06316	0.06316	0.01972	0.01972
$\kappa = 1600$	0.02522	0.02522	0.03825	0.03825

Table 4.1.2: Kapitza Resistance Values of Temperature Jump for Upper wall

$\kappa = 100$ LOWER WALL	0.7%
$\kappa = 1600$ LOWER WALL	1.4%
$\kappa = 100$ UPPER WALL	4.3%
$\kappa = 1600$ UPPER WALL	1.7%

Table 4.1.3: % Difference of temperature jump between 2walls and 7walls.

Periodic boundary conditions are employed along the x and z directions, emulating the perpetual continuation of the channel. In the y direction, each of the two walls consists of two [111]− oriented perfect Face-Center Cubic (fcc) lattice planes, with density $\rho^*_{wall} = 4m\sigma^{-3}$, which describes the density of the solid walls.

The interatomic interactions between the argon atoms are modelled through a Lennard-Jones (LJ) potential

$$\nu^{LJ}_{ij}(r_{ij}) = 4\varepsilon[(\sigma/r_{ij})^{12} - (\sigma/r_{ij})^{6}], \tag{4.1.1}$$

where i, j are the indices for two arbitrary particles in the system; r_{ij} is their interatomic distance, σ is the lennards jones lenght and ε is the characteristic energy level. For computational efficiency, interatomic interactions beyond a cut-off distance $r_c = 2.2\sigma$ are disregarded. The LJ parameters for the potential between argon particles are $\epsilon_{ll} = 1.0\varepsilon$ and $\sigma_{ll} = 1.0\sigma$, while for the wall-liquid interactions the values $\varepsilon_{wf} = 0.2\varepsilon$ and $\sigma_{wf} = 1.0\sigma$ are used. The liquid density is set to $\rho^*_l = 0.84m\sigma^{-3}$. The liquid mass is set to $m_l = 1m$ while the mass of the wall atoms range between $m_w = 1m$ to $m_w = 10m$. Given the system potential, the equations of motion for the particle i are given by

$$m\ddot{r}_i = -\sum_{i \neq j} \nabla V_{ij}, \tag{4.1.2}$$

where m is the mass, $\ddot{r}_i$ is the acceleration of the particles and $-\nabla V_{ij}$, is the negative gradient of the potential energy.

The wall particles are fixed onto their initial lattice sites by spring potentials, urging them to return to their equilibrium positions r_0 via a restoring force given by

$$\boldsymbol{F} = -\kappa(\boldsymbol{r}_i - \boldsymbol{r}_o), \tag{4.1.3}$$

where κ is the wall stiffness, a parameter vital to the realistic representation of the wall, $r_i - r_o$ is the particle displacement. Its value determines the strength of the bonds between the wall particles as well as their motion, which in turn will influence the rest of the system. For the current study, the values for κ range from $\kappa = 100\epsilon\sigma^{-2}$ to $\kappa = 6400\epsilon\sigma^{-2}$ [51].

In order to control the temperature of the system, each fcc plane of the walls is set to a specific

	$\kappa(\varepsilon\sigma^2)$	ε_{wf}	$\triangle T$	Mass(m)	Time step (τ)	Simulation run time
Case 1	100-6400	0.2	0.1	$m_w = m_1 - m_{10}$	0.001	4×10^7
Case 2	100-6400	0.2	0.2	$m_w = m_1 - m_{10}$	0.001	4×10^7
Case 3	100-6400	0.2	0.3	$m_w = m_1 - m_{10}$	0.001	4×10^7
Case 4	100-6400	0.2	0.4	$m_w = m_1 - m_{10}$	0.001	4×10^7

Table 4.1.4: Simulation Matrix for wall mass effect on Kapitza resistance with 5 High Powered Computing Nodes used and 765 simulation runs

temperature [112]. The regulation of the temperature is achieved by explicitly rescaling the per-atom velocities, averaging them up to the desired temperature. The lower wall is constantly set to $T^* = 1.2\epsilon k_B^{-1}$, while the temperature of the top wall ranges from $T^* = 1.3\epsilon k_B^{-1}$ to $T^* = 1.6\epsilon k_B^{-1}$.

The simulation step employed in this study is $\delta t = 0.001\tau$. An initial equilibration phase of 4×10^7 time-steps takes place to allow the temperature and energy of the system to settle. The simulations are then performed for a further 4×10^7 time-steps through the micro-canonical ensemble (NVE). Codes (LAMMPS and C++) were developed and implemented in Cranfields' University high- performance computer known as ASTRAL XC3000 supercomputer with multiple core processor system having 32TB storage capacity. The simulation matrix is shown in Table 4.1.4

4.1.2 Results and Discussion

Trends of increasing temperature with decreasing Kapitza resistance have been given by molecular dynamics [113-114] and experiments [115] which is due to inelastic phonon interface scattering. The Kapitza resistance of wall-fluid interphase as a function of vibrating frequency of the wall atoms with various dimensionless mass is shown in Fig.4.2(a) lower wall and Fig.4.2(b) upper wall - Fig. 4.5(a) lower wall and Fig. 4.5(b) upper wall with $\Delta T = 0.1\varepsilon\kappa_B^{-1} - 0.4\varepsilon\kappa_B^{-1}$. These Figures shows the temperature jumps as a function of $\sqrt{\kappa/m_w}$ for different values of wall mass (m_w). The curves show that for lower values of the bonding stiffness, the temperature jump significantly increases with increasing the wall mass (m_w) at the lower wall. As κ increases, the significance of the mass, which has so far been the dominant factor in affecting the temperature jumps, decreases. Consequently, with increasing m_w the rate of increase is reduced. Higher temperature jump is seen in the upper wall. Fig. 4.2(b)-4.5(b) shows that for lower and higher values of bonding stiffness, the temperature jump increases further with increasing mass.

Fig. 4.6(a and b) to Fig. 4.11(a and b) sheds light on how the atomic mass of the wall influences the propagation of heat across the solid-liquid interface. For comparison purposes, with Fig.4.2(a and b) - Fig. 4.5(a and b) which shows the temperature jump across the wall of mass $m_w = 1m - 10m$ against κ for different temperature gradients ΔT. The nature of the

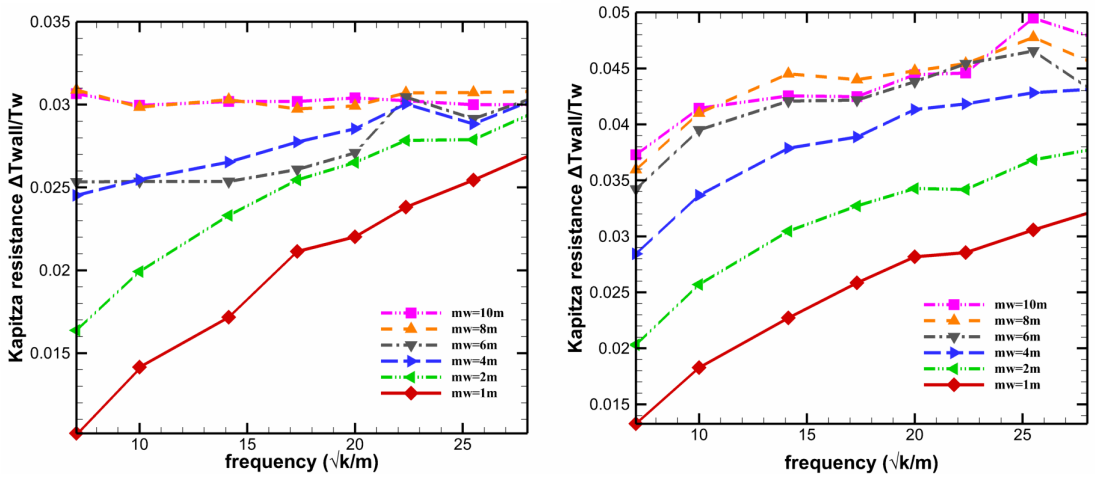

a) Lower wall b)Upper wall

Figure 4.2: Kapitza resistance for $m_w = 1m - 10m$ for a) lower wall and b) upper wall with $\varepsilon_{w-f} = 1.0$ and $\Delta t = 0.1$ for values of frequency

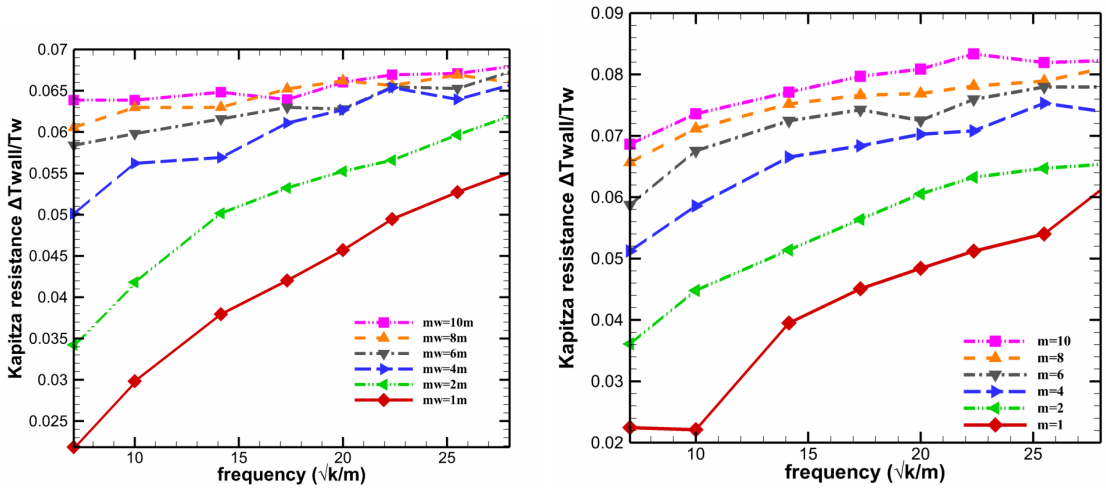

a) Lower wall b)Upper wall

Figure 4.3: Kapitza resistance for mass $m_w = 1m - 10m$ for a) lower and b) upper wall with $\varepsilon_{w-f} = 1.0$ and $\Delta t = 0.2$ for values of phonon frequency

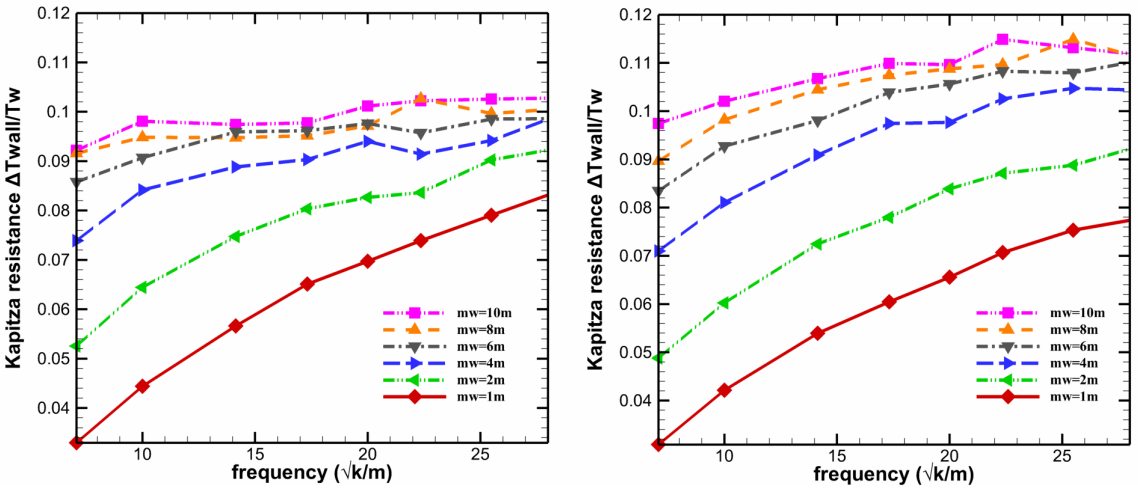

a) Lower wall b)Upper wall

Figure 4.4: Kapitza resistance for mass $m_w = 1m - 10m$ for a) lower and b) upper wall with $\varepsilon_{w-f} = 1.0$ and $\Delta t = 0.3$ for values of phonon frequency

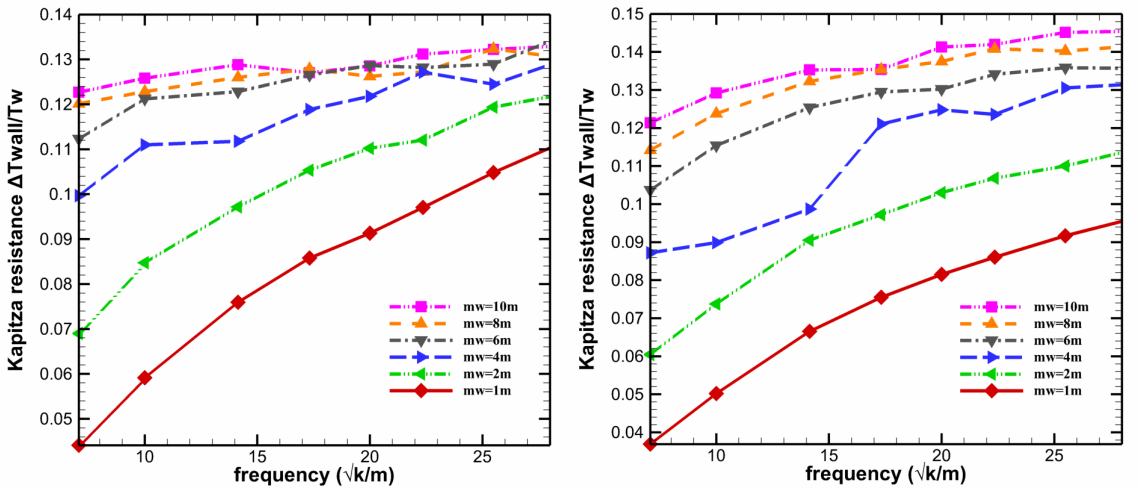

a) Lower wall b)Upper wall

Figure 4.5: Kapitza resistance for mass $m_w = 1m - 10m$ for a) lower and b) upper wall with $\varepsilon_{w-f} = 1.0$ and $\Delta t = 0.4$ for values of phonon frequency

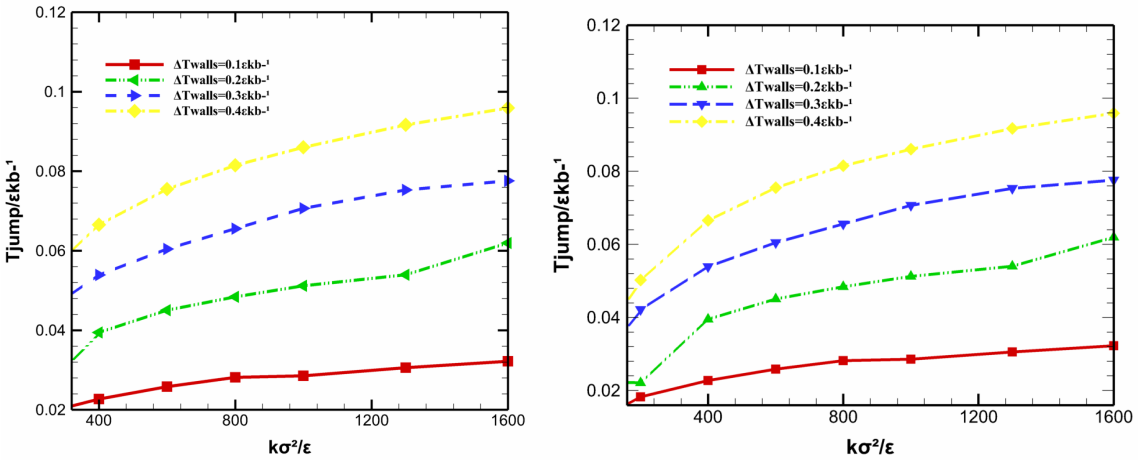

a) Lower wall b)Upper wall

Figure 4.6: Kapitza resistance for $m_w = 1m_f$ for a) lower and b) upper wall with $\varepsilon_{w-f} = 1.0$ and $\Delta t = 0.1 - 0.4$ for various values of stiffness constant

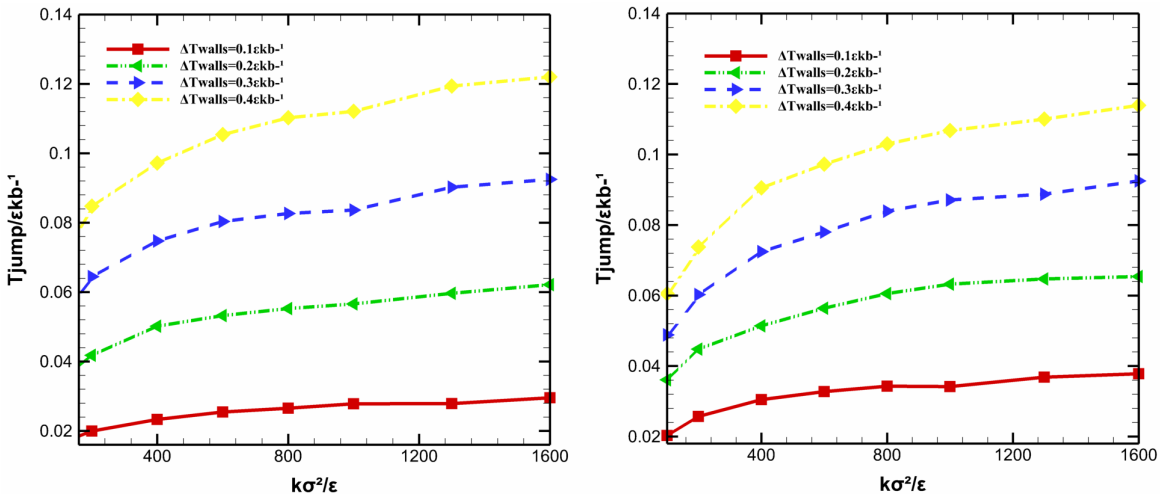

a) Lower wall b)Upper wall

Figure 4.7: Kapitza resistance for $m_w = 2m_f$ for a) lower and b) upper wall with $\varepsilon_{w-f} = 1.0$ and $\Delta t = 0.1 - 0.4$ for various values of stiffness constant

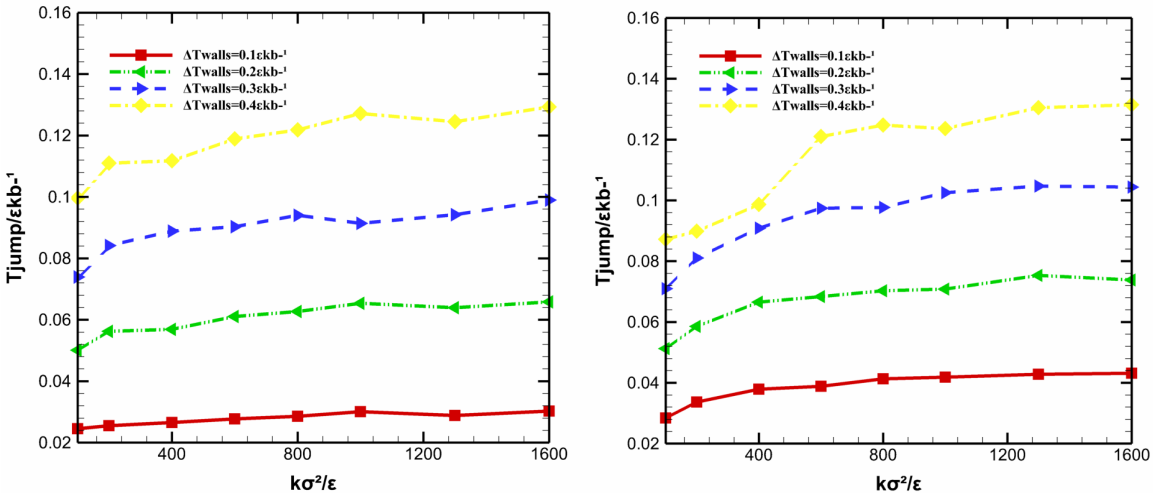

a) Lower wall b)Upper wall

Figure 4.8: Kapitza resistance for $m_w = 4m_f$ for a) lower and b) upper wall with $\varepsilon_{w-f} = 1.0$ and $\Delta t = 0.1 - 0.4$ for various values of stiffness constan

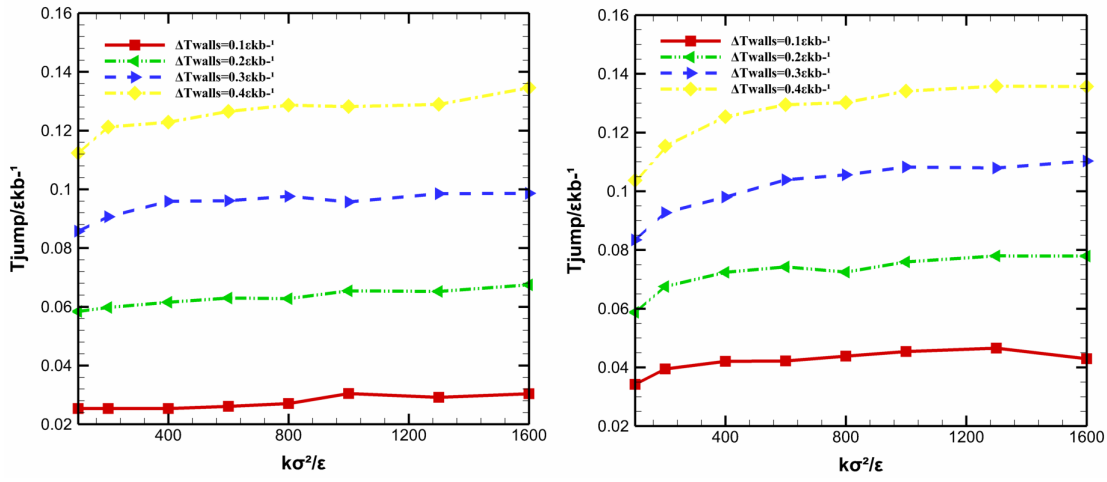

a) Lower wall b)Upper wall

Figure 4.9: Kapitza resistance for $m_w = 6m_f$ for a) lower and b) upper wall with $\varepsilon_{w-f} = 1.0$ and $\Delta t = 0.1 - 0.4$ for various values of stiffness constan

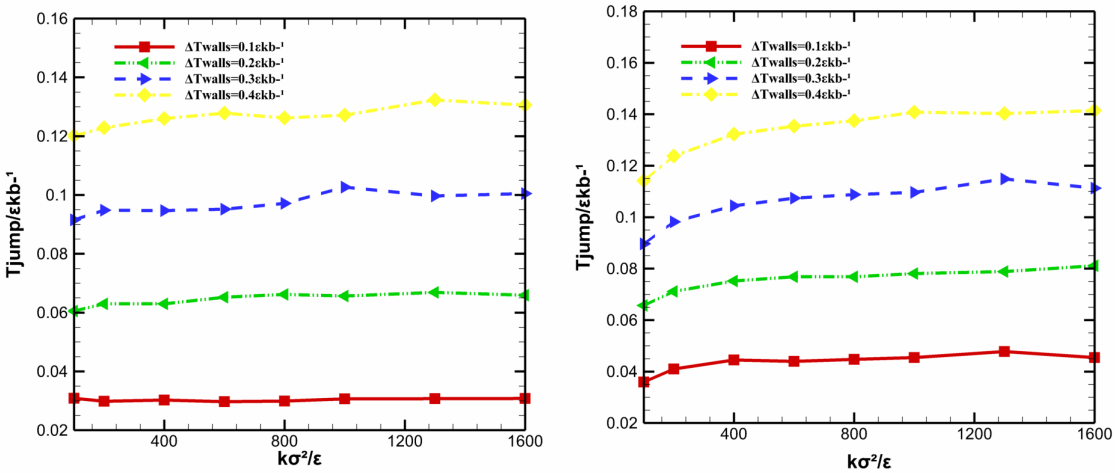

a) Lower wall b)Upper wall

Figure 4.10: Kapitza resistance for $m_w = 8m_f$ for a) lower and b) upper wall with $\varepsilon_{w-f} = 1.0$ and $\Delta t = 0.1 - 0.4$ for various values of stiffness constant

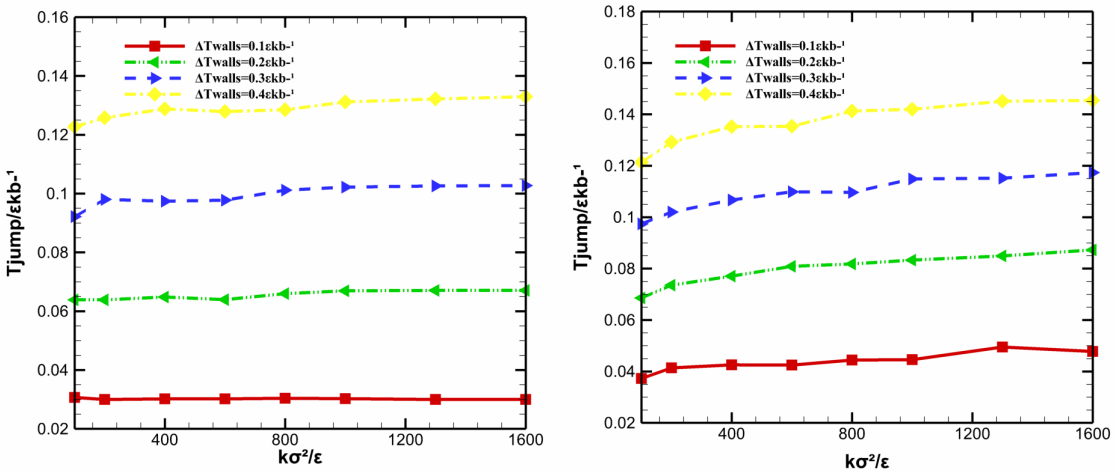

a) Lower wall b)Upper wall

Figure 4.11: Kapitza resistance for $m_w = 10m_f$ for a) lower and b) upper wall with $\varepsilon_{w-f} = 1.0$ and $\Delta t = 0.1 - 0.4$ for various values of stiffness constant.

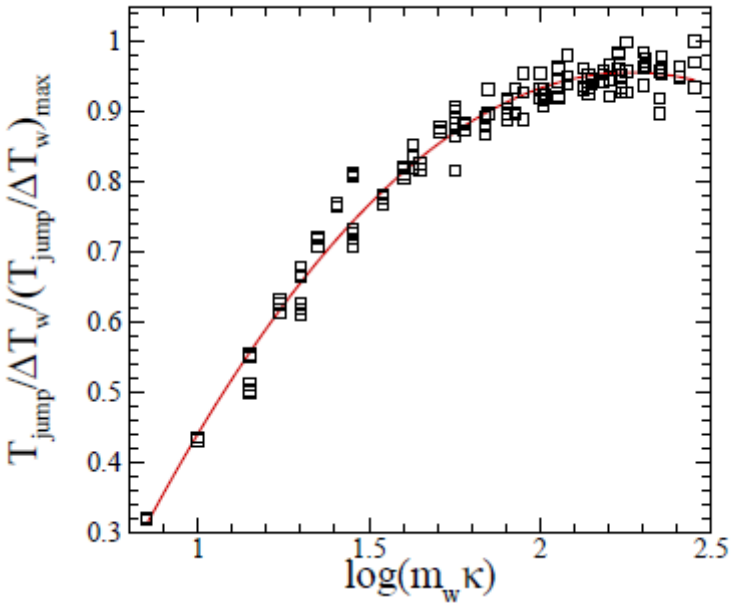

Figure 4.12: Master curve describing the temperature jump as a function of the product of the bonding stiffness and wall mass.

curves are identical, with the temperature jump increasing with the bonding stiffness [21], a result attributed to the smaller amplitude of oscillation for larger values of κ. The rate of increase is more exaggerated for lower values of the bonding stiffness and decreases with increasing κ, gradually reaching a plateau. Although higher values of ΔT add an offset to the curves, the correlation between the temperature jump and κ is not affected.

The aforementioned behaviour is attributed to a change in the vibrational motion of the wall particles. As Fig. 4.5(a and b) suggests, different values of m_w, leave the amplitude of oscillation unaffected for low values of the bonding stiffness. Since the average kinetic energy of the wall particles is bounded by the fixed temperature of the walls, the increasing mass inevitably reduces the frequency of oscillation resulting in fewer collisions between the wall and liquid particles and, in turn, a less efficient transfer of energy across the interface.

Fig. 4.12 shows that the temperature jumps across a solid-liquid interface is not a function of the harmonic frequency $\sqrt{\kappa/m_w}$ but instead changes as the fifth-order polynomial function.

$$\frac{(T_{jump}/\triangle T)}{(T_{jump}/\triangle T)_{MAX}} = -0.1054\,[log(m_w k)]^5 + 0.9304\,[log(m_w k]^4$$

$$-5.1428\,[log(m_w k]^2 - 3.6668 log(m_w k) + 1.0266, \tag{4.1.4}$$

where T_{jump} is the temperature jump of the solid-liquid interface,ΔT is the temperature difference

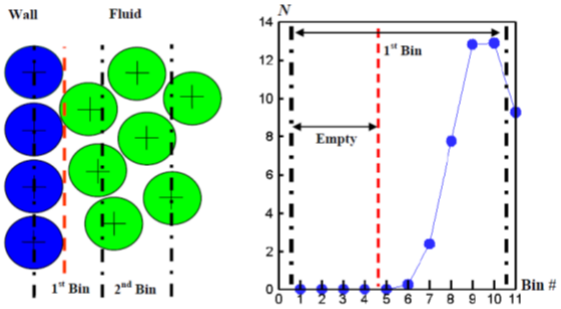

Figure 4.13: Schematics of 1st-4th Neigbouring bins. See in [116] p 57.

between the upper and lower walls, m_w is the mass of wall and k is the stiffness constant.

The curve shows a sudden increase at the lower values, whose rate decreases gradually reaching an asymptote. The "master" curve can potentially be extended to include the effects of the wetting of the solid surface and liquid density, providing a collective description of the thermal resistance across solid-liquid interfaces.

4.1.2.1 Density Distribution of Wall Particles and Fluid in Interface and Nanopore

The theoretical method that is used to calculate the phonon density of state (PDOS($\rho\omega$)) is by lattice dynamics which quantify the thickness of the vibrational state. The PDOS in thin films is expressed as;

$$\rho(\omega') = \frac{1}{(2\pi)^2} \int \sum_{v} \sum_{j} \sum_{\beta} \delta[\omega(k,v) - \omega' \Big| e_{j,}\beta(k,v)^2 \Big| dk], \tag{4.1.5}$$

where j-summation is over thin film atoms in the primitive cell, $\beta - summation$ is over 3 Cartesian cordinates, $e_{j,}\beta(k,v)$ and j is the $\beta - component$ of phonon polarization vector for mode (k,v). The molecular dynamics simulation of the effect of mass and stiffness constant of $\left(\kappa = 6400\varepsilon\sigma^{-2} - 100\varepsilon\sigma^{-2}\right)$ on the density distribution is given in Fig. 4.14-4.20.

Fig. 4.13 shows a diagramatic representation of the density profile of fluid across a solid-liquid interface and nanochannel [116]. The 1st bin is partly occupied by wall and fluid molecules making the bins not appropriate to know the boundary or interface. However, if the 1st bin is made 10times smaller in comparison to the molecular diameter, then the 1st-4th bin have to be made finer and occupied by wall molecules, leaving some empty fine bins which are occupied by the liquid molecules, that is $\sim 60\%$ of the 1st bin of the wall. There is a limit to this correction, because at the interface, a motionless fluid that is attached to a solid wall is formed, which causes a film known as Nernst film discovered by Nernst in 1904; this film thickness is caused by molecular adhesion between the solid and the fluid.

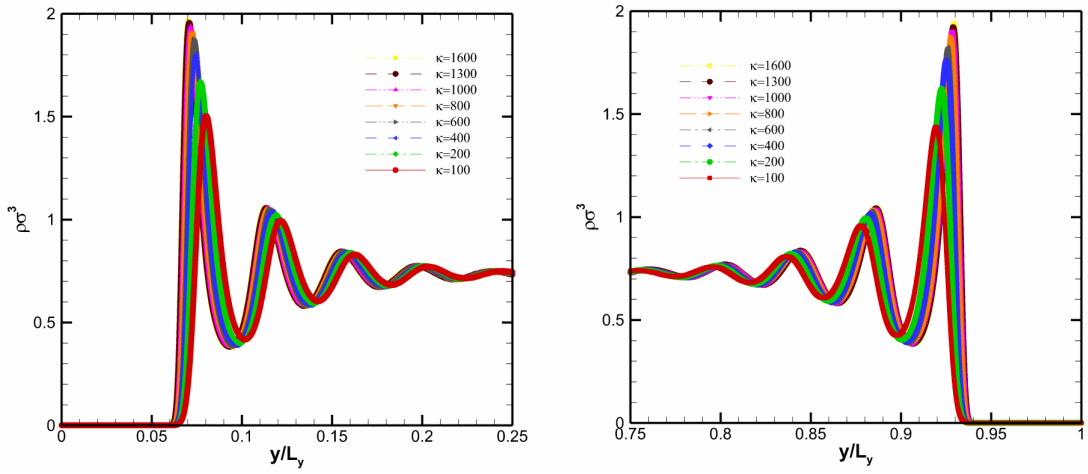

a) Lower wall b)Upper wall

Figure 4.14: Density profiles for fluid with mass $m_w = 2m$, *pore* size $= 20.5\sigma$ and temperature of a) lower wall $T = 1.2$ and b) Upper wall $T = 1.3$) for fluid at various values of spring stiffness

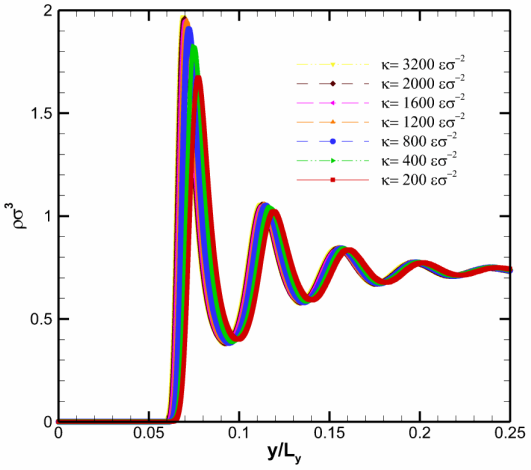

Figure 4.15: Density profiles of fluid for mass $m_w = 4m$, *pore* size $= 20.5\sigma$ and temperature of a) lower wall $T = 1.2$ and b) Upper wall $T = 1.3$) for fluid at various values of spring stiffness

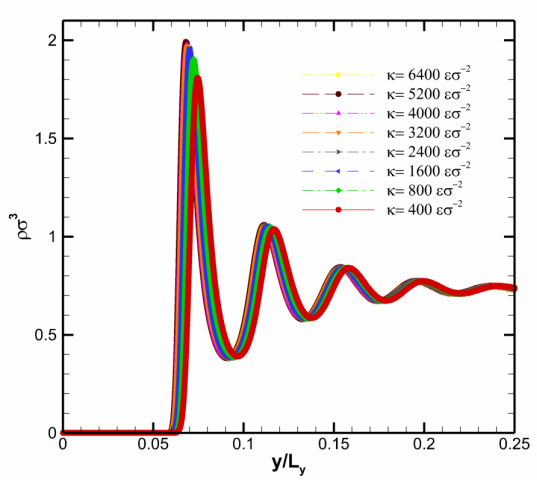

Figure 4.16: Density profiles of fluid for mass $m_w = 8m$, *pore* size $= 20.5\sigma$ for fluid at higher values of spring stiffness

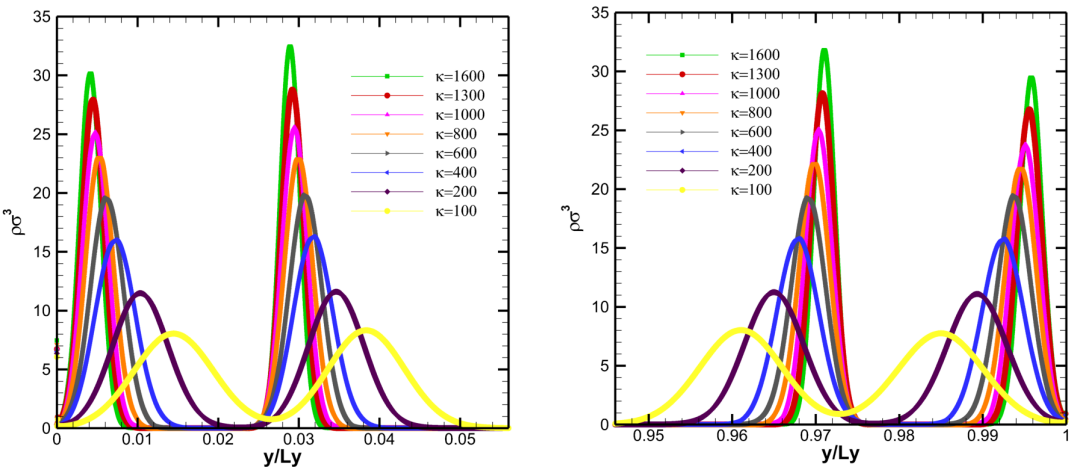

a) Lower wall b)Upper wall

Figure 4.17: Density profiles for mass $m_w = 1m$ and temperature of (lower wall $T = 1.2$ and Upper wall $T = 1.3$) for solid wall at various values of wall mass frequency

This makes the density profile of the fluid start from the 5th bin and making the 1st-4th bin look empty, as these bins are occupied by motionless fluid and wall particles, Hence, space is always present in the interface between the wall and the fluid in molecular dynamics simulation of density profile in a solid-fluid interface.

The results presented in Fig. 4.14-Fig. 4.20 show the effect of wall mass on the fluid and wall density distribution in the interface and across the nanochannel. Various mass of the wall ranging from $m_w = 1_m - 10_m$ with fluid mass constant at $m_w = 1m$ are considered for the upper and lower wall. The plots show that the density of the molecules increases at the walls and oscillates

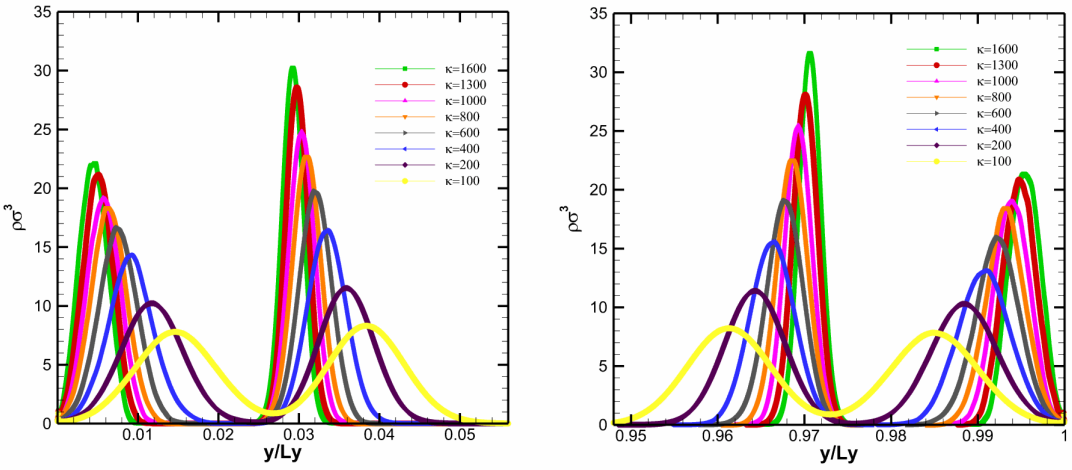

a) Lower wall b)Upper wall

Figure 4.18: Density profiles for mass $m_w = 4m$ and temperature of (lower wall $T = 1.2$ and Upper wall $T = 1.3$) for solid wall at various values of wall mass frequency

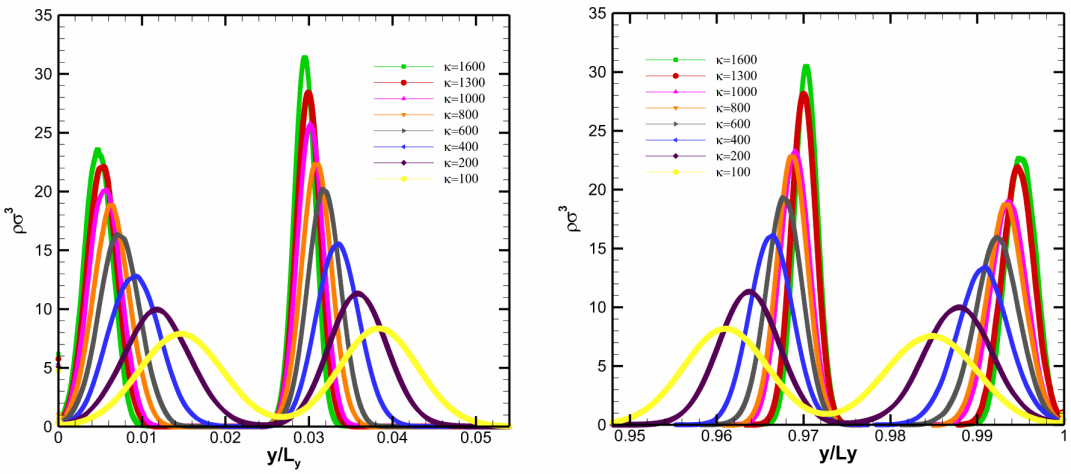

a) Lower wall b)Upper wall

Figure 4.19: Density profiles for mass $m_w = 6m$ and temperature of (lower wall $T = 1.2$ and Upper wall $T = 1.3$) for solid wall at various values of wall mass frequency

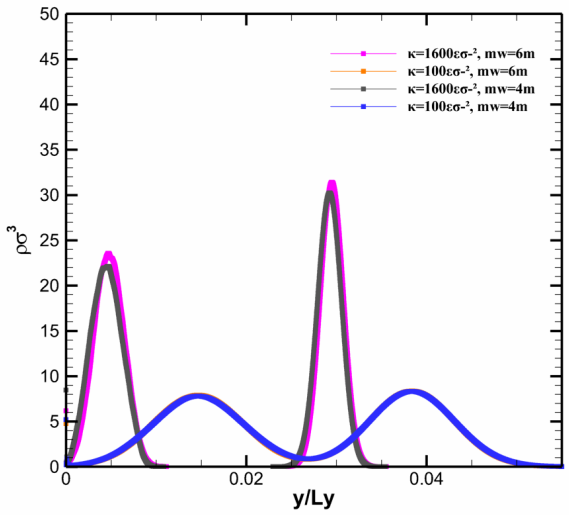

Figure 4.20: Density profiles near the lower wall for $m_w = 1m$ and $m_w = 6m$ for low and high values of the wall bonding stiffness

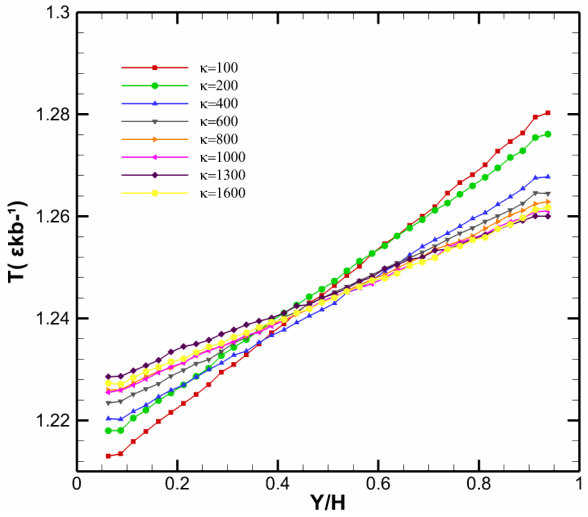

Figure 4.21: Temperature distribution for m_w = 2m, $\varepsilon_{w-f} = 0.4$ and $\Delta t = 0.1$ for various values of stiffness constant

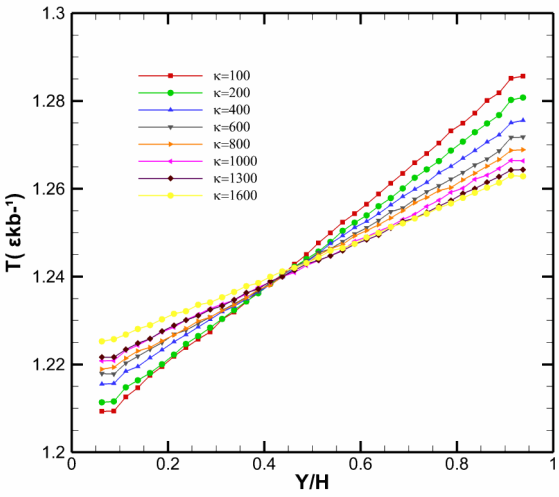

Figure 4.22: Temperature distribution for $m_w = 2m$, $\varepsilon_{w-f} = 0.6$ and $\Delta t = 0.1$ for various values of stiffness constant

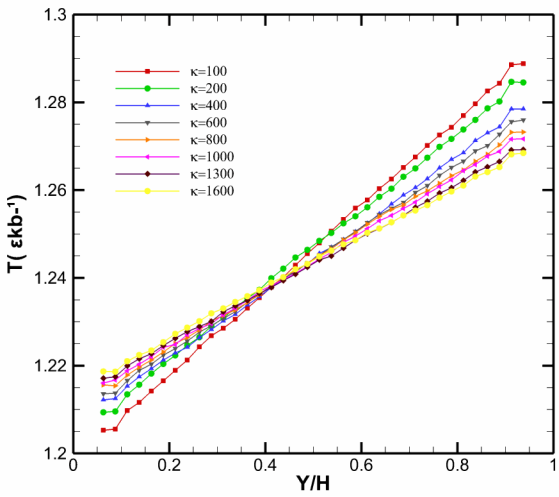

Figure 4.23: Temperature distribution for $m_w = 2m$, $\varepsilon_{w-f} = 0.8$ and $\Delta t = 0.1$ for various values of stiffness constant

into the free stream. Large density oscillations near the wall was observed straightening out at distances from $5\sigma - 7\sigma$ away from the wall and towards the channel centre. The density profile pattern, is unchanged with variation of stiffness constant. Values of surface stiffness constant have shown particles in the fluid will oscillate with greater amplitudes going further into the free stream and withstanding fluid molecules from getting close to the wall. Increasing the surface stiffness constant from $k = 100\varepsilon\sigma^{-2} - 6400\varepsilon\sigma^{-2}$ leads to non-linear and slight increment of the density peak of the first layer of fluid towards an asymptotic value, which is in agreement with other studies [112]. The results also describe density profile for higher wall mass and shows that the asymptotic density is obtained for small values of surface stiffness constant. As the frequency scales with $1/\sqrt{mw}$ the frequency spectrum becomes narrower for larger values of wall mass, making the density of the first layer of fluid approach an asymptotic value quicker. Several values of mass were applied with the density peaks remaining in the same location for mass value, with peak increasing for heavier mass of wall. The varying mass have an impact on the oscillating frequency of the wall particles with less effect on the amplitudes that are mostly controlled by the stiffness constant and the temperature of the wall. An increase of the mass of the wall leads to an increase in vibrating periods of the wall, thereby causing the molecules of the liquid to develop a stronger contact layer in the interface.

Fig. 4.14(a and b)-4.16(a and b) shows the fluid density profile of a nanochannel with pore size *pore* size $= 20.5\sigma$, lower wall temperature $T_w = 1.2$ and upper wall $T_w = 1.3$. These parameters were implemented with stiffness constant $\left(\kappa = 6400\varepsilon\sigma^{-2} - 100\varepsilon\sigma^{-2}\right)$. Higher mass was observed to increase the liquid density slightly with oscillations going towards the centre of the channel. The curves ascertain that the fluid molecules are distributed in an orderly manner close to the walls, showing the presence of wall-fluid interaction. These peaks of fluid formed in the wall oscillate to the centre of the pore as reported in a recent study [51]. Higher values of bonding stiffness are also seen to increase the density of the lower and upper wall, with both walls having constant number density due to the dominant influence of the wall mass. The fluid layering was observed to have the first peak reaching its maximum and approaching asymptotic values faster, with subsequent density peaks oscillating and penetrating into the in-plane fluid layers.

Fig. 4.17(a and b)-Fig.4.19(a and b) shows the Lower and Upper wall density profiles of wall particles for various values of the bonding stiffness. The atomic mass of the wall particles is $m_w = 1m$ and the temperature difference between the upper and lower walls is $\Delta T = 0.1\epsilon k_B^{-1}$. The fluid layering was observed to have the first peak reaching its maximum and approaching asymptotic values faster with subsequent density peaks getting lower and penetrating into the in-plane fluid layers. The two density layers represent the two fcc lattice planes that make the

wall; the right profile corresponds to the wall particles adjacent to the liquid. As the stiffness of the wall increases, so do the restoring forces. Restrictions of the amplitude of oscillation of the wall particles are seen to stay closer to their initial lattice sites. Hence, an increasing value of κ narrows the density profiles and increases their maximum value. Although both lattice planes exhibit the same behaviour, it is more profound on the adjacent layer due to its strong interaction with the liquid particles. Fig. 4.19 shows the same case for $m_w = 6m$. The salient observation is the significant effect of the mass on the profile, corresponding to the lower plane, whose maximum value increases much faster with increasing κ for $m_w = 6m$ in comparison to the equivalent systems for $m_w = 1m$. In contrast, the plane adjacent to the liquid is almost unaffected.

To further understand the effect of mass on the oscillatory nature of the wall planes, a direct comparison between the density profiles of the lower wall, for $m_w = 1m$ and $m_w = 6m$ for bonding stifnesses $\kappa = 100\epsilon\sigma^{-2}$- $\kappa = 1600\epsilon\sigma^{-2}$, is made in Fig. 4.17 - Fig. 4.19. For lower spring potentials, the density profiles experience marginal changes for different wall masses. The amplitude of the oscillation is also seen to be unaffected by a change in mass. For the higher values of κ, the increase in m_w causes the density profile in direct contact to the liquid to shift slightly to the right, with a small decrease in its maximum value. The oscillation of the lower plane, which is harmonic, due to the lack of direct collisions with the liquid particles, decreases in amplitude and increases in frequency for higher values of the atomic mass. The contrast between the profiles of the two lattice planes indicates an an-harmonicity of the wall particles directly interacting with the liquid, and also confirms that the theoretical (and harmonic) spring frequency $\sqrt{\kappa/m_w}$ might not be sufficient to describe the thermal or Kapitza resistance.

Fig.4.20 shows the difference between the two wall lattice density profiles for the highest and lowest bonding stiffness and energy intermolecular interaction strength. Lower values of bonding stiffness κ reveals almost constant density peaks with a slight shift in position. Changes in the wall intermolecular interaction strength (e_{ww} and e_{wwf}) does not affect the density profile and maximum peak at lower κ. The density peaks for both lattices increases with higher values of stiffness and e_{ww}. The maximum density value of the right lattice is seen to be greater than the left for higher values of e_{ww} with the right lattice density profile shifting away from the liquid and the left lattice density profile shifting towards the liquid, relative to the higher stiffness, showing an-harmonicity in the lattice site and temperature jump in the interface.

4.1.2.2 Temperature Distribution of Fluid in Nanopore

The temperature distribution in a nanofluidic channel with the presence of wall-fluid interaction energy strength (ε_{wf}) was studied [116]. Their result is similar to this study. They also reported

a Fourier like behaviour of the temperature profile in the nanochannel. They further observed a temperature jump at the fluid-wall interface which they reported was due to molecules of the fluid close to the wall boundary having different thermal velocity from the wall. The local temperature is mostly defined by the thermal velocities of particles that also cause momentum transfer between the fluid and the wall. If the wall-fluid interaction is weak the momentum transfer will be small, However, if the fluid-fluid interaction is stronger and dominantly affects closer molecules, more thermal motion is produced, hence an increase in temperature. The situation of these scenario brings about quick changes in the distribution of local kinetic energy, which is responsible for the jump in temperature at the interface. This jump is also due to the scattering of phonons due to different phonon frequencies of the two media. Fig.4.21-4.23 shows a linear temperature jump at the walls of the nanofluidic channel, which is similar to previous study [116]. The temperature jump increases with an increase in stiffness in the lower wall and decreases with an increase in stiffness at the upper wall. The temperature profiles cross each other almost at the same point, due to the difference in lower and upper wall temperature.

4.1.3 Chapter Summary

An investigation into the effect of the atomic mass on the Kapitza resistance has been carried out. The temperature jump have indicated that for higher values of the atomic mass, the frequency of oscillation must decrease in order to satisfy constant average kinetic energy constraints dictated by the fixed temperature of the wall. The lower frequency translated into a smaller number of collisions between the wall and liquid particles, which inevitably led to a less efficient transfer of energy and temperature jump at the solid-liquid interface. As a result, for low values of κ, the Kapitza resistance was dominated by the mass of the wall particles, while as κ increases, the mass effect faded and the bonding stiffness dictated the temperature jump. The density profiles of the walls have indicated that for lower values of the wall bonding stiffness, the amplitude of oscillation of its atoms is unaffected by a change in mass. Finally, the temperature jump correlated with the product of the bonding stiffness and wall mass $log(m_w k)$, rather than the frequency of harmonic springs $\sqrt{\kappa/m_w}$ [55].

Chapter 5

Effect of Wall Interaction on the Kapitza resistance

5.1 Introduction

Previous MD studies focused on the energy interaction strength of fluid-solid interaction in interfaces and fluid confined in nanochannels or nanopore [107-116], with none of these studies investigating how the vibrating wall interaction intermolecular energy strength affects the Kapitza resistance, temperature and density distribution across interfaces and nanofluidic channels. Studies of the effect of the energy interaction strength between particles in the solid wall, on the Kapitza resistance at the solid-liquid interfaces, and nanofluidic channels are very scarce if not non-existent. Therefore, the purpose of this chapter is to implement MD wall-wall thermal model in investigating the effect of the energy interaction strength (ε_{ww}) of a vibrating solid wall on the Kapitza resistance, temperature and density distribution across solid-liquid interfaces and nanofluidic channels.

The objectives of this chapter are to develop a 3D molecular dynamics algorithms and codes of the simulation domain and thermal wall model with wall-wall intermolecular interaction energy (ε_{ww}). To determine the frequency of the vibrating wall atoms using molecular dynamics simulation. To investigate the effect of wall-wall lattice intermolecular interaction energy strength (ε_{ww}) for pore size of 20.5σ at various vibrating frequencies and stiffness constant, ranging from $\kappa = 100\varepsilon\sigma^{-2} - 1600\varepsilon\sigma^{-2}$ on the Kapitza resistance, temperature profiles and density distribution across solid-liquid interfaces and nanofluidic channels. Finally, to compare the effect of the highest and lowest ε_{ww} on the Kapitza resistance, temperature, and density distribution across the interfaces and nanofluidic channels.

The investigation shows the effect of the presence of wall particle energy intermolecular interaction strength (ε_{ww}) on the temperature jump, Kapitza resistance, temperature profiles and density distribution across solid-liquid interfaces and nanopore. A wall model that mimics real

	$\kappa(\varepsilon\sigma^2)$	ε_{ww}	ε_{wf}	$\triangle T$	Mass(m)	Time step (τ)	Simulation run time
Case 1	100-1600	0.2	0.4	0.1	$m_w = 2m_f$	0.001	4×10^7
Case 2	100-1600	0.2	0.6	0.1	$m_w = 2m_f$	0.001	4×10^7
Case 3	100-1600	0.2	0.8	0.1	$m_w = 2m_f$	0.001	4×10^7
Case 4	100-1600	0.4	0.4	0.1	$m_w = 2m_f$	0.001	4×10^7
Case 5	100-1600	0.4	0.6	0.1	$m_w = 2m_f$	0.001	4×10^7
Case 6	100-1600	0.4	0.8	0.1	$m_w = 2m_f$	0.001	4×10^7
Case 7	100-1600	0.6	0.4	0.1	$m_w = 2m_f$	0.001	4×10^7
Case 8	100-1600	0.6	0.6	0.1	$m_w = 2m_f$	0.001	4×10^7
Case 9	100-1600	0.6	0.8	0.1	$m_w = 2m_f$	0.001	4×10^7

Table 5.1.1: Simulation Matrix for Wall-Wall intermolecular interaction energy strength effect on Kapitza resistance with 10 High Powered Computing Nodes used and 2800 simulation runs.

wall in the nanoscale was implemented using simple harmonic formulations. The mass of the wall is $m_w = 2m_f$ with different values of e_{ww} and e_{wf} and bonding stiffness κ. The results show different density profiles in two lattice sites in the solid, and density profiles in the liquid near the wall. Higher values of spring constant κ, and wall-wall with wall-fluid intermolecular interaction energy strength (e_{ww} and e_{wf}) gave maximum density peaks in the solid and fluid, developing a temperature jump at the solid-liquid interface. Lower values of e_{ww} produce a higher temperature jump and Kapitza resistance. This study provides an insight into the relationship between the temperature jump, mass ratio of the solid and liquid, the bonding stiffness κ, the wall-wall and wall-fluid intermolecular interaction energy strengths e_{ww} and e_{wf} at the solid-liquid interface of nanofluidic channels.

5.1.1 Simulation Method

To study thermal transport in interfaces and nanofluidic channels, structures are set up like the molecular dynamics experiment in [51]. The simulation domain is modelled to investigate the effect of the combination of wall-wall interaction and various values of mean vibrating frequency of the solid media, on the Kapitza resistance, density and temperature distribution across interfaces, and nanofluidic channels. Lennard-Jones pair potential describes the wall-fluid and wall-wall interactions. The fluid dimensionless parameters used are $\varepsilon_{w-f} = 0.8$, $\varepsilon_{w-w,} = 0.2, 0.4, 0.6$, and spring constant $100\varepsilon\sigma^{-2} - 1600\varepsilon\sigma^{-2}$. The stiffness constant influences the thermal oscillations of the molecular particles and determines the amount of energy and momentum transferred across the interface. The stiffness also correlates the phonon frequency of the lattice in the solid and influences the thermal vibration.

The particles of the walls are fixed to the equilibrium lattice location r_o with the earlier values of spring constants obeying the Liderman criterion of melting, which do not allow the particles to melt and also do not allow the wall particles to oscillate outside the value that is not allowable

Figure 5.1: Simulation system configuration of nanofluidic channel with harmonic springs.

in time steps of molecular simulations [117-118]. Lennard Jones cut-off distance $r_c = 2.2$ was applied to reduce the computational cost. The simulation system consists of 10,000 atoms with solid or wall atoms of 2,500 divided into four regions, with two regions at the top and two regions below, with atoms connected with a simple harmonic spring having a fixed dimensionless mass at $m_w = 2m_f$, and temperature of $T = 1.3\epsilon k_B^{-1}$ at the top wall and $T = 1.2\epsilon k_B^{-1}$ at the bottom wall, harmonically thermostated with the temperature rescaling method. The fluid atom consists of 7,500 atoms with dimensionless mass of $m_f = 1m$ placed in two parallel walls with height, H along the $y - axis$. The simulation configuration is made up of a periodic boundary condition at the z and x direction with a shrink wrap at the y-direction. The height of the nanochannel is $L_y = 20.5\sigma$ with width $L_z = 17.0\sigma$ and length $L_x = 16.0\sigma$. The geometrical configuration is shown in Fig.5.1. The walls are positioned as fcc lattice with orientation x(0 -1 1); y(1 1 1); z(-2 1 1). Different mean vibrating frequencies of the wall particles were obtained by running an MD simulation of the wall layers with the stiffness constant used earlier. The equations of motion are integrated using the verlet algorithm [2], with a time step $\tau = 0.001$ and thermo-style of 50,000. The system is performed with micro-canonical ensemble with simulation run time of 40,000,000 and equilibration run of 40,000,000. Simulations were set-up and implemented using Large-scale Atomic/Molecular Massively Parallel Simulator LAMMPS [176]. The simulation matrix is summarized in Table 5.1.1.

The MD simulation was performed to obtain the vibrational mean frequency at each stiffness value with a simulation run of 4×10^5 time steps. Fig.5.2 shows the results of the mean frequency dispersion and vibration of the walls, evolving with time for stiffness constants $k = (100{-}1600\varepsilon\sigma^{-2})$ across the simulation domain. The intermolecular response of a monoatomic crystal structure is simplified by a one degree of freedom (DOF) spring-mass system. The lattice crystal oscillates to generate the mean vibrating frequencies $fr = 1.5, 2.0, 2.7, 3.2, 3.6, 3.9, 4.5, 5.0$ at stiffnesses $k = (100 - 1600\varepsilon\sigma^{-2})$ of the wall particles.

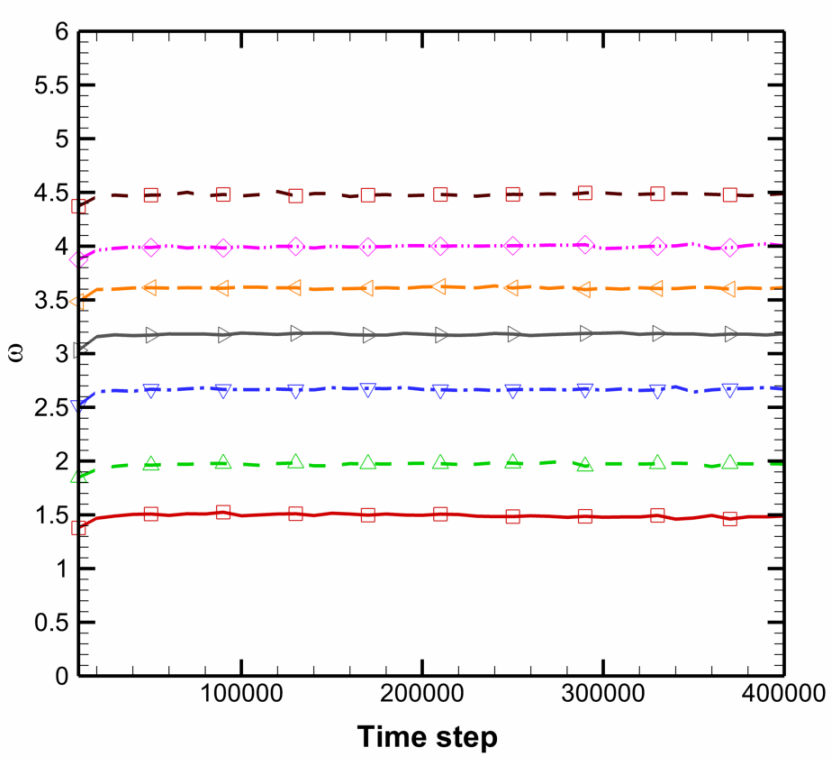

Figure 5.2: Solid wall mean vibrational frequency dispersion for stiffness constant $100\varepsilon\sigma^{-2}$ – $1600\varepsilon\sigma^{-2}$.

5.1.2 Results and Discussion

The understanding of thermal transport at nanoscale is still at its infancy [2], but it is accepted that large phonon scattering in the surfaces of an interface is the reason for high Kapitza resistance and low thermal conductivity [119-120]. The Kapitza resistance of this work is obtained by determining the temperature jump of the fluid-wall interface and the heat flux of the wall region by Non-equilibrium molecular dynamics simulation. The temperature across the pore is determined by the thermal motion of the fluid, which is achieved by dividing the simulation domain into 40bins.The temperature of each bin is obtained from the kinetic energy of the particles in the fluid bins, based on the streaming velocity of particles in the bin and is obtained by the expression

$$T = \sum_{j=1}^{N_i} m(v_f - v_i)^2/(3N_s - \delta_f)k_B \tag{5.1.1}$$

where m is the mass of particles, v_f, v_i are the current and mean velocities in the bin, N_s is the bin size, δ is the bin degree of freedom and k_B the Boltzmann constant. The velocity rescaling method was used to thermostat the wall atoms, rescaling the velocities of the vibrating walls in 4bins at each time step, maintains the temperature of the walls, at the set temperature ranging

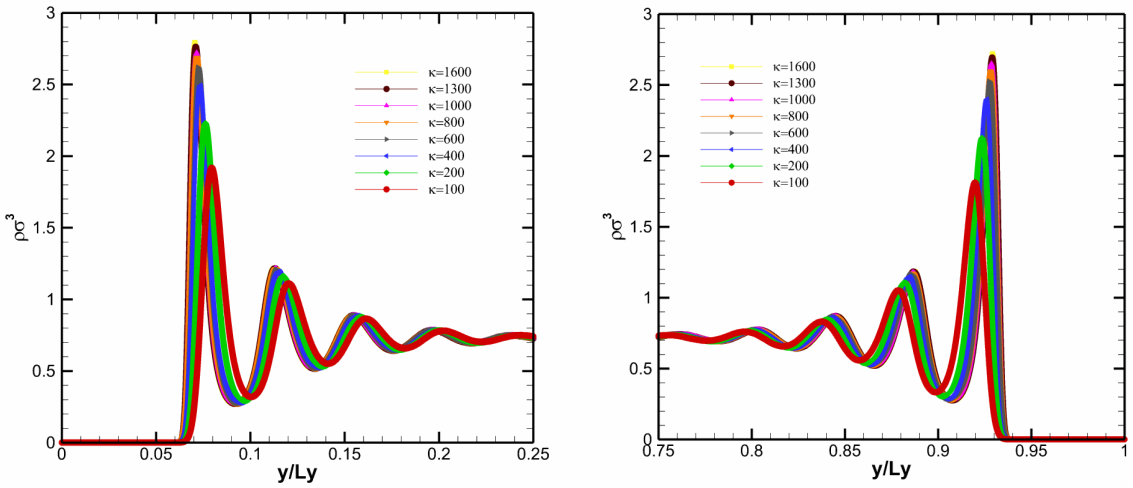

a) Lower wall b)Upper wall

Figure 5.3: Density Profiles of fluid for $m_w = 2m$, *pore* size $= 20.5\sigma$, $e_{ww} = 0.2$, $e_{wf} = 0.4$ for various values of stiffness constant κ.

from $T_w = 1.2\epsilon k_B^{-1}$ for the lower wall and $T_w = 1.3\epsilon k_B^{-1}$ for the upper wall. This technique obtains the desired wall temperature (T_w) of the bin by the difference between the total kinetic energy E of the wall and the energy obtained in the process of rescaling the velocity in each bin, $\Delta E = E_T - 3NkT_w/2$. The heat flux ($q$) across the wall is obtained by calculating the average of the difference in energy, $q =< \Delta E > /(\Delta t.A)$, as the change of energy with time is constant because of the thermostat over the wall surface, then $q = T_w$. The Kapitza resistance is obtained by $K_w = \Delta T/T_w$. $\triangle T$ is the difference in temperature between adjacent bins at the interface given as $\triangle T = T_{fluid} - T_{wall}$.

5.1.3 Density Distribution across Interface and Nanopore

Fig. 5.3 (a and b) - Fig. 5.10(a and b). shows the effect of energy interaction strength of the wall and fluid (e_{ww},e_{wf}) and bonding stiffness κ on the density distribution across the interface and nanopore. The figure ascertains that the fluid molecules are distributed in an orderly way close to the walls, showing the presence of wall-fluid interaction. These peaks of fluid formed in the wall oscillates to the centre of the pore as reported in most studies [114]. The wall with temperature difference $\triangle T = 0.1\epsilon k_B^{-1}$, was simulated with wall bonding stiffness $100\varepsilon\sigma^{-2} - 1600\varepsilon\sigma^{-2}$ and $e_{ww} = 0.2$; $e_{wf} = 0.4$ for the lower and upper walls respectively. Higher values of bonding stiffness increase the density of the lower and upper wall, with the lower wall having smaller temperature values, showing higher density than the upper wall. The fluid layering was observed to have the first peak reaching its maximum and approaching asymptotic values faster, with subsequent density peaks oscillating and getting lower and penetrating into the in-plane fluid layers [121].

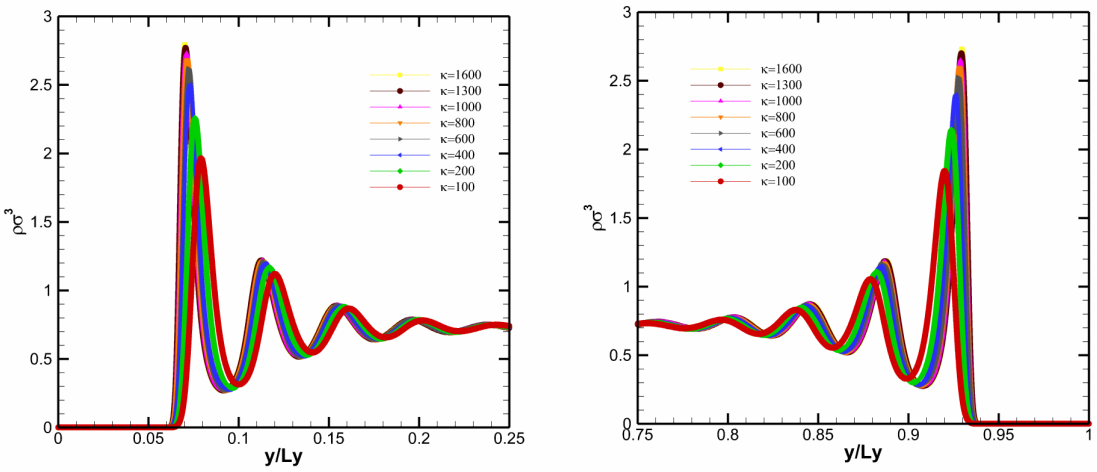

a) Lower wall b)Upper wall

Figure 5.4: Density Profiles of fluid for $m_w = 2m$, *pore* size $= 20.5\sigma$, $e_{ww} = 0.2$, $e_{wf} = 0.6$ for various values of stiffness constant κ.

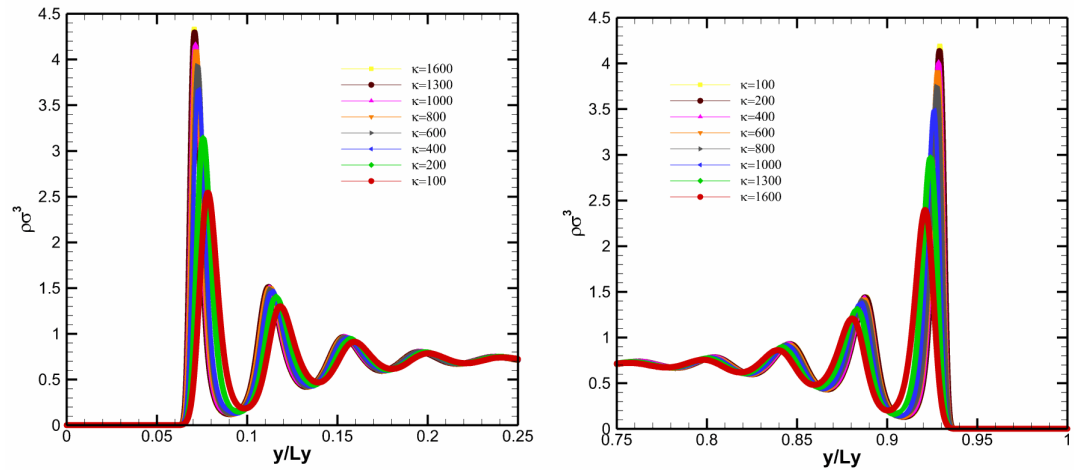

a) Lower wall b)Upper wall

Figure 5.5: Density Profiles of fluid for $2m$, *pore* size $= 20.5\sigma$, $e_{ww} = 0.2$, $e_{wf} = 0.8$ for various values of stiffness constant κ.

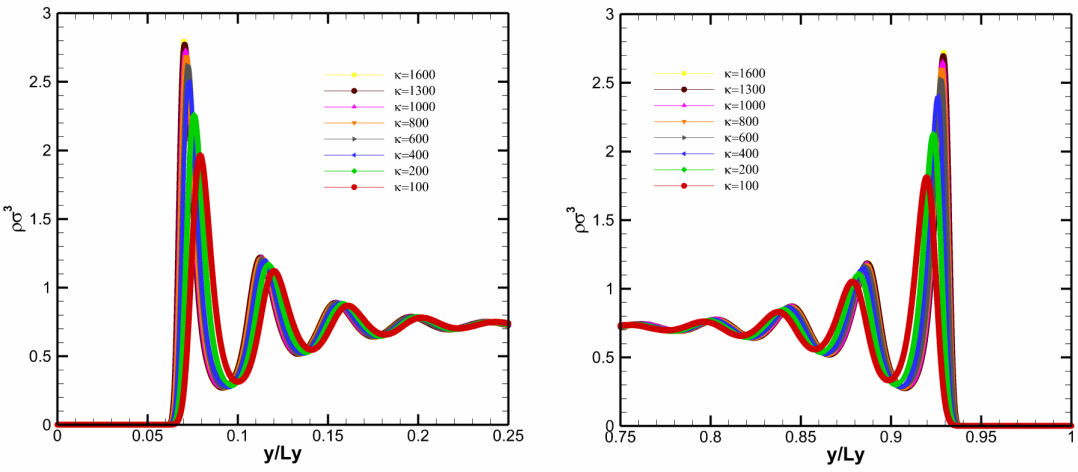

a) Lower wall b)Upper wall

Figure 5.6: Density Profiles of fluid for $m_w = 2m$, *pore* size $= 20.5\sigma$, $e_{ww} = 0.4$, $e_{wf} = 0.4$ for various values of stiffness constant κ.

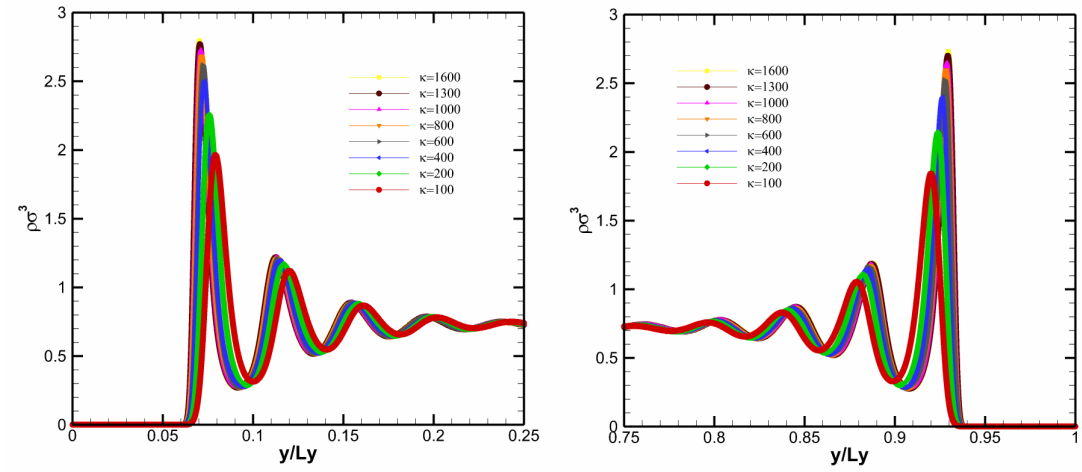

a) Lower wall b)Upper wall

Figure 5.7: Density Profiles of fluid for $m_w = 2m$, *pore* size $= 20.5\sigma$, $e_{ww} = 0.4$, $e_{wf} = 0.6$, for various values of stiffness constant κ.

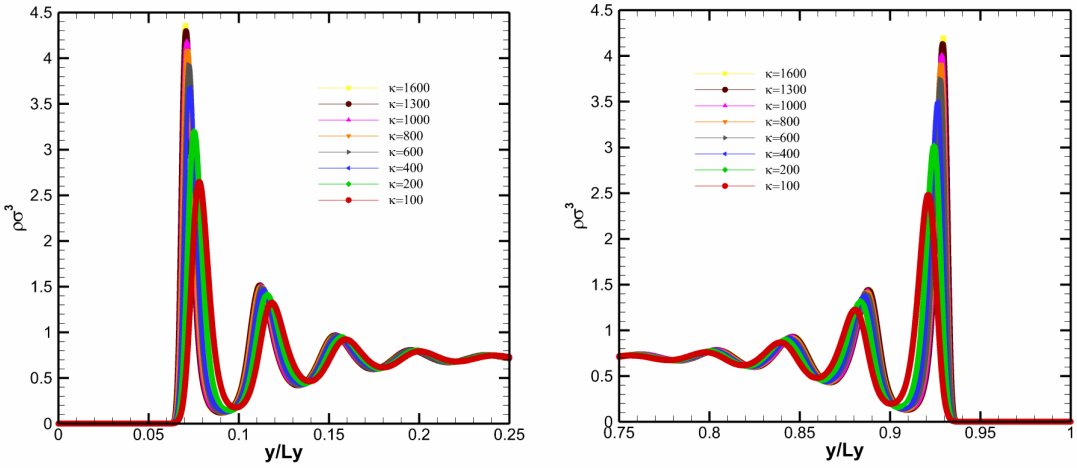

a) Lower wall b)Upper wall

Figure 5.8: Density Profiles of fluid for $m_w = 2m$, *pore* size $= 20.5\sigma$, $e_{ww} = 0.4$, $e_{wf} = 0.8$ for various values of stiffness constant κ.

Fig. 5.11 and Fig. 5.12 show the influence of wall particle energy intermolecular interaction strength on the density profile of the lower wall for different bonding stiffness. The two density layers of the lower wall describes two fcc lattice planes that are positioned in the wall. The mass of the wall is $m_w = 2m_f$ with $e_{ww} = 0.2$; $e_{wf} = 0.4 - 6$ and wall temperature difference of $\triangle T = 0.1\epsilon k_B^{-1}$. The amplitude of oscillation of the lattice density profiles of the wall is restricted and stay close to their original site as the values of the stiffness κ of the wall particles increases, making an increasing value of the bonding stiffness cause the density profile to narrow, with maximum peak corresponding to the highest value of κ. Though the density of the two lattice planes undergoes similar behaviour, its effect is more pronounced at the lattice adjacent to the liquid, and this phenomenon is due to the strong intermolecular interaction between the right wall lattice and the liquid. Fig.5.13-Fig.5.17 shows a much higher density as the energy interaction strength of the fluid is increased from e_{wf} =0.4, to $e_{wf} = 0.8$. The oscillating particles gradually attains a constant value of number density 0.86 which corresponds to the density of argon. Fig.5.18 shows a higher wall density profile with higher energy intermolecular interaction strength in the wall particles with $e_{ww} = 0.6$; $e_{wf} = 0.4$. Fig.5.19-Fig.5.20 shows similar patterns with Fig.5.14 but with higher density at e_{wf} =0.8.

Futher explanations are given for the density pattern in Fig.5.11-Fig.5.20, the plots shows the wall density profiles of wall particles for various values of the bonding stiffness. The two density layers as earlier observed represent the two fcc lattice planes that make the wall; the right profile corresponds to the wall particles adjacent to the liquid. As the stiffness of the wall increases, so do the restoring forces. The density profiles of the two lattices in the solid is seen to have

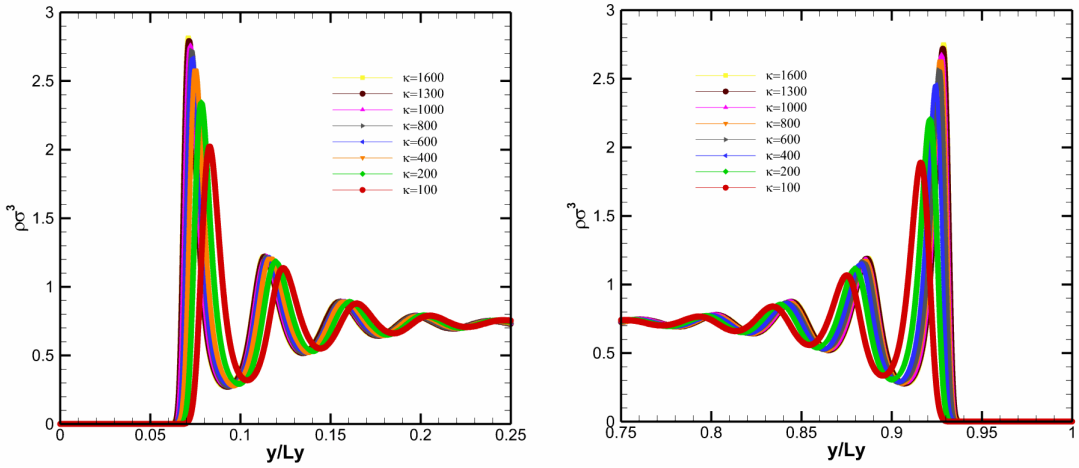

a) Lower wall b)Upper wall

Figure 5.9: Density Profiles of fluid for $m = 2m$, *pore* size $= 20.5\sigma$, $e_{ww} = 0.6$, $e_{wf} = 0.4$ for various values of stiffness constant κ.

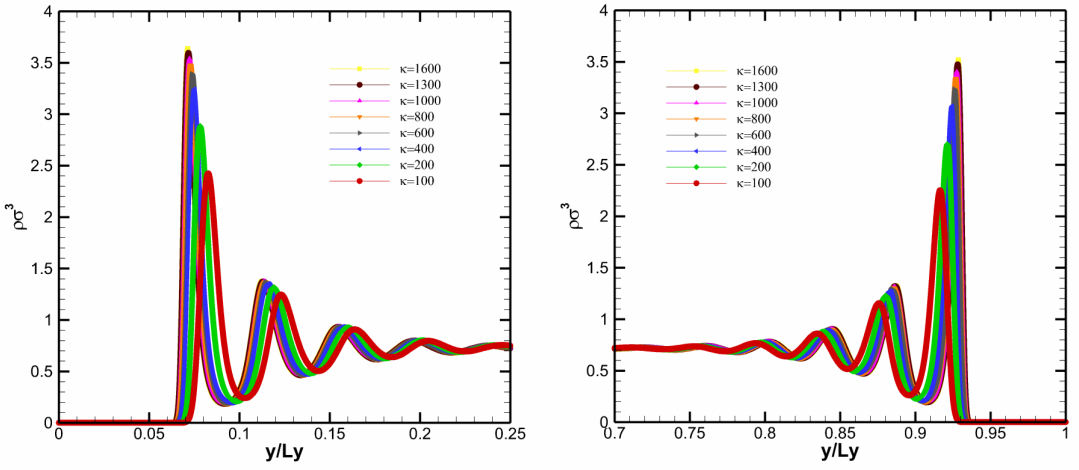

a) Lower wall b)Upper wall

Figure 5.10: Density Profiles of fluid for $m = 2m$, *pore* size $= 20.5\sigma$, $e_{ww} = 0.6$, $e_{wf} = 0.6$ for various values of stiffness constant κ.

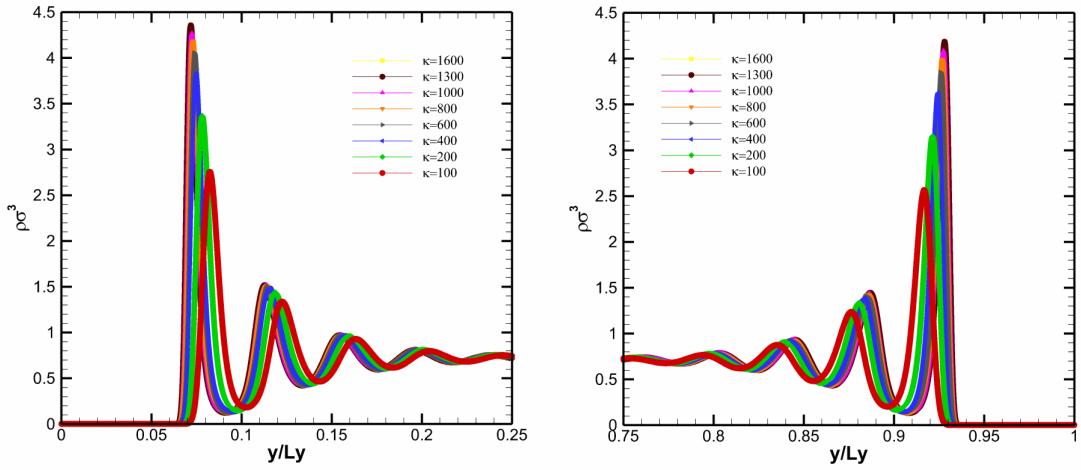

a) Lower wall b)Upper wall

Figure 5.11: Density Profiles of fluid for $m_w = 2m$, *pore* size $= 20.5\sigma$, $e_{ww} = 0.6$, $e_{wf} = 0.8$ for various values of stiffness constant κ.

maximum peaks at the highest bonding stiffness. The density layers of the left lattice plane also increases remarkably for higher values of e_{ww} and increasing stiffness constant κ. Restrictions of the amplitude of oscillation of the wall particles are seen to stay closer to their initial lattice sites. Hence, an increasing value of κ narrows the density profiles and increases their maximum value. Although both lattice planes exhibit the same behaviour, it is more profound on the adjacent layer, due its strong interaction with the liquid particles. As e_{ww} increases, the density peaks of both lattices increases and subsequently increases the density peak in the interface. Hence showing that e_{ww} influences the density of both lattices and the solid-liquid interface. The reason for this is because of the position of the two lattices in relation to the liquid, making the farther left lattice having smaller collision with the liquid molecules and the right lattice having larger collision, due to its proximity to the interface. Theoretically, this means there is a relationship between the temperature jump, the bonding stiffness κ the energy intermolecular interaction strength of the wall-wall and wall-fluid interface.

Fig.5.21-5.26 shows the effect of wall particle energy interaction strength of $e_{ww} = 0.2-0.6$ and wall-fluid energy interaction strength of e_{wf} =$0.4-0.8$ with various wall vibrational frequencies, on the temperature distribution across the nanopore. Fluid thermal transport in nanopore, generated by temperature gradient is investigated. Heat is seen to be transported from the high to low-temperature wall causing a temperature gradient with a linear profile. The temperature profile is obtained by averaging the kinetic energy in each bin with bin thickness $\delta_o = 0.025$. For all frequency of vibration, there is a difference in temperature between the wall and the fluid, and a temperature jump is observed at the interface of the fluid and wall. For higher frequency of wall

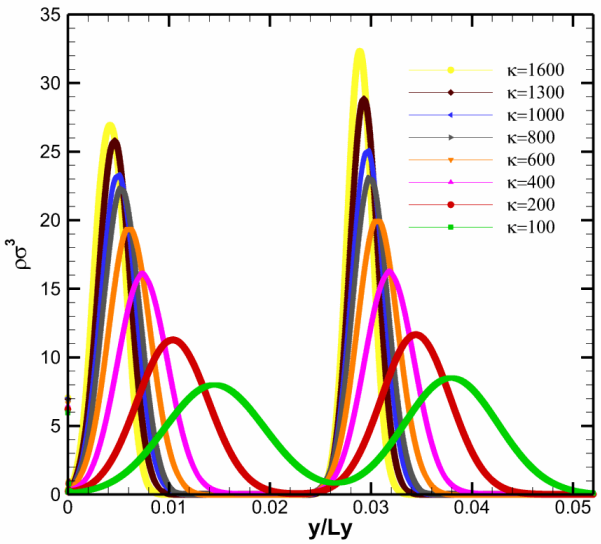

Figure 5.12: Density Distribution in Solid Wall for $m_w = 2m$, $e_{ww} = 0.2$, $e_{wf} = 0.4$ for various values of stiffness constant κ.

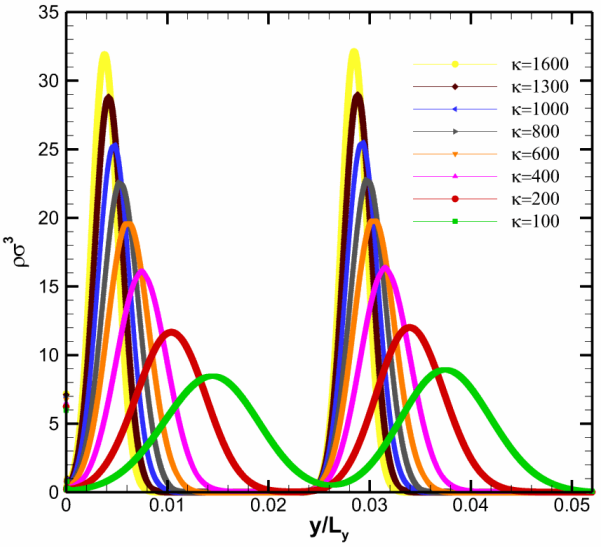

Figure 5.13: Density Distribution in Solid Wall for $m_w = 2m$, $e_{ww} = 0.2$, $e_{wf} = 0.6$ for various values of stiffness constant κ.

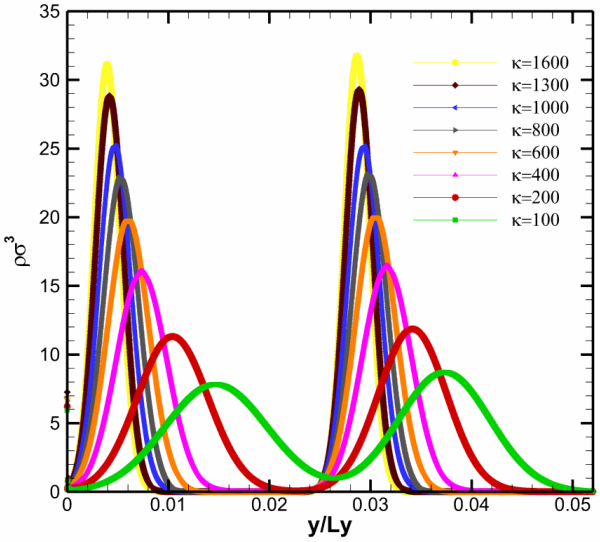

Figure 5.14: Density Distribution in Solid Wall for $m_w = 2m$, $e_{ww} = 0.2$, $e_{wf} = 0.8$ for various values of stiffness constant κ.

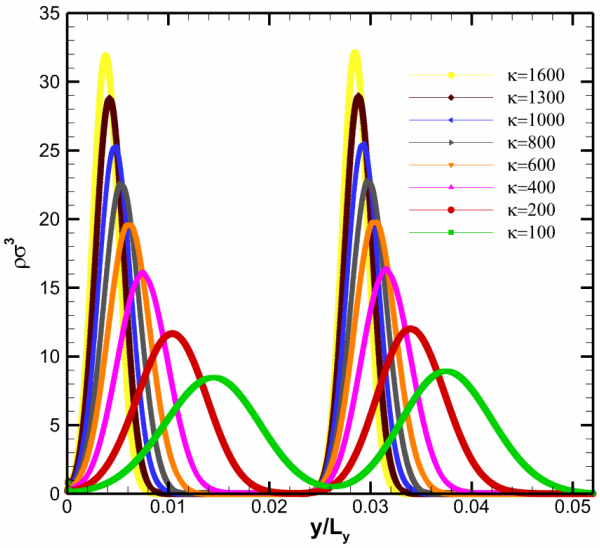

Figure 5.15: Density Distribution in Solid Wall for $m_w = 2m$, $e_{ww} = 0.4$, $e_{wf} = 0.4$ for various values of stiffness constant κ.

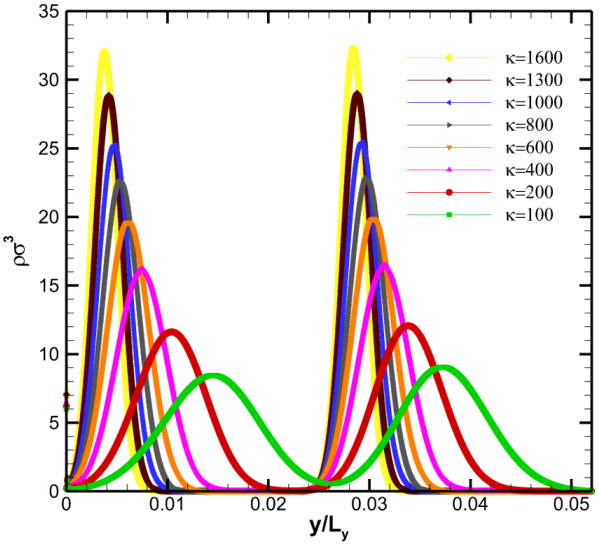

Figure 5.16: Density Distribution in Solid Wall for $m_w = 2m$, $e_{ww} = 0.4$, $e_{wf} = 0.6$ for various values of stiffness constant κ.

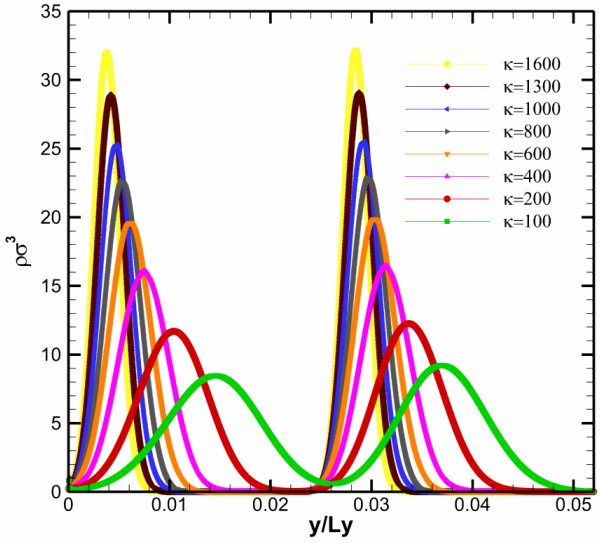

Figure 5.17: Density Distribution in Solid Wall for $m_w = 2m$, $e_{ww} = 0.4$, $e_{wf} = 0.8$ for various values of stiffness constant κ.

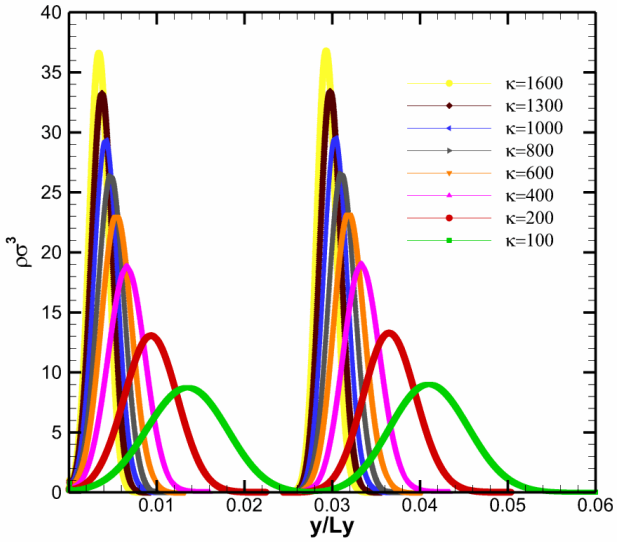

Figure 5.18: Density Distribution in Solid Wall for $m_w = 2m$, $e_{ww} = 0.6$, $e_{wf} = 0.4$ for various values of stiffness constant κ.

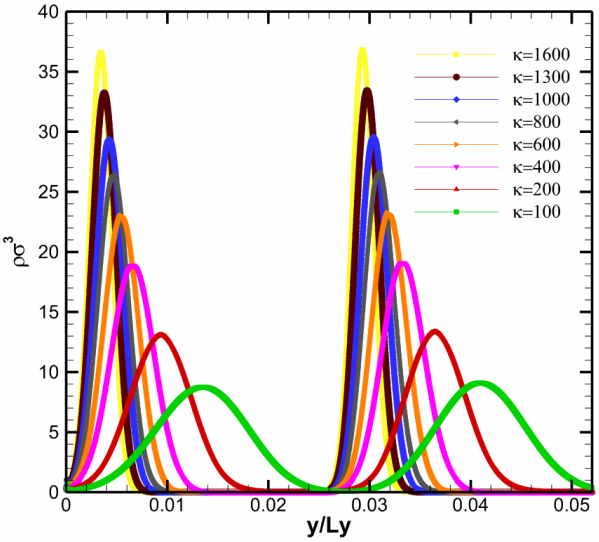

Figure 5.19: Density Distribution in Solid Wall for $m_w = 2m$, $e_{ww} = 0.6$, $e_{wf} = 0.6$ for various values of stiffness constant κ.

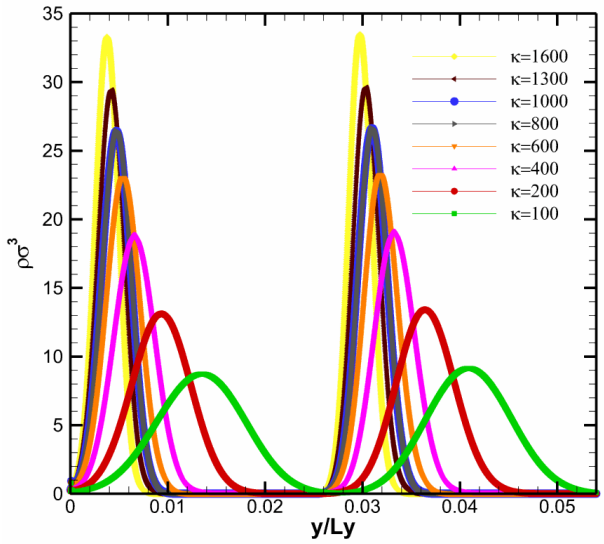

Figure 5.20: Density Distribution in Solid Wall for $m_w = 2m$, $e_{ww} = 0.6$, $e_{wf} = 0.8$ for various values of stiffness constant κ.

vibration the temperature profile and the temperature jump is seen to increase at the lower wall and decrease at the upper wall.

The temperature of the fluid and the temperature jump decreases as the wall particle energy interaction strength increases causing a decrease in the Kapitza resistance. The frequency of vibration of the wall further influences the friction in the fluid-wall interface and plays a prominent role in the temperature distribution and heat transfer in the nanopore. A straight forward way of explaining the linear increase and relationship between the temperature and Kapitza resistance across the interface indicates the presence of thermal transport is not in doubt. The plots also show that as the temperature increases across the nanopore, there is better matching of the phonon density of state at lower frequency and temperature. Hence the higher heat transfer and increase in temperature across the nanopore.

5.1.4 Temperature Distribution of Fluid in Nanopore

Thermal interactions in nanoscale fluid flow, with regards to the effect of wall-wall interaction energy strength on the heat transport across interfaces and nano-pore is scarce and unavailable. The MD interactive wall-wall model of this study has made it possible to study nano-scale interfacial thermal interaction with energy and momentum exchange between wall and fluid. Making it possible for excess heat in the fluid to be transferred to the wall, with thermostated wall dissipating the heat. For weaker wall-fluid interactions, a momentum deficit is developed which causes modifications in the distribution of the kinetic energy and obtaining a temperature jump.

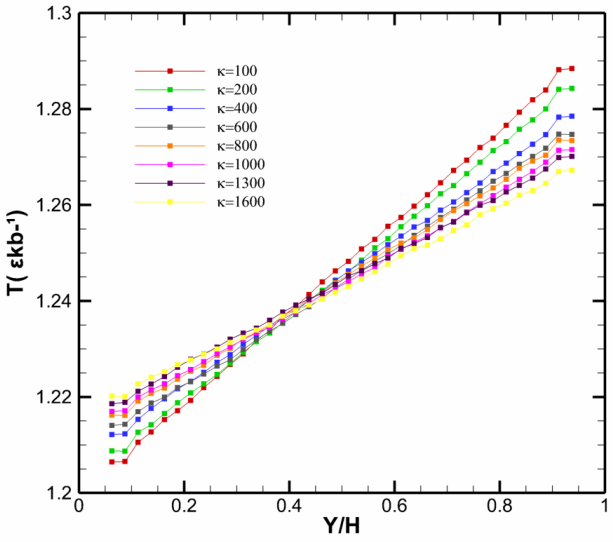

Figure 5.21: Temperature Profiles across Nanopore for $m_w = 2m$, $e_{ww} = 0.2$, $e_{wf} = 0.8$ for various values of stiffness constant κ.

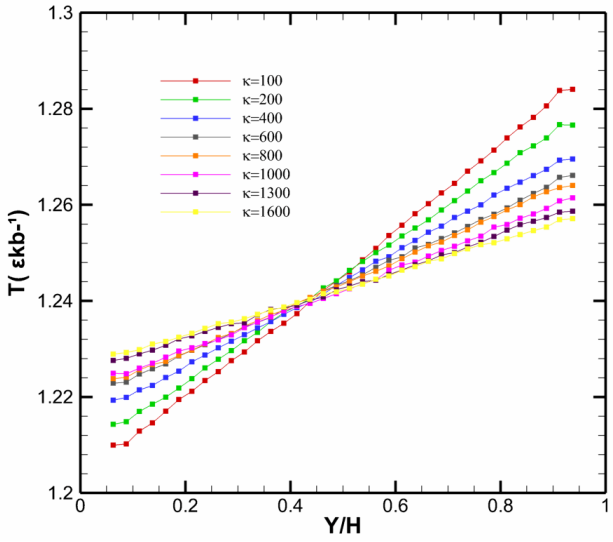

Figure 5.22: Temperature Profiles across Nanopore for $m_w = 2m$, $e_{ww} = 0.4$, $e_{wf} = 0.4$ for various values of stiffness constant κ.

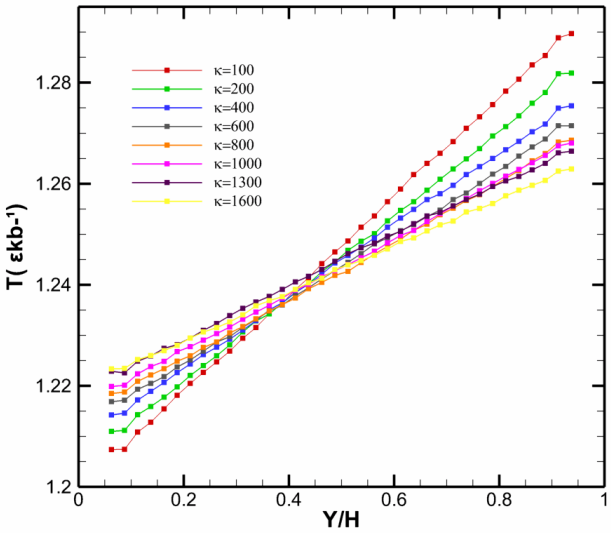

Figure 5.23: Temperature Profiles across Nanopore for $m_w = 2m$, $e_{ww} = 0.4$, $e_{wf} = 0.6$ for various values of stiffness constant κ.

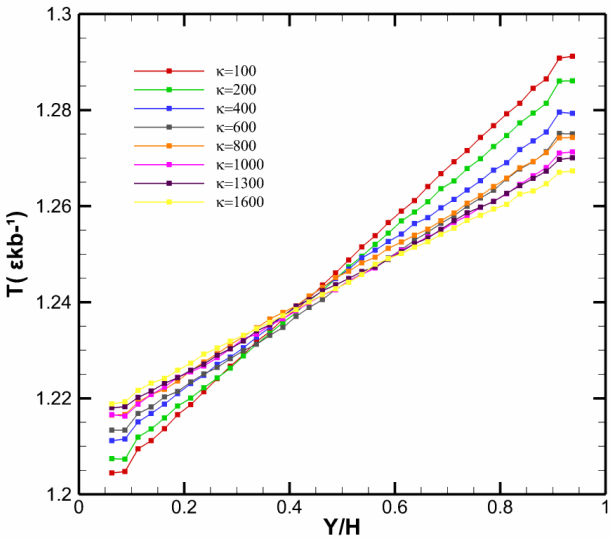

Figure 5.24: Temperature Profiles across Nanopore for $m_w = 2m$,$e_{ww} = 0.4$, $e_{wf} = 0.8$ for various values of stiffness constant κ.

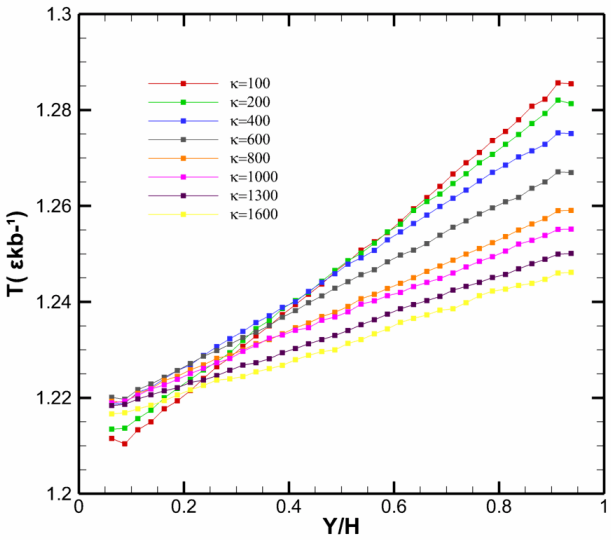

Figure 5.25: Temperature Profiles across Nanopore for $m_w = 2m$, $e_{ww} = 0.6$, $e_{wf} = 0.4$ for various values of stiffness constant κ.

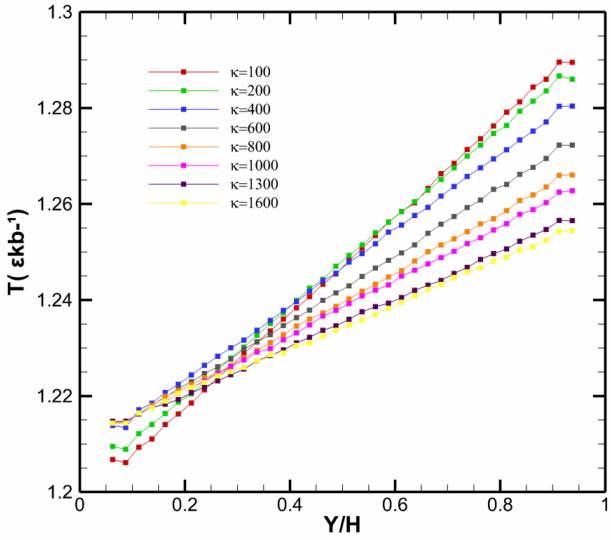

Figure 5.26: Temperature Profiles across Nanopore for $m_w = 2m$, $e_{ww} = 0.6$, $e_{wf} = 0.8$ for various values of stiffness constant κ.

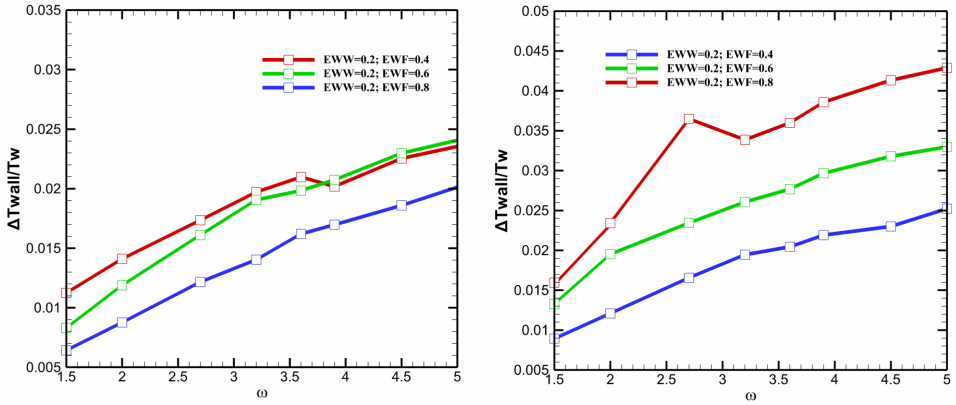

a) Lower wall b)Upper wall

Figure 5.27: Kapitza Resistance for a) lower and b) upper wall of $m_w = 2m_f$, $e_{ww} = 0.2$, $e_{wf} = 0.4 - 0.8$ as a function of wall frequency.

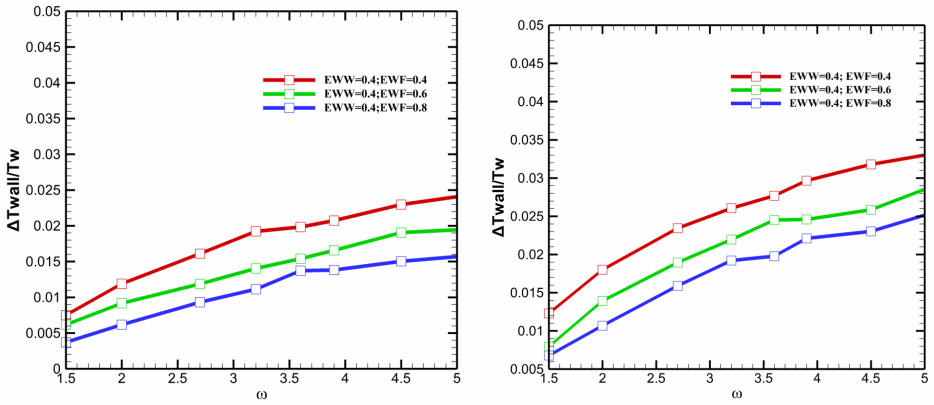

a) Lower wall b)Upper wall

Figure 5.28: Kapitza Resistance for a) lower and b) upper wall of $m_w = 2m_f$, $e_{ww} = 0.4$, $e_{wf} = 0.4 - 0.8$ as a function of wall frequency.

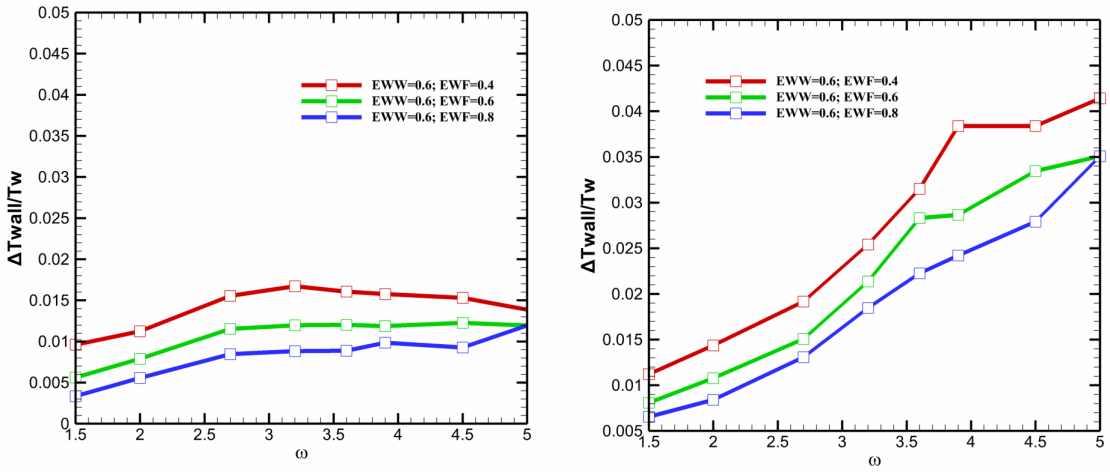

a) Lower wall b)Upper wall

Figure 5.29: Kapitza Resistance for a) lower and b) upper wall of $m_w = 2m_f$, $e_{ww} = 0.6$, $e_{wf} = 0.4 - 0.8$ as a function of wall frequency.

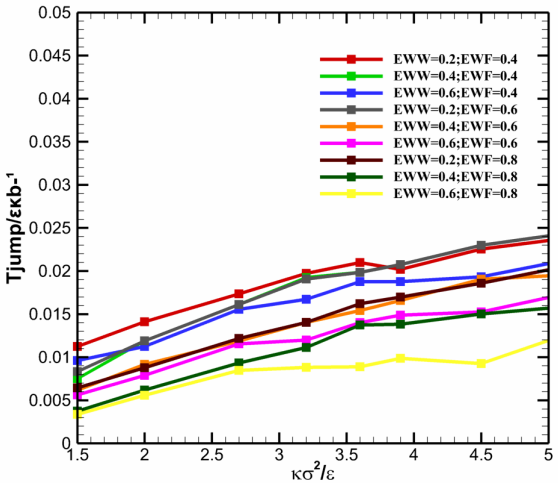

Figure 5.30: Kapitza Resistance of $m_w = 2m_f$, for all e_{ww} and e_{wf} as a function of wall frequency.

5.1.5 Kapitza Resistance of Interface and Fluid in Nanopore

The effect of wall particle interaction strength e_{ww}, and stiffness constant on the Kapitza resistance at the solid-liquid interfaces and nanopore is shown in Fig. 5.27(a and b)-Fig. 5.29(a and b). The plot shows the effect of e_{ww} and e_{wf} on the heat and energy transfer across the solid-liquid interface with wall mass $m_w = 2m_f$. The energy intermolecular interaction strength of the wall particle is set at $e_{ww} = 0.2 - 0.6$ while keeping the fluid-wall energy interaction strength at $e_{wf} = 0.4 - 0.8$. The Kapitza resistance was seen to increase with higher wall vibrational frequency. The temperature jump increases with the wall vibrational frequency and decreases as e_{ww} and e_{wf} increases. Fig. 5.30 shows the temperature jump or Kapitza resistance as a function of the frequency, $(k/m)^{0.5}$ for all values of e_{ww} and e_{wf} with mass of wall $m_w = 2m_f$ for different values of wall vibrating frequency. The temperature jump and kapitza resistance increases with decreasing values of e_{ww}. The Kapitza resistance is seen to increase as the wall vibrating frequency increases.The combined effect of lower values of e_{ww} and e_{wf} causes the temperature jump and Kapitza resistance to increase further.

5.1.6 Chapter Summary

A wall-wall Molecular dynamics thermal model have been applied to study the effect of wall particle energy intermolecular interaction strength (e_{ww}) with various values of wall vibrational frequencies on the Kapitza resistance, density distribution and temperature across interfaces and nanofluidic channels, with mass kept constant at $m_w = 2m_f$. The result shows that the Kapitza resistance increases with wall particle vibrational frequency and decreases in the presence of wall particle energy intermolecular interaction strength (e_{ww}). The Kapitza resistance and temperature jump

is observed to be highest with higher wall particle vibrational frequency, and lowest wall particle energy intermolecular interaction strength ($e_{ww} = 0.2$). The wall particle energy intermolecular interaction strength (e_{ww}) and wall vibrational frequency is also seen to influence the density peaks of the wall and fluid interfacial particles, as higher vibrational frequency and increasing wall energy intermolecular interaction strength (e_{ww}) obtains higher density peaks at the wall and fluid interface. There is a correlation between the maximum density peak of the wall and the temperature jump across the interface of the nanofluidic channel. An increase in (e_{ww}) increases the density peaks of the wall and interfacial fluid in the nanofluidic channel. A temperature gradient with a linear profile was observed across the nanofluidc channel. The thermal transport at the solid-liquid interface and across the nanofluidic channel reduced from the bottom wall to the top wall, as wall frequency vibration increases, though with the temperature remaining constant in the middle of the channel.

5. Effect of Wall Interaction on the Kapitza resistance

[1]

[1] This page is intentionally left blank

Chapter 6

Effect of Wall Size on the Kapitza resistance

6.1 Introduction

Materials having high nano-porosity with large surface area are beginning to find applications in gas adsorption, gasification, filtration, sequestration and desalination. To obtain good knowledge of these applications, an appropriate study of the structural configurations, surface area, pore connectivity and pore size have to be undertaken.

The objectives of this chapter are as follows; Develop 3D molecular dynamic algorithm and codes for the thermal wall-fluid and wall-wall model for a nanopore. Investigate the combined effects of lattice interaction intermolecular energy strength and smaller wall or pore size of 5σ, with stiffness constant, ranging from $\kappa = 100\varepsilon\sigma^{-2} - 1600\varepsilon\sigma^{-2}$ on the Kapitza resistance, temperature and density distribution across interfaces and nanopores. Compare the effects of wall size of 20.5σ, 10σ and 5σ on the Kapitza resistance, temperature and density distribution across the nanopores. Develop Lammps fix for wall model (theter_wall). Compare the molecular dynamic wall model with theoretical models such as; AMM, DMM and LDM.

The earlier chapters explained the methods and theoretical foundations of this project, with Chapters 4 and 5 dealing with developing molecular dynamics models applied in the investigation of the effects of wall mass and wall-wall intermolecular interaction energy strength on the Kapitza resistance, density and temperature distribution accross interfaces and nanofluidic channels. This chapter implements and develops a combination of wall-fluid and wall-wall molecular dynamic thermal model to investigate the effect of wall size (pore diameter) on the Kapitza resistance, density and temperature distribution across solid-liquid interfaces and nanofluidic channels..

The investigation reveal an increase in thermal transport and Kapitza resistance across the nanopore as the wall size and fluid molecular layer becomes smaller due to fewer bulk-like liquid

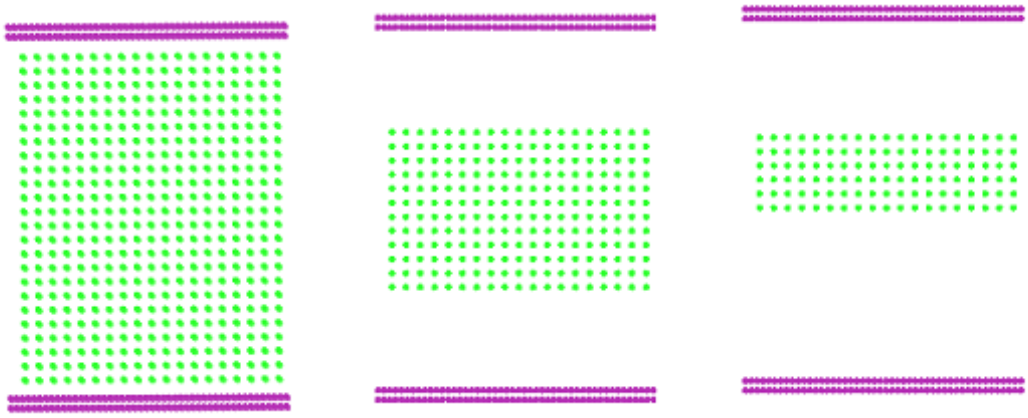

Figure 6.1: Various heights of nanopore

Sizes	1^{st} Channel	2^{nd} Channel	3^{rd} Channel	Boundary Condition
Lx	16.8σ	16.8σ	16.8σ	Periodic
Lz	17.0σ	17.0σ	17.0σ	Periodic
Ly	20.5σ	10σ	5σ	Periodic

Table 6.1.1: Simulation Domain for 3 channel nanopore sizes

layers formed. The density peaks are seen to increase with the increase in the channel pore size. Linear temperature profiles were observed in the simulation results. Temperature gap and Kapitza resistance is reported to increase as the channel pore size increases. The MD model was compared with analytical models which include, Acoustic mismatch model (AMM), Diffuse mismatch model (DMM) and Lattice dynamic model (LDM) with good agreement obtained.

6.1.1 Simulation Method for Nanopore

The simulation domain is modelled to investigate the effect of wall size on the Kapitza resistance, temperature profile and density distribution across interfaces and nanofluidic channels. The simulation domains consist of various sizes of three nanopores as shown in Fig. 6.1, with simulation matrix summarized in Table 6.1.1.

The simulation domain is modelled to investigate the effect of different sizes of wall channels on the Kapitza resistance, temperature and density distribution across interfaces and nanopores. The computational domain consists of liquid particles given the parameters of argon situated between two parallel solid walls. The channel walls are fixed perpendicularly to the y-direction with z and x directions being $L_z = 17.0\sigma$ and $L_x = 16.8\sigma$ respectively and $L_{y1} = 20.5\sigma$ for the first channel, $L_{y2} = 10\sigma$ for the second channel and $L_{y3} = 5\sigma$ for the third channel as described by Table 6.1.1. L_y denotes the distance separating the walls in the y-direction and σ the molecular length scale. The walls are positioned as fcc lattice with orientation x(0 -1 1); y(1 1 1); z(-2 1 1).

	$\kappa(\varepsilon\sigma^2)$	ε_{ww}	ε_{wf}	Size of Channel	$\triangle T$	Mass(m)	Time step (τ)
Channel 1	100-1600	0.2-0.6	0.4-0.8	20.5σ	0.1	$m_w = 2m_f$	0.001
Channel 2	100-1600	0.2-0.6	0.4-0.8	10σ	0.1	$m_w = 2m_f$	0.001
Channel 3	100-1600	0.2-0.6	0.4-0.8	5σ	0.1	$m_w = 2m_f$	0.001

Table 6.1.2: Simulation Matrix for pore size effect on Kapitza resistance with 10 High Powered Computing Nodes used and 7500 simulation runs

Lennard Jones pair potential describe the wall-fluid and solid-wall particle interactions. The fluid dimensionless parameters used are $\varepsilon_{f-f} = 1.0$, which is kept constant throughout the simulation $\varepsilon_{w-f} = 0.4 - 0.8$, $\varepsilon_{w-w,} = 0.2 - 0.6$, and spring constant $100\varepsilon\sigma^{-2} - 1600\varepsilon\sigma^{-2}$ with constant mass ratio $m_w = 2m$. The wall atoms are thermostated with the lower wall $T_w = 1.2\varepsilon k_B^{-1}$and the upper wall $T_w = 1.3\varepsilon k_B^{-1}$. The stiffness constant influences the thermal oscillations of the molecular particles and determines the amount of energy and momentum transfer across the interface [116]. The system is performed with micro-canonical ensemble with simulation run time of 4×10^7 and equilibration run time of 4×10^7.

The simulation matrix is summarised in Table 6.1.2.

6.1.2 Results & Discussion

There are pertinent questions that are currently asked, such as; can the pore size affect the Kapitza or thermal resistance of a nanofluidic channel? What will be the best pore size that will restrict or enhance thermal transport in nanofluidic channels? This section attempts to answer these questions, thereby giving fundamental understanding involving heat transfer and Kapitza resistance in the nanoscale. By varying the height of the channel and implementing MD thermal wall models, this section investigates the effect of pore size on the Kapitza resistance, density distribution and temperature profile in the nanopores.

6.1.3 Density Distribution of Fluid in Nanopore

Molecular dynamics simulation results, for density distribution of fluid in nanopores are presented. Fig. 6.2(a)-Fig. 6.2(b) shows density profiles and layering pattern for liquid atoms along the y-cordinate of the upper and lower walls with $e_{ww} = 0.2$, $e_{wf} = 0.4$. The channel width is in the z-direction with the flow along the x-direction. The flow is developed fully with no external force applied to the system. The effect of wall size $L_{y3} = 5\sigma$, various bonding stiffness κ and combinations of wall-wall with wall-fluid interaction strength of $\varepsilon_{ww} = 0.2 - 0.6$, $\varepsilon_{wf} = 0.4 - 0.8$ on the number density distribution of liquid molecules in each slab of bins are also discussed. Maximum peak close to the wall with oscillations fading into the centre and approaching bulk

value is observed. The oscillations have a local average maximum equilibrium position of 0.075. This pattern of layering has been reported in almost all molecular dynamics studies concerning density distribution in a nanochannel and nanopore. The layering has been reported by [44] as the repulsion of the liquid and wall atoms to maintain their equilibrium position. The layering pattern has been found to differ slightly while using different force field or potential interaction functions. The liquid molecules have a less closely packed structure near the valley of the profile compared to the bulk, making the energy require more liquid atom to be inserted in the valley, compared to inserting liquid atoms in the bulk. From this observation, it can be inferred that atomic interaction between solid-liquid and liquid-liquid layers are responsible for the fluctuation, which fades as the effect of these interaction decays. This liquid density in surface normal direction has an oscillatory density profile, which looks narrow and stretched because of the stiffness. The maximum peak of the first layer is observed to have a number density of 1.35 with the second layer having a slit roughly 1/8th of the liquid molecular size. The increased or constant spacing of the layers at large distances away from the wall surface shows the additional structuring with more overlaps and less packing. Two fluid layers with two maxima are also seen to be present having density starting from zero with peaks reaching maximum values, with oscillations fading to the centre, confirming repulsion at the wall-liquid interface and clearly showing the overriding influence of the wall structure [122]. The density is also seen to oscillate with a wavelength of a molecular order. The fluctuation of density ($\rho_{bin} - \rho_{average}$) gives the layering of liquid molecules. Again higher values of bonding stiffness increase the density of the lower and upper wall, with the lower wall having smaller temperature values, showing higher density than the upper wall. The fluid layering was observed to have the first peak reaching its maximum and approaching asymptotic values faster, with subsequent density peaks oscillating and getting lower and penetrating into the in-plane fluid layers. The presence of increasing density near the wall is because of more wetting of the wall surface. The profiles of the liquid structure oscillates near the wall and becomes bulk like near the centre. The liquid structure becomes uniform, describing the density of the bulk liquid. The number of liquid layers vary with changes in pore size or radii, due to the free energy which is influenced by the size of the pore and a factor of the separation distance or slit of the layers [123]. Previous theoretical models and molecular simulations have also described this pattern [124]. The closest peak to the wall is the highest, due to the strongest interaction between the walls and liquid causing an orderly or bulk like packing of the liquid particles. The second biggest peak is also influenced by the wall and the first peak, causing a few overlaps of atoms, with a lesser probability of atoms located in their required spot. Fig. 6.2(a) shows the liquid density profile of the lower wall with $T_w = 1.2\varepsilon k_B^{-1}$, there is also a typical layering pattern with two density

oscillations with maximum peak centre at 0.07 and a small shift in density maxima and minima for different stiffness. As the spring stiffness increases, the density is seen to increase with a small density fluctuation in the second layer and no further layer develops, this is due to the narrowness of the pore. The amplitude of the second layer is observed to be constant with its maximum peak located at equilibrium distance of 0.012. The density oscillations terminate at 0.15, achieving its bulk value as the oscillations propagates to the centre. Fig. 6.2(b) shows the liquid density profile for the upper wall with $T_w = 1.3\varepsilon k_B^{-1}$. The same layering pattern was observed with almost the same maxima and minima shifts and positions as the channel is symmetrical. From past simulations of this project, the larger sizes or radii have been seen to have more solid-like fluid density oscillations than the smaller radii, due to the free energy that is influenced by the size of the pore and a factor of the separation distance or slit of the layers.

Fig. 6.3(a) and 6.3(b) show that for higher wall-fluid energy intermolecular interaction strength of $e_{ww} = 0.2$, $e_{wf} = 0.6$ the liquid density increases in the lower and upper wall but with more increase in the lower wall. A third density oscillation is beginning to form at a maximum position of 0.17. Higher density fluctuations are also observed with increasing stiffness. Hence as k increases, liquid particle oscillation frequencies converge faster to maximum, making the highest packing, with subsequent particles move to the next layer. The second and third layer has density peaks that are in the same position as observed earlier. Figs. 6.4(a) and 6.4(b) show the fluid density profile for $e_{ww} = 0.2$, $e_{wf} = 0.8$. The density profile shows a first maximum peak number density value that is undoubtedly a solid. The second density peak value is also within the solid range with a slit span over 0.4. The liquid density profile oscillates towards the centre, showing the presence of Boltzmann distribution. The oscillation has a local maximum position of about 0.5. The liquid atoms have less overlap and properly packed structure near the wall as compared to the bulk. The energy required for more liquid atom to be inserted in the less overlapped structure is lower, compared to the bulk with more overlap and disorderly packed structure.

Fig. 6.5(a) and Fig.6.5(b) shows an increase in wall-wall interaction strength of $e_{ww} = 0.4$, $e_{wf} = 0.4$ for various values of stiffness constant k. The liquid density in surface normal direction also has an oscillatory density profile, which looks narrow and stretched because of the spring constant. The maximum peak fluid density with $\kappa = 1600\varepsilon\sigma^{-2}$ has its equilibrium position at 0.06 and the minimum density peak with $\kappa = 100\varepsilon\sigma^{-2}$ at 0.08 making an amplitude shift of 0.02. The third layer is seen to form its equilibrium position at 0.16 with oscillation amplitude spacing, and peak reduced. The increased spacing of the layers at large distances away from the wall surface, shows the additional structuring with more overlaps and less packing. The fluid density peaks have also been seen to increase with higher e_{ww}.

Fig. 6.6(a) and Fig. 6.6(b) show the lower and upper wall fluid density for $e_{ww} = 0.4$, $e_{wf} = 0.6$. Two maxima peaks are also observed with a gradual formation of a third maxima peak. The density profile rises from zero nearest the wall at 0.6, to a maximum peak with oscillation fading to the centre of the pore as in previous cases. The fluid density is seen to oscillate with a wavelength of molecular order, with a wall structure having large influence on the fluid-structure.

Fig. 6.7(a) and Fig. 6.7(b) shows upper and lower fluid density distribution for $e_{ww} = 0.4$,$e_{wf} = 0.8$. The density peak is seen to have increased further with maximum peak position at 0.075. There are only two peaks formed in this case, with the highest stiffness obtaining the maximum peak. The amplitude shift for this case is different as the peaks produced by $\kappa = 400\varepsilon\sigma^{-2} - 1600\varepsilon\sigma^{-2}$ seem to be in constant position with, a shift of peaks produced by $\kappa = 100\varepsilon\sigma^{-2} - 200\varepsilon\sigma^{-2}$ having the same position. It is also seen that higher e_{ww} have higher peaks or number density in the second layer. The equilibrium position of the maxima of the second layer is 0.11.

Fig. 6.8(a) and Fig. 6.8(b) show the local liquid density profile (ρz) for $e_{ww} = 0.6$, $e_{wf} = 0.4$. The maximum fluid density profile is seen to reduce but with a minimum density profile increasing. The second density peak is higher for the lower wall and reduced for the upper wall, this is due to the high e_{ww} and low e_{wf}. Farther away from the wall, the profile of the liquid structure becomes constant and bulk-like with no fluctuations. The lower wall is seen to have a higher density number than the upper wall. The density peak shifts, are seen to be pronounced with oscillations fading to the centre.

Fig 6.9(a) and Fig. 6.9(b) show the liquid density profile for $e_{ww} = 0.6$, $e_{wf} = 0.6$ for stiffness values ranging from $\kappa = 100\varepsilon\sigma^{-2} - 1600\varepsilon\sigma^{-2}$. The density peaks are seen to increase when compared to earlier simulation, due to an increase of e_{wf}. The maximum peak is the first layer oscillating and fading to the centre. The second layer is seen to have a weaker amplitude in the lower wall and higher amplitude in the upper wall. The density peaks of the first layer is seen to be close in number density to the second layer, with slight amplitude shift.

Fig 6.10(a) and Fig. 6.10(b) show the local fluid liquid density for $e_{ww} = 0.6$, $e_{ww} = 0.8$. Further and bigger increases in number density and peaks at the lower and upper wall are seen. The first layer has its maximum peak at the interface of the fluid and wall. Shifts in liquid density amplitude of the first layer close to the wall is seen with the highest stiffness, producing the maximum peak. Lesser values of stiffness show that solid-like particles formed as layers oscillating to a constant in the centre of the pore, due to increasing e_{wf}. From previous simulations and comparisons, higher e_{ww} is seen to increase the fluid density profile, but with greater influence by the e_{wf}.

The Figures for the second wall size $L_{y2} = 10\sigma$ are shown in appendix B.3 and Fig.7.0-Fig.7.23,

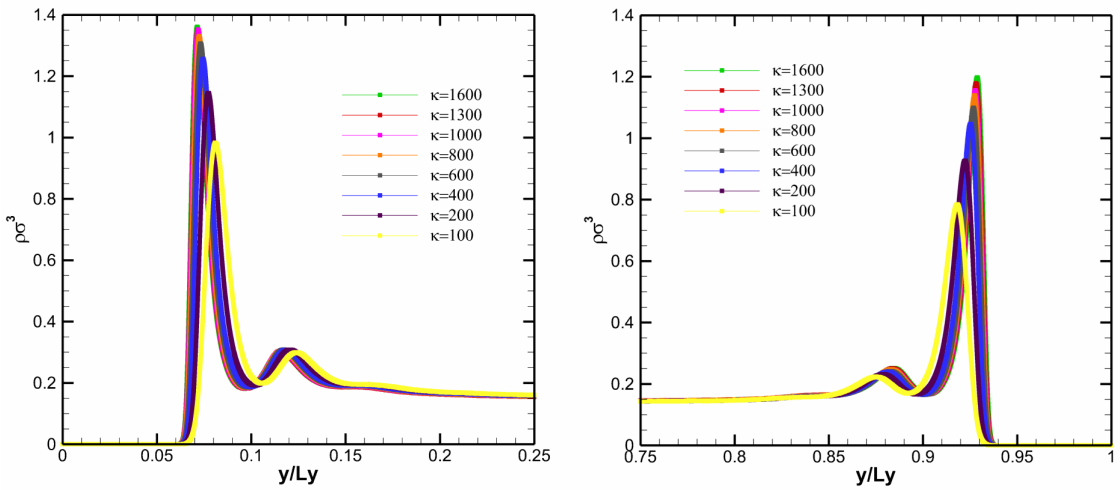

a) Lower wall b)Upper wall

Figure 6.2: Density Profiles of fluid for *pore* size $= 5\sigma$, $m_w = 2m$, $e_{ww} = 0.2$,$e_{ww} = 0.4$ for various values of stiffness constant κ.

having almost the same density profile and pattern with earlier shown Figures of the 1st channel $L_{y1} = 20.5\sigma$.

6.1.4 Density Distribution in Solid wall

Fig.6.11(a) lower wall and Fig.6.11(b) upper wall shows the solid-wall density for $e_{ww} = 0.2$, $e_{ww} = 0.4$ for various bonding stiffness k. The wall mass is $m_w = 2m_f$ with lower wall temperature $T_w = 1.2\varepsilon\kappa_B^{-1}$ and upper wall temperature $T_w = 1.3\varepsilon\kappa_B^{-1}$. The two density peaks represent two fcc lattice planes that constitute the wall. The number density is seen to be very characteristic of real solid with profiles narrow and stretched due to the stiffness constant. The amplitudes are seen to be wider in the lower stiffness and narrower in larger stiffness, confirming the effect of the stiffness. The maximum density peaks close to the wall-fluid interface, with the left-hand side lattice layer, also pronounced and smaller. Amplitude shifts are seen in the left and right density layer, with different maxima location of their peaks. The peaks of the two lattices with $\kappa = 100\varepsilon\sigma^{-2} - 1300\varepsilon\sigma^{-2}$ appear to have the same number density, with the maximum peak of $\kappa = 1600\varepsilon\sigma^{-2}$ highest. The lowest peaks of both lattices having $\kappa = 100\varepsilon\sigma^{-2}$ do not get to zero, this show high attraction and a wetting behaviour [122]. The minimum position of the trough is located at 0.025.

Fig. 6.12(a) and Fig. 6.12(b) show the two lattice density profiles for the lower and upper wall, with a temperature difference of $\Delta T = 0.1\varepsilon\kappa_B^{-1}$, mass of $m_w = 2m_f$ with $\varepsilon_{ww} = 0.2$ and $\varepsilon_{wf} = 0.6$. The number density of the two lattices is increasing due to higher ε_{wf}. At lower stiffness of $\kappa = 100\varepsilon\sigma^{-2}$, attraction of the molecules is seen to occur. The other stiffness of $\kappa = 200\varepsilon\sigma^{-2} - 1600\varepsilon\sigma^{-2}$

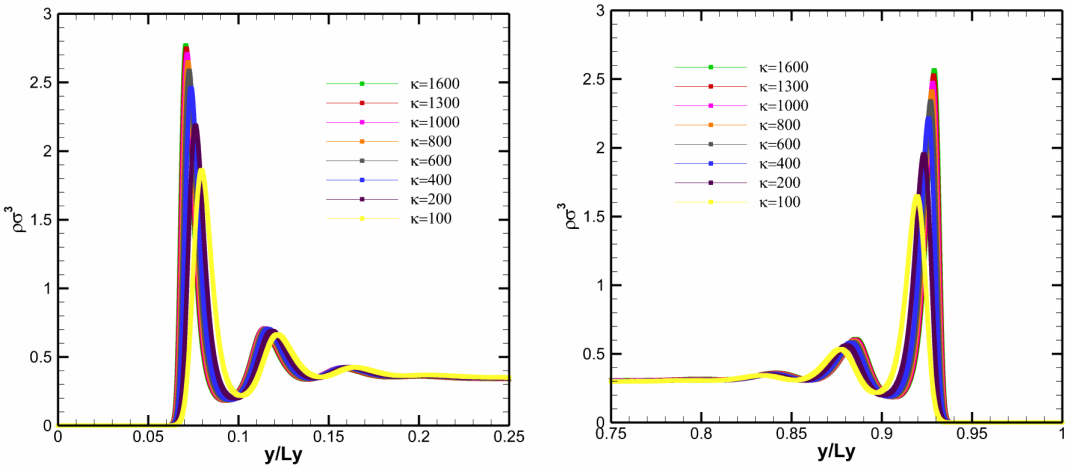

a) Lower wall b)Upper wall

Figure 6.3: Density Profiles of fluid for *pore* size $= 5\sigma$, $m_w = 2m$, $e_{ww} = 0.2$,$e_{ww} = 0.6$ for various values of stiffness constant κ.

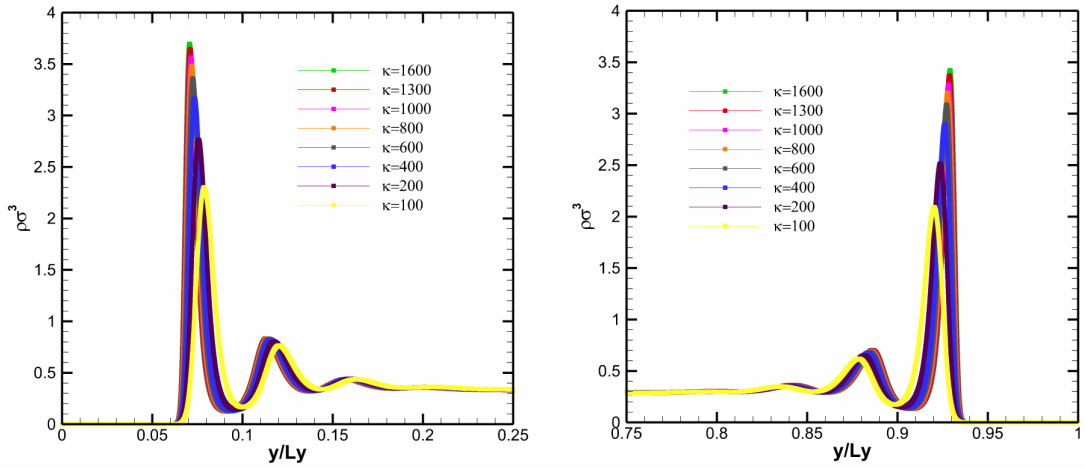

a) Lower wall b)Upper wall

Figure 6.4: Density Profiles of fluid for *pore* size $= 5\sigma$, $m_w = 2m$, $e_{ww} = 0.2$,$e_{ww} = 0.8$ for various values of stiffness constant κ.

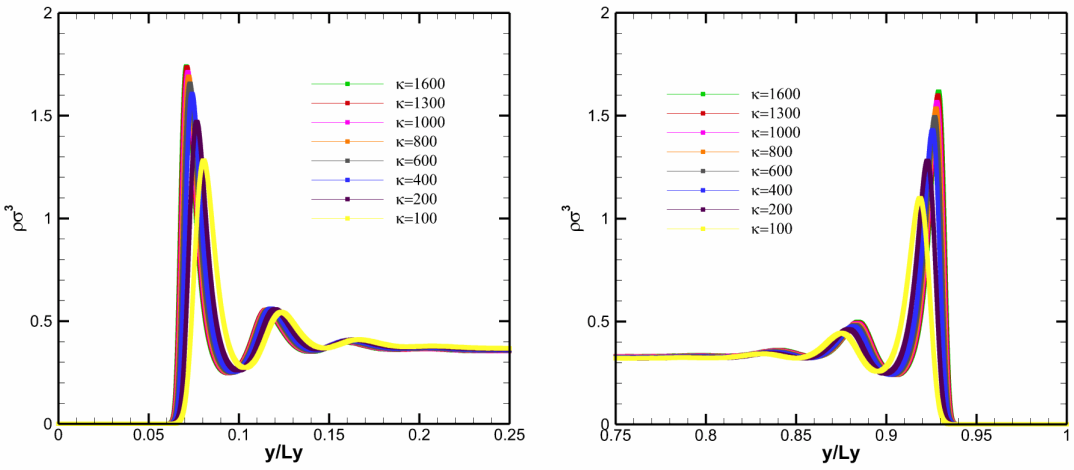

a) Lower wall b)Upper wall

Figure 6.5: Density Profiles of fluid for *pore* size $= 5\sigma$, $m_w = 2m$, $e_{ww} = 0.4$,$e_{ww} = 0.4$ for various values of stiffness constant κ.

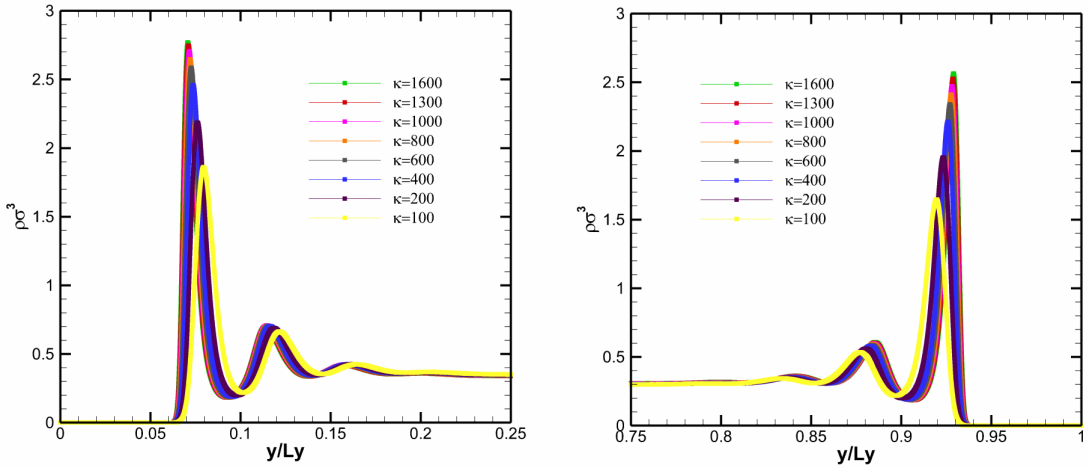

a) Lower wall b)Upper wall

Figure 6.6: Density Profiles of fluid for *pore* size $= 5\sigma$, $m_w = 2m$, $e_{ww} = 0.4$,$e_{ww} = 0.6$ for various values of stiffness constant κ.

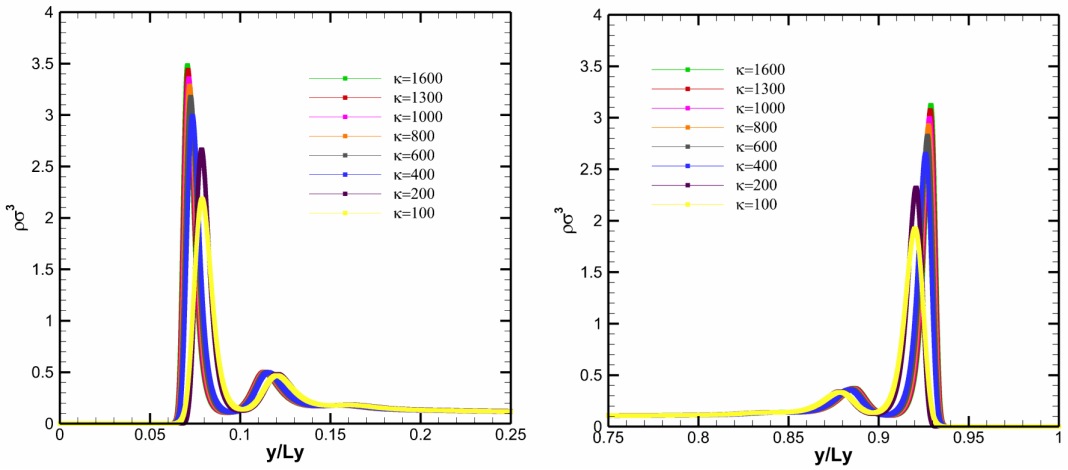

a) Lower wall b)Upper wall

Figure 6.7: Density Profiles of fluid for *pore* size $= 5\sigma$, $m_w = 2m$, $e_{ww} = 0.4$,$e_{ww} = 0.8$ for various values of stiffness constant κ.

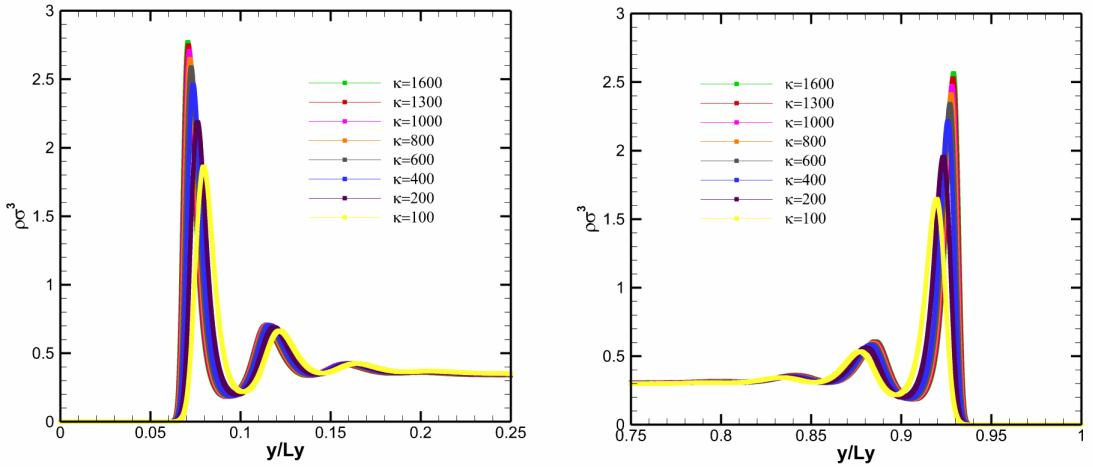

a) Lower wall b)Upper wall

Figure 6.8: Density Profiles of fluid for *pore* size $= 5\sigma$, $m_w = 2m$, $e_{ww} = 0.6$,$e_{ww} = 0.4$ for various values of stiffness constant κ.

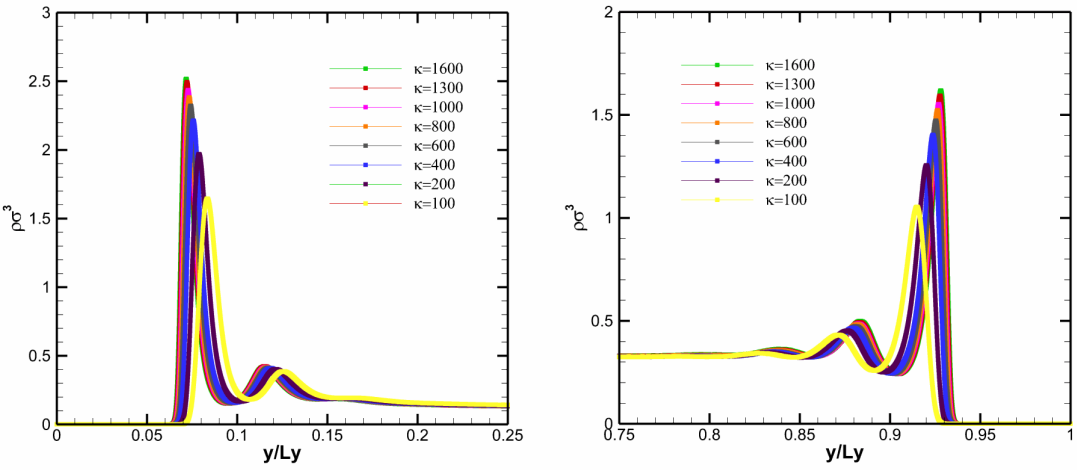

a) Lower wall b)Upper wall

Figure 6.9: Density Profiles of fluid for *pore* size $= 5\sigma$, $m_w = 2m$, $e_{ww} = 0.6$,$e_{ww} = 0.6$ for various values of stiffness constant κ.

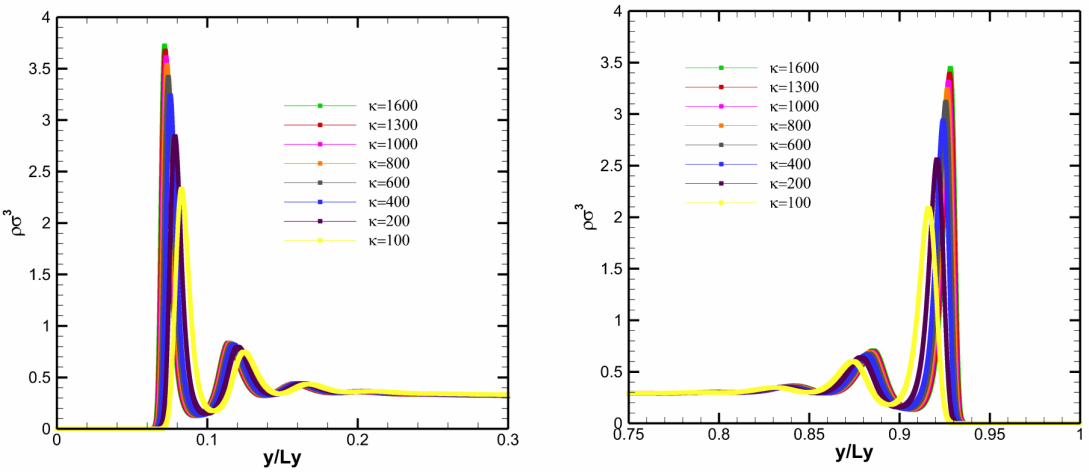

a) Lower wall b)Upper wall

Figure 6.10: Density Profiles of fluid for *pore* size $= 5\sigma$, $m_w = 2m$, $e_{ww} = 0.6$,$e_{ww} = 0.8$ for various values of stiffness constant κ.

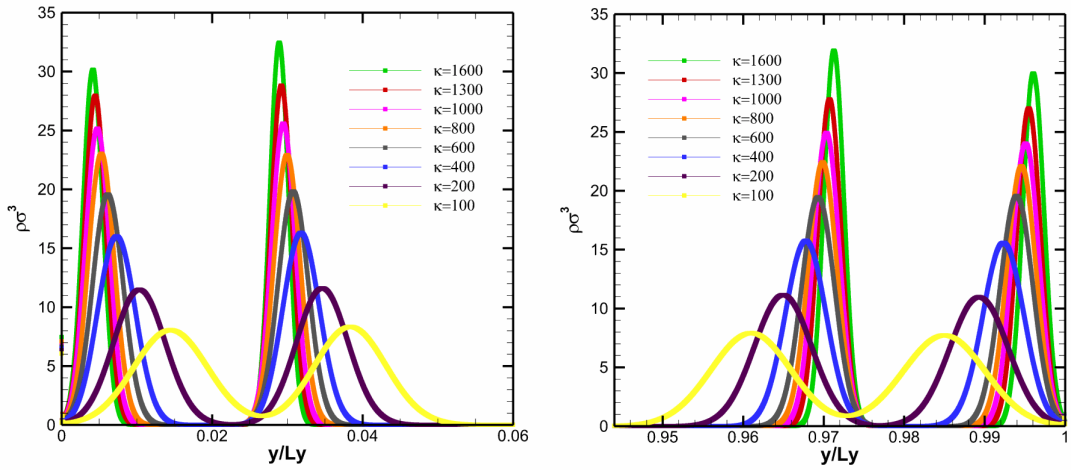

a) Lower wall b)Upper wall

Figure 6.11: Density Distribution in Solid Wall for $m_w = 2m$, $e_{ww} = 0.2$,$e_{ww} = 0.4$ for various values of stiffness constant κ.

exhibits repulsive behaviour. The amplitudes and peaks of all the lattice layers are constant with pronounced shifts. The trough and the minima position of the two lattice peaks of $\kappa = 100\varepsilon\sigma^{-2}$ and $\kappa = 200\varepsilon\sigma^{-2}$ is located at 0.026 and 0.022 with $\kappa = 400\varepsilon\sigma^{-2} - 1600\varepsilon\sigma^{-2}$at 0.02. Fig. 7.13 (a) and Fig. 7.13(b) shows the wall density profile as a function of the wall thickness with $\varepsilon_{ww} = 0.2$ and $\varepsilon_{wf} = 0.8$. The maximum peak number density with $\kappa = 1600\varepsilon\sigma^{-2}$ of the right lattice is seen to be higher than the left lattice and peaks increasing with stiffness. Particle attraction was also noticed in the lowest peaks of the two lattices, with minima shifting to 0.027 in the lower wall and 0.0973 in the upper wall.

Fig 6.14(a) and Fig. 6.14(b) show the solid density profile for $\varepsilon_{ww} = 0.4$ and $\varepsilon_{wf} = 0.4$. The density strength increases as the stiffness increases. The maximum density strength of the two lattices is also seen to increase with a slight shift in amplitude for the higher stiffness and a pronounced shift in amplitude for the lower stiffness. The two lowest peaks in the lattices have a minima position at 0.0265 at the lower wall and 0.0976 at the upper wall and are seen to exhibit attraction between their particles. Fig. 7.15(a) and Fig. 7.15(b) show the solid density profile for $\varepsilon_{ww} = 0.4$ and $\varepsilon_{wf} = 0.6$. The wall density strength shows slight increase in the two lattices. The streching of the lattice layers by the spring constant is also evident. The maximum peaks and other density peaks remain the same in both lattices. A slight shift in amplitude of higher stiffness is also seen with bigger amplitude shift in the smaller layers. The lowest peak with $\kappa = 100\varepsilon\sigma^{-2}$ still showed an attractive behavior with the minima position at 0.026 for the lower wall and 0.094 for the upper wall. There is a noticeable shift in minima position of $\kappa = 200\varepsilon\sigma^{-2}$ at 0.978 in the upper wall, with other higher stiffness and repelling particles still maintaining same minima

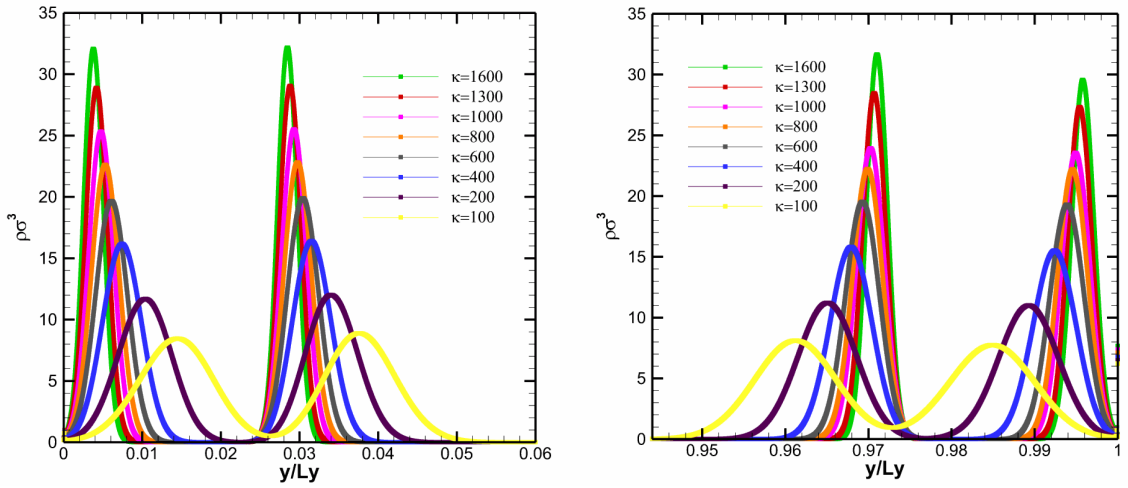

a) Lower wall b)Upper wall

Figure 6.12: Density Distribution in Solid Wall for $m_w = 2m$, $e_{ww} = 0.2$,$e_{ww} = 0.6$ for various values of stiffness constant κ.

position.

Fig. 6.16(a) and Fig. 6.16(b) show the upper and lower wall density profile for $\varepsilon_{ww} = 0.4$ and $\varepsilon_{wf} = 0.8$. The two lattices are still noticed with density strength slightly decreasing. The right lattice layer has a slightly higher density peak than the left lattice layer. The density peaks of the other two lattice layers, are seen to be constant, with peaks increasing with an increase in stiffness constant. One unique phenomenon observed is that the oscillation shifts to the right, when compared with other figs, that shifts to the left. The minima position is located at 0.0278 for the lower wall and 0.0972 for the upper wall.

Fig. 6.17(a) and Fig. 6.17(b) show the upper and lower wall density profile for $\varepsilon_{ww} = 0.6$ and $\varepsilon_{wf} = 0.4$ for various stiffness constant k. The density peaks and strengths for both lattices are constant for $\kappa = 100\varepsilon\sigma^{-2} - 1300\varepsilon\sigma^{-2}$, However, with a slight increase in number density in the maximum peak with $\kappa = 1600\varepsilon\sigma^{-2}$ of the right lattice compared to the left. Attractive behaviour of the two lowest peaks $\kappa = 100\varepsilon\sigma^{-2} - 200\varepsilon\sigma^{-2}$ and lattices are observed, while repulsive lattice behavior is observed for all other stiffness. The minima position for the lowest peaks of the two lattices is in 0.0273 for the lower wall and 0.973 for the upper wall.

Fig 6.18(a) and Fig. 6.18(b) shows the density distribution for lower and upper solid wall having $\varepsilon_{ww} = 0.6$ and $\varepsilon_{wf} = 0.6$ with $\Delta T = 0.1\varepsilon\kappa_B^{-1}$. The density strength of both lattices is seen to be overwhelmingly increased when compared to earlier figures. The number density of the right lattice is higher than the number density of the left lattice. Shifts in amplitude are also recorded for all peaks in the two lattices but this time the lowest peaks of both lattices having the same minima got to zero, showing a repulsive behaviour in these lattices. The minima position of the

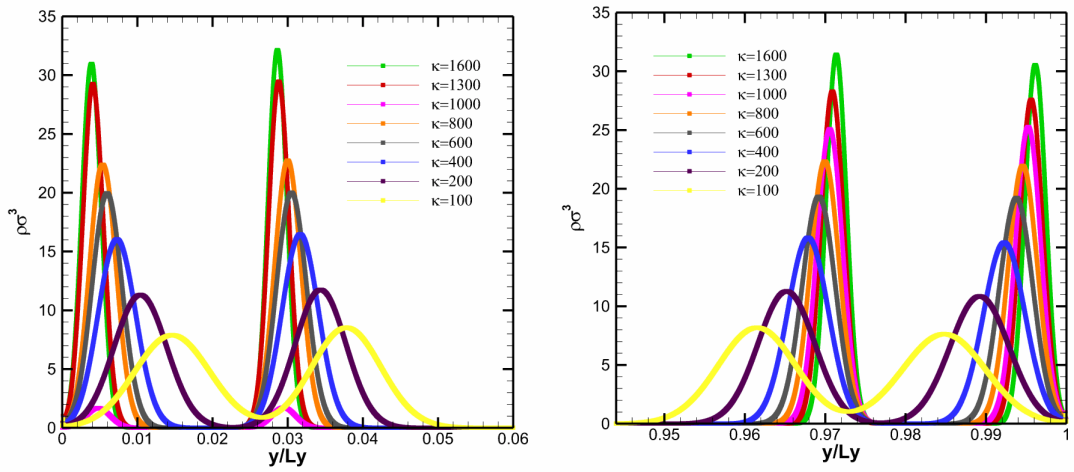

a) Lower wall b)Upper wall

Figure 6.13: Density Distribution in Solid Wall for $m_w = 2m$, $e_{ww} = 0.2$,$e_{ww} = 0.8$ for various values of stiffness constant κ.

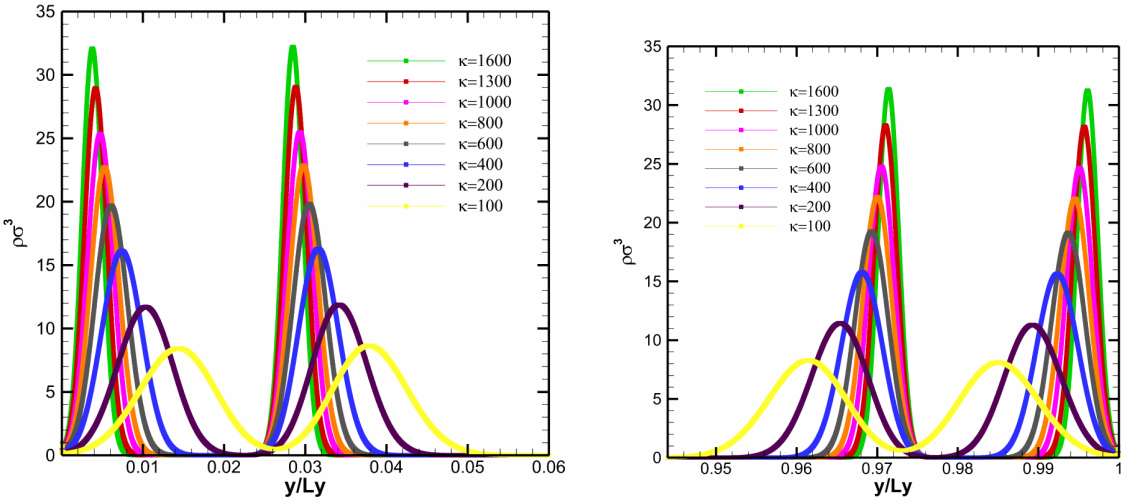

a) Lower wall b)Upper wall

Figure 6.14: Density Distribution in Solid Wall for $m_w = 2m$, $e_{ww} = 0.4$,$e_{ww} = 0.4$ for various values of stiffness constant κ.

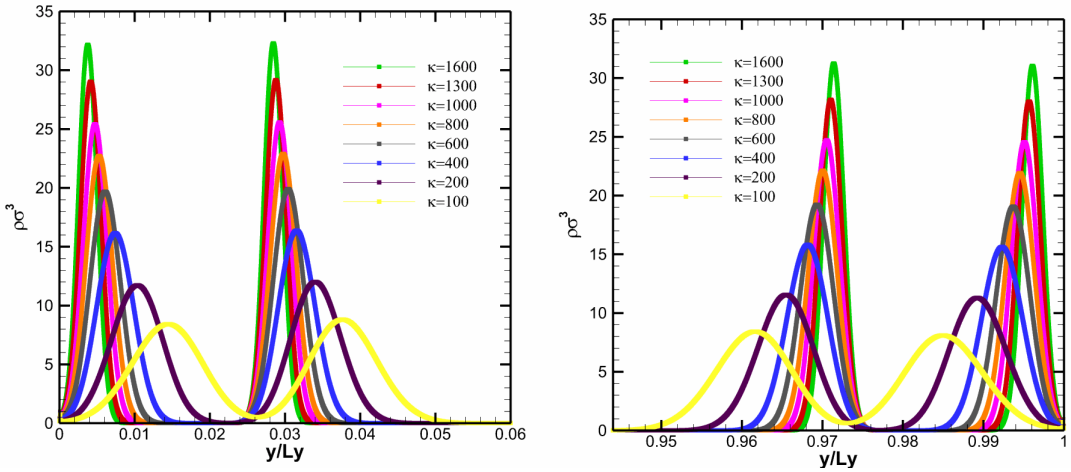

a) Lower wall b)Upper wall

Figure 6.15: Density Distribution in Solid Wall for $m_w = 2m$, $e_{ww} = 0.4$,$e_{ww} = 0.6$ for various values of stiffness constant κ.

lowest two lattices is 0.028 for the lower wall and 0.972 for the upper wall.

Fig. 6.19(a) and Fig. 6.19(b) show the two lattice density profiles for the lower and upper wall with temperature difference of $\Delta T = 0.1\varepsilon\kappa_B^{-1}$, mass of all $m_w = 2m_f$ with $\varepsilon_{ww} = 0.6$ and $\varepsilon_{wf} = 0.8$. The density strength and number density of both lattices is the highest so far, compared to all other results. The density layers are seen to be narrow for the lower stiffness $\kappa = 100\varepsilon\sigma^{-2} - 200\varepsilon\sigma^{-2}$. The peaks of both lattices are constant in density numbers, but with only a slight increase in the right lattice. The trough of the two lowest lattice peaks $\kappa = 100\varepsilon\sigma^{-2}$ are also seen to reach zero at both walls, showing a repulsion behavior. The position of the minima of the lowest peaks is at 0.0282 for the lower wall and 0.973 for the upper wall.

6.1.5 Temperature Distribution of Fluid in Nanopore

The temperature across the pore is determined by the thermal motion of the fluid and is achieved by dividing the simulation domain into 40bins with size 0.025 for the temperature profile.The bin temperature is computed from the expression

$$T(z_i) = \frac{1}{3k_B(J_M - J_N + 1)\sum_{i=1}^{N} H_n(z_{i,j}) \times \sum_{j=J_N}^{J_M}\sum_{i=1}^{N} H_n(z_{i,j}) m_i \left[v_{i,j}^{\alpha} - u^{\alpha}(z_i)\right]^2}. \quad (6.1.1)$$

The function $H_n(z_{i,j})$ is defined such that $H_n(z_{i,j}) = 1$ if $(n-1)\triangle z < z_i < n\triangle z$, otherwise $H_n(z_{i,j}) = 0$. Subscript j represents the j time steps with J_N and J_M time steps. α denotes x, y or z, m_i is the mass of fluid $v_{ij}$and u_{ij} are the mean and average velocities respectively. In steady state $u^z(z_i)$ and $u^y(z_i)$ have zero value for all bins.

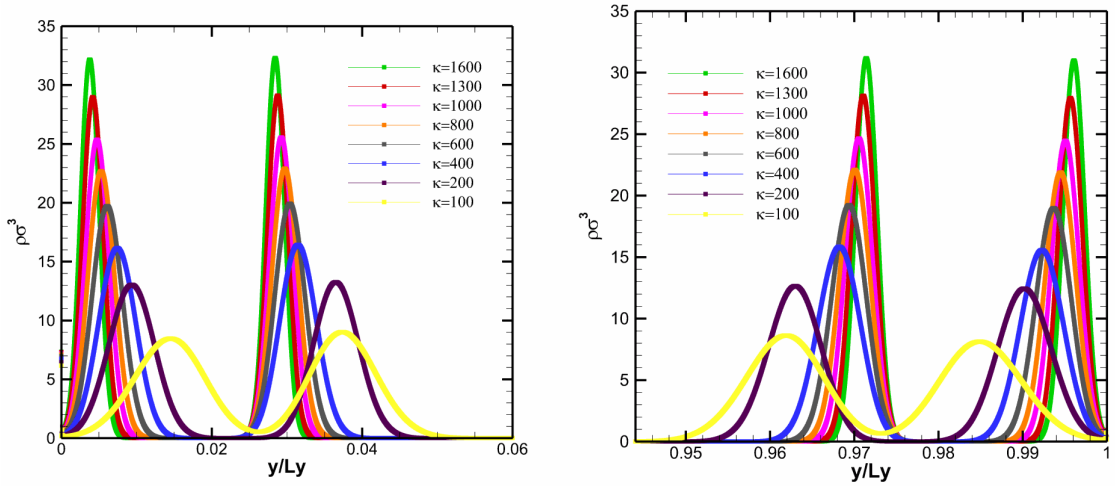

a) Lower wall b)Upper wall

Figure 6.16: Density Distribution in Solid Wall for $m_w = 2m$, $e_{ww} = 0.4$,$e_{ww} = 0.8$ for various values of stiffness constant κ.

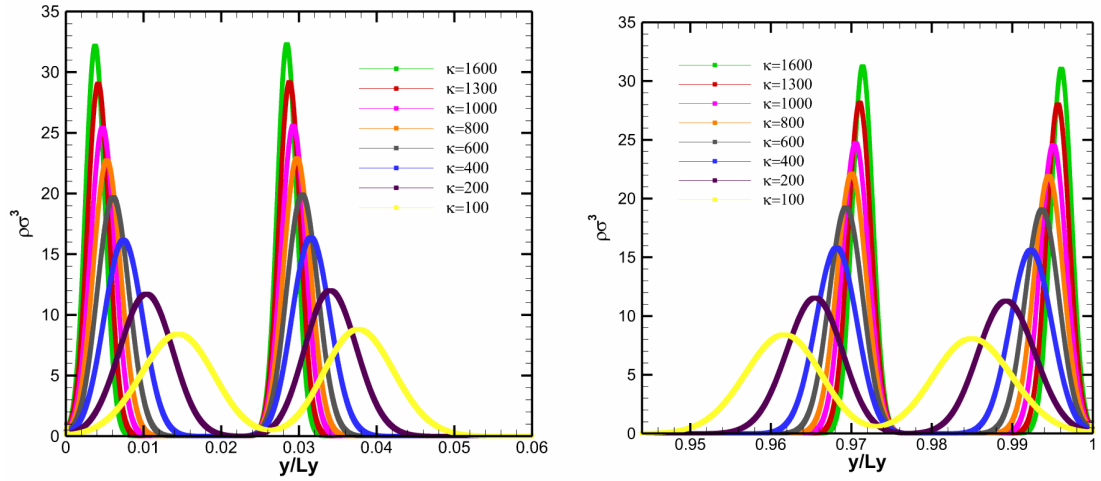

a) Lower wall b)Upper wall

Figure 6.17: Density Distribution in Solid Wall for $m_w = 2m$, $e_{ww} = 0.6$,$e_{ww} = 0.4$ for various values of stiffness constant κ.

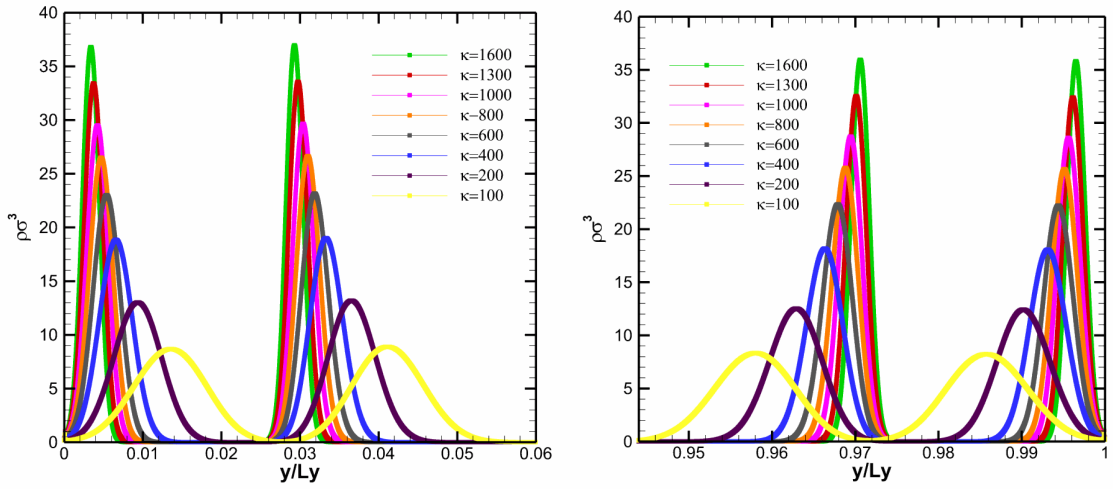

a) Lower wall b)Upper wall

Figure 6.18: Density Distribution in Solid Wall for $m_w = 2m$, $e_{ww} = 0.6$,$e_{ww} = 0.6$ for various values of stiffness constant κ.

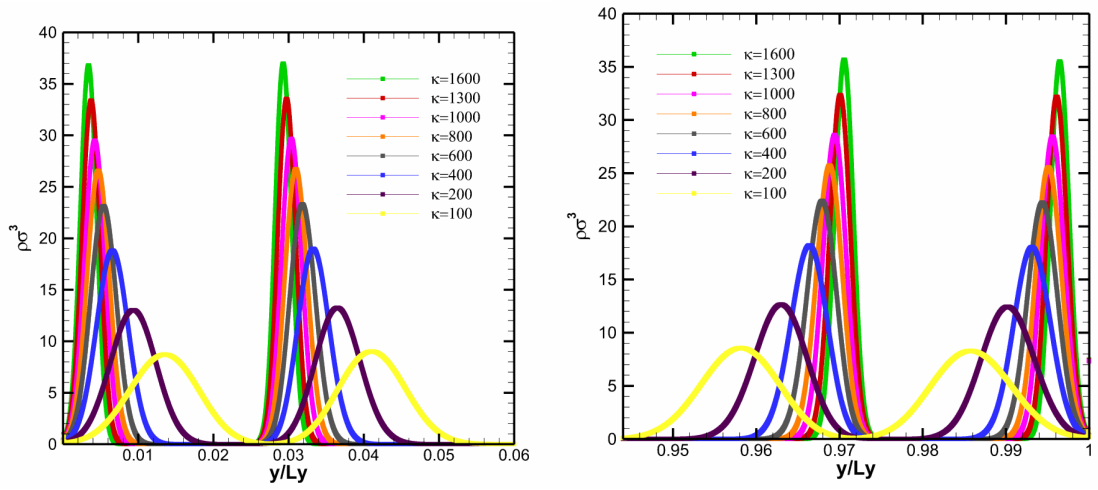

a) Lower wall b)Upper wall

Figure 6.19: Density Distribution in Solid Wall for $m_w = 2m$, $e_{ww} = 0.6$,$e_{ww} = 0.8$ for various values of stiffness constant κ.

6. Effect of Wall Size on the Kapitza resistance

Fluid thermal transport in a nanopore due to temperature gradient is investigated. Thermal oscillation frequency is approximated and expressed as $\omega = \sqrt{\frac{\kappa}{m}}$. Various values of $\kappa = 100\varepsilon\sigma^{-2} - 1600\varepsilon\sigma^{-2}$ represents the stiffness constant.

Fig. 6.20 shows the temperature profiles across the nanopore for a temperature difference of $\Delta T = 0.1\varepsilon\kappa_B^{-1}$, mass $m_w = 2m_f$ with $\varepsilon_{ww} = 0.2$ and $\varepsilon_{wf} = 0.4$ (wall surface wettability) and stiffness constant ranging from $\kappa = 100\varepsilon\sigma^{-2} - 1600\varepsilon\sigma^{-2}$. For high attractive walls, MD investigations have reported large layering phenomena of liquid particles close to the surface, with this effect modifying the thermal conductance in the interface. Temperature jump is observed in the lower and the upper wall, due to the effect of temperature, ε_{ww} and ε_{wf}, resulting to different Kapitza resistance in the lower and upper walls. The temperature jump arises, due to different thermal velocity of particles near the wall interface causing momentum transfer. High wettability have been widely reported to reduce the temperature jumps at the interface. Different temperature gradient corresponding to different stiffness values are seen.

For higher stiffness, the temperature profile and jump is seen to increase with increasing stiffness, but at the upper wall the temperature jump is seen to decrease with increasing stiffness, showing the effect of temperature on the thermal transport and temperature jump. The equilibrium point as observed in larger channel is seen to be established. For the smaller wall, the position is observed to diminish. This equilibrium position in the nanopore has been affected and seen to be weakly developed, due to the reduction of the size of the channel to 5σ. The temperature gradient is seen to increase with reducing stiffness, which depicts that the temperature effect of the upper wall dominates the thermal transport, compared to the effect of the stiffness, ε_{ww} , ε_{wf} and channel size.

Fig. 6.21 shows the temperature profile for $\varepsilon_{ww} = 0.2$ and $\varepsilon_{wf} = 0.6$. The difference between the temperature jumps is seen to be smaller in the lower wall, with an increase in temperature jump. However, in the upper wall the temperature jump is seen to increase clearly with decreasing stiffness. The equilibrium position is seen to be diminished, due to the size of the channel. The temperature gradient is seen to have increased with increase in heat transfer. The effect of the upper local temperature is beginning to reduce making the temperature gradient parallel to each other. The total height of the temperature jumps for all stiffness in the lower wall is seen to be smaller than the upper wall making the diminishing of the equilibrium position sustained. It is observed that at low fluid densities with large stiffness the momentum transfer is less effective between the liquid and the wall molecules and gives higher Kapitza resistance. However, at the higher wall the temperature increases and momentum transfer increases, giving a lower Kapitza resistance with higher stiffness constant.

Fig. 6.22 shows the temperature profile across the nanopore for $\varepsilon_{ww} = 0.2$ and $\varepsilon_{wf} = 0.8$. The temperature gradient is seen to be bigger; hence higher heat transport. The formation of the equilibrium position is seen to further diminish. The height of the temperature jump has become smaller in both the upper and lower wall, with reduced difference between the temperature jump of the highest and lowest stiffness causing heat transfer to probably increase. The temperature gradients of all the stiffness are beginning to converge. Fig. 6.23 show the temperature profiles for $\varepsilon_{ww} = 0.4$ and $\varepsilon_{wf} = 0.4$ for various stiffness constant k. The temperature jump is seen to increase with stiffness at the lower wall and decrease with stiffness at the upper wall. The equilibrium position is also seen to be diminished. The temperature jump for both the lower and upper wall is reduced with an increase in ε_{ww}, this shows higher heat transport.

Fig. 6.24 shows the temperature profile across the nanopore of 5σ for $\varepsilon_{ww} = 0.4$ and $\varepsilon_{wf} = 0.6$ with various stiffness constant. Further reduction of the temperature jump at the lower wall is observed. The equilibrium position is totally distorted. The temperature jump at the upper wall is also seen to reduce as the stiffness increases. The increase in ε_{wf} is causing a reduction in temperature jump and an increase of heat transfer and linear temperature variation as the stiffness increases across the nanopore. Fig. 6.25 shows the temperature profile for $\varepsilon_{ww} = 0.4$ and $\varepsilon_{wf} = 0.8$. Further reduction of the total temperature jump in the lower and upper walls, with the increase of ε_{ww} is seen, showing an increase of heat transport across the pore. However, the influence of ε_{wf} on the temperature jump and heat transfer across the nanopore is dominant. The equilibrium position is further diminished with the temperature gradient not crossing each other and obtaining a constant temperature point.

Fig. 6.26 shows the temperature profiles across nanopore of $\Delta T = 0.1\varepsilon\kappa_B^{-1}$, mass of wall $m_w = 2m_f$, $\varepsilon_{ww} = 0.6$ and $\varepsilon_{wf} = 0.4$ for various stiffness constant. The equilibrium position is seen to be almost removed, showing the effect of pore radii and size. The total temperature jump in the lower wall for all stiffness is seen to be very small, compared to the upper wall with large ranges of temperature jump with increasing stiffness. The temperature jump in the upper wall is seen to reduce with increasing stiffness. The large temperature jump in the upper wall affects the overall temperature gradient, thereby reducing the heat transfer across the nanopore.

Fig. 6.27 show the temperature profile across the nanopore with $\varepsilon_{ww} = 0.6$ and $\varepsilon_{wf} = 0.6$. The equilibrium position is also diminished with a smaller total temperature jump in the lower wall and a larger temperature jump in the upper wall. The increase of ε_{wf} compensates for the high-temperature jump causing the heat transfer across the nanopore to increase. Fig. 6.28 shows the temperature profile across the nanopore for $\varepsilon_{ww} = 0.6$ and $\varepsilon_{wf} = 0.8$. Increasing ε_{wf} has shown to reduce the total temperature jump in the lower and upper wall, thereby increasing the

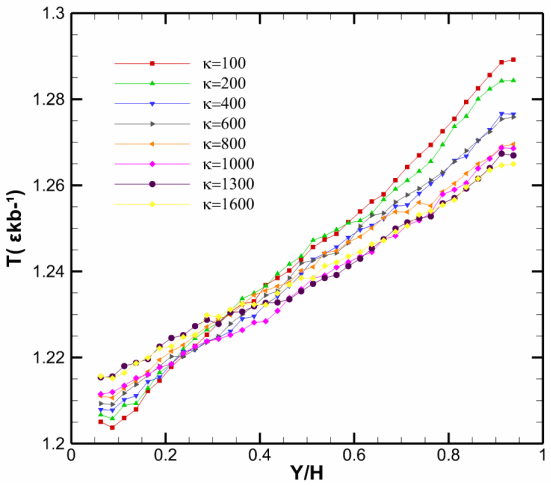

Figure 6.20: Temperature Profiles across nanopore of 5σ, for $m_w = 2m$, $e_{ww} = 0.2$, $e_{wf} = 0.4$ for various values of stiffness constant κ.

heat transfer across the nanopore. The temperature jump is seen to reduce with increasing stiffness at the upper wall, though single values of stiffness with the temperature jump is seen to increase.

The heat transfer across a nanopore of radii and size 5σ has been revealed to increase with an increase in ε_{ww} and ε_{wf} . The effect of ε_{wf} in thermal transfer is seen to be dominant across the nanopore. The temperature jump increases with higher stiffness in the lower wall and decreases with higher stiffness in the upper wall. The equilibrium position is seen to diminish as the nanopore reduces, reducing the Kapitza resistance and increasing the heat transfer across the nanopore. From these findings smaller nanopores will be suitable for applications in desalination, filtration and gasification.

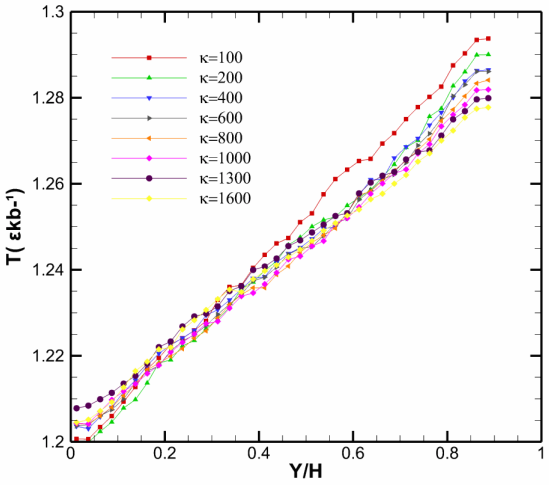

Figure 6.21: Temperature Profiles across nanopore of 5σ, for $m_w = 2m$, $e_{ww} = 0.2$, $e_{wf} = 0.6$ for various values of stiffness constant κ

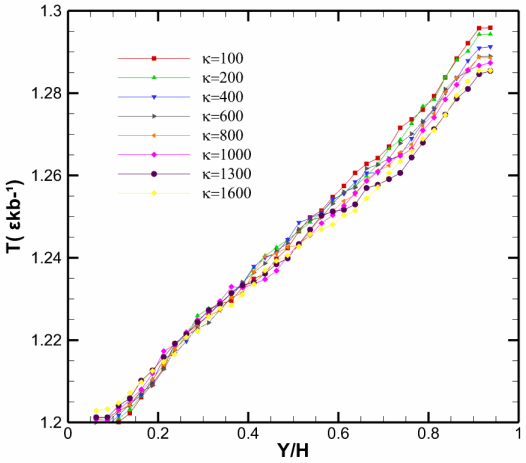

Figure 6.22: Temperature Profiles across nanopore of 5σ, for $m_w = 2m$, $e_{ww} = 0.2$, $e_{wf} = 0.8$ for various values of stiffness constant κ

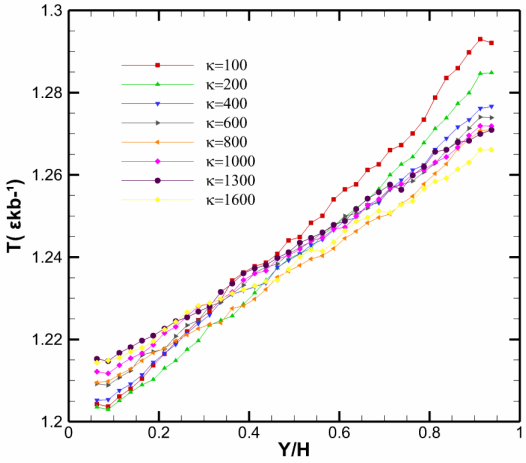

Figure 6.23: Temperature Profiles across nanopore of 5σ, for $m_w = 2m$, $e_{ww} = 0.4$, $e_{wf} = 0.4$ for various values of stiffness constant κ

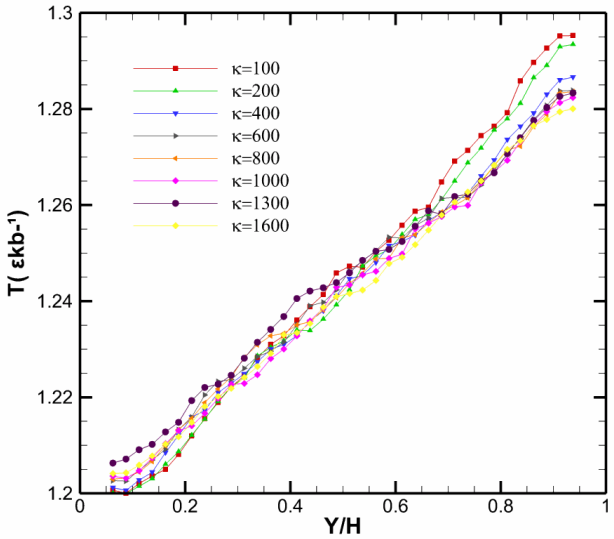

Figure 6.24: Temperature Profiles across nanopore of 5σ, for $m_w = 2m$, $e_{ww} = 0.4$, $e_{wf} = 0.8$ for various values of stiffness constant κ

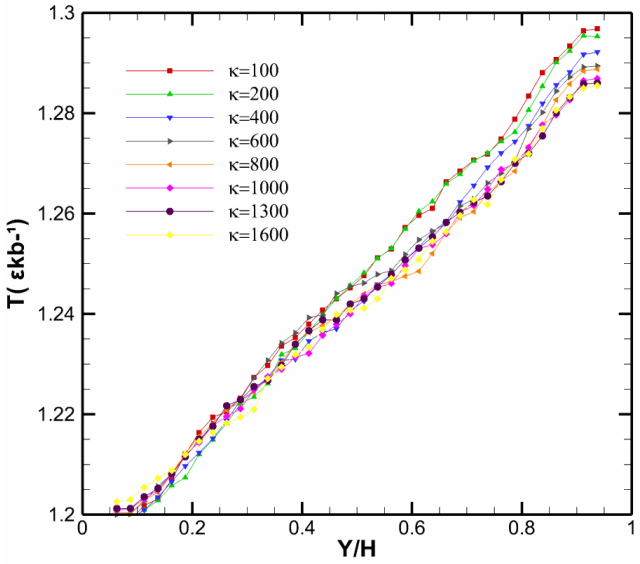

Figure 6.25: Temperature Profiles across nanopore of 5σ, for $m_w = 2m$, $e_{ww} = 0.4$, $e_{wf} = 0.8$ for various values of stiffness constant κ

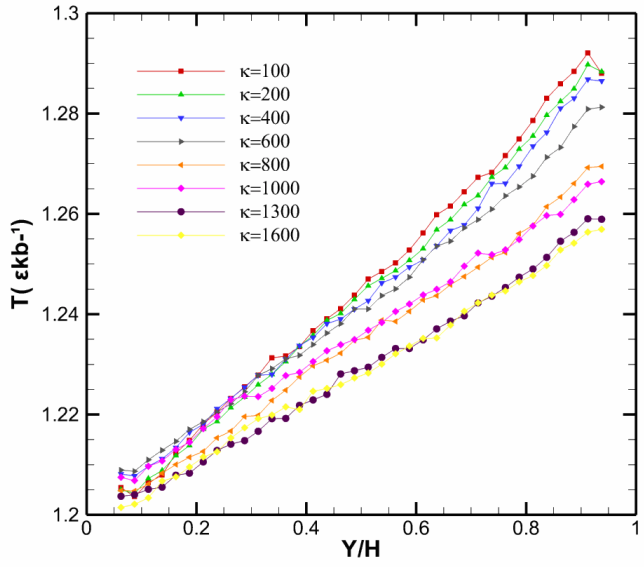

Figure 6.26: Temperature Profiles across nanopore of 5σ, for $m_w = 2m$, $e_{ww} = 0.6$, $e_{wf} = 0.4$ for various values of stiffness constant κ

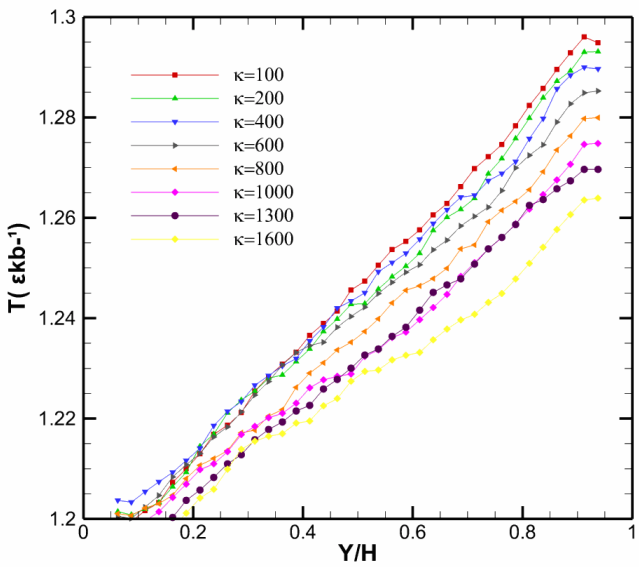

Figure 6.27: Temperature Profiles across nanopore of 5σ, for $m_w = 2m$, $e_{ww} = 0.6$, $e_{wf} = 0.6$ for various values of stiffness constant κ

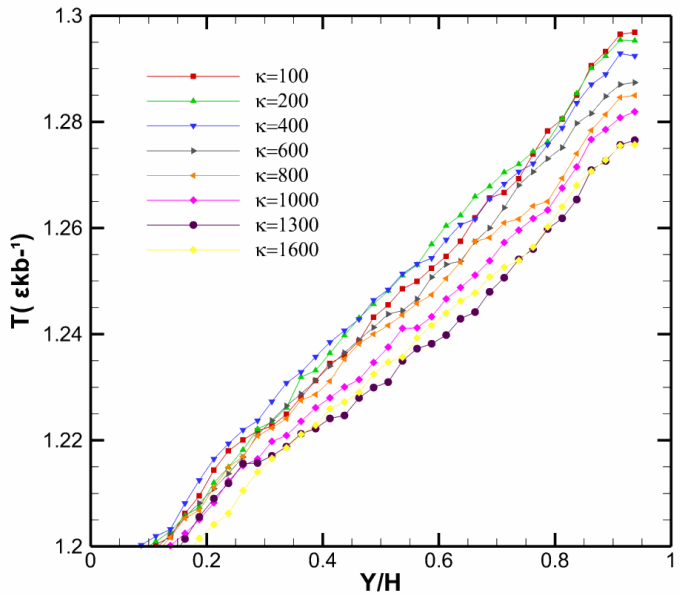

Figure 6.28: Temperature Profiles across nanopore of 5σ, for $m_w = 2m$, $e_{ww} = 0.6$, $e_{wf} = 0.8$ for various values of stiffness constant κ.

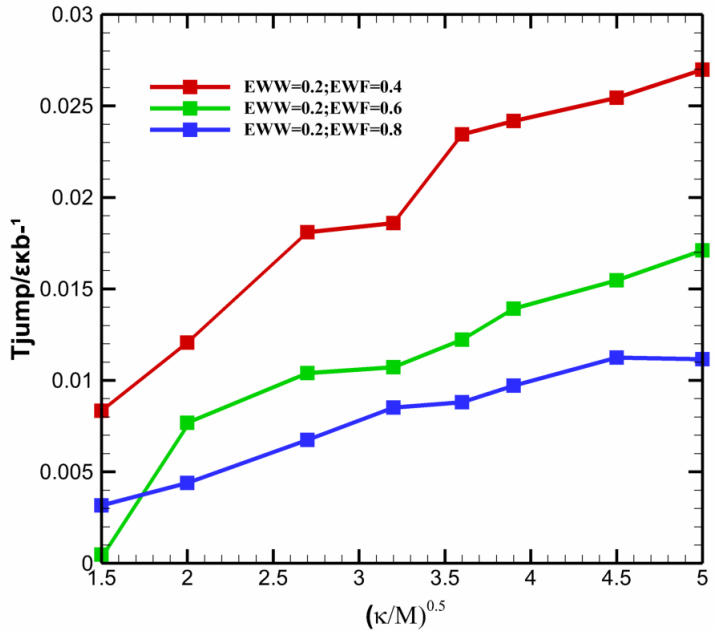

Figure 6.29: Kapitza Resistance of 5σ nanopore with $m_w = 2m_f$, $e_{ww} = 0.2$ $e_{wf} = 0.4 - 0.8$ as a function of wall frequency.

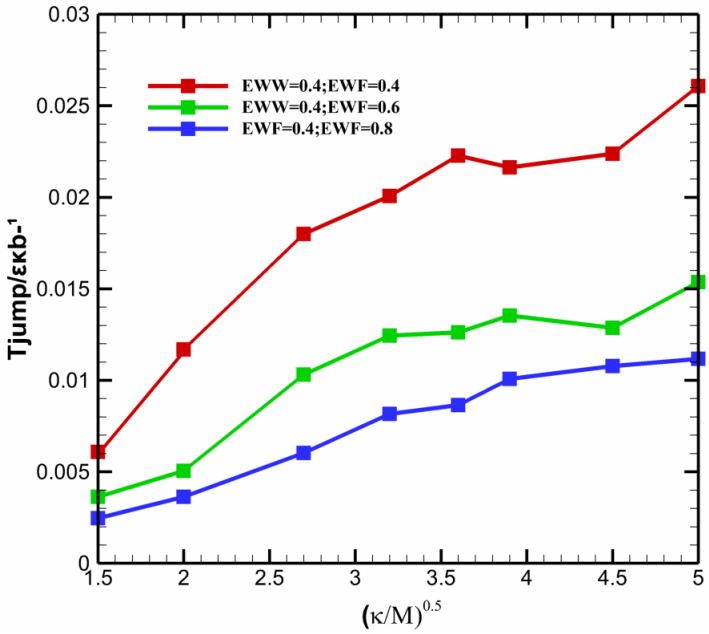

Figure 6.30: Kapitza Resistance of 5σ nanopore with $m_w = 2m_f$, $e_{ww} = 0.4$ $e_{wf} = 0.4 - 0.8$ as a function of wall frequency.

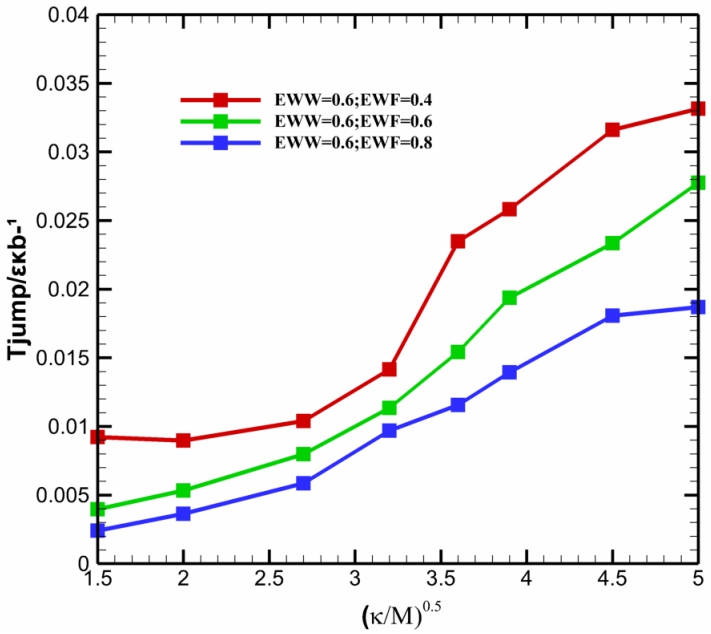

Figure 6.31: Kapitza Resistance of 5σ nanopore with $m_w = 2m_f$, $e_{ww} = 0.6$ $e_{wf} = 0.4 - 0.8$ as a function of wall frequency.

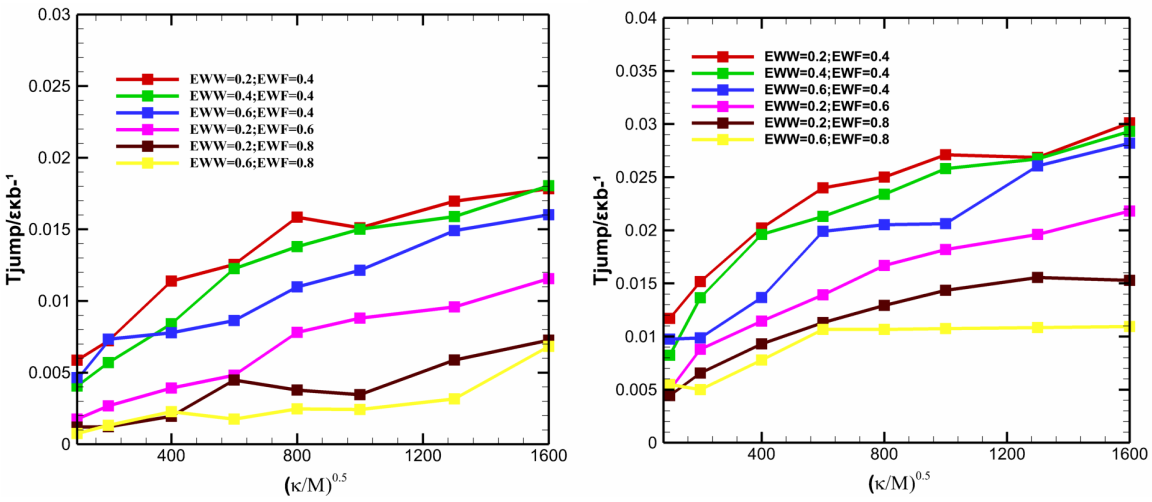

a) Lower wall b)Upper wall

Figure 6.32: Kapitza Resistance of 10σ nanopore with $m_w = 2m_f$, $e_{ww} = 0.2 - 0.6$, $e_{wf} = 0.4 - 0.8$ as a function of wall frequency.

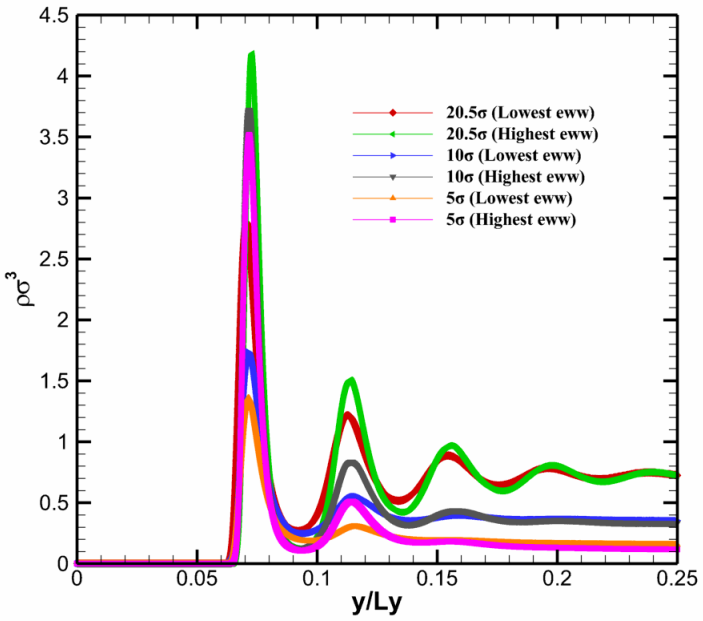

Figure 6.33: Density Profiles of Fluid for $m_w = 2m_f$, lowest $\varepsilon_{ww} = 0.2$, highest $\varepsilon_{ww} = 0.6$ for various nanopore sizes.

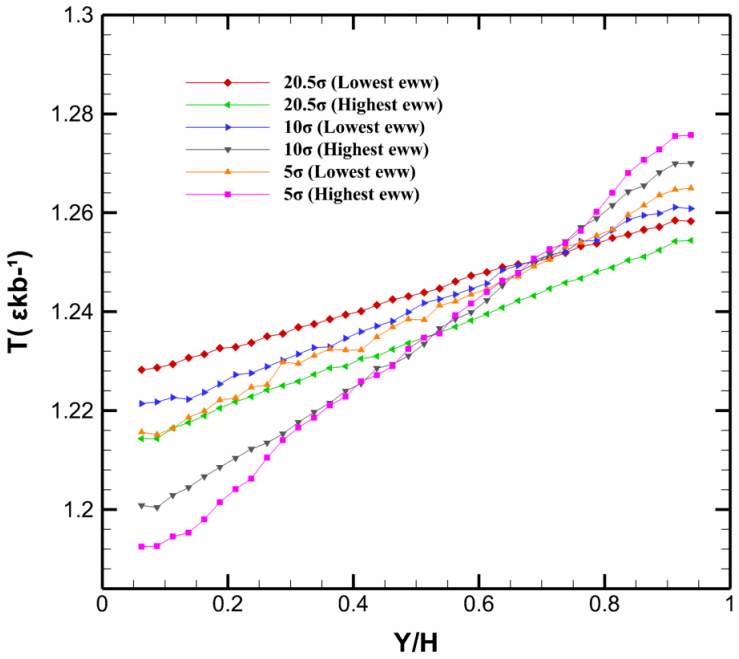

Figure 6.34: Temperature Profiles of Fluid for $m_w = 2m_f$, lowest $\varepsilon_{ww} = 0.2$, highest $\varepsilon_{ww} = 0.6$ for various nanopore sizes.

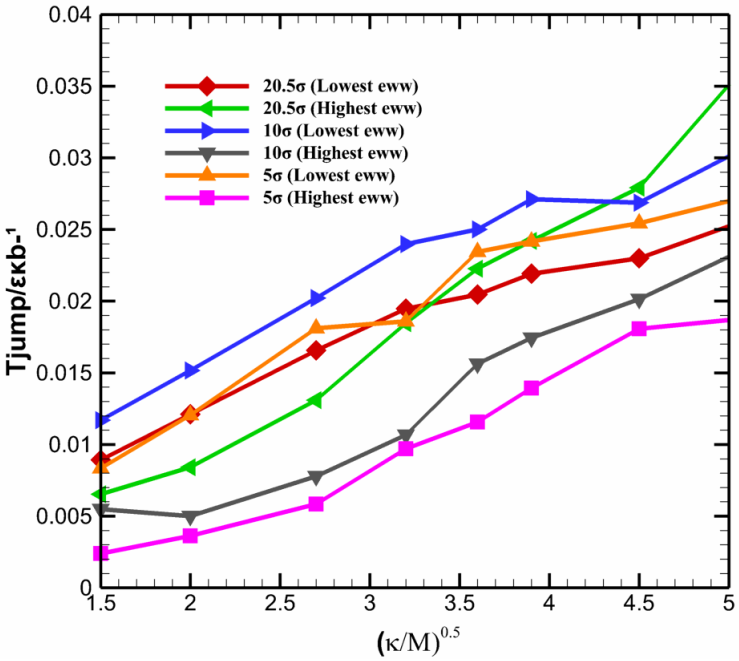

Figure 6.35: Kapitza Resistance of Fluid for $m_w = 2m_f$, lowest $\varepsilon_{ww} = 0.2$, highest $\varepsilon_{ww} = 0.6$ for various nanopore sizes.

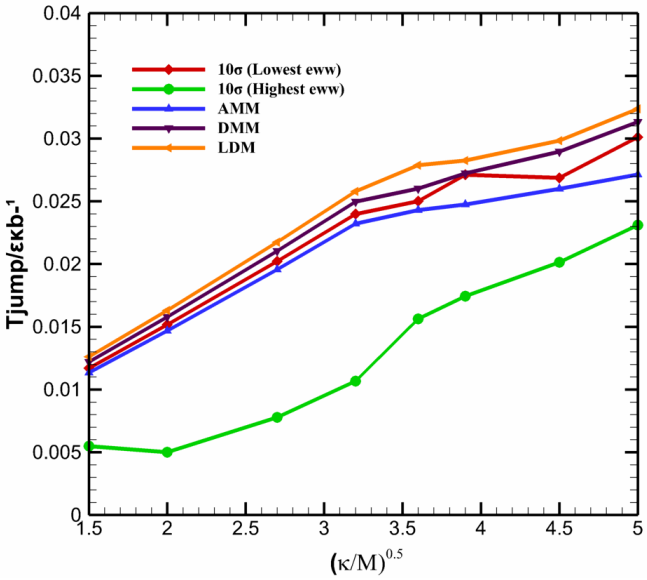

Figure 6.36: The Kapitza resistance calculated with AMM, DMM, LDM and MD Simulation with $m_w = 2m_f$, lowest $\varepsilon_{ww} = 0.2$, highest $\varepsilon_{ww} = 0.6$ for nano-pore size of 10σ.

6.1.6 Kapitza Resistance of Fluid in the Nanopore

Fig. 6.29 shows the Kapitza resistance across the nanopore of 5σ for $\Delta T = 0.1\varepsilon\kappa_B^{-1}$, mass of wall $m_w = 2m_f$ with $\varepsilon_{ww} = 0.2$ and $\varepsilon_{wf} = 0.4 - 0.8$ as a function of the harmonic frequency of the wall particles. The plot shows that the Kapitza resistance reduces as the wettability ε_{wf} increases. As the wettability increases the thermal motion of the particles reduces, this inhibits the flow of heat and momentum transfer between the fluid and the wall. At a lower frequency, the Kapitza resistance reduced slightly as the wettability increased, with a dramatic reduction of Kapitza resistance as ε_{wf} reduces at higher frequency. Showing the importance of inelastic phonon transfer in influencing the Kapitza resistance.

Fig. 6.31 shows the Kapitza resistance of $\varepsilon_{ww} = 0.6$ and $\varepsilon_{wf} = 0.4 - 0.8$ as a function of frequency. The Kapitza resistance is seen to reduce with a higher combination of ε_{ww} and ε_{wf} in lower frequency. The Kapitza resistance in lower frequency also reduces with decreasing ε_{wf} .

Fig. 6.32 shows the Kapitza resistance across the nanopore of 10σ for $\Delta T = 0.1\varepsilon\kappa_B^{-1}$, mass of wall $m_w = 2m_f$ with $\varepsilon_{ww} = 0.2 - 0.6$ and $\varepsilon_{wf} = 0.4 - 0.8$ as a function of the harmonic frequency of the wall particles. The Kapitza resistance is seen to increase with increasing frequency across the nanopore for all combinations of ε_{ww} and ε_{wf} .

The Kapitza resistance at a higher frequency is seen to reduce dramatically as ε_{wf} increases. The effect of ε_{ww} and ε_{wf} on the Kapitza resistance across the 10σ nanopore also show that the Kapitza resistance increases with an increase in wall vibrational frequency. The Kapitza resistance at low and high frequency is seen to reduce with increasing wettability ε_{wf} though with more reduction at higher frequency. The Kapitza resistance reduces with high ε_{ww} at low frequency, showing that the influence of ε_{wf} on the Kapitza resistance across the nanopore is dominant but nevertheless the presence of ε_{ww} has shown to have a remarkable influence on the Kapitza resistance. The Kapitza resistance is seen to be the highest at high frequency, low ε_{ww} and high ε_{wf}.

Fig. 6.33 shows the density distribution or profile in a 5σ, 10σ and 20.5σ nanopore size with the highest and lowest wall-wall intermolecular interaction energy strength (ε_{ww}) for all sizes considered. The density profile is seen to be highest in the biggest pore/radii (20.5σ) having $\varepsilon_{ww} = 0.6$, showing that a combination of large pore size and ε_{ww} forms the highest solid like interface in the nanopore. The pore size with the highest ε_{ww} are seen to have higher peaks compared to the same size with lower ε_{ww}. The ε_{ww} is the dominant factor responsible for higher density in the interface. More layers with higher peaks are seen to be formed by higher pore sizes and higher ε_{ww}. The 20.5σ with the highest and lowest ε_{ww} is seen to have four layers, though with

20.5σ and highest $\varepsilon_{ww} = 0.6$ having more maximum peaks. The density peaks reduce as the pore sizes gets smaller and as ε_{ww} goes from highest to lowest. This study is directly relevant to thermal conductivity enhancement in nanoparticles, which is mainly due to the bulk like formation of base fluid layers instigated by the nanoparticles [125-126]. This result clearly shows that nanoparticles and nanofluid solutions can be engineered for thermal enhancement and storage by reducing and increasing ε_{ww} and the size/radii of pore channels.

Fig. 6.34 shows the temperature profile across nanopore of size /radii 5σ, 10σ and 20.5σ at their respective highest and lowest ε_{ww}. It is clearly seen that heat and mass transfer is highest with the 5σ having the lowest $\varepsilon_{ww} = 0.2$, due to its least resistance and bulk like molecular impediments in allowing fluid and heat to flow through its pores quickly because of the formation of fewer layers and small peaks. Their applications will be very relevant in filters for gasification and desalination [16-19].

Fig.6.35 shows the Kapitza resistance across the nanopore of size 5σ, 10σ and 20.5σ as a function of the frequency of vibration of the wall molecules. The smallest size/radii having 5σ with the highest $\varepsilon_{ww} = 0.6$ is seen to have the lowest Kapitza resistance at low and high frequency. The Kapitza resistance is also seen to increase with frequency for all values of pore size and ε_{ww}. The highest pore size 20.5σ and highest $\varepsilon_{ww} = 0.6$ is seen to have the highest Kapitza resistance at higher frequency. For high Kapitza resistance as a result of its bulk like layering, inelastic phonon heat transfer will be prevalent, propagating in the fluid to form networks with other bulk like layering.

In summary this section has attempted to answer the two important questions asked at the beggining of the discussion. From the analysis and results it is evident that the pore size affects the thermal or Kapitza resistance across interfaces and nanofluidic channels. The results have also shown that for the best and highest Kapitza resistance to be obtained, a combination of high e_{ww} depicting specifically engineered material interface properties and channel thickness should be achieved. This will bring a step closer, an end to the era of trial and error in choosing the best material properties and configuration for novel engineering applications.

6.1.7 Comparison of Molecular Dynamics with Theoretical Models

Molecular Dynamic Simulation plays a role in the interpretation of theoretical and experimental data. It must be noted that all measured quantities in molecular dynamics are averaged. Due to this reason, comparison of theoretical and MD simulations can be over-interpreted or under-interpreted. Comparing simulation data with a theoretical model, one must put in mind the assumptions made by the theoretical model and the ensemble considered by the molecular model.

There is also a reason to be careful so that data compared with the theoretical model relates to the same assumptions and thermodynamic condition, describing the same physical scenario.

To compare with the MD model, the widely acceptable models for the calculation of the Kapitza resistance, such as the acoustic mismatch models AMM, diffuse mismatch models (DMM) and lattice dynamics models (LDM) are used. These are models that are currently used to determine the Kapitza resistance between two dissimilar media. The AMM and DMM consider only bulk properties of dissimilar materials while calculating the Kapitza resistance, with no account of the material properties near the interface, but the LDM includes the material properties. The acoustic mismatch model (AMM) bases its assumption on specular phonon transmission and reflection, which means interfacial walls are treated in continuum. The transmissivity and Kapitza resistance of the simulation interface is obtained using the AMM method [127]. The diffuse mismatch model [DMM] was proposed to be better than the AMM [128]. The model postulates that incident phonons undergo diffuse scattering that is elastic at the interface at both sides of the media. The DMM method was used to obtain the Kapitza resistance of the simulation domain parameters. The lattice dynamics model (LDM) was applied to obtain the Kapitza resistance between fcc lattices with better results obtained [124]. The LDM calculates transmissivity by the ratio of the transferred incident energy flux of both media. The LDM interface normally applies to models consisting of fcc lattices A and B, the right side B is represented by the wall crystal with a harmonic approximation, and the left side A, is a solid argon crystal [124]. The level of the dissimilarities of the interface is ascertained by setting the intermolecular interaction energy strength of the wall particles in LDM that gives the material properties of the wall to the model. The methods described are used to obtain the AMM, DMM and LDM with the parameters of the simulation system. The lattices used in the model are monoatomic fcc lattice.

Fig. 6.36 shows a comparison between the MD model, AMM, DMM and LDM of nanopore size of 10σ and lowest $\varepsilon_{ww} = 0.2$ with highest $\varepsilon_{ww} = 0.6$. The MD model with $\varepsilon_{ww} = 0.2$ is in close agreement with the AMM, DMM, and LDM. The walls with very high ε_{ww}, deviates largely from the rest. This is due to the high wall particle interaction which is absent in the other models. The LDM predicts the largest Kapitza resistance which is in agreement with a previous study [124]. MD obtained Kapitza resistance, is due to its ability to show and obtain interface inelastic phonon scattering with increasing an-harmonicity of particle interaction [129]. A detailed reason, why the increase in inelastic phonon scattering at the interface, is reported in previous studies [99]. They reported that increase in inelastic phonon scattering at the interface increases phonon transmission coefficients and reduces the Kapitza resistance. Their study was adapted for Si/Ge interface akin to the wall-fluid interface. They explained that incident phonons from the Si-wall have frequency

higher than the maximum frequency of Ge atoms due to the boundary condition imposed on the Si-wall. They predicted that energy can be transmitted if there is inelastic scattering of phonons into two phonons having lower frequency, thereby increasing the thermal conductance and reducing the Kapitza resistance across the interface. The MD model of this work shows inelastic scattering and an-harmonicity as observed in the different amplitudes shifts obtained in the wall. This study shows that the calculated Kapitza resistance for LDM is 9% higher than DMM and DMM is 6% larger than MD with MD, 4% higher than AMM, which is in agreement with previous studies [87, 126, 98, 109]. They also reported that the Kapitza resistance increases with the phonon density of state, which is directly related to the frequency. These predictions have been confirmed by this MD study.

Chapter 7

Conclusion and Future Work

7.1 Conclusions

A Maxwel-Einstien solid molecular dynamics thermal wall model that allows dual energy and momentum transport exchange across solid-liquid interfaces and nanofluidic channels have been developed. The developed modeling approach imposes isothermal boundary conditions on the walls by the application of a themostat on the atomic wall layers. The thermal wall model was applied to study the thermal transport and Kapitza resistance across interfaces and nanofluidic channels.

The current study uses liquid argon at constant density, consisting of two [111]− oriented perfect Face-Centre Cubic (fcc) lattice planes. The results for the Kapitza resistance obtained in this study were similar to predictions of AMM, DMM and LDM analytical models. Previous MD studies have mostly investigated steady planar flows for simple atomic fluids at single state point in a nanochannel, with less studies, on nanoscale interfacial thermal transport. This study has provided a better understanding of nanoscale interfacial thermal transport.

The investigation considers the effects of the mass, wall intermolecular interaction energy strength and channel pore size on the Kapitza resistance and thermal transport across interfaces and nanofluidic channels. Studying these effects are not possible with continuum hypothesis such as lattice Boltzmann models, due to the fact that the lattices of their atoms and molecular interaction are not taken into account in these models.

The first detailed study determined the effect of mass and stiffness of the wall particles on the Kapitza resistance, temperature profile and density distribution across solid-liquid interfaces and nanofluidic channels implementing a wall-fluid molecular dynamics thermal wall model. The density profiles of the walls indicated that, for lower values of the wall bonding stiffness, the amplitude of oscillation of its atoms is unaffected by a change in mass. Hence, for higher values of

the wall mass, the frequency of oscillation must decrease, in order to satisfy constant average kinetic energy constraints, dictated by the fixed temperature of the wall. The lower frequency translated into a smaller number of collisions between the wall and liquid particles, which inevitably led to a less efficient transfer of energy and temperature jump at the solid-liquid interface. As a result, for low values of κ, the Kapitza or thermal resistance was dominated by the mass of the wall particles, while as κ increased, the mass effect faded and the bonding stiffness dictated the temperature jump. Finally, the temperature jump correlated with the product of the bonding stiffness and wall mass rather than the frequency of harmonic springs $\sqrt{\kappa/m_w}$ [55].

The second study determined the effect of the presence of wall particle energy intermolecular interaction strength on the Kapitza resistance, temperature profile and density distribution across solid-liquid interfaces and nanofluidic channels applying wall-wall molecular dynamics thermal wall model. The results revealed different density profiles in 2 lattice sites in the solid, and density profiles in the liquid near the walls. Higher values of spring constant κ and intermolecular interaction energy strengths $(e_{ww}; e_{wf})$ produced maximum density peaks in the solid and fluid, developing temperature jump at the solid-liquid interface. Lower values of e_{ww} produced higher temperature jump and Kapitza resistance. The presence of intermolecular interaction energy strength of the wall (e_{ww}) is reported to influence the formation of higher density peaks in the solid-liquid interface, this finding is novel.

The third and final study determined the effect of wall size or pore diameter on the Kapitza resistance, temperature profile and density distribution across solid-liquid interfaces and nanofluidic channels applying a combination of wall-wall and wall-fluid molecular dynamics thermal wall model. Investigations included three pore sizes of 5σ, 10σ and 20.5σ at their respective highest and lowest ε_{ww}. The results reveal that the mass and heat transfer is highest in the 5σ, pore, having the lowest ε_{ww}, due to its least resistance in allowing fluid to flow through its pores quickly without bulk-like fluid impediments. The Kapitza resistance is also reported to increase with wall particle vibrational frequency for all values of pore size and ε_{ww}. The highest pore size and wall intermolecular interaction energy strength of 20.5σ and $\varepsilon_{ww} = 0.6$ respectively is seen to have the highest Kapitza resistance at higher wall vibrational frequency. Due to its high Kapitza resistance as a result of its bulk-like layering, inelastic phonon heat transfer is prevalent, propagating in the fluid to form networks with other bulk like layering. The application of this phenomena can lead to the tuning of the Kapitza resistance from imposed properties of a nanomaterial which can increase the figure of merit in space engineering applications, enhancement of computer processors, thermal enhancement in nanofluids, optimization of thermal barrier coatings used in the combustion chamber of propulsion systems, and development of nanofilters for sequestration and desalination.

7.2 Future work

Molecular dynamic simulation gives an insight into the structural properties of fluids that are yet to be attained by experimental studies. MD also gives flexibility, compared to experiments that are found to be very expensive at the nanoscale. As computing power increases, MD will become an important method in the investigation of bulk fluids, and may likely be as popular as the continuum formulation. MD studies in future will involve the detailed and bulk investigation of ionic liquids, pharmaceuticals, bio-materials, dense polymer and composite structures. This will be driven by the need for fundamental understanding of nanoscale phenomena and profits from companies as a result of its successful applications.

For fluids confined in a nanochannel, a bright future is envisaged. As computing power and efficiency increases nanofluidic applications will grow rapidly. Currently commercially applicable molecular dynamic studies have been focused on polymeric-composite-fluids interface and flow of fluid around carbon nanotubes and graphene.

Thermal transport at nanoscale interfaces and nanochannels have also been reported to be relevant to obtain better performance in many Engineering Systems and this is another growing area of research. This is the area of research that is focused on, and investigated in this work. From the literatures reviewed and the research undertaken, the following future work is recommended.

- Applying morse and tersoff pair potentials to study thermal transport and Kapitza resistance across interfaces and nanofluidic channels.
- Developing a meta model that allows for molecular and continuum transition.
- Investigation of phonon propagation and dispersion using particle wave molecular dynamics in understanding thermal transport and Kapitza resistance across interfaces, supperlatices and nanochannels.
- Developing kernels to predict the non-local stress for confined fluids in a nanofluidic channel.
- Determining the shear rate, kinematic viscosity and density variations in nanochannels to aid in better understanding of coupling between energy and momentum transport.

7. Conclusion and Future Work

[1]

[1] This page is intentionally left blank

Bibliography

[1] Dosch, H. and Van de Voorde, M. (2009), "Gennesys", White Paper, A New European Partnership between Nanomaterials Science & Nanotechnology and Synchrotron Radiation and Neuron Facilities, Max-Planck-Insititut für Metalforschung, Stuttgart.

[2] Rapaport, D. C. (2004), "The art of molecular dynamic simulation". (2nd ed), Cambridge University press, United Kingdom.

[3] Dismukes, J., Ekstrom, L., Steigmeier, E., Kudman, I. and Beers, D. (1964), "Thermal and Electrical Properties of Heavily Doped Ge-Si Alloys up to 1300° K", Journal of Applied Physics, vol. 35, no. 10, pp. 2899-2907.

[4] Chen, G., Dresselhaus, M., Dresselhaus, G., Fleurial, J. and Caillat, T. (2003), "Recent developments in thermoelectric materials", International Materials Reviews, vol. 48, no. 1, pp. 45-66.

[5] Ju, Y. and Goodson, K. (1999), "Phonon scattering in silicon films with thickness of order 100 nm", Applied Physics Letters, vol. 74, no. 20, pp. 3005-3007.

[6] Love, M. S., & Anderson, A. C. (1990), "Estimate of phonon thermal transport in amorphous materials above 50 K". Physical review. B, Condensed matter, vol. 42, no.3, pp. 1845-1847.

[7] Escobar, R. A. and Amon, C. H. (2007), "Influence of phonon dispersion on transient thermal response of silicon-on-insulator transistors under self-heating conditions", Journal of heat transfer, vol. 129, no. 7, pp. 790-797.

[8] Landry E., S. (2009), "Thermal Transport by Phonons Across Semiconductor Interfaces, Thin Films, and Superlattices". (Ph.D. thesis). Department of Mechanical Engineering, Carnegie Mellon University.

[9] Duda, John C., Pamela M. Norris, and Patrick E. Hopkins. (2011), "On the Linear Temperature Dependence of Phonon Thermal Boundary Conductance in the Classical Limit." Journal of Heat Transfer, vol.133, no. 7, pp. 074501.

[10] Tully, J. C. (1980), “Dynamics of gas–surface interactions: 3D generalized Langevin model applied to fcc and bcc surfaces”. The Journal of Chemical Physics, vol 73, pp. 1975.

[11] Suzuki, T. O., D (2000), "Intermolecular energy transfer at a solid-liquid interface", Microscale Thermophysical Engineering, vol. 4, no. 3, pp. 189-196.

[12] Huxtable, S. T., Cahill, D. G., Shenogin, S., Xue, L., Ozisik, R., Barone, P., Usrey, M., Strano, M. S., Siddons, G. and Shim, M. (2003), "Interfacial heat flow in carbon nanotube suspensions", Nature materials, vol. 2, no. 11, pp. 731-734.

[13] Xue, L., Keblinski, P., Phillpot, S., Choi, S. and Eastman, J. (2003), "Two regimes of thermal resistance at a liquid–solid interface", The Journal of chemical physics, vol. 118, pp. 337.

[14] Venkatasubramanian, R., Siivola, E., Colpitts, T. and O’quinn, B. (2001), "Thin-film thermoelectric devices with high room-temperature figures of merit", Nature, vol. 413, no. 6856, pp. 597-602.

[15] Sisan, T. B., & Lichter, S. (2011). The end of nanochannels. Microfluidics and nanofluidics, 11(6), 787-791.

[16] Preston, G. M., Carroll, T. P., Guggino, W. B., & Agre, P. (1992), “Appearance of water channels in Xenopus oocytes expressing red cell CHIP28 protein”. Science, vol. 256, no.5055, pp. 385-387.

[17] Hummer, G., Rasaiah, J. C., & Noworyta, J. P. (2001), “Water conduction through the hydrophobic channel of a carbon nanotube”. Nature, vol.414, no.6860, pp.188-190.

[18] Thomas, J. A., & McGaughey, A. J. (2008), “Reassessing fast water transport through carbon nanotubes”. Nano letters, vol.8, no.9, pp.2788-2793.

[19] Holt, J. K., Park, H. G., Wang, Y., Stadermann, M., Artyukhin, A. B., Grigoropoulos, C. P., ... & Bakajin, O. (2006), “Fast mass transport through sub-2-nanometer carbon nanotubes”. Science, vol.312, no.5776, pp.1034-1037.

[20] Kalweit, M. (2008), “Molecular Modelling of meso and Nanoscale Dynamics”.(Phd Aerospace Sciences thesis), School of Engineering, Cranfield.

[21] Kim, B. H., Beskok, A. and Cagin, T. (2008), "Thermal interactions in nanoscale fluid flow: molecular dynamics simulations with solid–liquid interfaces", Microfluidics and Nanofluidics, vol. 5, no. 4, pp. 551-559.

[22] Murad, S. and Puri, I. K. (2008), "Thermal transport across nanoscale solid-fluid interfaces", Applied Physics Letters, vol. 92, no. 13, pp. 133105-133105-3.

[23] Murad, S. and Puri, I. K. (2008), "Molecular simulation of thermal transport across hydrophilic interfaces", Chemical Physics Letters, vol. 467, no. 1, pp. 110-113.

[24] Murad, S. and Puri, I. K. (2009), "Thermal transport through a fluid–solid interface", Chemical Physics Letters, vol. 476, no. 4, pp. 267-270

[25] Carlborg, C. F., Shiomi, J. and Maruyama, S. (2008), "Thermal boundary resistance between single-walled carbon nanotubes and surrounding matrices", Physical review B, vol. 78, no. 20, pp. 205406.

[26] Konatham, D. and Striolo, A. (2009), "Thermal boundary resistance at the graphene-oil interface", Applied Physics Letters, vol. 95, no. 16, pp. 163105-163105-3.

[27] Shenogina, N., Godawat, R., Keblinski, P. and Garde, S. (2009), "How wetting and adhesion affect thermal conductance of a range of hydrophobic to hydrophilic aqueous interfaces", Physical Review Letters, vol. 102, no. 15, pp. 156101.

[28] Ge, Z., Cahill, D. G. and Braun, P. V. (2006), "Thermal conductance of hydrophilic and hydrophobic interfaces", Physical Review Letters, vol. 96, no. 18, pp. 186101.

[29] Liu, Q., Jiang, P. and Xiang, H. (2010), "Molecular dynamics simulation of thermal conductivity of an argon liquid layer confined in nanospace", Molecular Simulation, vol. 36, no. 13, pp. 1080-1085.

[30] Xue, L., Keblinski, P., Phillpot, S., Choi, S. and Eastman, J. (2004), "Effect of liquid layering at the liquid–solid interface on thermal transport", International Journal of Heat and Mass Transfer, vol. 47, no. 19, pp. 4277-4284.

[31] Liang, Z. and Tsai, H. (2011), "Thermal conductivity of interfacial layers in nanofluids", Physical Review E, vol. 83, no. 4, pp. 041602.

[32] Klein, M. L., & Shinoda, W. (2008). "Large-scale molecular dynamics simulations of self-assembling systems". Science, vol. 321, no. 5890, pp. 798-800.

[33] Peter, Brian J., Helen M. Kent, Ian G. Mills, Yvonne Vallis, P. Jonathan G. Butler, Philip R. Evans, and Harvey T. McMahon. (2004) "BAR domains as sensors of membrane curvature: the amphiphysin BAR structure." Science vol. 303, no. 5657, PP. 495-499.

[34] Markvoort, A., Hilbers, P. and Nedea, S. (2005), "Molecular dynamics study of the influence of wall-gas interactions on heat flow in nanochannels", Physical review E, vol. 71, no. 6, pp. 066702.

[35] Ohara, T. and Torii, D. (2005), "Molecular dynamics study of thermal phenomena in an ultrathin liquid film sheared between solid surfaces: The influence of the crystal plane on energy and momentum transfer at solid-liquid interfaces", Journal of Chemical Physics, vol. 122, no. 21, pp. 214717-214717.

[36] Hu, M., Michel, B. and Poulikakos, D. (2011), "Surface functionalization mechanisms of enhancing heat transfer at solid-liquid interfaces", Journal of Heat Transfer, vol. 133, pp. 082401-082401

[37] Yamamoto, K., Takeuchi, H. and Hyakutake, T. (2006), "Characteristics of reflected gas molecules at a solid surface", Physics of Fluids, vol. 18, pp. 046103.

[38] Cieplak, M., Koplik, J. and Banavar, J. R. (2001), "Boundary conditions at a fluid-solid interface", Physical Review Letters, vol. 86, no. 5, pp. 803-806.

[39] Dadzie, S. K. and Méolans, J. G. (2004), "Anisotropic scattering kernel: generalized and modified Maxwell boundary conditions", Journal of Mathematical Physics, vol. 45, pp. 1804.

[40] Cercignani, C. and Lampis, M. (1971), "Kinetic models for gas-surface interactions", Transport Theory and Statistical Physics, vol. 1, no. 2, pp. 101-114.

[41] Lord, R. (1991), "Some extensions to the Cercignani–Lampis gas–surface scattering kernel", Physics of Fluids A: Fluid Dynamics, vol. 3, pp. 706.

[42] Nguyen, T. X., Cohaut, N., Bae, J. and Bhatia, S. K. (2008), "New method for atomistic modeling of the microstructure of activated carbons using hybrid reverse Monte Carlo simulation", Langmuir, vol. 24, no. 15, pp. 7912-7922.

[43] Thompson, P. A. and Robbins, M. O. (1990), "Shear flow near solids: Epitaxial order and flow boundary conditions", Physical Review A, vol. 41, no. 12, pp. 6830.

[44] Koplik, J., Banavar, J. R. and Willemsen, J. F. (1989), "Molecular dynamics of fluid flow at solid surfaces", Physics of Fluids A: Fluid Dynamics, vol. 1, pp. 781.

[45] Neto, C., Evans, D. R., Bonaccurso, E., Butt, H. and Craig, V. S. (2005), "Boundary slip in Newtonian liquids: a review of experimental studies", Reports on Progress in Physics, vol. 68, no. 12, pp. 2859.

[46] Bocquet, L. and Barrat, J. (2007), "Flow boundary conditions from nano-to micro-scales", Soft Matter, vol. 3, no. 6, pp. 685-693.

[47] Arab, M., F. Picaud, M. Devel, C. Ramseyer, and C. Girardet. (2004), "Molecular selectivity due to adsorption properties in nanotubes." Physical Review B, vol. 69, no. 16, pp. 165401.

[48] Drikakis, D., & Asproulis, N. (2010), "Multi-scale computational modelling of flow and heat transfer. International Journal of Numerical Methods for Heat & Fluid Flow", vol. 20, no.5, pp. 517-528.

[49] Asproulis, N., & Drikakis, D. (2013), "An artificial neural network-based multiscale method for hybrid atomistic-continuum simulations". Microfluidics and nanofluidics, vol.15, no. 4, pp. 559-574.

[50] Yang, W., Wei, D., Jin, X., & Liao, Q. (2007), "Molecular dynamics simulation of the formation of polymer networks. Macromolecular theory and simulations", vol.16, no.5, pp. 548-556.

[51] Asproulis, N., & Drikakis, D. (2011), "Wall-mass effects on hydrodynamic boundary slip". Physical Review E, vol.84, no.3, pp. 031504.

[52] Espinosa, S., Asproulis, N., & Drikakis, D. (2014), "Chemotherapy efficiency increase via shock wave interaction with biological membranes: a molecular dynamics study". Microfluidics and Nanofluidics, vol.16, no. 4, pp. 613-622.

[53] McGaughey, A. J., & Kaviany, M. (2004), "Quantitative validation of the Boltzmann transport equation phonon thermal conductivity model under the single-mode relaxation time approximation". Physical Review B, vol.69, no.9, pp. 094303.

[54] Barrat, J. L., & Chiaruttini, F. (2003), "Kapitza resistance at the liquid—solid interface". Molecular Physics, vol.101, no.11, pp. 1605-1610.

[55] Kim, B. (2012), "Thermal resistance at a liquid–solid interface dependent on the ratio of thermal oscillation frequencies". Chemical Physics Letters, vol.554, pp. 77-81.

[56] Katok, A., & Hasselblatt, B. (1995), "Introduction to the modern theory of dynamical systems". Cambridge, Cambridge.

[57] Khinchin, A. I. (1949), "Mathematical foundations of statistical mechanics". Courier Dover Publications.

[58] Dettmann, C. P., & Cohen, E. G. D. (2000), "Microscopic chaos and diffusion. Journal of Statistical Physics", vol.101, no.3-4, pp.775-817.

[59] Cecconi, F., Cencini, M., & Vulpiani, A. (2007), “Transport properties of chaotic and non-chaotic many particle systems. Journal of Statistical Mechanics: Theory and Experiment”, vol.2007, no.12, P12001.

[60] Bernardi, Stefano, et al. (2012), "Ergodicity of a single particle confined in a nanopore." Journal of Statistical Physics, vol.148, no.6, pp. 1156-1169.

[61] Donev, Aleksandar, Salvatore Torquato, and Frank H. Stillinger. (2005), "Pair correlation function characteristics of nearly jammed disordered and ordered hard-sphere packings." Physical Review E, vol. 71, no. 1, pp. 011105.

[62] Kalyuzhnyi, Yu V., S. T. Cui, P. T. Cummings, and H. D. Cochran. (1999), "Distribution functions of a simple fluid under shear: Low shear rates." Physical Review E, vol. 60, no. 2, pp. 1716.

[63] Evans, D. J., & Morriss, G. P. (2007), “Statistical mechanics of nonequilibrium liquids”. Anu E Press.

[64] Zhao, H. and Freund, J. (2004), "Lattice-dynamical calculation of phonon scattering at ideal Si–Ge interfaces", Journal of Applied Physics, vol. 97, no. 2, pp. 024903.

[65] Wang, J. and Wang, J. (2007), "Characteristics of phonon transmission across epitaxial interfaces: a lattice dynamic study", Journal of Physics: Condensed Matter, vol. 19, no. 23, pp. 236211.

[66] Pettersson, S. and Mahan, G. (1990), "Theory of the thermal boundary resistance between dissimilar lattices", Physical Review B, vol. 42, no. 12, pp. 7386.

[67] Kimmer, C., Aubry, S., Skye, A. and Schelling, P. K. (2007), "Scattering of phonons from a high-energy grain boundary in silicon: Dependence on angle of incidence", Physical Review B, vol. 75, no. 14, pp. 144105.

[68] Nan, Ce-Wen, and R. Birringer. (1998), "Determining the Kapitza resistance and the thermal conductivity of polycrystals: A simple model." Physical Review B, vol. 57, no.14, pp. 8264.

[69] Simons, S. (1974), "On the thermal contact resistance between insulators", Journal of Physics C: Solid State Physics, vol. 7, no. 22, pp. 4048.

[70] Chen, G. (2003), "Diffusion–transmission interface condition for electron and phonon transport", Applied Physics Letters, vol. 82, no. 6, pp. 991-993.

[71] Hamilton, J. D. (1994). “Time series analysis”, (Vol. 2). Princeton: Princeton university press.

[72] Wang, J. (2010), “Key issues of classical molecular dynamics simulation”. Lambert Academic Publishing, Berlin.

[73] Glattli, A; Daura,X; VanGunstrene, F.W.(2002), “Derivation of an improved simple charge model for liquid water: SPC/A &SPC/L”. Journal of chemical Physics. Vol. 116. No.22. pp.9812-

9827.

[74] Walser, R., Mark, E and van Gunsteren, W.F. (2000), “Comparison of different schemes to treat long-range electrostatic interactions in molecular dynamics simulations of a protein crystal”. J.med.chem., Vol.44, pp.1530-1539.

[75] Levitt,M; Hirshberg,M; Sharon,R; Laidig, K.W; Dagget, V. (1997), “Calibration and Testing of a water model for simulation of the molecular dynamics of protiens and nucleic acids in solution”. Journal of Phys.Chem B, Vol. 101, No.25.

[76] Mark, P and Nilsson, L. (2001), “Structure and dynamics of the TIP3P,SPC and SPC/E water models at 298K. J.Phys.Chem.A, Vol.105, No.43, pp.9954-9959.

[77] Mahoney, W. M and Jorgensen, L.M. (2001), “Quantum, intramolecular flexibility, and polarizability effects on the reproduction of the density anomaly of liquid water by simple potential functions ”. J.Chem.Phys., Vol.115, No.23, pp.10758-10768.

[78] Takeuchi, H. (2008), “Development of an efficient geometry optimization method for water clusters”. J.Chem.Inf.model. Vol.48, No. 11, pp.2226-2233.

[79] Van der Spoel,D., Van Maaren, P.J and Berendsen, J.C. (1998), “A systematic study of water models for molecular simulation: Derivation of water models optimized for use with a reaction field”. Journal of chemical physics Vol.108. No. 24. pp.10220-10230.

[80] Falcioni, M., Isola, S., & Vulpiani, A. (1990), “Correlation functions and relaxation properties in chaotic dynamics and statistical mechanics” . Physics Letters A, vol.144, no.6, pp. 341-346.

[81] Gan, H. H., & Eu, B. C. (1992), “Theory of the nonequilibrium structure of dense simple fluids: Effects of shearing”. Physical Review A, vol.45, no.6, pp. 3670.

[82] Lue, L. and Evans, D. J. (2000), "Configurational temperature for systems with constraints", Physical Review E, vol. 62, no. 4, pp. 4764.

[83] Delhommelle, J. and Evans, D. J. (2001), "Configurational temperature thermostat for fluids undergoing shear flow: application to liquid chlorine", Molecular Physics, vol. 99, no. 21, pp. 1825-1829.Delhommelle, J., [84] Petravic, J. and Evans, D. J. (2003), "Reexamination of string phase and shear thickening in simple fluids", Physical Review E, vol. 68, no. 3, pp. 031201.

[85] Braga, C. and Travis, K. P. (2006), "Configurational constant pressure molecular dynamics", The Journal of chemical physics, vol. 124, pp. 104102.

[86] Nosé, S. (1984), "A molecular dynamics method for simulations in the canonical ensemble", Molecular Physics, vol. 52, no. 2, pp. 255-268.

[87] Hoover, W. G. (1985), "Canonical dynamics: Equilibrium phase-space distributions", Physical Review A, vol. 31, no. 3, pp. 1695.

[88] Stoner, R., Maris, H., Anthony, T. and Banholzer, W. (1992), "Measurements of the Kapitza conductance between diamond and several metals", Physical Review Letters, vol. 68, no. 10, pp. 1563.

[89] Brooks Iii, C. L., and Martin Karplus. (1983), "Deformable stochastic boundaries in molecular dynamics." The Journal of chemical physics, vol. 79, no. 12, pp. 6312-6325.

[90] Barisik, M. and Beskok, A. (2012), "Boundary treatment effects on molecular dynamics simulations of interface thermal resistance", Journal of Computational Physics, vol. 231, no. 23, pp. 7881-7892.

[91] Shi, Z., Barisik, M. and Beskok, A. (2012), "Molecular dynamics modeling of thermal resistance at argon-graphite and argon-silver interfaces", International Journal of Thermal Sciences, vol. 59, pp. 29-37.

[92] Noid, W. G., Liu, P., Wang, Y., Chu, J. W., Ayton, G. S., Izvekov, S., ... & Voth, G. A. (2008), "The multiscale coarse-graining method. II. Numerical implementation for coarse-grained molecular models". The Journal of chemical physics, vol.128, no.24, pp. 244115.

[93] Maroo, S. C. and Chung, J. (2010), "A novel fluid–wall heat transfer model for molecular dynamics simulations", Journal of Nanoparticle Research, vol. 12, no. 5, pp. 1913-1924.

[94] Pollack, Gerald L. (1969), "Kapitza resistance", Reviews of Modern Physics, vol. 41, no. 1, pp. 48.

[95] Callaway, J. (1959), "Model for lattice thermal conductivity at low temperatures", Physical Review, vol. 113, no. 4, pp. 1046.

[96] Merabia, S. and Termentzidis, K. (2012), "Kapitza thermal conductance at the interface between Lennard-Jones crystals using non-equilibrium molecular dynamics simulations", Journal of Physics: Conference Series, Vol. 395, IOP Publishing, pp. 012115.

[97] Devpura, Patrick E. Phelan, Ravi S. Prasher, Amit. (2001), "Size effects on the thermal conductivity of polymers laden with highly conductive filler particles." Microscale Thermophysical Engineering, vol. 5, no. 3, pp. 177-189.

[98] Ruijie, Z., Yunfei, C. and Meihui, L. (2009), "A Modified Thermal Boundary Resistance Model for FCC Structures".

[99] Swartz, E. T. and Pohl, R. O. (1989), "Thermal boundary resistance", Reviews of Modern Physics, vol. 61, no. 3, pp. 605.

[100] Chalopin, Y. and Volz, S. (2013), "A microscopic formulation of the phonon transmission at the nanoscale", Applied Physics Letters, vol. 103, no. 5, pp. 051602.

[101] Young, D. and Maris, H. (1989), "Lattice-dynamical calculation of the Kapitza resistance between fcc lattices", Physical review B, vol. 40, no. 6, pp. 3685.

[102] Hopkins, P. E., Norris, P. M. and Duda, J. C. (2011), "Anharmonic phonon interactions at interfaces and contributions to thermal boundary conductance", Journal of Heat Transfer, vol. 133, no. 6, pp. 062401.

[103] Li, B., Lan, J. and Wang, L. (2005), "Interface thermal resistance between dissimilar anharmonic lattices", Physical Review Letters, vol. 95, no. 10, pp. 104302.

[104] Plimpton, S. (1995), "Fast parallel algorithms for short-range molecular dynamics", Journal of Computational Physics, vol. 117, no. 1, pp. 1-19.

[105] Tuckerman, D. B., & Pease, R. F. W. (1981), "High-performance heat sinking for VLSI". Electron Device Letters, IEEE, vol.2, no.5, pp. 126-129.

[106] Eastman, J. A., Choi, S. U. S., Li, S., Yu, W., & Thompson, L. J. (2001), "Anomalously increased effective thermal conductivities of ethylene glycol-based nanofluids containing copper nanoparticles". Applied Physics Letters, vol. 78, no.6, pp. 718-720.

[107] Maruyama, Shigeo, and Tatsuto Kimura. (1999), "A study on thermal resistance over a solid-liquid interface by the molecular dynamics method." Therm. Sci. Eng, vol.7. no.1, pp. 63-68.

[108] Maroo, Shalabh C., and J. N. Chung. (2008), "Molecular dynamic simulation of platinum heater and associated nano-scale liquid argon film evaporation and colloidal adsorption characteristics." Journal of colloid and interface science, vol. 328, no.1, pp. 134-146.

[109] Nedea, S. V., et al. (2009), "Heat transfer predictions for micro-/nanochannels at the atomistic level using combined molecular dynamics and Monte Carlo techniques." Journal of Heat Transfer, vol. 131, no.3, pp. 033104.

[110] Pham, An Truong, Murat Barisik, and Bohung Kim. (2014), "Molecular dynamics simulations of Kapitza length for argon-silicon and water-silicon interfaces." International journal of precision engineering and manufacturing, vol.15, no.2, pp. 323-329.

[111] Bernardi, S., Todd, B. and Searles, D. J. (2010), "Thermostating highly confined fluids", The Journal of chemical physics, vol. 132, no. 24, pp. 244706.

[112] Asproulis, Nikolaos, and Dimitris Drikakis, (2010) "Boundary slip dependency on surface stiffness." Physical Review E, vol 81, no. 6, pp. 061503.

[113] Chen, Y., Li, D., Yang, J., Wu, Y., Lukes, J. R. and Majumdar, A. (2004), "Molecular dynamics study of the lattice thermal conductivity of Kr/Ar superlattice nanowires", Physica B: Condensed Matter, vol. 349, no. 1, pp. 270-280.

[114] Stevens, R. J., Zhigilei, L. V. and Norris, P. M. (2007), "Effects of temperature and disorder on thermal boundary conductance at solid–solid interfaces: Nonequilibrium molecular dynamics simulations", International Journal of Heat and Mass Transfer, vol. 50, no. 19, pp. 3977-3989.

[115] Lyeo, H. and Cahill, D. G. (2006), "Thermal conductance of interfaces between highly dissimilar materials", Physical Review B, vol. 73, no. 14, pp. 144301.

[116] Kim, Bo Hung. (2009), "Molecular dynamics simulations of heat transfer in nanoscale liquid films." PhD diss., Texas A&M University.

[117] Priezjev, N. V. (2007), "Effect of surface roughness on rate-dependent slip in simple fluids", The Journal of chemical physics, vol. 127, no. 14, pp. 144708.

[118] Barrat, J. and Hansen, J. (2003), "Basic concepts for simple and complex liquids", Cambridge University Press.

[119] Maiti, A., Mahan, G. and Pantelides, S. (1997), "Dynamical simulations of nonequilibrium processes—heat flow and the kapitza resistance across grain boundaries", Solid State Communications, vol. 102, no. 7, pp. 517-521.

[120] Dames, C. and Chen, G. (2003), "Theoretical phonon thermal conductivity of Si/Ge superlattice nanowires", Journal of Applied Physics, vol. 95, no. 2, pp. 682-693.

[121] Sofos, F. D., Karakasidis, T. E. and Liakopoulos, A. (2009), "Effects of wall roughness on flow in nanochannels", Physical Review E, vol. 79, no. 2, pp. 026305.

[122] Travis, K. P., & Gubbins, K. E. (2000), "Poiseuille flow of Lennard-Jones fluids in narrow slit pores". The Journal of Chemical Physics, vol.112, no.4, pp. 1984-1994.

[123] Kalyuzhnyi, Yu V., S. T. Cui, and H. D. Cochran. (2000), "Distribution functions of a simple fluid under shear. II. High shear rates." Physical Review E, vol. 63, no. 1, pp. 011209.

[124] Cui, S. T., Cummings, P. T., & Cochran, H. D. (2001), "Molecular simulation of the transition from liquidlike to solidlike behavior in complex fluids confined to nanoscale gaps". The Journal of Chemical Physics, vol.114, no.16, pp. 7189-7195.

[125] Li, Jie, and Clement Kleinstreuer. (2008), "Thermal performance of nanofluid flow in microchannels." International Journal of Heat and Fluid Flow, vol.29, no. 4, pp. 1221-1232.

[126] Le, Y., Chen, J. and Wang, W. (2004), "Study on the silica hollow spheres by experiment and molecular simulation", Applied Surface Science, vol. 230, no. 1, pp. 319-326.

[127] Snyder, N. (1970), "Heat transport through helium II: Kapitza conductance", Cryogenics, vol. 10, no. 2, pp. 89-95.

[128] Schelling, P. K., Phillpot, S. R. and Keblinski, P. (2002), "Comparison of atomic-level simulation methods for computing thermal conductivity", Physical Review B, vol. 65, no. 14, pp. 144306.

[129] He, Yuping, and Giulia Galli. (2012), "Microscopic origin of the reduced thermal conductivity of silicon nanowires." Physical review letters, vol.108, no. 21, pp. 215901.

[130] Van den Akker, E. A. T., A. J. H. Frijns, A. A. van Steenhoven, and P. Hilbers. (2008), "Heat transfer between walls and fluids: MD simulations with vibrating walls." In Proceedings of the 1st European Conference on Microfluidics (MicroFlu'08).

2

[2]This page is intentionally left blank

Appendix A

A.1 Derivation of Equations For particle and Wall Motion.

The potential energy describes the interaction between two atoms or molecules in molecular dynamics and the potential energy that has a negative gradient which gives the force and is expressed [130] as

$$F = \frac{\partial v}{\partial r} = -\nabla r(V). \tag{7.2.1}$$

The differential equation of particle position is expressed as

$$\frac{\partial^2 x}{\partial t^2} = \frac{-v(x-y)}{m}, \tag{7.2.2}$$

where m is the mass particle mass, v the potential energy. The wall motion is obtained by the force between the particle and wall including the spring. With spring constant k_w, the differential equation describing the wall position is given as

$$\frac{\partial^2 y}{\partial t^2} = \frac{v^{'}(x-y) - k_w y}{M}, \tag{7.2.3}$$

where m - the mass of wall part exposed to interaction. The second term on the right describes the spring-wall interaction. Initial conditions are expressed as

$$x[0]x_0, x'[0] = v, \frac{k_w}{2}y[0]^2 + \frac{M}{2}y'[0] = E_w y[0]\sqrt{\frac{2E_w}{k_w}cos(\phi)}, \tag{7.2.4}$$

where ϕ describes the initial phase of wall $0 \leq \phi < 2\pi$. This equation solves numerically in 1-D. MD gives the solution for the position, energy and velocity of the solid and particles interacting. If a particle contacts with a non vibrating wall, energy is not exchanged, the outgoing velocities will be equal to the incoming velocity. A situation where particles hit a wall that is vibrating, the outgoing velocity becomes smaller, showing an exchange of energy from the particle wall.

A.2 Exchange of Energy

Three dimensionless parameters can be derived from dimensional analysis

$$\delta = \sqrt{\frac{2E_w}{k_w\sigma^2}}, \tag{7.2.5}$$

and,

$$\lambda = \frac{\frac{1}{2}mv_0^2 + v(x_0)}{k_B T_w}, \tag{7.2.6}$$

also,

$$\mu = \frac{M}{m}, \tag{7.2.7}$$

where δ - dimensionless wall amplitude directly relates to temperature. λ the ratio of energy of wall and particles; μ is mass ratio of particles and wall part involved in interaction. The total energy of particles both potential and kinetic relates to the three dimensionless parameters and is expressed [130] as

$$E_T = E_T(t, \delta, \lambda, \mu, \phi), \tag{7.2.8}$$

where δ, λ, and μ, are three dimensionless parameters,ϕ is the initial phase of wall and t is the time.

Friction at the wall-fluid interface is a very common phenomenon in contact surfaces and the acoustic impedance is sensitive to friction at the surface of the wall. Contacting and interfacial friction gives a resonant shift of frequency f_0 and damping rate shift D. D and f_0 are expressed as

$$f_0 = \frac{1}{2d}\sqrt{\frac{c}{\rho}}; f_0 = \frac{1}{2\pi}\sqrt{\frac{k}{m}}, \tag{7.2.9}$$

$$D = -\frac{\Delta E}{2E_x}, \tag{7.2.10}$$

where ρ, c, and d are density, stiffness and thickness, E is mechanical energy during x-vibration cycle. The friction force for the wall-fluid interface is given as

$$\sigma_{xz} = -\bar{\eta}(v_0 - u_0), \tag{7.2.11}$$

where $\bar{\eta}$- frictional coefficient, v_0 and u_0 - shear velocities of fluid and wall at interface, the term

$\frac{\partial v_s}{\partial z}(v_0 - u_0)$ is the velocity slip. For big friction coefficient, the slip velocity is negligible, which is the same as no-slip condition. The frequency shift and the mass of particles are related with the assumption that the mass is infinitely stiff and can be expressed as

$$\Delta f = \frac{-2f_0}{\sqrt{c\rho}}\Delta m, \tag{7.2.12}$$

where Δf is the frequency shift, Δm is the change in mass and f_0 the resonant frequency of system that is not loaded. When there is a fluid-wall interface the energy of vibration is damped into the fluid from the wall, the damping is due to the transmission of phonons across the wall-fuid interface. For continuum system the wave propagation can be solved by determining (ΔD) damping factor change and (Δf) shift of natural frequency of the wall affecting the fluid. The expression is given as

$$\Delta f = -f_0^{\frac{3}{2}}\sqrt{\frac{\rho_f \eta}{\pi \rho_w c_w}}, \tag{7.2.13}$$

and

$$\Delta D = -2\pi\frac{\Delta f}{f_0}. \tag{7.2.14}$$

The equation for the solid oscillating wall in the y-direction is expressed as

$$M\omega^2 = M\omega_0^2 y + F_t, \tag{7.2.15}$$

where F_t the frictional force, y the wall displacement and M the mass, of wall. ω_0 the resonance frequency at rest, ω the current frequency the equation becomes

$$\Delta\omega_f = \omega - \omega_0 = \frac{F_t}{2M\omega_0 y}. \tag{7.2.16}$$

The shift of frequency $\triangle f$ with rate of damping shift ΔD is split into the real and imaginary parts and is expressed as

$$\triangle f = \frac{Im(\Delta\omega)}{2\pi}, \tag{7.2.17}$$

and

$$\Delta D = \frac{R_e(\Delta\omega)}{f_0}. \tag{7.2.18}$$

Boundary conditions that can consider inertia of density distribution in the 1^{st} layer of fluid and

Kapitza length models can be integrated into the equations which are expressed as

$$\frac{\Delta f}{f_0} = -\frac{1}{2z}\sqrt{\frac{\rho_f \eta_d \omega}{2}}, \tag{7.2.19}$$

and

$$\frac{\Delta D}{2\pi} = \frac{1}{2z}\sqrt{\frac{\rho_f \eta_d \omega}{2}}, \tag{7.2.20}$$

with the ratio of frequency shift $\frac{\Delta f}{f_0}$ with daamping shift $\frac{\Delta D}{2\pi}$ expressed as

$$\frac{\Delta D}{2\pi} - \left|\frac{\Delta f}{f_0}\right| = \frac{1}{\pi z}\sqrt{\frac{\rho_f \eta_d \omega}{2}}. \tag{7.2.21}$$

These resonators can be divided into the spring model and shear wave model.

The spring mode is expressed as

$$z = \sqrt{km}, \tag{7.2.22}$$

and

$$f_0 = \frac{1}{2\pi}\sqrt{\frac{k}{m}}, \tag{7.2.23}$$

and

$$\frac{\Delta f}{f_0} = \frac{-1}{2z}\sqrt{\frac{\rho_f \eta_f \omega}{2}}, \tag{7.2.24}$$

gives

$$\Delta D = -2\pi\frac{\Delta f}{f_0}, \tag{7.2.25}$$

the shear-wave model is expressed as

$$z = \sqrt{c\rho}, \tag{7.2.26}$$

and

$$f_0 = \frac{1}{2d}\sqrt{\frac{c}{\rho}}, \tag{7.2.27}$$

and

$$\frac{\Delta f}{f_0} = \frac{1}{\pi z}\sqrt{\frac{\rho_f \eta_f \omega}{2}}, \tag{7.2.28}$$

gives

$$\Delta D = -2\pi \frac{\Delta f}{f_0}, \tag{7.2.29}$$

where Z - the impedance, f_0 the resonant frequency, Δf the frequency shift, ΔD the rate of damping, c the modulus(shear), ρ density, η_f viscosity of fluid, k the spring constant, m the mass of solid and ω the angular frequency.

3

[3]This page is intentionally left blank

Appendix B

B.1 LAMMPS CODE FOR NANOCHANNEL

dimension 3

boundary p s p

atom_style atomic neighbor 0.3 bin neigh_modify delay 5

create geometry

#lattice fcc 4.0 orient x 0 -1 1 orient y 1 1 1 orient z -2 1 1 #region box block 0 12.0 0 20.0 0 4.0 #units box

lattice fcc 4.0 region box block 0 16.83 0 23.5 0 17.007 #units box

create_box 2 box

#regions

region 1 block INF INF 0.0 1.0 INF INF #units box

region 2 block 0.2 16.5 1.5 22.0 0.2 17.0 #units box

region 3 block INF INF 22.5 23.5 INF INF #units box

region 1a block INF INF 0.0 0.5 INF INF #units box

region 1b block INF INF 0.5 1.0 INF INF #units box

region 1c block INF INF 0.5 1.0 INF INF #units box

3c block INF INF 23.0 23.5 INF INF #units box

#create_atoms

#lattice fcc 4.0 orient x 0 -1 1 orient y 1 1 1 orient z -2 1 1

lattice custom 4.0 a1 0.707106 0 0 a2 0.353553 0.577305 0.61237343 a3 0.353553 0 0.61237343 basis 0 0 0 # sosto

create_atoms 1 region 1

create_atoms 1 region 3

lattice fcc 0.81 create_atoms 2 region 2

mass 1 1.0

mass 2 1.0

group lower region 1

group upper region 3

group lower1 region 1a

group upper3 region 3c

LJ potentials

pair_style hybrid lj/cut 2.2

pair_coeff 1 1 none # wall-wall

pair_coeff 2 2 lj/cut 1.0 1.0 2.2 # fluid-fluid

pair_coeff 1 2 lj/cut 0.2 1.0 2.2 # wall-fluid

compute mobile all temp velocity all create 1.0 482748 temp mobile

compute newtemp flow temp/partial 0 0 1

fix 1 all nve

fix templwal11 lower1 temp/rescale 10 1.2 1.2 0.02 1.0 fix templwal12 lower2 temp/rescale 10 1.2 1.2 0.02 1.0

fix templwal2b2 upper2 temp/rescale 10 1.3 1.3 0.02 1.0 fix templwal3b2 upper3 temp/rescale 10 1.3 1.3 0.02 1.0

compute ke flow ke/atom

variable temp atom c_ke/1.5

compute 3d flow temp

thermo 50000

#Run

timestep 0.001

thermo 500000

run 40000000

fix c1an flow ave/spatial 1 40000000 40000000 y lower 0.025 density/number vy v_temp units reduced file dens.profile run 40000000

B.2 C^{++} CODES FOR THERMAL WALL MODEL

```
#include "stdlib.h"
    #include "string.h"
    #include "fix_disp_wall.h"
    #include "atom.h"
    #include "domain.h"
    #include "comm.h"
    #include "error.h"
    #include "math.h"
    #include "update.h"
    #include "math.h"
    #include "region.h"
    #include "force.h"
    using namespace LAMMPS_NS;
    /* ———————————————————————————————- */
    FixDispWall::FixDispWall(LAMMPS *lmp, int narg, char **arg) : Fix(lmp, narg, arg) {
    //if (narg < 3) error->all("Illegal fix freq/wall command");
    int *type = atom->type; double *mass = atom->mass; double **v = atom->v; double **x =
atom->x; int *mask = atom->mask; int nlocal = atom->nlocal;
    // MPI_Status status; // MPI_Request request; MPI_Comm_rank(world,&me);
    nevery =atoi(arg[3]); nprint =atoi(arg[4]); iregion = domain->find_region(arg[5]);
    Region *region = domain->regions[iregion];
    sizeWall=0; for (int i = 0; i < nlocal; i++) { if(mask[i] & groupbit) { if(region->match(x[i][0],x[i][1],x[i][2]))
{ sizeWall++; } } } velWall= (double *) malloc(nlocal*sizeof(double)); velWall_prev= (dou-
ble *) malloc(nlocal*sizeof(double)); yinit=(double *) malloc(nlocal*sizeof(double)); /* if (size-
Wall!=0) { velWall= (double *) malloc(sizeWall*sizeof(double)); velWall_prev= (double *) mal-
loc(sizeWall*sizeof(double)); //num_freq=(double *) malloc(sizeWall*sizeof(double)); printf("brika
poia exoun proc=%d\n",comm->me); } else //there is a possibility that some proc don't have
wall particles { velWall= (double *) malloc(2*sizeof(double)); velWall_prev= (double *) mal-
loc(2*sizeof(double)); //num_freq=(double *) malloc(2*sizeof(double)); printf("brika poia den
exoun proc=%d\n",comm->me); } */ for (int i = 0; i < nlocal; i++) // if(mask[i] & groupbit) {
velWall[i]=v[i][1]; velWall_prev[i]=v[i][1]; yinit[i]=x[i][1]; }
    if (me==0) pFile = fopen("frequency.txt", "a+"); freqTot=0; dispTot=0;
```

```
MPI_Barrier (world); // printf("bgeno apo constructor\n"); // MPI_Barrier (world);
}
FixDispWall::~FixDispWall() { // printf("Eimai se destructor\n"); if (me == 0) fclose(pFile);
} /* ---------------------------------------------------------- */
int FixDispWall::setmask() {
// printf("eimai se set of mask\n"); int mask = 0; mask |= FixConst::END_OF_STEP; //
printf("bgeno apo set of mask\n");
return mask; }
/* void FixFreqWall::setup(int vflag) { printf("eimai se set up\n"); end_of_step(); } */
/* ---------------------------------------------------------- */ void FixDispWall::end_of_step()
{
//if(update->ntimestep % nevery != 0) return;
double **x = atom->x; double **v = atom->v; int *mask = atom->mask; int nlocal = atom-
>nlocal; double dtv=update->dt; //double freqTot; int freqTotSum; int sizeWallSum; double
meanfreq; double dispTotSum; double meandisp; double t_collision, lam,t_collision1,cm; int j;
Region *region = domain->regions[iregion];
// printf("exo mpei se end of step proc=%d\n",comm->me); //MPI_Barrier (world);
j=0; //Add the number of sign changes in the y component of the velocity
for (int i = 0; i < nlocal; i++) { if(mask[i] & groupbit) { if(region->match(x[i][0],x[i][1],x[i][2]))
{
//velWall[i]=v[i][1]; if (v[i][1]*velWall_prev[i] < 0) { //num_freq[i]++; freqTot++; dispTot+=fabs(yinit[i]-
x[i][1]); //printf("Coordinates: %f, %f, %f \n", x[i][0], x[i][1], x[i][2]); //printf("Brika kati\n");
//prepei na metrisoume poses fores prostithetai gia na to diairesoume meta ! }
velWall_prev[i]=v[i][1]; } } }
//Write every 10.000 time-steps the averadge number (per atom) of epanalipseon
freqTotSum=0; sizeWallSum=0; MPI_Allreduce(&freqTot,&freqTotSum,1,MPI_INT,MPI_SUM,world);
MPI_Allreduce(&sizeWall,&sizeWallSum,1,MPI_INT,MPI_SUM,world); MPI_Allreduce(&dispTot,&dispTotSum,1,
if (me==0) { meanfreq=freqTotSum / (2*sizeWallSum*nprint*update->dt); meandisp=dispTotSum/(freqTotSum*size
lam=1/(sqrt(2)*0.81*3.14); cm=sqrt((2.0*force->boltz*1.1)/atom->mass[2]); t_collision=0.5*lam*sqrt(atom-
>mass[2]/(force->boltz*1.1)); t_collision1=(sqrt(3.14)*lam)/(2*cm); fprintf(pFile,"%10d %10d
%5g %5e %10d %5g %5g %5g\n",update->ntimestep, freqTotSum, meanfreq, meandisp, sizeWall-
Sum,t_collision,t_collision1,1/meanfreq); fflush(pFile); } freqTot=0; dispTot=0; }
//MPI_Barrier (world); // printf("Teleiosa apo end of step proc=%d\n",me);
}*/
```

B.3 GRAPHS OF VARIOUS EWW AND EWF FOR 10σ CHANNEL SIZE

ifdef FIX_CLASS

FixStyle(gridanalysis, FixGridAnalysis)

#else

#ifndef LMP_FIX_GRID_ANALYSIS_B_H #define LMP_FIX_GRID_ANALYSIS_B_H

#include "fix.h"

namespace LAMMPS_NS { //
// definitions //
#define GRIDANALYSIS_MAX_STRING_LEN 128 #define GRIDANALYSIS_NUM_MQS 17
// number of macroscopic quantities #define GRIDANALYSIS_MEM_RESERVE 1000 // memory reserve for local arrays #define GRIDANALYSIS_MAX_CELL.

// // class FixGridAnalysis //
class FixGridAnalysis : public Fix { private: // local types struct TTensor { Memory* memory;
// pointer for memory class int m_size; //total size = res[0]*res[1]*res[2] double* xx, * xy, * xz;
double* yx, * yy, * yz; double* zx, * zy, * zz;

TTensor(Memory* cmemory); ~TTensor(); void AllocMemory(int nsize, char* szField); void FreeMemory(); void SetZero(); void AddTensor(TTensor& t2); void MulScalar(double f); };

struct TData { Memory* memory; // pointer for memory class

// 3D arrays for the cell values double* num; // number of atoms double* mass; // cell mass double* numdens; // number density double* dens; // density double* px, * py, * pz; // translational momentum double* vx, * vy, * vz; // translationel velocity double* lx, * ly, * lz; // angular momentum double* wx, * wy, * wz; // angular velocity double* ekin_tot; // total kinetic energy double* ekin_trans; // translational kinetic energy double* ekin_rot; // rotational kinetic energy double* ekin_int; // internal kinetic energy double* epot; // potential energy double* etot; // potential energy double* T; // temperature double* P; // pressure TTensor PT; // pressure tensor

//auxiliary variables TTensor it;// inertia tensor //functions TData(Memory* cmemory); ~TData(); void AllocMemory(int nsize, int* aiMQs); void FreeMemory(); void SetZero(int nsize); //sets everything to zero }; struct TIndex{int x,y,z;}; struct TIndexCW // index for cell weighting { int nC; //cell index int nMirror; // bit coding for mirror x:0, y:1, z:2 double f; };

public: // public functions FixGridAnalysis(class LAMMPS *, int, char **); ~FixGridAnaly-

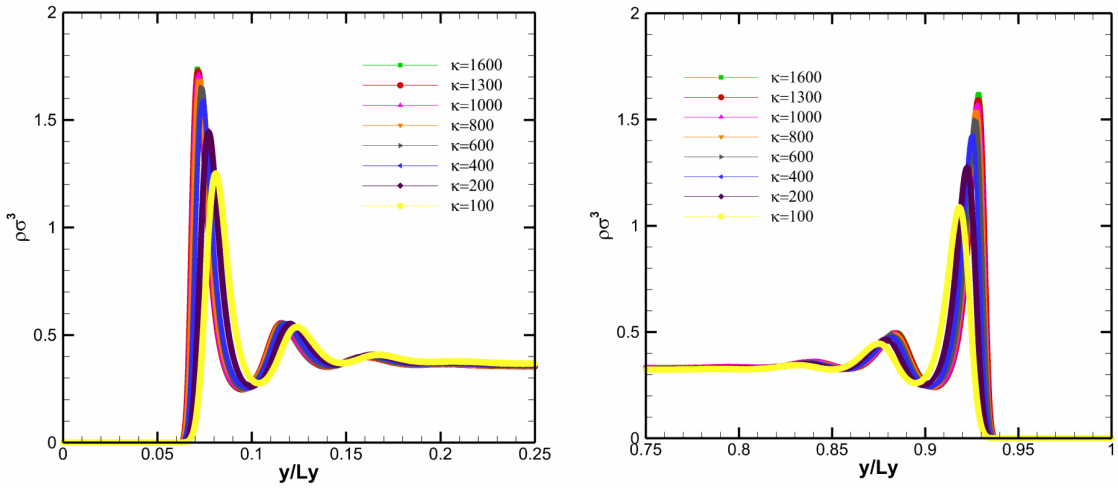

a) Lower wall b)Upper wall

Figure 7.1: Density Profiles of fluid for *pore* size $= 10\sigma$, $m_w = 2m$, $e_{ww} = 0.2$,$e_{ww} = 0.4$ for various values of stiffness constant κ.

sis(); int modify_param(int, char **); int setmask(); //void init(); void end_of_step();

private: // private functions void FillAtomCellArray(); void FillAtomCellArray_NGP(); void FillAtomCellArray_CIC(); inline int GetCellIndex(int I, int J, int K); inline void GetCellIndexInv(int nC, int& I, int& J, int& K); inline void Apply_pbc(double* x_in, double* x_out); void GetDomainInfo(); inline void GetMirroredPosition(double* xo, double* xm); inline double GetMirroredX(double xo); inline double GetMirroredY(double yo); inline double GetMirroredZ(double zo); void CalcInstantData(); void SumUpAverageData(); void AverageData(); void PrintFileHeader(); // print grid file header void PrintFileZone(); // print grid file zone void PrintCellValueFileHeader(int nCV); //print cell value file header void PrintCellValues(); // print cell value file values void PrintMQofCell(TData& data, FILE* pFile, int nI, int nJ, int nK, int nColWidth); // print the MQs of cell nI, nJ, nK

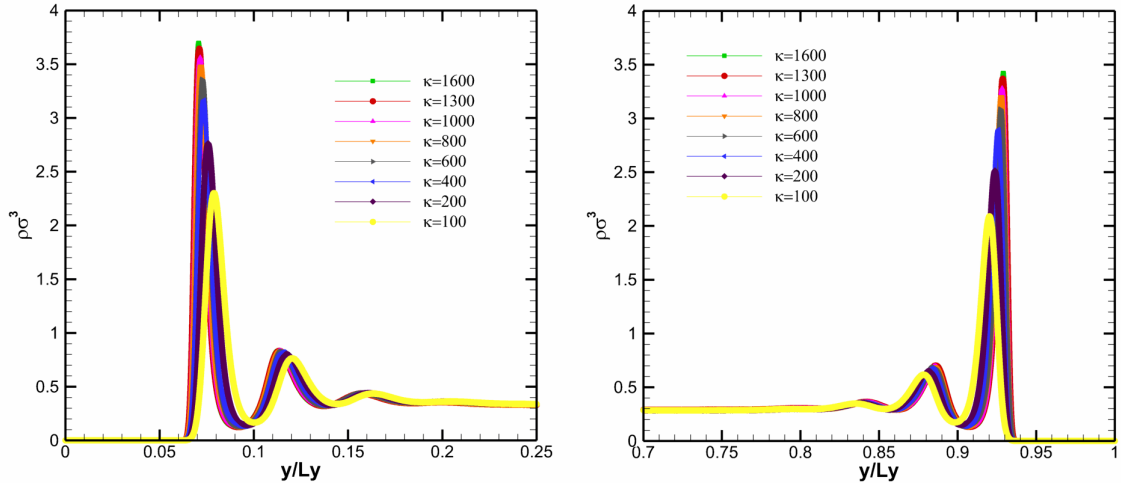

a) Lower wall b)Upper wall

Figure 7.2: Density Profiles of fluid for *pore* size $= 10\sigma$, $m_w = 2m$, $e_{ww} = 0.2$,$e_{ww} = 0.8$ for various values of stiffness constant κ.

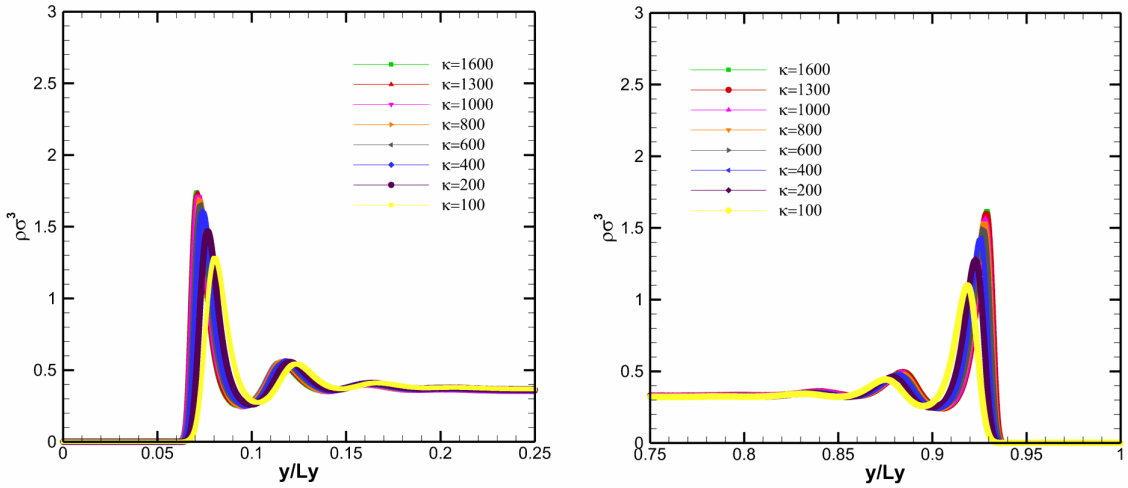

a) Lower wall b)Upper wall

Figure 7.3: Density Profiles of fluid for *pore* size $= 10\sigma$, $m_w = 2m$, $e_{ww} = 0.4$,$e_{ww} = 0.4$ for various values of stiffness constant κ.

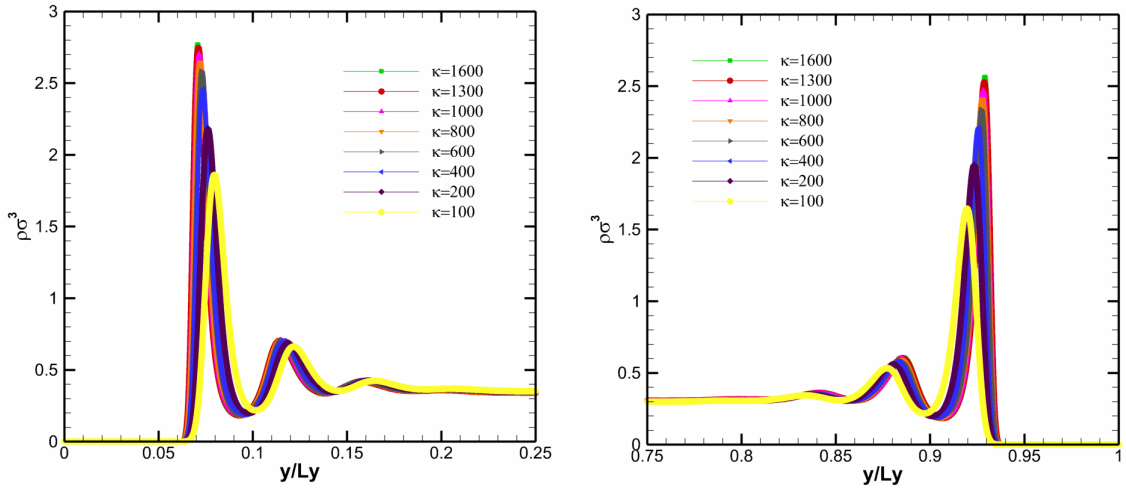

a) Lower wall b)Upper wall

Figure 7.4: Density Profiles of fluid for *pore* size = 10σ, $m_w = 2m$, $e_{ww} = 0.4$,$e_{ww} = 0.6$ for various values of stiffness constant κ.

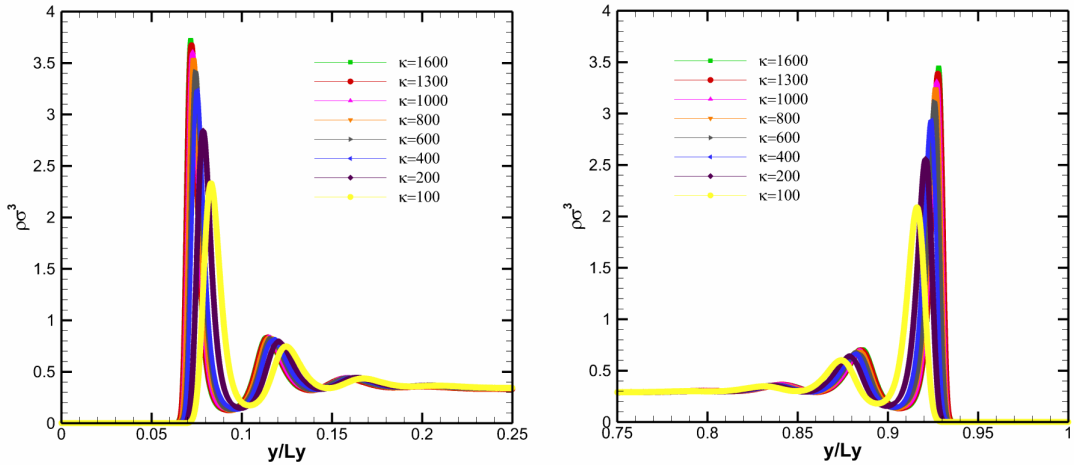

a) Lower wall b)Upper wall

Figure 7.5: Density Profiles of fluid for *pore* size = 10σ, $m_w = 2m$, $e_{ww} = 0.6$,$e_{ww} = 0.8$ for various values of stiffness constant κ.

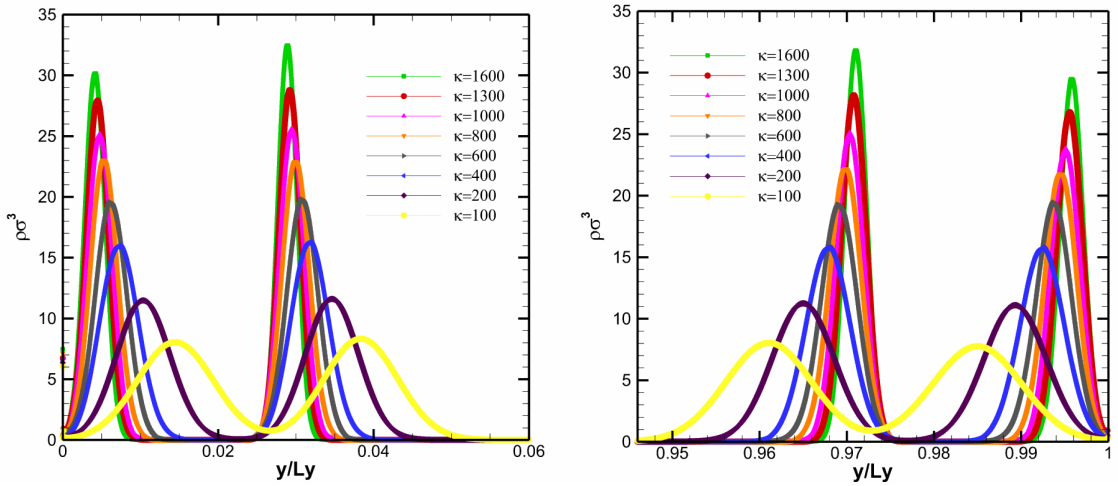

a) Lower wall b)Upper wall

Figure 7.6: Density Distribution in Solid Wall for $m_w = 2m$, $e_{ww} = 0.2$,$e_{ww} = 0.4$ for various values of stiffness constant κ.

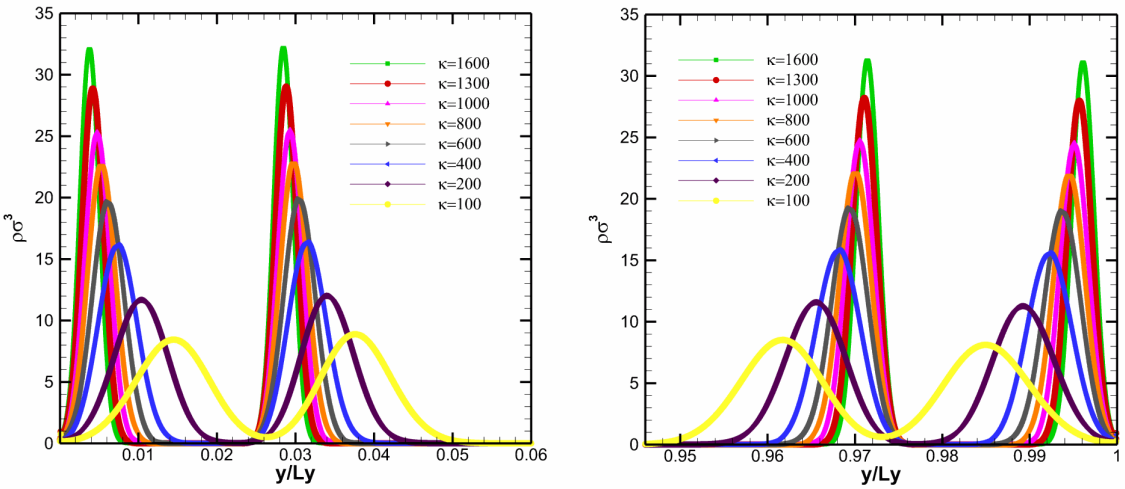

a) Lower wall b)Upper wall

Figure 7.7: Density Distribution in Solid Wall for $m_w = 2m$, $e_{ww} = 0.2$,$e_{ww} = 0.6$ for various values of stiffness constant κ.

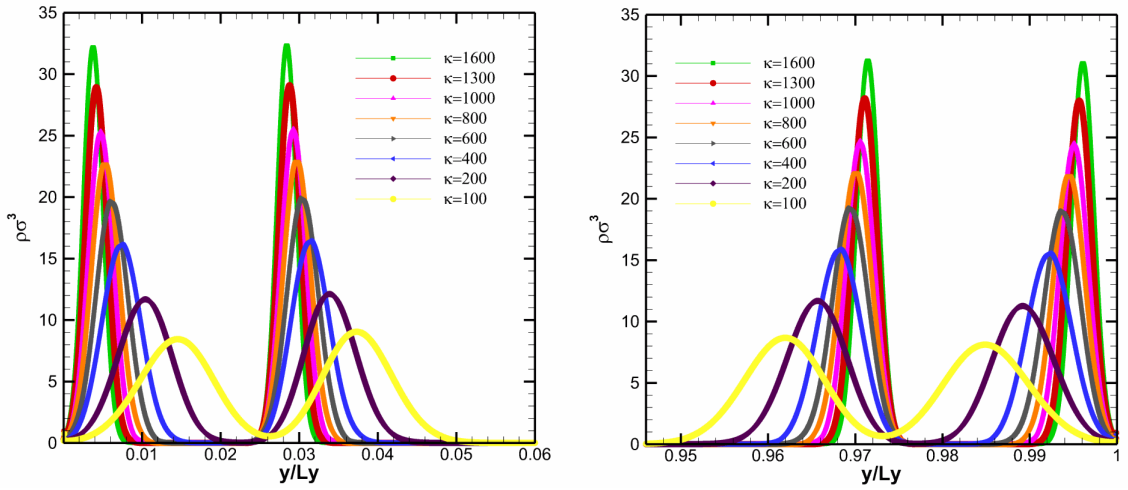

a) Lower wall b)Upper wall

Figure 7.8: Density Distribution in Solid Wall for $m_w = 2m$, $e_{ww} = 0.2$,$e_{ww} = 0.8$ for various values of stiffness constant κ.

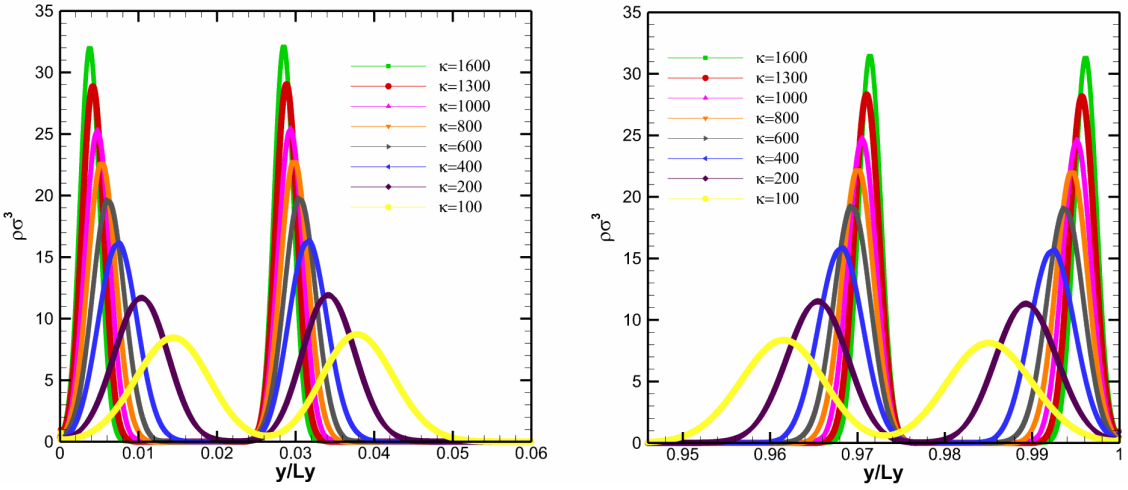

a) Lower wall b)Upper wall

Figure 7.9: Density Distribution in Solid Wall for $m_w = 2m$, $e_{ww} = 0.4$,$e_{ww} = 0.4$ for various values of stiffness constant κ.

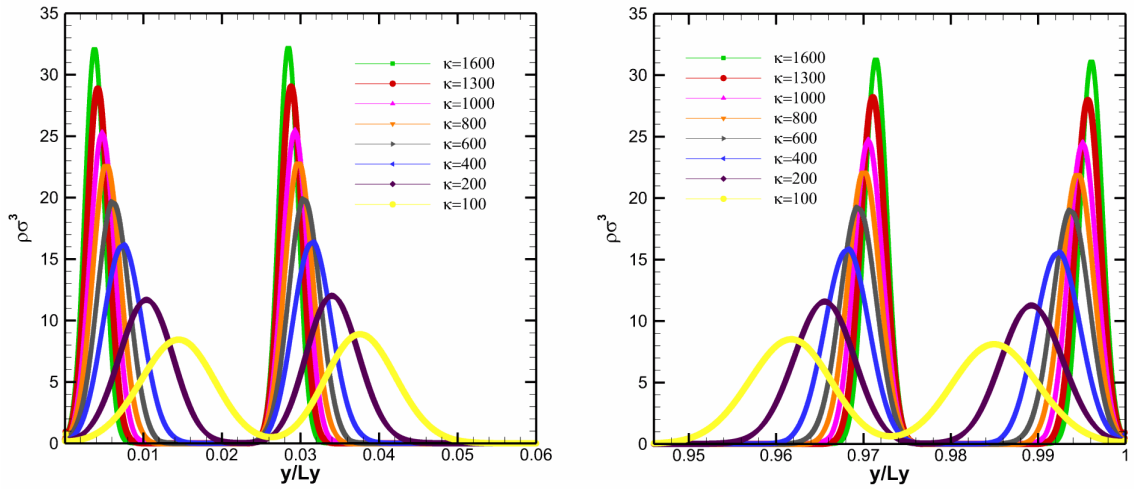

a) Lower wall b)Upper wall

Figure 7.10: Density Distribution in Solid Wall for $m_w = 2m$, $e_{ww} = 0.4$,$e_{ww} = 0.6$ for various values of stiffness constant κ.

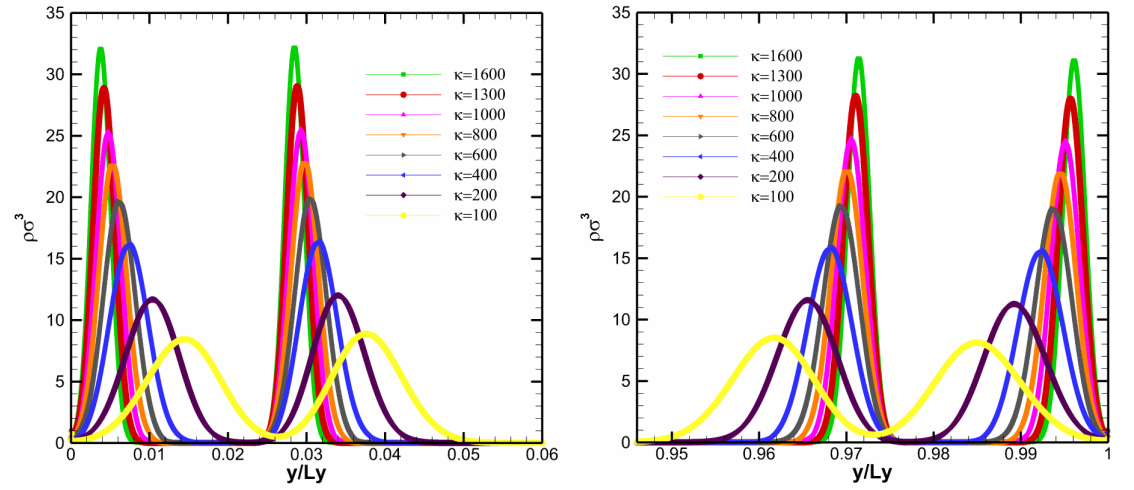

a) Lower wall b)Upper wall

Figure 7.11: Density Distribution in Solid Wall for $m_w = 2m$, $e_{ww} = 0.4$,$e_{ww} = 0.8$ for various values of stiffness constant κ.

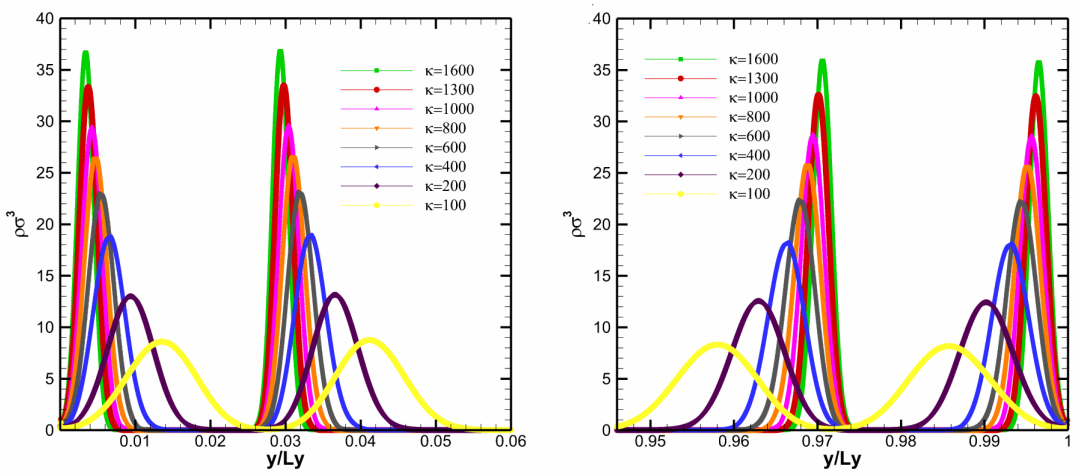

a) Lower wall b)Upper wall

Figure 7.12: Density Distribution in Solid Wall for $m_w = 2m$, $e_{ww} = 0.6$,$e_{ww} = 0.4$ for various values of stiffness constant κ.

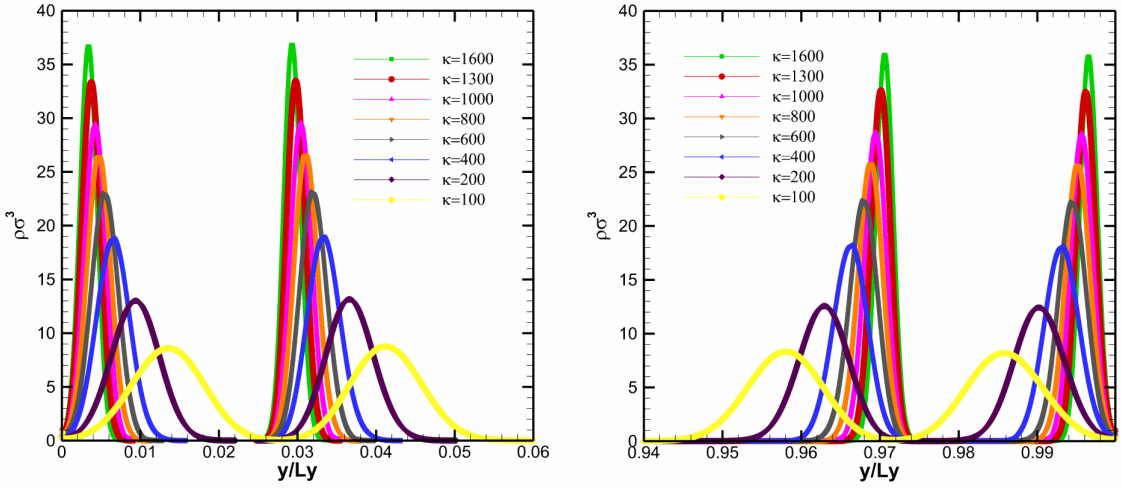

a) Lower wall b)Upper wall

Figure 7.13: Density Distribution in Solid Wall for $m_w = 2m$, $e_{ww} = 0.6$,$e_{ww} = 0.6$ for various values of stiffness constant κ.

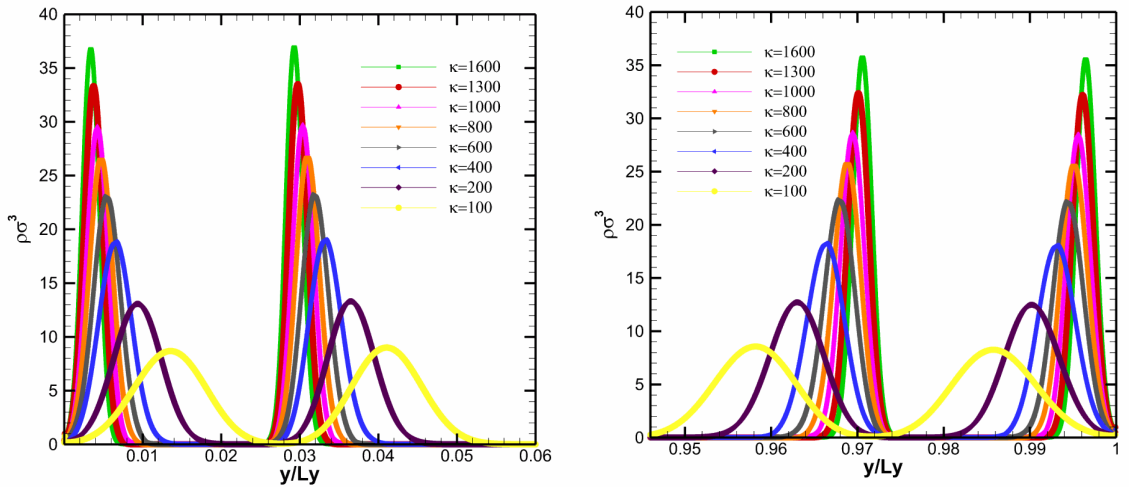

a) Lower wall b)Upper wall

Figure 7.14: Density Distribution in Solid Wall for $m_w = 2m$, $e_{ww} = 0.6$,$e_{ww} = 0.8$ for various values of stiffness constant κ.

void CalcNum(); void CalcMass(); void CalcNumDens(); void CalcDens(); void CalcTrans-Mom(); void CalcAngMom(); void CalcTransVel(); void CalcAngVel(); void CalcEkinTot(); void CalcEkinTrans(); void CalcEkinRot(); void CalcEkinInt(); void CalcEpot(); void CalcEtot(); void CalcTemp(); void CalcPressureTensor(); void CalcPressure(); void SetVelocity(); void SetTemper-ature();

private: // private attributes char m_szFileName[GRIDANALYSIS_MAX_STRING_LEN]; // name of the output file char m_szName[GRIDANALYSIS_MAX_STRING_LEN]; // name of the analysis double m_lo[3]; // lower corner of the grid double m_hi[3]; // upper corner of the grid int m_res[3]; // resolution of the grid (number of cells in each dimension) int m_nCells; // total number of cells: m_res[0]*m_res[1]*m_res[2] int m_nType; // which atom type to che //int m_nEvery; // perform calculation every m_iEvery timestep int m_nAve; // average results over m_iEvery calculations int m_nPrintGrid; //Flag to switch printing the grid on/off (0->off, otherwise->on) int m_anMQOut[GRIDANALYSIS_NUM_MQS]; // macroscopic quantities to put out int m_anMQCalc[GRIDANALYSIS_NUM_MQS]; // macroscopic quantities to calculate enum TCW {CW_NGP, CW_CIC} m_cw; // atom to grid node weighting scheme

int m_anSizeIndex; // size of the m_aIndex array int m_anSizeIndexStart; // size of the m_aIndexS array TIndexCW* m_aIndex; // cell index and weighting for each atoms int* m_anIndexStart; // array with the pointer for each atom to m_aIndex.

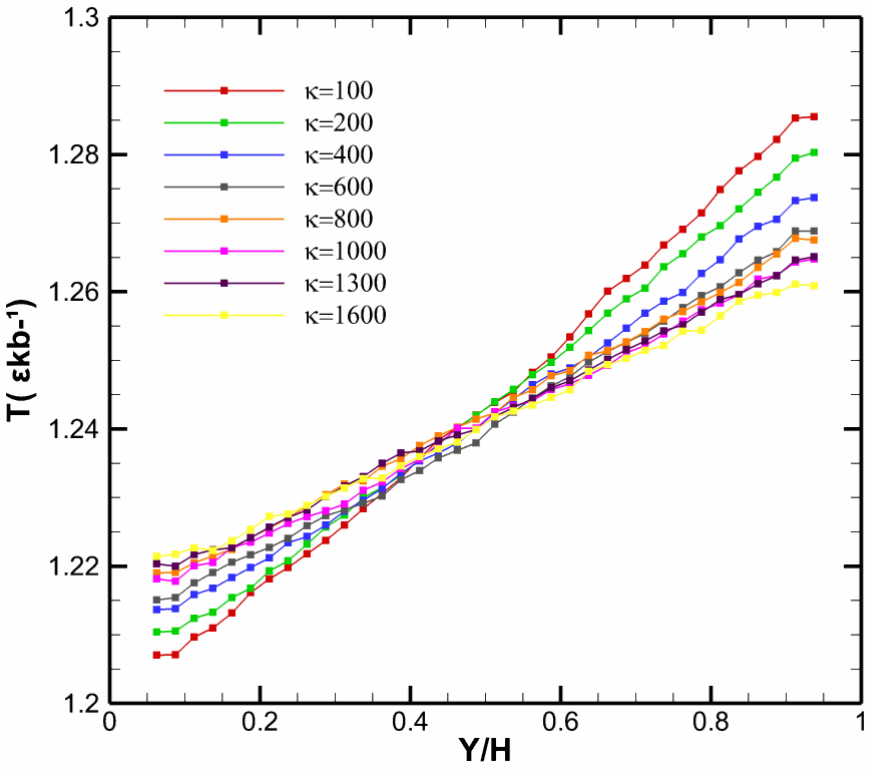

Figure 7.15: Temperature Profiles across nanopore of 10σ, for $m_w = 2m$, $e_{ww} = 0.2$, $e_{wf} = 0.4$ for various values of stiffness constant κ.

TData m_IData; // instantaneous data TData m_SData; // summed up data TData m_AData; // average data

int me,nprocs; // rank of the proces FILE* m_pFile; // pointer to the output file double m_dCell[3]; // cell size in each dimension struct { double* x; double* y; double* z; }m_CellCentre; // arrays with positions of the cell centre int m_nNumSum; // over how many times was already summed up

int m_nNumCellValues; // number of cell value outputs char m_aszCVFileName[GRIDANALYSIS_MAX_CELLV // names of the cell values files FILE* m_apCVFile[GRIDANALYSIS_MAX_STRING_LEN]; // file pointer for the files of the cell values TIndex m_aCVIndex[GRIDANALYSIS_MAX_STRING_LEN]; // index of the cell values enum TCVTYPE {CVMEASURE, CVAVERAGE} m_nCVType; // print cell values based on measurments or averages //domain stuff struct{ double half[3]; // half position of the simulation box double prd[3]; // length simulation box }m_domain;

struct TVelocity { int nOn; // flag whether to set the velocity double SetVel[3]; // velocity to be set at every measurement double* dvx, * dvy, * dvz; // translationel velocity } m_Velocity;

struct TTemperature { int nOn; // flag whether to set the temperature correction on double SetTemp; // temperature to be set at every measurement double* f; // multiplication factor

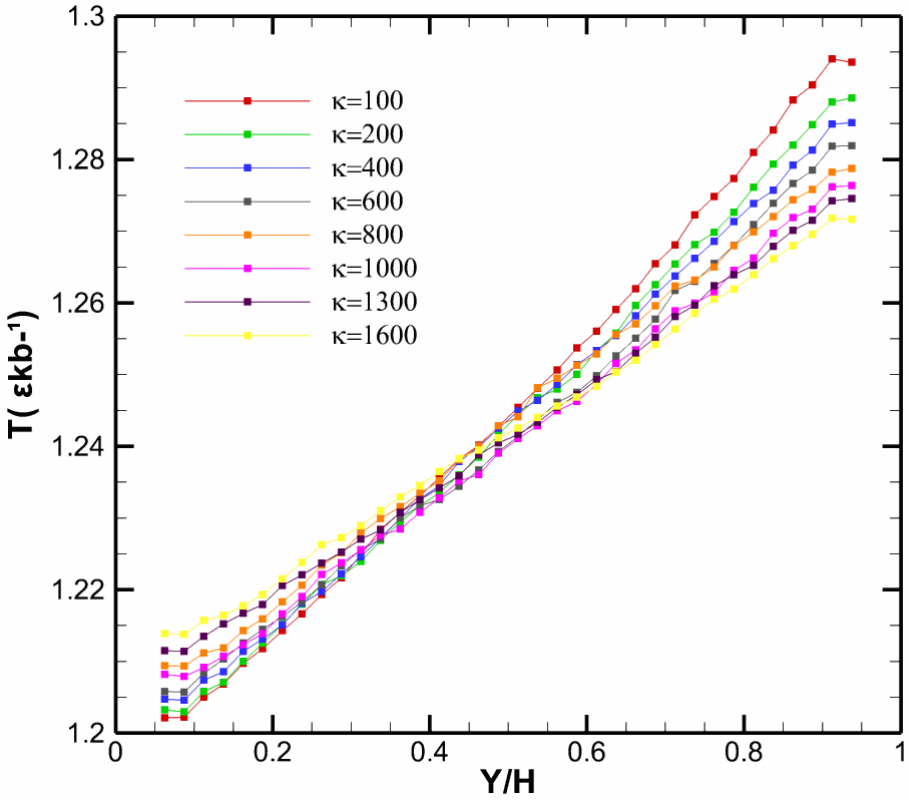

Figure 7.16: Temperature Profiles across nanopore of 10σ, for $m_w = 2m$, $e_{ww} = 0.2$, $e_{wf} = 0.6$ for various values of stiffness constant κ.

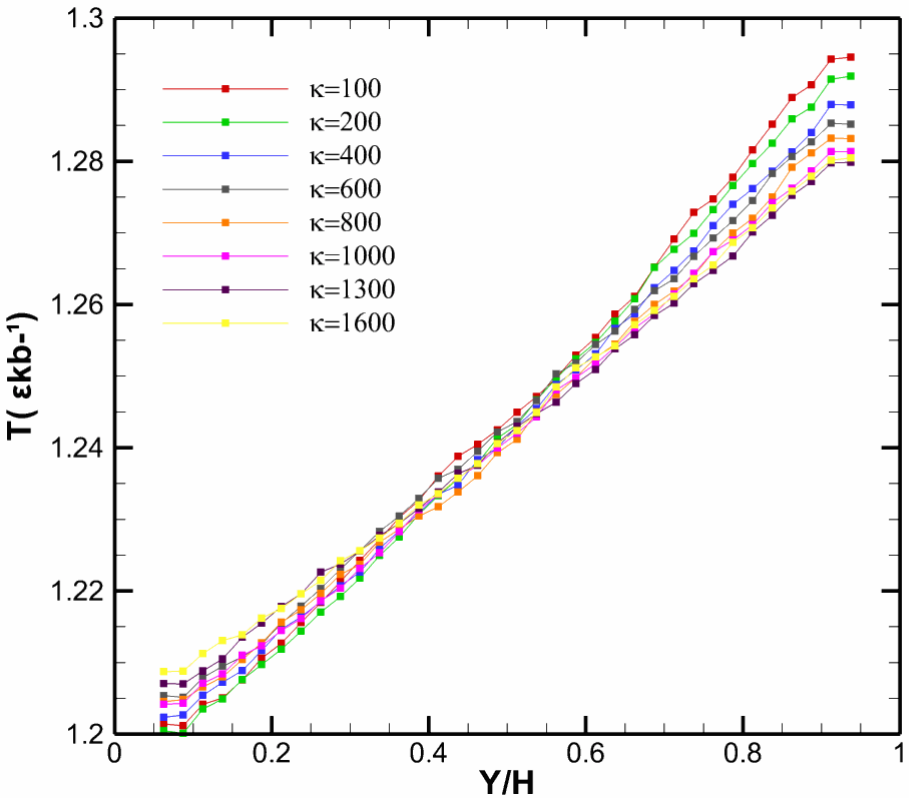

Figure 7.17: Temperature Profiles across nanopore of 10σ, for $m_w = 2m$, $e_{ww} = 0.2$, $e_{wf} = 0.8$ for various values of stiffness constant κ.

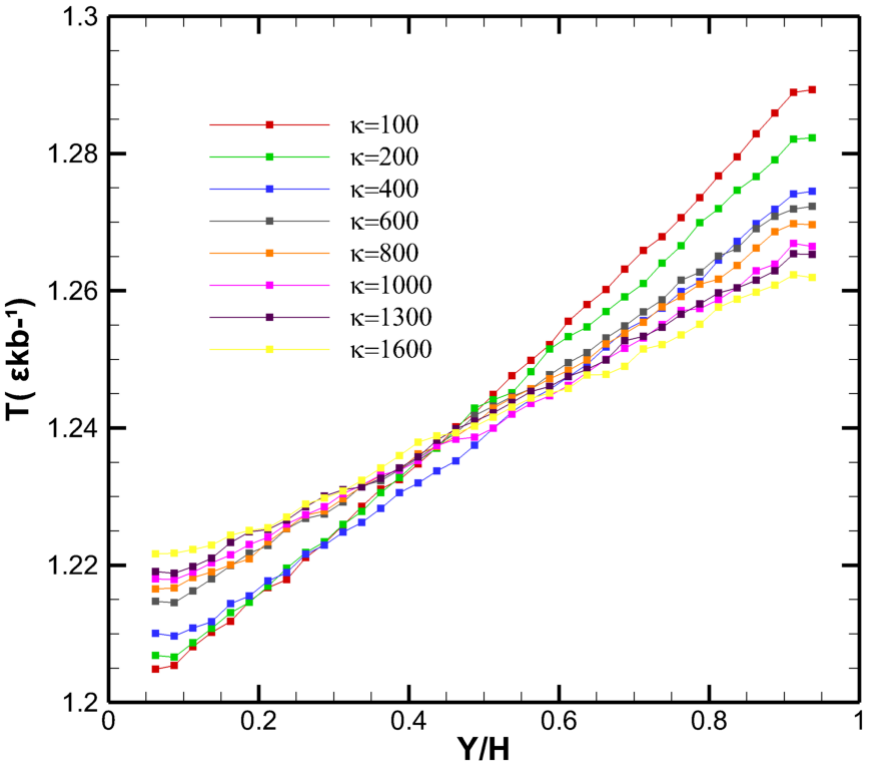

Figure 7.18: Temperature Profiles across nanopore of 10σ, for $m_w = 2m$, $e_{ww} = 0.4$, $e_{wf} = 0.4$ for various values of stiffness constant κ.

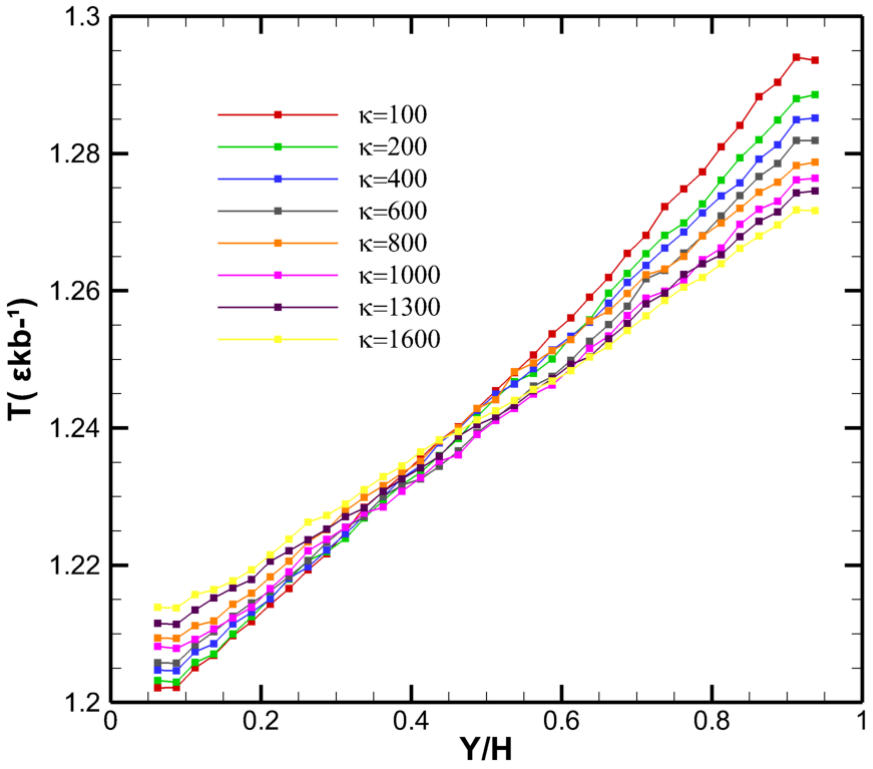

Figure 7.19: Temperature Profiles across nanopore of 10σ, for $m_w = 2m$, $e_{ww} = 0.4$, $e_{wf} = 0.6$ for various values of stiffness constant κ.

double* cax; // correction sum double* cay; // correction sum double* caz; // correction sum } m_Temperature;

int m_IgnoreVelocitiy[3]; // flags for each dimension whether to consider the velocity 0.0 in this direction

};

inline int FixGridAnalysis::GetCellIndex(int I, int J, int K) { return I*m_res[1]*m_res[2] + J*m_res[2] + K; }

inline void FixGridAnalysis::GetCellIndexInv(int C, int& I, int& J, int& K) { I = C/(m_res[1]*m_res[2]); int CR = C - I*m_res[1]*m_res[2]; J = CR/m_res[2]; K = CR - J*m_res[2]; };

}//end namespace #endif #endif

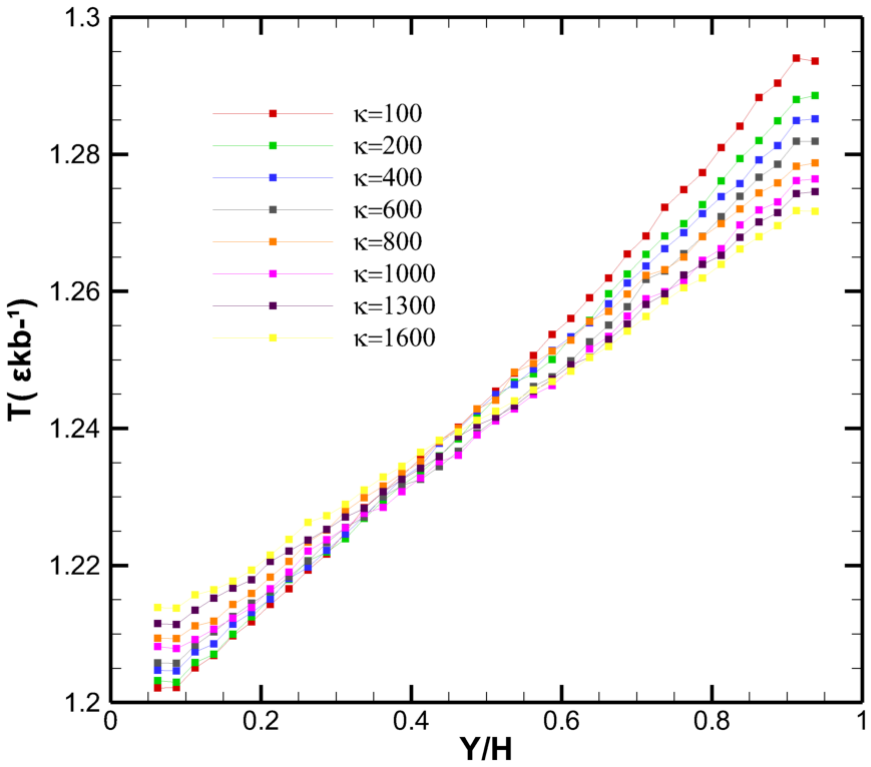

Figure 7.20: Temperature Profiles across nanopore of 10σ, for $m_w = 2m$, $e_{ww} = 0.4$ $e_{wf} = 0.8$ for various values of stiffness constant κ.

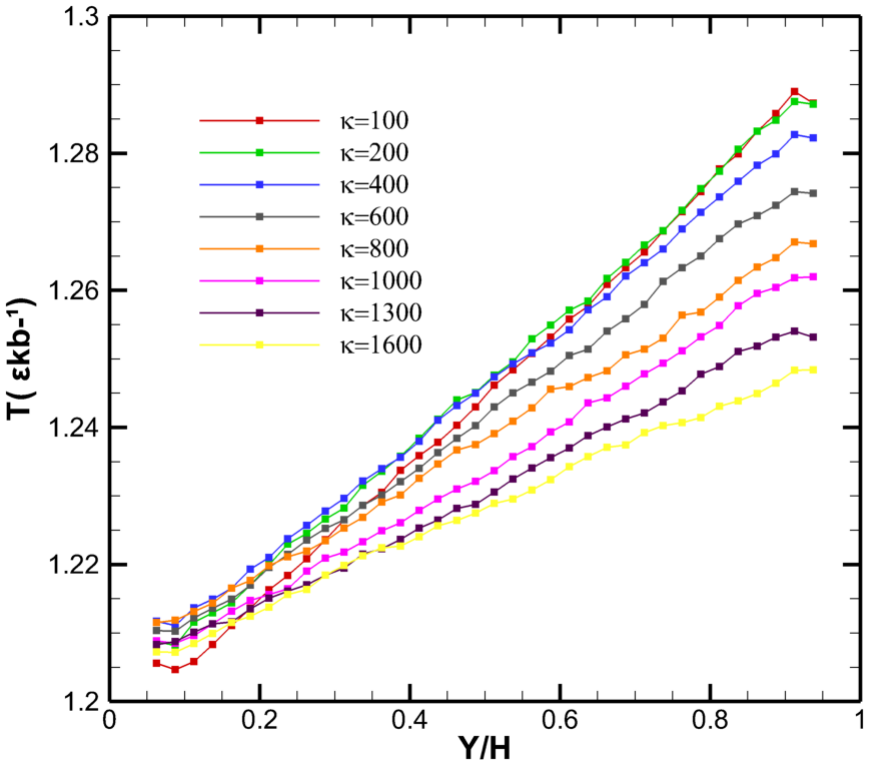

Figure 7.21: Temperature Profiles across nanopore of 10σ, for $m_w = 2m$, $e_{ww} = 0.6$, $e_{wf} = 0.4$ for various values of stiffness constant κ.

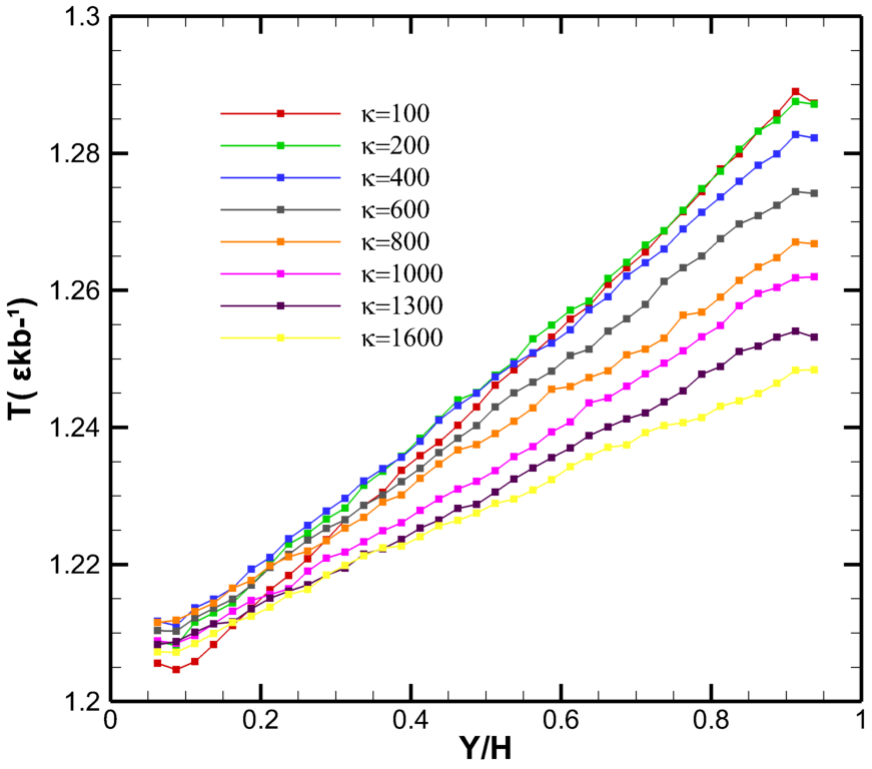

Figure 7.22: Temperature Profiles across nanopore of 10σ, for $m_w = 2m$, $e_{ww} = 0.6$, $e_{wf} = 0.6$ for various values of stiffness constant κ.

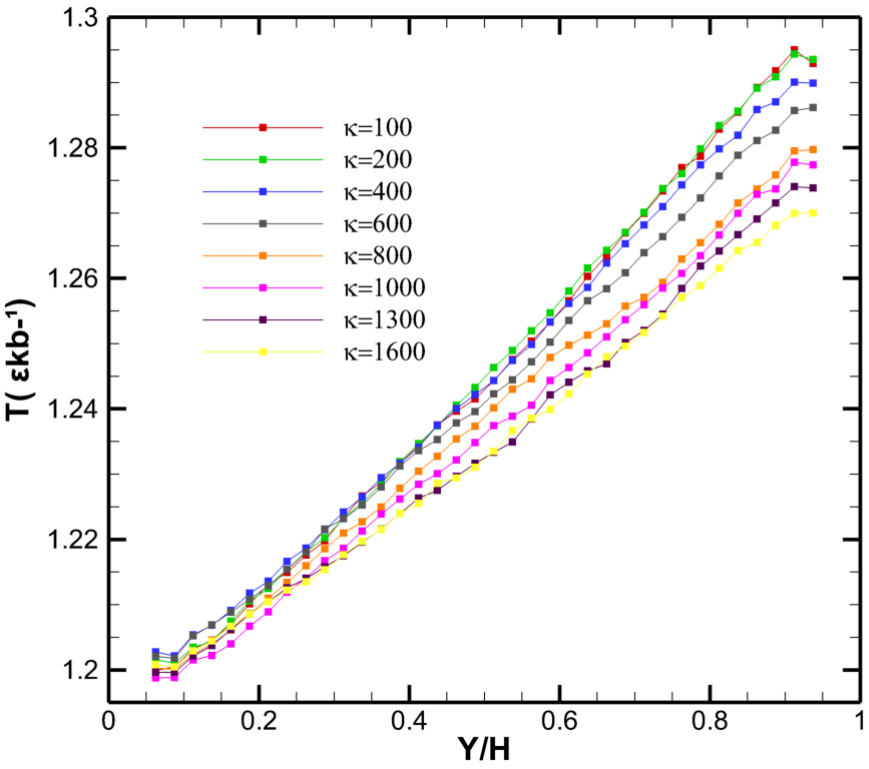

Figure 7.23: Temperature Profiles across nanopore of 10σ, for $m_w = 2m$, $e_{ww} = 0.6$, $e_{wf} = 0.8$ for various values of stiffness constant κ.